UNIVERSITY OF
Southampton
Optoelectronics
Research Centre

Towards micro-ring resonators for quantum sources and rotation sensors

Author:
Miranda Theresa TURVEY

Supervisor:
Dr. James GATES
& Prof. Peter G. R. SMITH

A thesis submitted in fulfillment of the requirements for the degree of Doctor of Philosophy

in the

Optical Engineering & Quantum Photonics Group
Zepler Institute

August 2020

Declaration of Authorship

I, Miranda Theresa TURVEY, declare that this thesis titled, "Towards micro-ring resonators for quantum sources and rotation sensors" and the work presented in it are my own. I confirm that:

- This work was done wholly or mainly while in candidature for a research degree at this University.
- Where any part of this thesis has previously been submitted for a degree or any other qualification at this University or any other institution, this has been clearly stated.
- Where I have consulted the published work of others, this is always clearly attributed.
- Where I have quoted from the work of others, the source is always given. With the exception of such quotations, this thesis is entirely my own work.
- I have acknowledged all main sources of help.
- Where the thesis is based on work done by myself jointly with others, I have made clear exactly what was done by others and what I have contributed myself.

Signed: _____

Date: _____

"Necopinatius etiam necopinatius"

("Curioser and curioser"), Ludovici Carroll, Alicia in Terra Mirabili

UNIVERSITY OF SOUTHAMPTON

Abstract

FEPS
Zepler Institute

Doctor of Philosophy

Towards micro-ring resonators for quantum sources and rotation sensors

by Miranda Theresa TURVEY

Optical ring resonators have been studied since the first lasers were produced in the late 60s. Since then, they have become established as in many and varied fields, in particular sensing, due to their ability to sense a multitude of parameters through their effect on the optical path length of the light confined within the ring. Silica, with its low loss in the near-IR, has become ubiquitous in optics. Flame hydrolysis has been used since the 80s in order to produce lowloss, high purity glass layers at high deposition rates for planar lightwave circuits, primarily silica-based. However, germania, often described as structurally analogous to silica, shows potential as an alternative as a glass-former due to its potential for outstripping silica's low loss further into the mid-IR. This work explores the development of i) Planar high germania-content glasses for damascene and UV-written ring resonators and ii) Flame hydrolysis deposition techniques for high germania-content glasses onto glass and ceramic rods for UV written and CO_2 laser-machined rod resonators. Development of these is with a view to their use in Sagnac rotation sensing and exploitation of germania's comparatively high nonlinearity to produce frequency comb sources. To that end, flame hydrolysis deposition of germanate glasses onto various substrates and geometries is explored and characterisation of these devices described.

Acknowledgements

I'd like to thank my supervisors, Peter Smith and James Gates for endless patience, support and practical assistance, along with Paula and the rest of the group, past and present, all of whom have helped me in some way at one time or another, in particular Matt Posner, Paul Gow, Senta Jantzen and Peter Cooper.

Additionally, I have to give much credit to Glenn Topley for help in design and construction of the frame for rods and holder for UV writing, Miguel Nunez-Velasquez for providing an OVD germania sample, and helpful discussions, Shahab Gorajoobi for valuable assistance with characterisation, Sarah Stebbings and my technical partners at DSTL and Pascal Del'Haye and his group at NPL for collaborating on FHD-fabricated CO_2 laser-machined rods.

Most importantly, I must thank my family for encouragement and support, especially my Mother, Rose, and Mum-in-law, Wendy. But most of all, I must thank my husband, Andy, for endless support and belief in me when I had none, and Maya, for keeping me constantly on my toes since September 2017 (& arguably before!). I could not have survived this without you...

Contents

List of Figures

List of Tables

List of Abbreviations

WGM	**W**hispering **G**allery **M**ode
WDM	**W**avelength **D**ivision **M**ultiplexing
QED	**Q**uantum **E**lectro **D**ynamics
FWM	**F**our **W**ave **M**ixing
NIST	**N**ational **I**nstitute of **S**tandards & **T**echnology
NPL	**N**ational **P**hysical **L**aboratory
GNSS	**G**lobal **N**ational **S**atellite **S**ystems
GPS	**G**lobal **P**ositioning **S**ystem
RLG	**R**ing **L**aser **G**yroscope
IFOG	**I**nterferometric **F**ibre **O**ptic **G**yroscope
SWaP	**S**ize **W**eight **a**nd **P**ower
MEMS	**M**icro **E**lectro-**M**echanical **S**ystem
DSTL	**D**efence **S**cience & **T**echnology **L**aboratory
FHD	**F**lame **H**ydrolysis **D**eposition
DUV	**D**irect **U**ltraviolet **W**riting
CCW	**C**ounter **C**lock **W**ise
CW	**C**lock **W**ise
FSR	**F**ree **S**pectral **R**ange
FWHM	**F**ull **W**idth **H**alf **M**aximum
TE	**T**ransverse **E**lectric
TM	**T**ransverse **M**agnetic
ZRO	**Z**ero **R**ate **O**utput
ARW	**A**ngular **R**andom **W**alk
ESOP	**E**igen **S**tate **O**f **P**olarization
RMOG	**R**esonant **M**icro-**O**ptical **G**yroscope
PM	**P**hase **M**odulation
PD	**P**hoto **D**iode
LIA	**L**ock- **I**n **A**mplifier
LPCVD	**L**ow **P**ressure **C**hemical **V**apour **D**eposition
RIE	**R**eactive **I**on **E**tching
ZDW	**Z**ero **D**ispersion **W**avelength
ODC	**O**xyen- **D**eficient **C**entre
OVD	**O**utside **V**apour **D**eposition
mCVD	**m**odified **C**hemical **V**apour **D**eposition
PLC	**P**lanar **L**ightwave **C**ircuit
CTE	**C**oefficient of **T**hermal **E**xpansion
VAD	**V**apour-phase **A**xial **D**eposition
peCVD	**p**lasma **e**nhanced **C**hemical **V**apour **D**eposition
RF	**R**adio **F**requency
MFC	**M**ass **F**low **C**ontroller
HF	**H**ydro **F**luoric acid
SEM	**S**canning **E**lectron **M**icroscope
EDX	**E**nergy **D**ispersive **X**-ray spectroscopy

GDMS	**G**low-**D**ischarge **M**ass **S**pectroscopy
ToFSIMS	**T**ime **o**f **F**light **S**econdary **I**on **M**ass **S**pectroscopy
PPTOFMS	**P**lasma **P**rofiling **T**ime **O**f **F**light **M**ass **S**pectroscopy
IPA	**I**so-**P**ropyl **A**lcohol
NOMV	**N**eutral **O**xygen **M**ono-**V**acancy
NODV	**N**eutral **O**xygen **D**i-**V**acancy
EPR	**E**lectron **P**aramagnetic **R**esonance

List of Symbols

L	Path length	m
r	Ring radius	m
Ω	Rate of rotation	$^\circ$ s^{-1} or rad s^{-1}
L_+	Increased path length due to Sagnac effect	m
L_-	Reduced path length due to Sagnac effect	m
t^+	Increased round-trip travel time due to Sagnac effect	s
t^-	Reduced round-trip travel time due to Sagnac effect	s
A	Area enclosed by ring	m^2
ϕ	Phase	rad
λ	Wavelength	m
k	Wavenumber	m^{-1}
$n(r)$	Refractive index	
R_1	Inner ring radius	m
R_2	Outer ring radius	m
n_1	Refractive index of ring	
n_2	Refractive index of cladding	
n_{eff}	Effective refractive index	
Ψ	Wave function	
β_θ	Constant of separation for solution of Helmholtz equation	rad m^{-1}
λ_{res}	Resonant wavelength	m
m	Mode number	
C_1, C_2, C_3, C_4	Constants for solution of the Helmholtz equation	
I_m	Modified Bessel function of the 1st kind	
J_m	Bessel function of the 1st kind	
Y_m	Modified Bessel function of the 2nd kind	
$H_m^{(2)}$	Hankel function of the 2nd kind, of order m	
E_θ	Electric field	Vm^{-1}
H_θ	Magnetic intensity	Am^{-1}
t	Self-coupling coefficient	
t^*	Self-coupling coefficient	
κ	Cross-coupling coefficient	
κ^*	Cross-coupling coefficient	
α	Round-trip loss	
E_{iw}	Electric field incident in the waveguide	Vm^{-1}
E_{tr}	Electric field coupled from the ring to the waveguide	Vm^{-1}
E_{tw}	Electric field incident on the ring	Vm^{-1}
E_{ir}	Electric field coupled back into the waveguide	Vm^{-1}
Q	Q-factor	
D	Diameter	m
P_{pd}	Power at photo-detectors	W
B	Measurement bandwidth	Hz
η	Quantum efficiency	

Ω_K	Error in angular rate due to Kerr effect	rad s^{-1}
ζ	Nonlinear susceptibility	$(m/V)^{n-1}$
F	Finesse	
ΔP	Difference in power between the CW and CCW beams	W
$\chi^{(3)}$	Third-order nonlinearity	m^2V^{-2}
ω	angular frequency	rad

Dedicated to the late Mike Garrod…

Chapter 1

Introduction

1.1 Introduction

Optical ring resonators are rings in which light is confined by the refractive index contrast between the ring and its cladding. Due to the periodic boundary condition, the field is replicated after each round-trip, and only discrete wavelengths which are integer multiples of their optical path length are supported. Enhancement of the field intensity through constructive interference of resonant wavelengths results in a spectrum of sharp resonances with extremely high Q-factors [1]. An increasingly popular subject for research, ring resonators have myriad applications in areas such as sensing, including gyroscopes [2], lasers [3][4], communications, signal processing, nonlinear optics – including frequency comb sources [5], quantum optics [1] and biological and chemical analysis [6][7].

Mathematically, the light confined within ring resonators is closely related to whispering gallery modes (WGM). The term was coined by Lord Rayleigh (John William Strutt) in 1910 to describe the apparent refocussing effect of the curved surface of the dome on sound waves in the "whispering gallery" (so-called as a whisper at one location may be heard at any other location around the circumference of the circular gallery) in the dome of St. Paul's Cathedral in 1878 [8]. He experimented using a whistle and a candle to produce and detect the resonant standing waves and most significantly, suggested that the propagation and confinement of these modes was also applicable to electromagnetic waves. This was later verified experimentally by Raman [9], complementing previous work on scattering and solutions of Maxwell's equations in dielectric spheres by Mie [10][11]and Debye [12][13].

Although many of the underlying principles of whispering gallery modes and ring resonators had been established in the early twentieth century, the potential for use in inertial sensing was not immediately apparent. The use of ring resonator-based gyroscopes as part of an inertial sensing system relies on the Sagnac effect, the proportionality of rotation rate to interference fringe shift of counter propagating beams in a rotating ring as described by Georges Sagnac in 1913[1] [14][16]. However, in Sagnac's set-up, a ring radius of 1m rotating at 10°hr^{-1} would yield a difference in path length of only approximately 4pm [17] and thus the Sagnac effect as a means of rotation sensing was deemed impractical and little research was carried out in this area for many decades. An early form of ring resonator, in the form of a looped

[1]Georges Sagnac had sought to disprove Einstein's special relativity in favour of the concept of the "aether", the medium through which electromagnetic waves were presumed to propagate according to the prevailing hypothesis of the time and believed his results did so [14] (it was correctly (relativistically) interpreted both before and after Sagnac's experiment by von Laue in 1911 [15] and Langevin in 1921 [16]). It is thus ironic that this effect in fact provides validation of the theory of relativity [16].

dielectric wire was studied by Richtmyer in 1939 and he noted the high Q [18], for which ring resonators are often cited as having great potential as sensing devices. However, it was not until the advent of the laser in the early 60s [19] that high Q optical ring resonators truly became a possibility [17], and an opportunity to exploit the Sagnac Effect as a means of rotation sensing initially using ring lasers finally presented itself.

The earliest description of the concept of a ring resonator was by Marcatili in 1969. Over the course of the following decade, ring lasers, passive fibre ring resonators [20] and finally planar ring resonators were developed [21][22], with rotation sensing using the latter suggested by Ezekiel and Balsamo [23]. An integrated optical ring resonator in silver ion-exchanged glass followed in 1983 by Walker & Wilkinson [24] and many other materials throughout the eighties and nineties and into the present [25]. Meanwhile, microfabrication techniques for planar lightwave circuits were developed [26] including UV writing [27] and novel glasses fabricated as they continue to be to this day [26], allowing low loss and high Q, amongst other useful properties, through precise fabrication and low-loss materials. Silica had become ubiquitous as a glass for fibres and photonic integrated circuits [26] due to its low loss, relative ease of producing high quality, high purity layers and strength [28] and indeed, more recent research into ring resonators is still largely carried out using silica based glasses [29]. These advances in glass fabrication enabled the use of ring resonator-based devices in wavelength division multiplexing (WDM) [30], optical delay lines [30], wavelength filters [31], label-free bio- and molecular sensing [6][7], frequency comb sources, frequency metrology [32], optical clocks [33], reversible logic [34], as a source of entangled photons [35] and in cavity QED, while reducing the footprint of these devices [13].

Due to their high Q and small mode volume, intensities in high Q ring resonators may easily reach that required for nonlinear effects at relatively low power [13], making them ideal for devices which benefit from effects such as, for example, that of four-wave mixing (FWM) in frequency combs [36], allowing a link between the microwave and optical parts of the EM spectrum [37]. Frequency combs, the culmination of work on mode-locked lasers by Hänsch beginning in the 70s, came to fruition in 1990 with the first frequency comb based on mode-locked lasers [38][39]. The first frequency comb based on a ring resonator was demonstrated in 2007 by Del'Haye et al. [40]. Since then, disc and rod resonator frequency combs have been demonstrated by Vahala et al. [5] and Papp & Diddams [41], and octave-spanning resonators by Del'Haye et al. [42], opening up the possibility of compact, self-referencing combs for frequency metrology and sensing [43].

Since the late nineties, ring and other resonator geometries for various types of sensing based on WGM has become a very popular area of research, as is the development of appropriate materials and techniques for fabrication of these devices. Current research has progressed such that Q as high as 10^{10} has been recorded in a silica resonator [32], and ring resonator-based rotation sensing is widely researched in institutions globally: At Zhejiang University in China [44], progress towards overcoming the problems of polarization [45] and the Kerr nonlinearity [46] in ring and racetrack resonators has been made along with further improvements to sensitivity via phase modulation [47]. At the National Institute for Standards & Technology (NIST) in the US and the National Physical Laboratory (NPL) in Teddington, U.K. [48] high Q CO_2 laser-machined rods are being researched and in the Vahala group

at California Institute of Technology (Caltech) dispersion control in disc resonators is showing potential [49], with much collaboration between the latter three [48][49].

1.2 Motivation

Global navigational satellite systems (GNSS) are widely used by military, commercial aerospace and consumers and have, since the emergence of the global positioning system (GPS) in the early 90s, provided an accurate system of navigation [50]. However, GNSS do not always fulfil military requirements of accuracy, availability and security: they can be spoofed, jammed [51], denied, tactically unwise and unavailable [52]. While strapdown (i.e. rigidly attached to the moving body rather than using a stable platform which remains aligned to a global frame regardless of rotation) inertial navigation technology exists and in some cases, such as that of ring laser gyroscopes (RLGs) and interferometric fibre optic gyroscopes (IFOGs), has reached commercial maturity [20]. The question of whether such technology is adequate inevitably depends on the application.

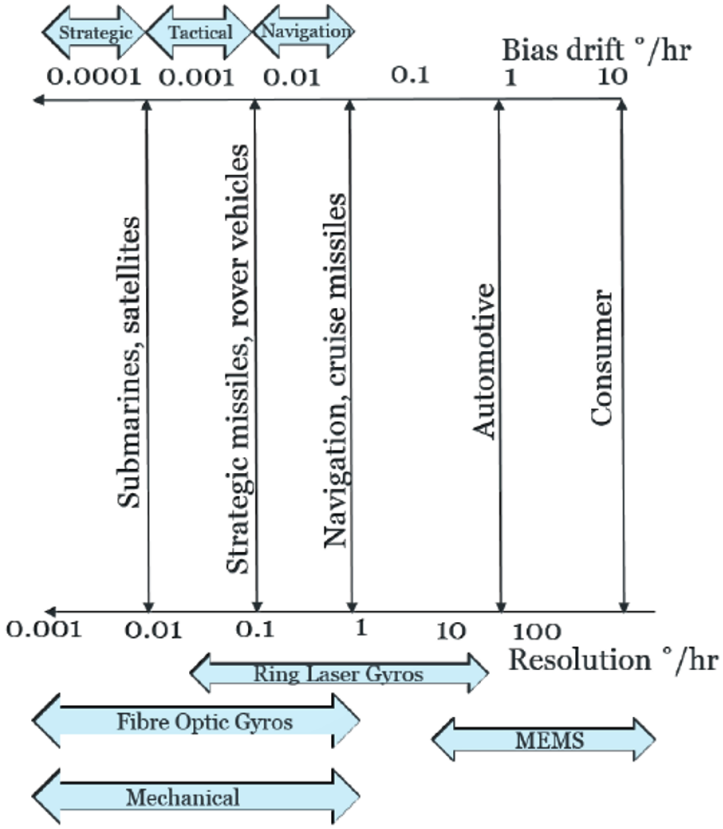

FIGURE 1.1: Approximate bias drift and resolution required for various inertial navigation applications. Diagram produced by the author having reviewed open-source literature describing typical resolution and bias drifts of common inertial sensing technologies and military requirements [2][55][56][57].

Low SWaP (size, weight and power) is often required (e.g. in satellites), as is high resolution (e.g. in strategic missiles), low bias drift over long integration periods for (submarine or subterranean navigation) and robustness, especially for applications in the field. Figure 1.1 summarises a range of applications in terms of their required resolution and bias drift, along with the main current technologies with their typical ranges of resolution and bias for comparison.

Mechanical gyroscopes have been used for many years and remain one of the most accurate methods of inertial sensing but their size makes them unsuitable for many applications and moving parts make them less durable. RLGs have good resolution and bias drift in comparison to other methods, but the resolution is nevertheless "navigation grade" ($0.01 >$ bias drift $> 0.001^{\circ}\text{hr}^{-1}$ [53]) rather than "strategic grade" ($< 0.0001\ ^{\circ}\text{hr}^{-1}$ bias drift [53]) [54] and bias drift is unacceptably high over long integration periods [20]. The large ring diameter required for high resolution makes miniaturization almost impossible [2][55][56]. RLGs also suffer from backscattering of counter-propagating beams, resulting in the lock-in effect, wherein counter-propagating beams couple to each other at low rotation rates, resulting in an apparent zero rotation rate [2]. Interferometric fibre-optic gyroscopes have better resolution and bias drift than RLGs, however, they are highly sensitive to external influences such as temperature and bias drift is still too high for applications with long integration times [20]. Both RLGs and IFOGs are unsuitable for applications where low size and weight are required (e.g. in micro/nanosatellites (see figure 1.1)), as they require extremely long path lengths on the order of 10^2 - 10^3m in order to reach "strategic" grade sensitivity to rotation [2][55][56] and require thermal control in order to do so [54], hindering miniaturization. It is also noted that many of the commercially available RLG and IFOG-based inertial navigation systems still use GNSS as a back-up or as a means of re-calibration [57]. One of the few technologies which can be easily miniaturized is micro-electro-mechanical systems (MEMS). However, these currently lack the high resolution and low bias drift required for many applications and show poor durability due to driving of the proof mass at frequencies near to resonance [54]. It is therefore reasonable to conclude that there is, at present, no technology which has all of the following:

- High resolution (on the order of metres)
- Low bias drift over long integration periods (days rather than hours)
- Small SWaP (idealy backpack-sized with a diode laser source)
- Robustness (resistance to shock, insensitivity to external influences)

A high resolution, low bias drift (i.e. stable over long integration periods), compact, robust inertial navigation system is therefore desirable. Ring resonators may be made compact, with large Q and thus resolution, are not reliant on external signals other than an appropriate laser source, are robust, durable due to the lack of moving parts and largely unaffected by external influences. There are a multitude of applications in a defence context for a high-Q ring resonator (summarised in fig. 1.2), as part of an inertial navigation/measurement system or in other applications such as label-free biosensing [6], chemical sensing [7] and quantum information processing [35]. The possibility of using diode lasers as sources [58] aids compactness and ease of deployment in the field. The development of a high Q ring resonator also lends itself to creation of a frequency comb source and the possibility of optical clocks [5], accurate clocks being another essential part of an inertial sensing system. There are many other defence applications which may be made possible by high Q ring resonators, either as the main component or part of a system, such as structural health monitoring of vehicles, microsurgery, augmented reality, wearable sensors, robotics, surveying and quantum information processing (see figure 1.2).

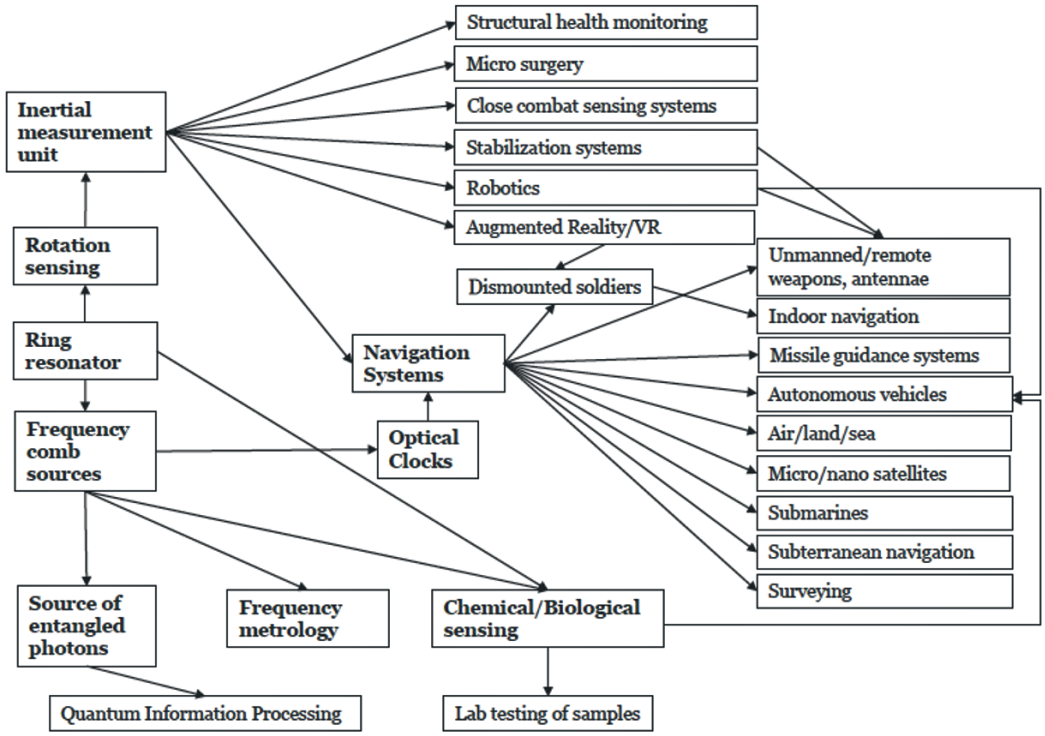

FIGURE 1.2: A summary of various ring resonator-based applications for defence. Diagram by the author, based on open-source literature.

While much of the current research into ring resonators is based on silicon or silica devices, the use of germania, a structural analogue of silica, is worthy of investigation. This is due to its potential for; lower loss at longer wavelengths, outstripping silica as wavelengths move further into the mid-IR [59]; higher nonlinear susceptibility, approximately four times that of silica [60]; and greater UV photosensitivity [61][62], offering the possibility of direct UV written rings and rods with the possibility of developing frequency comb sources.

This work is funded by DSTL, the motivation being to provide a proof-of-concept ring resonator-based rotation sensor as a platform for a compact, portable inertial sensing system, with the additional interest to further other applications, e.g. frequency combs, especially in the context of defence.

1.3 Thesis outline

The layout of this thesis is as follows:

Chapter 2 reviews the background concepts of ring resonators and their use in sensing, in particular rotation sensing, and their use as frequency comb sources. The current state of technology is discussed along with the problems to be overcome in order to make ring resonator based sensing a reality.

Chapter 3 briefly reviews literature relating to fabrication of germanate glass samples and outlines the working of the flame hydrolysis deposition (FHD) system. The deposition, consolidation and material characterisation of planar GeO_2-SiO_2 layers on silicon, silica and sapphire substrates is discussed.

Chapter 4 describes doping using both the flame hydrolysis deposition (FHD) system and solution doping and subsequent characterisation in order to produce high quality, low-loss, photosensitive germanate glass layers on silicon, silica and sapphire substrates.

Chapter 5 describes the main photosensitivity models of germanate glasses, outlines the working of the direct UV writing (DUV) system and discusses the results of direct UV writing of planar germanate glasses.

Chapter 6 describes the adaptations to FHD and UV writing systems in order to deposit photosensitive germanate glass on to silica, sapphire and alumina rods and tubes, their characterisation and discusses the results of direct UV writing of germanate rods.

Chapter 7 concerns the optical characterisation of rod and ring resonators using tapered fibre coupling, contrasted with that of a racetrack resonator fabricated by Ma's group at Zheijiang University, including collaboration on CO_2 laser-machined rod resonators with Pascal Del'Haye's group at NPL as an alternative to direct UV writing of rods.

Chapter 8 summarises the work detailed in the previous chapters, discusses what further work would be useful in order to continue the progress of the project, and concludes with what further research is necessary to make sensing, inertial sensing and frequency combs using ring resonators a reality.

1.4 Bibliography

[1] V. Van, "Optical Microring Resonators: Theory, Techniques, and Applications", *CRC Press*, 2016, ISBN 978-1-315-30350-5.

[2] C. Ciminelli, F. Dell'Olio, C. Campanella & M. N. Armenise, "Photonic Technologies for Angular Velocity Sensing", *Advances in Optics and Photonics*, 2 (2): 370-404, June 2010.

[3] A. Chiasera, Y. Dumeige, P. Feron, M. Ferrari Y. Jestin, G. N. Conti, S. Pelli, S. Soria & G. C. Righini, "Spherical Whispering-Gallery-Mode Microresonators", *Laser and Photonics Review*, 4 (3): 457-482, 2010.

[4] O. Schwelb, "Transmission, group delay, and dispersion in single-ring optical resonators and add/drop filters- a tutorial overview", *J. Lightwave Tech.*, 22 (5): 1380-1394, May 2004.

[5] S. B. Papp, K. Beha, P. Del'Haye, F. Quinlan, H. Lee, K. J. Vahala & S. A. Diddams, "Microresonator Frequency Comb Optical Clock", *Optica*, 1 (1): 10-14, July 2014.

[6] M. S. Luchansky and R. C. Bailey, "Ring Resonator Optical Gyroscopes: Parameter Optimization and Robustness Analysis", *Analytical Chemistry*, 84 (2): 793-821, January 2012.

[7] Y. Sun & X. Fan," Optical ring resonators for biochemical and chemical sensing", *Anal. Bioanal. Chem.*, (399): 205-211, 2011.

[8] Strutt, John William, " The Problem of the Whispering Gallery", *Cambridge Library Collection - Mathematics*, (5): 617-620, 2009.

[9] C. V. Raman & G. A. Sutherland, "Whispering Gallery Phenomena at St. Paul's Cathedral", *Nature*, (108): 42, 1921.

[10] G. Mie, "Beiträge zur Optik trüber Medien, speziell kolloidaler Metallösungen" ("Contributions to the optics of turbid media, particularly of colloidal metal solution"), 25 (3): 377-445, *Ann. Phys. Lpz.*, 1908.

[11] T. Wriedt & W. Hergert (Eds.), "The Mie Theory: Basics and Applications", Vol. 169 of Springer Series in Optical Sciences 169, pages 1-51, *Springer-Verlag Berlin Heidelberg*, 2012, ISBN 978-3-642-28738-1.

[12] P. Debye, "Der Lichtdruck auf Kugeln von beliebigem Material", *Ann. Phys. Lpz.*, 335 (11): 57-136, 1909.

[13] D. V. Strekalov, C. Marquandt, A. B. Matsko, H. G. L. Schwefel & G. Leuchs, "Nonlinear and quantum optics with whispering gallery resonators", *J. Optics*, (18): 1-43, November 2016.

[14] H. C. Lefevre, "The fiber-optic gyroscope, a century after Sagnac's experiment: The ultimate rotation-sensing technology?", *R. C. Physique*, (15): 851-858, 2014.

[15] M. von Laue,"Über einen Versuch zur Optik der bewegten Körper", Münchener Sitzungsberichte 405-412, July 1911 (Wikisource translation, "On an experiment on the optics of moving bodies", 2017).

[16] G. Pascoli, "The Sagnac effect and its interpretation by Paul Langevin", *C. R. Physique*, (18): 563-569, 2017.

[17] W. W. Chow, J. Gea-Banacloche, L. M. Pedrotti, V. E. Sanders, W. Schleich & M. O. Scully, "The ring laser gyro", *Rev. Mod. Phys.*, 57 (1): 61-104, January 1985.

[18] R. D. Richtmyer, "Dielectric resonators", *J. Appl. Phys.*, 10 (6): 391-398, 1939.

[19] C. G. B. Garrett, W. Kaiser & W. L. Bond, "Stimulated Emission into Optical Whispering Modes of Spheres", *Phys. Rev.*, 124 (6): 1807-1809, December 1961.

[20] V. M. N. Passaro, A. Cuccovillo, L. Vaiani, M. De Carlo & C. E. Campanella, "Gyroscope Technology and Applications: A Review in the Industrial Perspective", *Sensors*, (17): 2284-2305, October 2017.

[21] M. Miyagi & G. L. Yip, "Design theory of high-Q optical ring resonator with asymmetric three-layered dielectrics", *Opt. Quantum Electron.*, 10 (5): 425-433, 1978.

[22] T. Itanami & S. Shindo, "Channel Dropping Filter for Millimeter-Wave Integrated Circuits", *IEEE Transactions on Microwave Theory and Techniques*, MTT-26 (10): 759-764, October 1978.

[23] S. Ezekiel & S. R. Balsamo, "Passive ring resonator laser gyroscope", *Appl. Phys. Lett.*, 30 (9): 478-480, May 1977.

[24] R. G. Walker & C. D. W. Wilkinson, "Integrated optical ring resonators made by Silver Ion Exchange in Glass", *Appl. Opt.*, 22 (7): 1029-1035, April 1983.

[25] F. Morichetti, C. Ferrari, A. Canciamilla & A. Melloni, "The first decade of coupled resonator optical waveguides: Bringing Slow Light to Applications", *Laser & Photonics Rev.*, 6 (1): 74-96, 2012.

[26] G. C. Righini & A. Chiappini, "Glass optical waveguides: a review of fabrication techniques", *Opt. Eng.*, 53 (7): 7819-1-7819-14, July 2014.

[27] G. D. Maxwell & B. J. Ainslie, "Demonstration of a directly written directional coupler using UV-induced photosensitivity in a planar silica waveguide", *Electronics Lett.*, 31 (2): 95-96, January 1995.

[28] J. Ballato & P. Dragic, "Rethinking Optical Fiber: New Demands, Old Glasses", *J. Am. Ceram. Soc.*, 96 (9): 2675-2692, 2013.

[29] G. C. Righini, Y. Dumeige, P. Feron, M. Ferrari, G. Nunzi Conti, D. Ristic & S. Soria, "Whispering gallery mode microresonators: Fundamentals and applications", *Rivista Del Nuovo Cimento*, 34 (7): 435-488, 2011.

[30] W. Bogaerts, P. De Heyn, T. Van Vaerenbergh, K. DeVos, S. Kumar Selvaraja, T. Claes, P. Dumon, P. Bienstman, D Van Thourhout & R. Baets, "Glass optical waveguides: a review of fabrication techniques", *Laser Photonics Rev.*, 6 (1): 47-73, 2012.

[31] D. H. Geuzebrook & A. Driessen, "Ring Resonator-based wavelength filters", *Phys. Rev. Lett.*, (107): 063901, 2018.

[32] A. Pasquazi, M. Peccianti, L. Razzari, D. J.Moss, S. Coen, M. Erkintalo, Y. K. Chembo, T. Hansson, S. Wabnitz, P. Del'Haye, X. Xue, A. M. Weiner, R. Morandotti, "Micro-combs: A novel generation of optical sources", *Phys. Reports*, (729): 1-81, 2018.

[33] T. Kippenberg, "Microresonator-Based Optical Clock", *Nature Photonics*, 6 (6): 440-449, July 2012.

[34] Y. Tian, Z. Liu, T. Ying, H. Xiao, Y. Meng, L. Deng, Y. Zhao, A. Guo, M. Liao, G. Liu & J. Yang, "Experimental demonstration of an optical Feynman gate for reversible logic operation using silicon micro-ring resonators", *Nanophotonics*, 7 (1): 333-337, 2018.

[35] D. Grassani, S. Azzini, M. Liscidini, M. Galli, M. J. Strain, M. Sorel, J. E. Sipe, & D. Bajoni, "Micrometer-Scale Integrated Silicon Source of Time-Energy Entangled Photons", *Optica*, 2 (2): 88-94, February 2015.

[36] M. Ferrera, D. Duchesne, L. Razzari, M. Peccianti, Morandotti, Cheben, S. Janz, X. Xu, B. E. Little, S. Chu & D. J. Moss, "Low power four wave mixing in an integrated, micro-ring resonator with Q = 1.2 million", *Optics Express*, 17 (16): 14098-14103, August 2009.

[37] J. Ye, H.Schnatz & L.W. Hollberg, "Optical Frequency Combs", *IEEE J. Quantum Electronics*, 9 (4): 1236-1239, July 2003.

[38] T.W. Hänsch, "A Proposed Sub-Femtosecond Pulse Synthesizer Using Separate Phase-Locked Laser Oscillators", *Optics Comms.*, 80 (1): 440-449, December 1990.

[39] T.W. Hänsch, "Passion for Precision" (Nobel Lecture), *Euro. J. Chem. Phys & Phys. Chem.*, (7): 1170-1187, April 2006.

[40] P. Del'Haye, A. Schliesser, O. Arcizet, T. Wilken, R. Holzwarth & T. J. Kippenberg, "Optical frequency comb generation from a monolithic microresonator", *Nature*, (450): 1214-1217, December 2007.

[41] S. B. Papp & S. A. Diddams, "Spectral and temporal characterization of a fused quartz microresonator optical frequency comb", *Phys. Rev. A*, 84 (7): 053833-1-053833-7, 2011.

[42] P. Del'Haye, T. Herr, E. Gavartin, M. L. Gorodetsky, R. Holzwarth & T. J. Kippenberg, "Octave Spanning Tunable Frequency Comb from a Microresonator", *Phys. Rev. Lett.*, (107): 063901, 2011.

[43] S. Diddams, "The evolving optical frequency comb", *J. Opt. Soc. Am. B*, 27

(11): 51-62, 2010.

[44] H. Ma, S.Wang & Z. Jin, "Measurements of the excess loss of the crossed waveguide using optical waveguide ring resonators", *Optics Comms.*, (281): 6016-6018, December 2008.

[45] H. Ma, Y. Yan, Y. Chen & Z. Jin, "Improving Long-Term Stability of a Resonant Micro-Optic Gyro by Reducing Polarization Fluctuations", *IEEE Photonics*, 4 (6): 2372-2381, December 2012.

[46] H. Ma, X. Li, G. Zhang & Z. Jin, "Reduction of optical Kerr-effect induced error in a resonant micro-optic gyro by light-intensity feedback technique", *Appl. Optics*, 53 (16): 3465-3472, May 2014.

[47] L. Wang, H. Li, J. Zhang, H. Ma, X. Li & Z. Jin, "Measurements of the excess loss of the crossed waveguide using optical waveguide ring resonators", *Optics Comms.*, 387: 18-23, November 2017.

[48] S. B. Papp, P. Del'Haye & S. A. Diddams, "Mechanical Control of a Microrod-Resonator Optical Frequency Comb", *Physical Review X*, 36 (3): 1-7, March 2013.

[49] K. Y. Yang, K. Beha, D. C. Cole, X. Yi, P. Del'Haye, H. Lee, J. Li, D. Y. Oh, S. A. Diddams, S. B. Papp & K. J. Vahala, "Broadband Dispersion-Engineered Microresonator on a Chip", *Nature Photonics*, 6 (3): 440-449, July 2016.

[50] J. G. McNeff, "The Global Positioning System", *IEEE Transactions on Microwave Theory & Techniques*, 50 (3): 645-652, March 2002.

[51] R. T. Ioannides, T. Pany, & G. Gibbons, "Known vulnerabilities of global navigation satellite systems, status, and potential mitigation techniques", *Proceedings of the IEEE*, 104 (6): 1174-1194, June 2016.

[52] Y. Wu, H. Zhu, Q. Du & S. Tang, "A Survey of the Research Status of Pedestrian Dead Reckoning Systems Based on Inertial Sensors", *Int'l J. Automation & Computing*, 16 (1): February 2019.

[53] J. J. Allen, "Micro-System Inertial Sensing Technology Overview", Sandia Report produced for the US Department of Energy, April 2009.

[54] M. A. Guillen-Torres, "Feasibility of Optical Gyroscopic Sensors in Silicon-On-Insulator Technology", (Thesis), University of British Columbia, August 2015.

[55] M. A. Guillen-Torres, E. Cretu, N. A. F. Jaeger & L. Chrostowski, "Ring Resonator Optical Gyroscopes: Parameter Optimization and Robustness Analysis", *J. Lightwave Tech.*, 30 (12): 1802-1817, June 2012.

[56] F. Dell'Olio, T. Tatoli, C. Ciminelli and M. N. Armenise, "Recent Advances in Miniaturized Optical Gyroscopes", *J. Europ. Opt. Soc. Rap. Public*, 9 (9): 14013-1-14013-14, March 2014.

[57] K. Li, B. Hu, L. Chang & Y. Li, "Comparison of direct navigation mode and

indirect navigation mode for integrated SINS/GPS", *Transactions of the Institute of Meas. & Control*, 38 (1): 3-13, 2016.

[58] N. G. Pavlov, S. Koptyaev, G. V. Lihachev, A. S. Voloshin, A. S. Gorodnitskiy, M. V. Ryabko, S. V. Polonsky & M. L. Gorodetsky, "Narrow-linewidth lasing and soliton Kerr microcombs with ordinary laser diodes", *Nature Photonics*, (12): 694-698, November 2018.

[59] S. Shibata, U Y. Fukui, T. Oonishi, T. Yano, M. Yamane & S. Sakaguchi, "Intrinsic Optical Losses of GeO_2-P_2O_5-Al_2O_3 Glasses for Optical Fibers", *Opt. Fiber Tech.*, (3): 90-95, 1997.

[60] M. J. Holmes, D. L. Williams & R. J. Manning, "Highly Nonlinear Optical Fiber for All-Optical Processing Applications", *IEEE Photonics Tech. Lett.*, 7 (345): 1045-1047, September 1995.

[61] C. Jing, H. Shan, C. Zhang & J. Chu, "Preparation of thick GeO_2 glass film with high UV photosensitivity", *J. Non-Crys. Sol.*, (356): 2884-2888, 2010.

[62] Y. Watanabe, J. Nishii, H. Moriwaki, G. Furuhashi, H. Hosono & H. Kawazoe, "Permanent refractive-index changes in GeO_2 glass slabs induced by irradiation with sub band gap light", *J. Non-Crys. Solids*, (239): 104-107, 1998.

Chapter 2

Background

2.1 Introduction

Ring resonator-based rotation sensing relies on the Sagnac effect, the rotation-induced phase shift between counter propagating beams confined in a circular path. This chapter explains the Sagnac effect with reference to its application to passive ring resonator-based rotation sensing devices. Ring resonators provide an ideal geometry for Sagnac effect-based gyroscopes as their potential for high Q makes compact size possible while retaining high resolution. Ring resonator principles are outlined with discussion of the practical considerations, fabrication challenges and requirements for their use in angular rate sensing. Optical gyroscopes in general are discussed, including the figures of merit used to assess their performance and the current state of research concerning rotation sensing. The influence of material on ring resonator parameters, rationale for fabricating such a device in glass, and use of germanate glasses is considered.

2.2 The Sagnac effect

The Sagnac effect concerns counter-propagating beams of light in a rotating loop. There is an effective reduction in path length, L, for the beam travelling against the direction of rotation and a corresponding increase for the other (see Fig. 2.1).

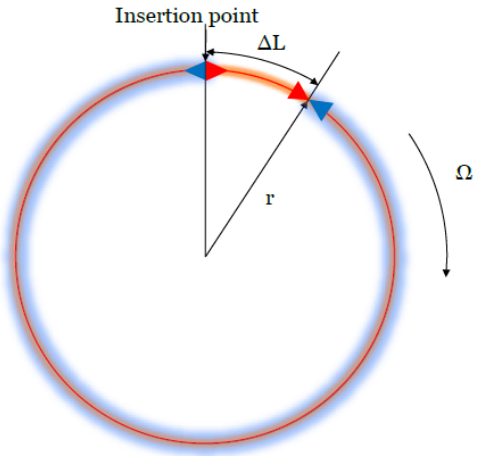

FIGURE 2.1: The Sagnac effect in a ring; Ω and r represent the rate of clockwise rotation and radius of the ring respectively. Blue denotes the CCW-travelling beam; red the CW; arrows indicate start and end of their respective path lengths.

This results in a phase difference between the two beams which is directly proportional to the rate of rotation, allowing calculation of the latter. The difference in path length between the two beams is given by $\Delta L = L^+ - L^-$, and their respective path lengths are:

$$L^+ = ct^+ = 2\pi r + \Omega r t^+ \tag{2.1}$$

$$L^- = ct^- = 2\pi r - \Omega r t^- \tag{2.2}$$

Where Ω, r, c, t+ and t- denote the rate of rotation, the radius of the ring, speed of light in a vacuum and the increased and reduced travel times for one revolution measured from the insertion point. This moves the insertion point by a distance ΔL along the circumference of the ring due to rotation for the CW and CCW beams respectively. Solving for t+ and t-, the time difference, Δt, between the CW and CCW beams reaching the insertion point is given by [1]:

$$\Delta t = \frac{4\Omega \cdot A}{c^2 - r^2\Omega^2} \tag{2.3}$$

Where A represents the area of the loop, i.e. πr^2. As $c^2 \gg r^2\Omega^2$, this is approximated to:

$$\Delta t = \frac{4\Omega \cdot A}{c^2} \tag{2.4}$$

As the phase shift, $\Delta\phi$, is:

$$\Delta\phi = \frac{2\pi\Delta L}{\lambda} \tag{2.5}$$

where $\Delta L = c\Delta t$, it follows that $\Delta\phi$, substituting in equation 2.4 is [1]:

$$\Delta\phi = \frac{8\pi\Omega \cdot A}{\lambda c} \tag{2.6}$$

The above equations are for the Sagnac effect in a vacuum. The presence of a dielectric medium introduces a difference in group velocity of the two beams. However, the resultant time and phase differences are independent of the refractive index and are thus identical to those given for the vacuum case for a first-order approximation [2]. As per equation 2.6, the phase shift between the two beams increases with the area of the ring, thus the minimum detectable rotation rate decreases correspondingly, so compact design of a Sagnac effect-based rotation sensor means that the device requires additional enhancement of the resolution in order to sense low rates of rotation. In the case of ring resonators, this is achieved via the high Q or, in a fibre ring gyroscope, by the use of multiple loops of fibre.

2.3 Ring resonator principles

2.3.1 Relevant equations, modes of planar ring resonators

A ring resonator consists of an optical waveguide in the form of a ring. Coupled light is confined by the refractive index contrast between the ring and the cladding. Resonance occurs when the optical path length, L, is an integer multiple of the wavelength of the light entering the ring. The modes in a planar ring resonator are governed by the wave equation and the time-independent solutions to it are reached via the Helmholtz equation with appropriate boundary conditions. A good description of the process for solving modes in a ring resonator is given by Van in [3].

$$\nabla^2 A + k^2 A = 0 \qquad \text{(generalised form of the Helmholtz equation)} \tag{2.7}$$

Where A represents the field and k the wavenumber where k=ω/c. The ring is considered in two dimensions using polar coordinates, with n_1 representing the refractive index of the ring and n_2 the refractive index of the cladding. Thus n(r) may be described as below:

$$n(r) = \begin{cases} n_1, & R_1 \leq r \leq R_2 \\ n_2, & r < R_1, r > R_2 \end{cases} \tag{2.8}$$

The Helmholtz equation then becomes:

$$\nabla^2 A + k^2 A = \frac{\partial^2 A}{\partial r^2} + \frac{1}{r}\frac{\partial A}{\partial r} + \frac{1}{r^2}\frac{\partial A^2}{\partial \theta^2} + n^2(r)k^2 A = 0 \tag{2.9}$$

$$A(r,\theta) = \begin{cases} H_z, & \text{quasi-TE modes} \\ nE_z, & \text{quasi-TM modes} \end{cases} \tag{2.10}$$

Equation 2.9 may be solved by separation of variables, where A(r, θ) = Ψ(r)Θ(θ):

$$\frac{\partial^2 \Theta}{\partial \theta^2} = \beta_\theta \Theta = 0 \tag{2.11}$$

$$\frac{\partial^2 \Psi}{\partial r^2} + \frac{1}{r}\frac{\partial \Psi}{\partial r} + \left[n^2(r)k^2 - \frac{\beta_\theta^2}{r^2} \right] \Psi = 0 \tag{2.12}$$

where β_θ^2 is the constant of separation and in this case the angular propagation constant. Since the ring supports only wavelengths which fit into it an integer number of times, $\beta_\theta = \frac{2\pi R n_{eff}}{\lambda}$= m, thus equation 2.11 has the boundary condition $\Theta(\theta) = \Theta(\theta + 2\pi)$ and its solutions are:

$$\Theta(\theta) = e^{im\theta} \qquad m = 0, 1, 2, 3... \tag{2.13}$$

Where m is the azimuthal mode number. This results in the resonance condition:

$$\lambda_{res} = \frac{n_{eff} L}{m} \qquad m = 1, 2, 3... \tag{2.14}$$

Equation 2.12 may now be written as:

$$\frac{\partial^2 \Psi}{\partial r^2} + \frac{1}{r}\frac{\partial \Psi}{\partial r} + \left[n^2(r)k^2 - \frac{m^2}{r^2} \right] \Psi = 0 \tag{2.15}$$

and its solutions are cylindrical harmonics known as Bessel functions:

$$\Psi(r) = \begin{cases} C_1 I_m(n_2 kr) & r < R_1 \\ C_2 J_m(n_1 kr) + C_3 Y_m(n_1 kr) & R_1 \leq r \leq R_2 \\ C_4 H_m^{(2)}(n_2 kr) & r > R_2 \end{cases} \tag{2.16}$$

Where I_m represents a modified Bessel function of the 1st kind, J_m a Bessel function of the 1st kind, Y_m a Bessel function of the 2nd kind, otherwise known as a Neumann function and H_m^2 a Hankel (also known as a Bessel function of the 3rd kind) function of the 2nd kind of order m. The further boundary conditions that Ψ is continuous at r=R, that E_θ is proportional to $\frac{1}{n^2}$ times the derivative of Ψ with respect to r for TE modes and that H_θ is proportional to the derivative of Ψ with respect to r for TM modes, allow the determination of the constants C_1, C_2, C_3 and C_4, resulting in the following expression [3]:

$$\Psi(r) = \frac{sI_m'(n_2 kR_1)Y_m(n_1 kR_1) - I_m(n_2 kR_1)Y_m'(n_1 kR_1)}{sH_m^{(2)'}(n_2 kR_2)Y_m(n_1 kR_2) - H_m^{(2)}(n_2 kR_2)Y_m'(N_1 kR_2)} \tag{2.17}$$

Where s = n_1=n_2 for TE modes and n_2=n_1 for TM.

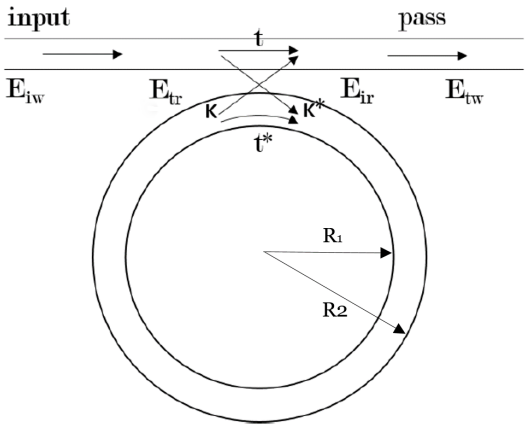

FIGURE 2.2: All-pass Ring Resonator or Notch Filter: t, κ and α represent the self-coupling coefficients, cross-coupling coefficients and decay constant respectively. E_{iw}, E_{tr}, E_{ir} and E_{tw} represent the electric fields incident in the waveguide, coupled from the ring to the waveguide, incident on the ring and coupled back into the waveguide.

The simplest form of a ring resonator is the all-pass or notch filter, shown in figure 2.2. Its spectrum consists of a series of evenly spaced resonant frequencies given by equation 2.14, their separation, known as the free spectral range, is given by equation 2.18 and shown in figure 2.3.

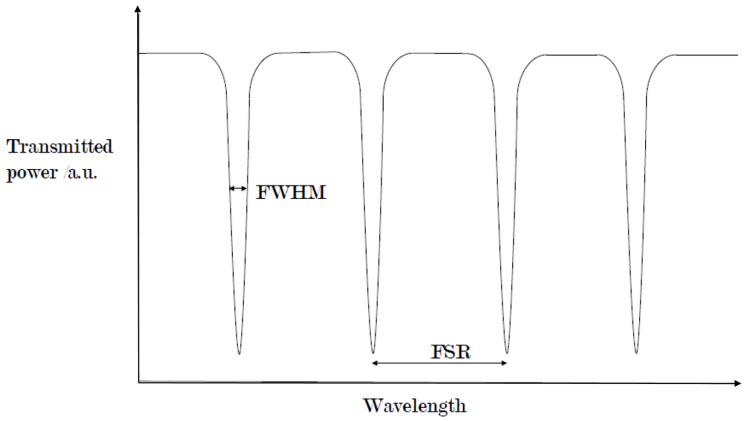

FIGURE 2.3: Ring resonator spectrum showing Free Spectral Range (FSR) and Full Width Half Maximum (FWHM).

$$FSR = \frac{\lambda^2}{n_{eff}L} \tag{2.18}$$

Coupling into the ring may be via a waveguide, prism, or tapered or angle-polished fibre and will require phase matching to the ring resonator modes for efficiency. In all of these the methods the electric field "spills out" and couples into the ring via evanescent tunnelling, its modes described by Hankel functions. Phase matching of the fibre and ring modes is required for efficient coupling. The field increases exponentially per round trip but is limited by the cavity decay rate, α [4], as per equation 2.19:

$$E_{tr} = \alpha e^{i\theta} E_{ir} \tag{2.19}$$

Where θ represents the phase and α the round trip loss in which we may include contributions from various loss mechanisms including coupling losses, with α=1 corresponding to a lossless cavity. A transfer matrix is given in [4] as below:

$$\begin{bmatrix} E_{tw} \\ E_{ir} \end{bmatrix} = \begin{bmatrix} t & \kappa \\ -\kappa^* & t^* \end{bmatrix} \begin{bmatrix} E_{iw} \\ E_{tr} \end{bmatrix} \tag{2.20}$$

Where the self-coupling and cross-coupling coefficients, t and κ, obey the coupling condition given below:

$$|t|^2 + |\kappa|^2 = 1 \tag{2.21}$$

From the transfer matrix given in 2.20, equation 2.19 and normalizing E_{iw} for simplicity, we obtain:

$$E_{tw} = t + \alpha\kappa e^{i\theta} E_{ir} \tag{2.22}$$

$$E_{ir} = -\kappa^* + \alpha t^* e^{i\theta} E_{ir} \tag{2.23}$$

With substitution and rearrangement, we obtain:

$$E_{ir} = \frac{-\kappa^*}{-\alpha t^* e^{i\theta} + 1} \tag{2.24}$$

$$E_{tr} = \frac{-\alpha\kappa^*}{-\alpha t^* + e^{-i\theta}} \tag{2.25}$$

$$E_{tw} = \frac{te^{-i\theta} - \alpha}{-\alpha t^* + e^{-i\theta}} \tag{2.26}$$

Circulating power in the ring is thus given by:

$$|E_{ir}|^2 = \frac{\alpha^2(1-|t|^2)}{1+\alpha^2|t|^2 - 2\alpha|t|cos(\theta+\phi)} = \frac{\alpha^2(1-|t|^2)}{(1-\alpha|t|)^2} \tag{2.27}$$

And the power in the waveguide is given by:

$$|E_{tw}|^2 = \frac{\alpha^2+|t|^2 - 2\alpha|t|cos(\theta+\phi)}{1+\alpha^2|t|^2 - 2\alpha|t|cos(\theta+\phi)} = \frac{(\alpha-|t|)^2}{(1-\alpha|t|)^2} \tag{2.28}$$

When the cavity decay rate is smaller than the cavity coupling rate, i.e. $\alpha <$ |t|, light couples into the ring and out again without any build-up of power and the ring is described as being overcoupled. When the reverse is true the ring is described as undercoupled and all the light coupled into the ring decays before it is able to couple back out. A special case, critical coupling occurs when the cavity decay rate and coupling rate are equal, and this results in the power in the waveguide, given by equation 2.28, being zero. Thus all the power is contained within the ring and constructive interference results in high Q. As per equation 2.27, power in the ring is at a maximum when t is at a maximum. It follows that in order to satisfy the coupling condition given by equation 2.21, κ must be correspondingly small (though non-zero), and thus weak coupling is required in order to maximise Q.

2.3.2 Q and finesse

Finesse and Q act as figures of merit for a ring resonator, giving an indication of the sharpness of the resonances, which is a limiting factor in sensitivity for sensing applications [5]. The finesse, F, is the sharpness of the resonances relative to the spacing between resonator modes, given by:

$$F = \frac{FSR}{FWHM} \tag{2.29}$$

The Q-factor of the ring is perhaps more frequently cited in the literature to quantify performance of a ring resonator, and is defined as the sharpness of the resonances relative to the central wavelength [6]:

$$Q = \frac{\lambda}{FWHM} \tag{2.30}$$

In the context of sensing applications, Q is particularly important as the maximum resolution, $\delta\Omega$ of a ring resonator gyroscope is inversely proportional to the product of Q, diameter and the square root of the power at the photodetector, as per equations 2.31, given below [7].

$$\delta\Omega = \frac{1}{QD\sqrt{P_{pd}}}\sqrt{\frac{2Bhc^3}{\lambda\eta}}\left(\frac{3600\times180}{\pi}\right)(^\circ h^{-1}) \tag{2.31}$$

The Angular Random Walk (ARW; See section 2.5.1), essentially the "white noise" which reduces resolution, is also affected as per the below equation [7]:

$$\delta\Omega = \frac{1}{QD\sqrt{P_{pd}}}\sqrt{\frac{2Bhc^3}{\lambda\eta}}\left(\frac{60\times 180}{\pi}\right)(^{\circ}\sqrt{h}^{-1}) \tag{2.32}$$

where P_{pd} is the optical power input, is the photodetector efficiency, B is the measurement bandwidth, h is the Planck constant, c is the speed of light in a vacuum, λ is the operating wavelength and D is the diameter. In practice, the shot noise of the photodetectors provide an absolute limit to the sensitivity of the system [7] although the effects of polarization rotation, scattering, Kerr nonlinearity and thermal effects result in a practical barrier to reaching this theoretical limit [8] (see following section).

2.4 Practical considerations

2.4.1 Loss

Since Q is inherently limited by loss, minimizing its various causes is essential. There are three main loss mechanisms: Material loss due to absorption at the operating wavelength, radiation loss [3] and waveguide loss, which includes the loss due to the dimensions, geometry, sidewall roughness and bend loss. Material loss may be minimised by judicious choice of material and operating wavelength, and use of a fabrication technique which produces high quality, high purity low-loss layers, such as FHD [9][10]. Propagation loss due to sidewall roughness scales with the square of the index contrast Δn, as well as being dependent on fabrication technique, while bend loss must be balanced with refractive index contrast and size [6][11], so the composition of core and clad must be carefully considered. For a high refractive index contrast, small rings are possible but with the caveat that polarization-induced effects are exacerbated [12] (see Section 2.4.3). For a silica-based glass, Geuzebrook and Driessen's review leads to an estimate of a minimum radius of around 25mm for a ring with an index difference of approximately 0.006 in order to keep total losses below 1dB per round-trip [6], which is in-keeping with Okamoto's estimate of a 25mm bend radius required for a Δn of 0.3% [11]. All of the loss mechanisms described contribute to the round-trip loss coefficient, α, which also includes coupling losses [13].

2.4.2 Scattering

A major source of noise in a ring resonator is scattering [14] due to defects in the material, which, in the case of Rayleigh scattering scales inversely with λ^4 [15], resulting in a reduction in Q and hence resolution in a gyroscope. A low-loss, high purity fabrication technique is therefore required, as well as careful design of the ring parameters and the choice of material. The noise caused by Rayleigh scattering may be overcome by phase modulation, as demonstrated by Ma's group (see section 2.5.2) [14][16].

2.4.3 Polarization rotation & birefringence

The model presented here is complicated by the phenomenon of polarization rotation, the exchange of power between hybrid modes, which are cited by Ma et al. as the largest source of error in optical ring resonator gyroscopes [8]. The two orthogonal polarizations present in the coupling waveguide are initially unable to transfer power between them. However, on coupling into the ring, modes which couple into the ring cease to be solely TE or TM, having components in both polarizations. They are thus no longer orthogonal, allowing power transfer between the two [6], the extent of which being dependent on the coupling coefficients for each polarization [17]. In any curved waveguide this phenomenon would complicate the design, however microring resonators are particularly susceptible to this phenomenon due to greater confinement of the modes and the cavity effect as a result of the high index contrast required due to the small bend radius [12]. Polarization rotation may also be exacerbated by the geometry of the ring, coupling distance, waveguide dimensions and birefringence, all of which are frequency-dependent [17]. Thus the geometry of the coupling waveguide and the ring itself may be carefully designed in order to suppress the undesired polarization, e.g. by having sloped sidewalls [17][12]. Alternatively, tilted Bragg gratings may be used in order to filter out the undesired

polarization [18]. Birefringence is highly temperature dependent [8], so control of the temperature (or use of a suitable "athermal" material[1]) is essential in order to minimise polarization rotation and fluctuations [12]. Spectrally, the result of polarization rotation is a second resonant dip seen on an oscilloscope trace or spectrum as the laser source is tuned, resulting in interference and intensity errors, its origin being temperature-induced birefringence which may be reduced by optimization of the working temperature combined with precise temperature control [8].

2.4.4 Kerr effect

The optical Kerr effect originates from slight differences and fluctuations in the relative power of the CW and CCW beams in a material with third order nonlinear susceptibility and this results in a corresponding difference in effective refractive index which is proportional to the square of the electric field, changing the effective optical path length. This effect may be compounded by self-focussing. The result is a non-zero, fluctuating gyroscope output when stationary, contributing to bias instability (see section 2.6.1). The error in angular rate is given by [7]:

$$\Omega_K = \frac{\lambda c \zeta F \Delta P}{4\pi^2 D A}(rads^{-1}) \tag{2.33}$$

Where ζ, F, ΔP, D and A represent the nonlinear susceptibility, finesse, difference in power between the CW and CCW beams, diameter and area of the ring respectively. While the Kerr effect is the smallest in comparison to the previous two effects [8], it nevertheless has a significant effect on the bias of a ring resonator-based rotation sensing system: A difference in proportion of 5×10^{-4} between the beams is enough to produce a bias of 10^{-3° hr^{-1} [19]. There are two possible ways of solving this problem: ensure that differences in power between beams are minimal or compensate for the Kerr effect. However, the bias due to the Kerr effect varies with the difference in intensity between the beams so some method of ensuring intensities of the CW and CCW beams are equal is more usually used. Ma's group have used a light intensity feedback method to ensure equal intensities of the two beams, wherein the photodetector output of the CW beam is demodulated at the frequency of the second harmonic and fed back to the phase-modulated input to the ring resonator for the CCW beam and vice versa, keeping the CW and CCW beams at equal intensity and reducing fluctuations. The technique works on the basis that the power of the 2nd harmonic demodulated signal is proportional to the power of the input to the ring resonator. This technique resulted in an apparent rate of rotation due to the Kerr effect of $1.33\times10^{-5^\circ}$s^{-1}, a factor of approximately 10^2 better in comparison to the original Kerr-induced drift [20].

2.4.5 Dispersion

All optical materials have dispersion, in which refractive index drops with wavelength: normal or anomalous dispersion is referred to according to the sign of $\frac{d^2n}{d\lambda^2}$. The decrease of refractive index with wavelength in the normal dispersion regime results in a shift in the position of modes towards the centre of the ring as wavelength increases, due to the decrease in effective index, resulting in an FSR which becomes progressively wider with wavelength. When using ring resonators as frequency comb sources a varying FSR is clearly a severe drawback and so dispersion

[1] i.e. Temperature insensitive, in particular having a thermo-optic coefficient as close as possible to zero.

must be controlled even if anomalous as both result in variation of the FSR. The Vahala group have used disc resonators made up of layered wedges of varying angle and refractive index in order to force the modes to sit at the same distance from the centre, overcoming dispersion and keeping a constant FSR [21]. However this technique requires challenging fabrication. In the case of ring resonator-based gyroscopes, however, the Sagnac effect is independent of refractive index [22] and can in fact be used to increase sensitivity to rotation at low rotation rates when working at around the zero-dispersion wavelength in the anomalous dispersion regime as the phase shifts of the CW and CCW beams are increased [23]. Anomalous dispersion is reliant on both the chromatic dispersion of the material, the dimensions of the waveguide, confinement and may be used to enhance nonlinearity [24], thus further consideration of index contrast and bend radius is necessary.

2.4.6 Temperature-induced effects & material

Temperature affects the thermal expansion coefficient, refractive index [7] and birefringence [8], and small fluctuations in temperature may result in large changes in resonant wavelength [7]. The increase in birefringence due to temperature can also result in undesired state of polarization gaining power [8]. However, one of the largest influences is the thermooptic coefficient, which can produce wavelength shifts of picometres. The choice of material is thus critical, affecting all of the temperature-related effects mentioned above as well as all of the phenomena discussed in this section. In summary, a low (intrinsic) loss, low birefringence, low thermal expansion coefficient, low thermo-optic coefficient material will aid stability, resilience to temperature and ultimately reliability of a ring resonator-based rotation sensor. Careful design of the geometry and fabrication of the ring and bus waveguides can be used to minimise the round-trip loss, polarization-induced noise, scattering and control dispersion. Appropriate use of phase modulation techniques and stabilization of the laser source and counter-propagating beams can minimize noise resulting from, for example, the Kerr effect.

There are several options for the type of material used: Glasses can have low loss and consequently very high Q, up to 10^{10} in a silica resonator [25], with low loss (silica 0.15dB/km) at its minimum, comparatively low thermal expansion coefficients [26] and can be relatively cheaply and easily fabricated. Chalcogenide glasses have high nonlinearity, show good stability to moisture, losses can be low and Q moderately high, on the order of 10^5 [27]. However, these glasses generally have lower losses, and thus higher Q-factors in the mid-infra-red (MIR) rather than NIR [27]. Semiconductor ring resonators such as the indium phosphide resonator described in [28] can have high Qs (in this case potentially as high as 10^6), as do silicon ring resonators such as the high Q rod resonators fabricated at NPL [29] although silicon's high thermooptic coefficient presents a challenge: silicon nitride is often cited as an alternative to silicon due to its potential for fabrication of athermal waveguides and rings [30]. Semiconductors also may have high nonlinearity and as fabrication techniques are well established, there is much potential for integration of components such as laser sources and signal processing on-chip [31][32]. However, they also have high thermal expansion coefficients and defect-free fabrication can be difficult [28]. Photonic crystals can show high Q on the order of 10^4 [32], though not to the ultrahigh Qs seen in for example, silica, due to their high intrinsic losses [33]. They have potential for high nonlinearity but at the cost of birefringence and difficulties with fabrication, especially machining, although complex microstructures

have been fabricated [32].

The choice of material will inevitably be different for a frequency comb source, where high nonlinearity is desirable in comparison to that for a gyroscope, where minimization of noise sources is of primary importance. This makes glasses a good choice for a ring resonator-based gyroscope, due to their low loss, low thermal expansion (in general) and ease of fabrication in comparison to photonic crystals or semiconductors. However, glasses do show some potential for nonlinearity depending on composition, meaning the fabrication of a frequency comb source is also possible.

2.4.7 Germanate glass

Having discussed the various practical considerations and linked these to the required material properties, an interim summary is helpful. The need for high Q, and thus low loss demands a choice of material with low intrinsic (material) loss and a low loss fabrication technique. The facilities available (flame hydrolysis deposition, direct UV writing) within the group make the use of germanate glass a possibility, and a resonator in pure or high germania content flame hydrolysis-deposited glass would be a novel approach. Germania has losses potentially lower than silica as wavelengths approach 2μm, from estimations based on its loss at shorter wavelengths and scattering relative to silica [34][35]. Its zero-dispersion wavelength is 1.74μm [36], and at this wavelength material losses are similar to those of silica at 1550 nm. The $\chi^{(3)}$ nonlinearity of germania, approximately four times that of silica [37] may aid four-wave mixing, aiding fabrication of a frequency comb source. Flame hydrolysis can produce high purity, low loss, high quality uniform layers [7], while direct UV writing avoids the sharp changes in index and surface roughness associated with etching or machining. An FHD photosensitive germanate glass would fulfil some of the requirements summarized above, the main drawback to this choice of material being temperature-related effects and polarization rotation due to the potentially higher index contrast in comparison to silicate glasses. The thermo-optic coefficient of germania is 19.4×10^{-6} in comparison to silica's 10.4×10^{-6} [38]: ring resonators fabricated in silica require temperature stabilization, and thus those in germania even more so. This requires the relationship between bias and temperature to be established, adequate control of temperature (ideally with higher tolerance to fluctuations), in order to reduce birefringence and control of polarization. However, the FHD system can easily be used to produce boron and phosphorus-doped glasses, which, while worthy of investigation in itself, can be exploited in order to tailor useful properties (thermal expansion, refractive index amongst others) to the fabrication of a direct UV written ring resonator. The versatility of the FHD system facilitates adaptation in order to deposit glass on to alternative geometries, such as silica, alumina and sapphire rods and tubes (as detailed in Chapter 6), and to fabricate "Damascene"[2] structures, where deposited soot is consolidated on a milled ring structure in a planar sample (the characterisation of which is briefly described in Chapter 7), the development of a system for precision-milling rings having already been the subject of research within the group [39].

[2] i.e. a ring-shaped trench filled with a material of higher refractive index.

2.5 Ring resonator gyroscopes

2.5.1 Figures of merit

There are several frequently referenced figures of merit for inertial sensing systems, the most obvious being the resolution, the minimum detectable angular rate in $^{\circ}\mathrm{hr}^{-1}$ [2]. Theoretically, the resolution is limited by the Q of the ring resonator and shot noise of photodetectors but in practice, noise sources such as backscattering, polarization rotation and the Kerr nonlinearity are more immediate problems [40]. Scale Factor in $\mathrm{V}/^{\circ}\mathrm{s}^{-1}$ is the variation in output signal per change in rotation speed [2][41], and it is this which makes ring resonators superior to other types of optical gyroscope as the large ring diameter is not critical as it would be in an RLG or IFOG as the enhancement of the field due to high Q increases the maximum resolution [40]. There are several different types of angular rate error, all of which contribute to larger errors in orientation due to integration. The Zero-Rate Output (ZRO) in $^{\circ}\mathrm{hr}^{-1}$ is the rate of rotation “detected" when the system is at a standstill, consisting of a slowly varying function, which is known as the bias drift, or bias instability [2] and white noise, or the Angular Random Walk (ARW) in $^{\circ}\sqrt{hr}^{-1}$ [42]. The latter is the random variation of apparent rotation rate in degrees per hour caused by stochastic noise. Bias is a constant angular error and is thus easily compensated for [43] by establishing the relationship between temperature and bias [8]. Bias drift, the fluctuating angular error rate, is another often quoted figure of merit [41], arising from noise sources such as temperature-induced birefringence, undesired eigenstates of polarization (ESOP) and backscattering [8].

2.5.2 Typical experimental set-up for ring resonator gyroscopes

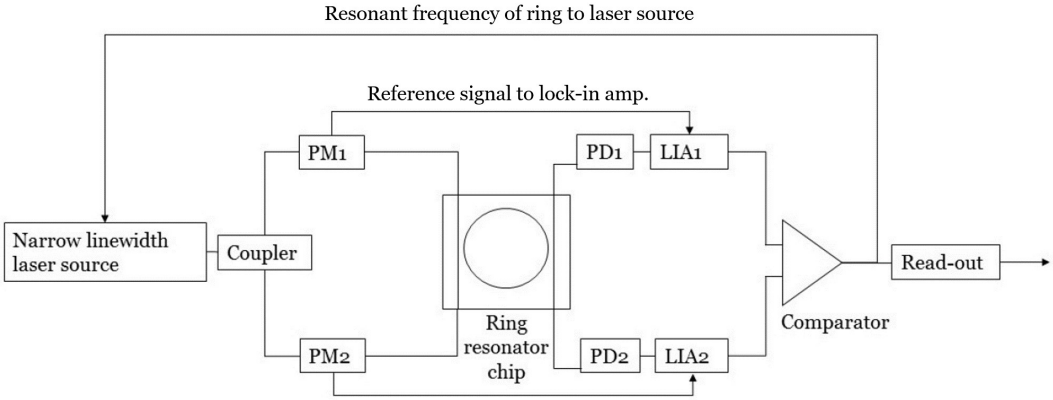

FIGURE 2.4: A schematic experimental set-up for a ring resonator gyroscope chip, using phase modulation to stabilise the laser and detect small Sagnac-induced phase shifts, based on those described in [7][39][44]. PM, PD and LIA denote a Phase Modulator, Photodetector and Lock-in Amplifi
er respectively.

The use of a ring resonator as part of a gyroscope requires a narrow linewidth laser source with some way of detecting and accurately measuring the difference between the co- and counter-propagating beams, signal processing and appropriate read-out in order to translate phase shift information to rotation rate. The Sagnac effect scales with area of the ring and even with a ring of tens of cm radius, the induced phase

shift is very small [44], with effective relative path differences on the order of 10^{-20} to 10^{-18} [45] and a phase shift of 7.8×10^{-8}rads^{-1} for a 5cm radius ring rotating at 7.3×10^{-5}rads^{-1} operating at 633 nm [46]. Therefore, a phase modulation technique similar to that used for IFOGs is used [47] (a typical experimental set-up is shown in fig. 2.4): The laser output is phase modulated in order that the signal may be extracted, i.e. demodulated, with minimal noise in order to accurately measure the phase shift induced by rotation of the ring. The phase modulation introduces sidebands at $f_0 + f_1$ and $f_0 + f_2$ and the carrier frequencies of the phase modulators, f_1 and f_2, are used as references for lock-in amplifiers to allow demodulation. The lock-in amplifier output of LIA1 is connected to the input of the fibre laser to lock the central frequency of the laser to the resonant frequency of the ring. Demodulation and subsequent determination of the rotation rate $\Delta\Phi$, relies on the demodulation slope at the resonance point, which is highly dependent on the phase modulation frequency [44]. Ma et al. found considerable improvement when using a double phase-modulation technique to further suppress the carrier signal, improving the bias stability from 0.15° s^{-1} to $1.85\times10^{-4^\circ}$s^{-1} [14]. This consisted of a set of phase modulators as described previously, with a second set to suppress any residual carrier before demodulation via an LIA and feedback to the laser to stabilize the central frequency and reduce fluctuations.

2.5.3 Current state of research: Inertial sensing, ring and rod resonators

At present, commercially available optical gyroscope-based inertial navigation systems such as those developed by Honeywell, Northrop and iX Blue are based on RLGs and IFOGs. However, much recent literature concerns resonant micro-optic gyroscopes (RMOGs), reporting more stable biases than seen in current commercially available technology. The Ma group at Zheijiang University has researched methods of overcoming scattering, polarization and Kerr effect in silica fibre ring resonators and waveguide and ring resonators fabricated by low pressure chemical vapour deposition (LPCVD) and reactive ion etching (RIE) [44][8][20]. This group has also reported improved bias stability by temperature control and a double phase-modulation technique to reduce carrier noise from phase modulation [14]. Using these techniques, bias has been reduced from 13.6 $^\circ$s^{-1} to 0.67°s^{-1} [8].

While temperature control is an obvious solution to one of the major problems of a high resolution optical gyroscope, temperature insensitivity is perhaps a more practical solution when considering low SWaP requirements, if one that will require much fabrication research. Athermal waveguides and rings have been fabricated in silicon nitride (SiN) [48] and silicon-on-insulator (SOI) chips clad with titania (TiO_2) and silicon nitride (Si_3N_4) [30] amongst other materials, and their relatively established fabrication techniques may lead to ring resonators and their required components for signal processing being integrated on-chip. NPL and NIST are collaborating on the development of laser-machined rod and disc resonators. A CO_2 laser is used to remove small areas of silica while the rod rotates, resulting in a rod with ridges, which are coupled in to via a tapered fibre. These resonators have ultra-high Q-factors of 1×10^9, and diameters between 200μm and 8mm [29]. However, a more robust coupling method is required in order to make this a practical geometry for an optical resonator gyroscope. There is some collaboration between the author and others in the Smith group at the University of Southampton and Pascal Del'Haye's group at NPL, with germanate rods in development (see chapter 7).

NPL and NIST have also fabricated disc resonators, including dispersion-engineered discs made up of layers of varying refractive index and angle [21]. A silica disc resonator of 2mm diameter was used as a frequency comb source with a Q of 6.3×10^6, showing potential for self-referencing with line-spacing similar to that of energy transitions in rubidium atoms [49].

Ciminelli et al. have fabricated a ring resonator in InGaAsP rib waveguides on indium phosphide. Loss was found to be 0.45dB/cm and Q around 6×10^5, with a footprint of about $10mm^2$. Resolution has been maximised by the use of a spiral design, increasing the area to perimeter ratio, and thus resolution. The shot noise-limited resolution is estimated to be around $10^\circ hr^{-1}$ and a bias drift of $1^\circ hr^{-1}$ and the authors state that read-out system has been designed, fabricated and tested [50]. Although the resolution and bias drift are inadequate for inertial navigation (fabricating systems on-chip generally increases losses) it represents progress towards integration of a rotation sensor on-chip. The characterisation set-up used is broadly similar to the generic one shown in figure 2.4.

Guillen-Torres et al. have modelled the effect of ring resonator parameters to find the optimal circumference, coupling coefficients and detuning in order to maximise resolution, constrained by loss values typical of SOI and SiN ring resonators. The authors found the optimal lengths to be on the order of a few metres and slight undercoupling, rather than critical coupling, was found to be advantageous as it maximises the extinction ratio and thus the spectral slope [51].

2.6 Summary

The Sagnac effect can be exploited using an optical ring resonator in order to sense rotation. The high Q seen in these structures causes an enhancement of the otherwise very small phase shift due to rotation, making miniaturization possible. The resolution of the device is ultimately shot-noise-limited, but reaching this limit requires control of polarization and birefringence, minimization of the Kerr effect, and reduction of the effects of Rayleigh scattering. These effects may be achieved by careful design of the ring geometry, especially balancing the size of the ring against its loss, and feedback to stabilize the laser source and phase modulation respectively. Indeed, much recent research on ring resonator gyroscopes is focussed on millimetre-size diameters in lowloss materials.

Temperature control is also important due to the thermo-optic effect, thermal expansion and temperature-induced birefringence. Sensitivity to rotation may be further increased by operation in the anomalous dispersion regime, close to the ZDW. Careful consideration of choice of material is essential to minimise loss, thus maximising Q, and to avoid large errors caused by the thermo-optic effect and other temperature and material related effects.

Much ring-resonator gyroscope based research is being carried out, with high Q, alternative geometries and integration on-chip showing potential to overcome the challenges of scattering, polarization and the Kerr effect in order to reach the shot-noise limit.

There is an opportunity, via the use of germanate glass, to move the operating wavelength to the 2μm region and beyond, which reduces fabrication tolerances and potentially achieves lower losses at its ZDW of around 1.74 μm than silica at its ZDW of around 1.3 μm [34][35], aiding high Q and thus resolution of a ring resonator gyroscope, or alternatively, exploiting its higher nonlinearity relative to silica in order to create a frequency comb source. Fabrication via FHD and UV writing or milling of a planar ring resonator and deposition of germanate glass onto a rod resonator add some novelty.

2.7 Bibliography

[1] R. Anderson, H. R. Bilger & G. E. Stedman, "'Sagnac' effect: A century of Earth rotated interferometers", *Am. J. Phys.*, 62 (11): 975-985, November 1994.

[2] M. A. Guillen-Torres, "Feasibility of Optical Gyroscopic Sensors in Silicon-On-Insulator Technology", (Thesis), University of British Columbia, August 2015.

[3] V. Van, "Optical Microring Resonators: Theory, Techniques, and Applications", CRC Press, ISBN 9781315303505, 2016.

[4] D. G. Rabus, "Ring Resonators: The Compendium" *Nature Photonics*, 6 (6): 440-449, July 2012.

[5] M. S. Luchansky & R. C. Bailey, "Ring Resonator Optical Gyroscopes: Parameter Optimization and Robustness Analysis", *Anal. Chem.*, 84 (2): 793-821, January 2012.

[6] D. H. Geuzebrook & A. Driessen, "Ring Resonator-based wavelength filters", *Phys. Rev. Lett.*, 107: 063901, 2018.

[7] C. Ciminelli, F. Dell'Olio, C. Campanella & M. N. Armenise, "Photonic Technologies for Angular Velocity Sensing", *Advances in Optics and Photonics*, 2 (2): 370-404, June 2010.

[8] H. Ma, Y. Yan, Y. Chen & Z. Jin, "Improving Long-Term Stability of a Resonant Micro-Optic Gyro by Reducing Polarization Fluctuations", *IEEE Photonics*, 4 (6): 2372-2381, December 2012.

[9] S. Garcia-Blanco, A. Glidle, J. M. Cooper R. M. De La Rue & J. S. Aitchison, "Characterization of Germanium-Doped Silica Layers Deposited by Flame-Hydrolysis", *Opt. Mat.*, 27: 365-371, 2004.

[10] T. Kominato Y. Ohmori H. Okazaki & M. Yasu, "Very Low-Loss GeO Doped Silica Waveguides Fabricated by Flame Hydrolysis Deposition Method", *Electronics Lett.*, 26 (5): 327-328, March 1990.

[11] K. Okamoto, "Fundamentals of Optical Waveguides", Academic Press, ISBN 0-12- 525095-9, 2000.

[12] F. Morichetti, A. Melloni & M. Martinelli, "Effects of Polarization in Optical Ring-Resonator-Based Devices", *J. Lightwave Tech.*, 24 (1): 573-585, January 2006.

[13] W. Bogaerts, P. De Heyn, T. Van Vaerenbergh, K. DeVos, S. Kumar Selvaraja, T. Claes, P. Dumon, P. Bienstman, D Van Thourhout & R. Baets, "Glass optical waveguides: a review of fabrication techniques", *Laser Photonics Rev.*, 6 (1): 47-73, 2012.

[14] H. Mao, H. Ma & Z. Jin, "Polarization maintaining silica waveguide resonator optic gyro using double phase modulation technique", *Optics Express*, 19 (5): 4632-4643, February 2011.

[15] S. O. Kasap, H. Ruda & Y. Boucher, "Cambridge Illustrated Handbook of Optoelectronics and Photonics" (Reprint Edition), Cambridge University Press, ISBN 978-1107404236, 2012.

[16] L. Wang, H. Li, J. Zhang, H. Ma, X. Li & Z. Jin, "Measurements of the excess loss of the crossed waveguide using optical waveguide ring resonators", *Optics Comms.*, 387: 18-23, November 2017.

[17] B. E. Little & S. T. Chu, "Theory of Polarization Rotation and Conversion in Vertically Coupled Microresonators", *IEEE Photonics Tech. Lett.*, 12 (4): 401-403, April 2000.

[18] H. Ma, J. Zhang Z. Chen & Z. Jin, "Tilted Waveguide Gratings and Implications for Optical Waveguide-Ring Resonator", *J. Lightwave Tech.*, 33 (19): 4176-4183, October 2015.

[19] W. W. Chow, J. Gea-Banacloche, L. M. Pedrotti, V. E. Sanders, W. Schleich & M. O. Scully, "The ring laser gyro", *Rev. Mod. Phys.*, 57 (1): 61-104, January 1985.

[20] H. Ma, X. Li, G. Zhang & Z. Jin, "Measurements of the excess loss of the crossed waveguide using optical waveguide ring resonators", *Appl. Optics*, 53 (16): 3465-3472, May 2014.

[21] K. Y. Yang, K. Beha, D. C. Cole, X. Yi, P. Del'Haye, H. Lee, J. Li, D. Y. Oh, S. A. Diddams, S. B. Papp & K. J. Vahala, "Broadband Dispersion-Engineered Microresonator on a Chip", *Nature Photonics*, 6 (3): 440-449, July 2016.

[22] G. B. Malykin, "Sagnac Effect in Ring Lasers and Ring Resonators: How Does the Refractive Index of the Optical Medium Influence the Sensitivity to Rotation?", *Physics Uspekhi*, 57 (7): 714-720, July 2014.

[23] X. Luo & Z. Li, "Passive Ring Resonator Gyroscope Using High-Order Dispersion", *Proc. of SPIE*, 6723: 67230I-1-67230I-5, 2007.

[24] L. Zhang, Y. Yue, R. G. Beausoleil & A. E. Willner, "Analysis and engineering of chromatic dispersion in silicon waveguide bends and ring resonators", *Optics Express*, 19 (9): 8102-8107, April 2011.

[25] A. Pasquazi, M. Peccianti, L.Razzari, D. J.Moss, S. Coen, M. Erkintalo, Y. K.Chembo, T. Hansson, S. Wabnitz, P. Del'Haye, X. Xue, A. M.Weiner, R. Morandotti, "Micro-combs: A novel generation of optical sources", *Physics Reports*, 729: 1-81, 2018.

[26] F. Fan & L. Xu, "Photonic Glasses", World Scientific Publishing Co. Pte. Ltd., ISBN 981-256-820-4, 2006.

[27] P. Ma, D. Choi, Y. Yu, Z.Yang, K. Vu, T. Nguyen, A. Mitchell, B. Luther-Davies & S. Madden, "High Q factor chalcogenide ring resonators for cavity-enhanced MIR spectroscopic sensing", *Optics Express*, 23 (15): 19969-19979, 2015.

[28] C. Ciminelli, F. Dell'Olio, M. N. Armenise, F. M. Soares & W. Passenberg, "High performance InP ring resonator for new generation monolithically integrated optical

gyroscopes", *Optics Express*, 21 (1): 556-564, January 2013.

[29] P. Del'Haye, S. Diddams & S. Papp, "Laser-machined ultra-high-Q microrod resonators for nonlinear optics", *Appl. Phys. Lett.*, 102 (22): 221119-1-221119-4, June 2013.

[30] L. He, Y. Guo, Z. Han, K. Wada, L. C. Kimerling, J. Michel, A. M. Agarwal, G. Lia & L. Zhang, "Broadband athermal waveguides and devices for datacom and telecom applications", *Proc. of SPIE*, 10537: 1-6, 2018.

[31] T. A. Ibrahim, "Nonlinear Optical Semiconductor Micro-Ring Resonators" (Thesis), University of Maryland, 2003.

[32] R. Chandrasekar, Z. J. Lapin, A. S. Nichols, R. M. Braun, & A. W. Fountain III, "Photonic integrated circuits for Department of Defense-relevant chemical and biological sensing applications: state-of-the-art and future outlooks", *Opt. Eng.*, 58 (2): 020901-01-020901-11, February 2019.

[33] G. C. Righini, Y. Dumeige, P. Feron, M. Ferrari, G. Nunzi Conti, D. Ristic & S. Soria, "Whispering gallery mode microresonators: Fundamentals and applications", *Rivista Del Nuovo Cimento*, 34 (7): 435-488, 2011.

[34] S. Shibata, U Y. Fukui, T. Oonishi, T. Yano, M. Yamane & S. Sakaguchi, "Intrinsic Optical Losses of GeO_2-P_2O_5-Al_2O_3 Glasses for Optical Fibers", *Opt. Fiber Tech.*, 3: 90-95, 1997.

[35] S. Sakaguchi & S. Todoroki, "Optical properties of GeO_2 glass and optical fibers", *Appl. Opt.*, 36 (27): 6809-6814, September 1997.

[36] E. M. Dianov & V. M. Mashinsky, "Germania-Based Core Optical Fibers", *J. Lightwave Tech.*, 23 (11): 3500-3508, November 2005.

[37] M. J. Holmes, D. L. Williams & R. J. Manning, "Highly Nonlinear Optical Fiber for All-Optical Processing Applications", *IEEE Photonics Tech. Lett.*, 7 (345): 1045-1047, September 1995.

[38] P. D. Dragic, M. Cavillon, A. Ballato & J. Ballato, "A unified materials approach to mitigating optical nonlinearities in optical fiber: II. B. The optical fiber, material additivity and the nonlinear coefficients", *Int. J. Appl. Glass Sci.*, 9: 307-318, 2018.

[39] P. A. Cooper, "Ultra-precision physical micro-machining for integrated optics" (Thesis), University of Southampton, 2015.

[40] F. Dell'Olio, T. Tatoli, C. Ciminelli & M. N. Armenise, "Recent Advances in Miniaturized Optical Gyroscopes", J. Europ. Opt. Soc. Rap. Public, 9 (14013): 1-14, March 2014.

[41] IEEE Aerospace and Electronic Systems Society, "IEEE Standard for Inertial Sensor Terminology", The Institute of Electrical and Electronics Engineers, Inc., 2007.

[42] K. Liu, W. Zhang,W. Chen, K. Li, F. Dai, F. Cui, X. Wu, G. Ma & Q. Xiao, "The

development of micro-gyroscope technology", *J. Micromech. Microeng.*, 19 (113001), 2009.

[43] O. J. Woodman, "An introduction to inertial navigation", University of Cambridge Technical Report, (696), 2007.

[44] L. Wang, H. Li, J. Zhang, H. Ma & Z. Jin, "Optimization of the sinusoidal phase modulation technique in resonant fiber optic gyro", *Optics Comms.*, 387: 18-23, 2017.

[45] Q. Wilmart, H. El Dirani, N. Tyler, D. Fowler, S. Malhouitre, S. Garcia, M. Casale, S. Kerdiles, K. Hassan, C. Monat, X. Letartre, A. Kamel, M. Pu, K. Yvind, L. K. Oxenlwe, W. Rabaud, C. Sciancalepore, B. Szelag & S. Olivier, "A Versatile Silicon-Silicon Nitride Photonics Platform for Enhanced Functionalities and Applications", *Appl. Sci.*, 9 (255), February 2019.

[46] H. C. Lefevre, "The fiber-optic gyroscope, a century after Sagnac's experiment: The ultimate rotation-sensing technology?", *R. C. Physique*, 15: 851-858, 2014.

[47] A. Shamir, "An overview of Optical Gyroscopes Theory, Practical Aspects, Applications and Future Trends" (Thesis), University of Tel Aviv, September 2006.

[48] C. Ciminelli, C. E. Campanella, F. Dell'Olio, C. M. Campanella & M. N. Armenise, "Theoretical investigation on the scale factor of a triple ring cavity to be used in frequency sensitive resonant gyroscopes", *J. Europ. Opt. Soc. Rap. Public.*, 8: 130501-7, July 2013.

[49] S. B. Papp, K. Beha, P. Del'Haye, F. Quinlan, H. Lee, K. J. Vahala & S. A. Diddams, "Microresonator Frequency Comb Optical Clock", *Optica*, 1 (1): 10-14, July 2014.

[50] C. Ciminelli, D. D'Agostino, G. Carnicella, F. Dell'Olio, D. Conteduca, H. P. M. M. Ambrosius, M. K. Smit & M. N. Armenise, "A High-Q InP Resonant Angular Velocity Sensor for a Monolithically Integrated Optical Gyroscope", IEEE Photonics, 8 (1): 6800418, February 2016.

[51] M. A. Guillen-Torres, E. Cretu, N. A. F. Jaeger & L. Chrostowski, "Ring Resonator Optical Gyroscopes: Parameter Optimization and Robustness Analysis", *J. Lightwave Tech.*, 30 (12): 1802-1817, June 2012.

Chapter 3

Flame hydrolysis deposition of planar germanate glasses

3.1 Introduction

Germania as a glass-former was first investigated in 1926 by Dennis & Laubengayer [1], and germanate glass further investigated by Krakau in 1939 [2]. In recent decades, germania has been considered for use in fibres and integrated optics as an alternative to silica [3], primarily due to its low loss in the near IR [4] and comparatively long zero-dispersion wavelength [5]. However, little research was carried out in the intervening years, and although often cited as a structural analogue to silica, germania glass properties remain poorly understood, and difficulties in fabricating pure germania layers and optical fibres have prevented adoption of germanate glass in place of silica [4][6]. Germania is, at present, most frequently used as a dopant where photosensitivity or a moderate increase in nonlinearity is desired [4].

The increased interest in germania glass in recent years is perhaps partly due to its potential for high photosensitivity: Oxygen deficient centres (ODCs; see section 5.1) occur far more in germania than in silica and are thought to be responsible for the UV-induced structural rearrangement which results in refractive index change [7]. Large photosensitive refractive index change allows the possibility of direct UV writing of waveguides and ring resonators with the strong confinement necessary for small bend radii, and its third-order nonlinear susceptibility is approximately four times that of silica [8] enhancing phenomena such as four-wave mixing which aids frequency comb spectrum generation [9].

A further justification for the renewed interest in germanate glasses lies in its comparison to silica. The zero-dispersion wavelength (ZDW) of germania is around 1.74μm [4][10], at which point its minimum loss is around 0.4dB/km taking into consideration absorption and scattering, which is very similar to the minimum loss of silica at its ZDW of around 1.27μm, making germania comparable to silica for devices operating at the zero-dispersion wavelength [4] and potentially better than silica for wavelengths further into the infra-red, where losses increase for silica, while falling to a minimum of 0.15dB/km for germania at a wavelength of around 2μm, calculated based on measured scattering properties of GeO_2 relative to SiO_2 in fibres and bulk glass samples [11].

Among the many methods of depositing planar glass layers, FHD is often considered the most economical for SiO_2-based glasses and its adaptability allows fabrication of a varied range of integrated optical devices [12] e.g. optical and microfluidic [13]. Flame hydrolysis deposition may be used to produce high quality, low-loss

[14][15] low-stress glass layers at high deposition rates [16]. The technique owes much to optical fibre fabrication, the reactions producing GeO_2 soot being similar to those involved in outside vapour deposition (OVD) and modified chemical vapour deposition (mCVD) [17]. The technique underwent much development (often in combination with Reactive Ion Etching (RIE) to produce PLCs for the telecomms industry [13], with much relevant research being undertaken at Nippon Telegraph and Telephone Corp. (NTT) in Tokyo and elsewhere in Japan [18].

This chapter explores the deposition and consolidation of high germania-content glass layers on silica, silicon and sapphire wafers in order to produce a low-loss, high quality (i.e. smooth, uniform, free of defects), UV-photosensitive glass suitable for fabrication of a ring resonator on the scale of a few millimetres. Knowledge of the structure and composition of the various layers deposited in these experiments is particularly useful in order to understand the origins of losses, defects, photosensitivity and any other qualities and phenomena (e.g. mechanisms of reactions with water) and to adjust the recipes in order to optimise desirable properties. To this end, various characterisation and analysis techniques were used, and are detailed in section 3.2.

3.1.1 FHD germanate glass & other fabrication techniques

Perhaps due to the ubiquity of silica in planar photonics, there is very little literature regarding flame hydrolysis of high germania-content layers. Most of the literature concerns Ge and GeO_2-doped silica layers, with correspondingly low germania-content. To the best of the author's knowledge, only one paper exists on the planar flame hydrolysis deposition of pure germania, by Sakaguchi [19] and one from the same group regarding "FHD"[1] of preform rods for fibre fabrication [11]. In the former, Sakaguchi notes the difficulties of deposition onto SiO_2 due to the mismatch in coefficient of thermal expansion (CTE), α, between silica (α=0.5x$10^{-6}K^{-1}$) and germania (α=7.5 x$10^{-6}K^{-1}$) and reports that consolidation on to silica proved impossible due to cracking of the layers [19] as a result. A sapphire substrate was used (due to its similar CTE to germania of α=8.0x$10^{-6}K^{-1}$) with a SiO_2-GeO_2 underclad with an index contrast of 0.8% relative to germania and this was successfully consolidated, albeit with a high propagation loss of 6dB/cm [19]. Similar losses were reported in OVD-fabricated samples [20]. The reactions taking place in OVD are similar to those in FHD [22], so these results are consistent with the idea that glass properties are highly dependent on the fabrication technique [21]. Previous work has acknowledged the difficulty of obtaining high germania-content samples due to crystallisation. However in this case, the percentage of crystalline germania was found to be reduced by reaction with chlorine during the drying step which is not present in the FHD process [23], and literature makes little mention regrading crystallinity in FHD germanate glass. Maurer & Schultz reported pure germania with a 63% GeO_2 cladding layer with losses of 6dB/cm at 800nm which were attributed to Rayleigh scattering and OH absorption but according to Dianov & Mashinsky, this result was not replicated [4]. Literature regarding low GeO_2-content glasses fabricated by FHD indicates potential for moderate to low loss and high UV photosensitivity. Notably, Kominato et al. reported a propagation loss of 0.01dB/cm, a round-trip loss of 0.5dB/cm and a finesse of 30 in an FHD-fabricated ring resonator of 0.75% index contrast (relative to silica; approximately 4% GeO_2) and 6.5mm radius [24]. Over all, the losses seen in FHD-fabricated high germania-content glasses

[1] The technique used in fact most resembles VAD due to the use of a rotating seed rod.

are higher than those in other techniques, e.g. VAD [25], mCVD [26] and peCVD [27][28], and close to those seen in OVD [20] and RF sputtering followed by laser machining reported in [29]. All techniques report higher losses than silica, although it has previously been acknowledged that germania may outstrip silica in terms of loss further in to the IR. It is perhaps safe to say, if nothing else, that germania's potential for low loss has not yet been fully exploited, although the potential for ring resonators in germanate glasses has been demonstrated, albeit at low GeO_2 contents.

TABLE 3.1: Fabrication of germanate glasses. Where ring resonators have been fabricated the round-trip loss and finesse if available are given. * denotes a percentage calculated from the index contrast reported.

Fabrication Technique	**% GeO_2**	**Loss at (λ)**	**Round-trip loss**	**Ref.**
FHD	pure	6dB/cm (633nm)	-	[19]
OVD	pure	6dB/cm (800nm)	-	[20]
VAD	pure	<1dB/km (1.39μm)	-	[25]
mCVD	75	20dB/km (1.85μm)	-	[26]
mCVD	74	100dB/km (2.3μm)	-	[27]
peCVD	30	0.2dB/cm (1553nm)	-	[28]
peCVD	19*	0.086dB/cm	<0.1dB/cm	[29]
FHD	5*	0.5dB/km	-	[31]
FHD	4*	0.01dB/cm	0.56dB/cm, F=30	[24]
RF sputtering + CO_2 laser machining		0.5dB/cm (1542nm)	-	[30]

3.1.2 The Flame Hydrolysis Deposition (FHD) system

In this section, the FHD system will be described. The system used in this research was based on one at the Centre for Integrated Photonics (CIP, now Huawei), and is one of only a few in the world. Prior to this research, the system had mainly been used to produce silicate samples via established recipes. The system was revamped and modified in 2017 in order to facilitate more complex recipes, allow control of the torch position and automate combination of different flow rates into the same recipe. Samples fabricated using the original system are coded NB and those on the new system PX, and these codes are included in the relevant results tables.

A schematic diagram of the FHD system is shown in figure 3.1. The system consists of a gas delivery system "bubblers" containing the halide precursors ($GeCl_4$, $SiCl_4$, PCl_3) and a BCl_3 bottle (see fig. 3.2 (A) & (B) respectively). The precursors sit in heated oil baths in order to produce vapours which are carried by the flow of nitrogen, which is regulated by a mass flow controller (MFC).

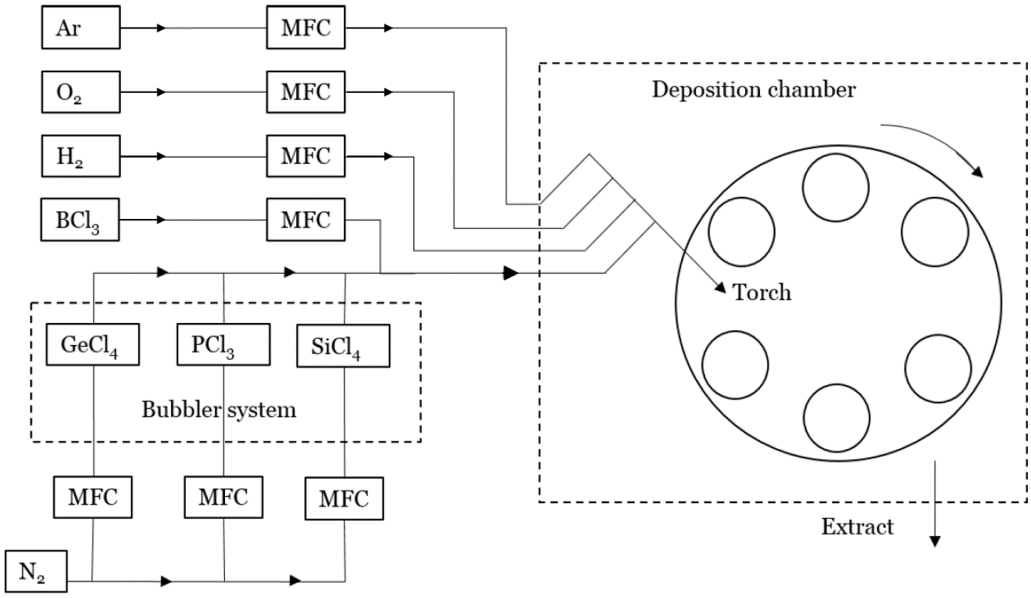

FIGURE 3.1: Schematic of the FHD System; MFC indicates a mass flow controller.

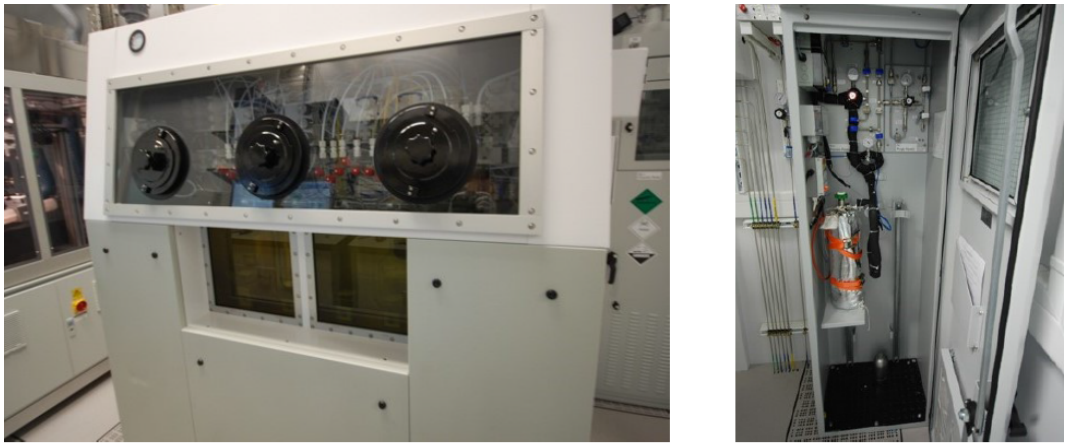

(A) (B)

FIGURE 3.2: (A) Bubbler cabinet containing the halide precursors $GeCl_4$, $SiCl_4$ and PCl_3. (B) BCl_3 bottle. (picture credit: J. Gates).

The resulting mixture of vapour precursors is injected from the bubbler via the torch into a hydrogen-oxygen flame, where they are hydrolysed and oxidised (dependent on temperature of the flame; above 1200 °C, oxidation is the dominant process [31]) to produce a soot of fine particles of the relevant oxide(s) onto the wafers via equations 3.1-3.4 below:

$$RCl_4 + O_2 \rightarrow RO_2 + 2Cl_2 \tag{3.1}$$

$$RCl_4 + 2H_2O \rightarrow RO_2 + 4HCl \tag{3.2}$$

$$4BCl_3 + 6H_2O \rightarrow B_2O_3 + 12HCl \tag{3.3}$$

$$PCl_3 + 5O_2 \rightarrow P_2O_5 + 6Cl_2 \tag{3.4}$$

Where R may represent either Si or Ge. The flow rates of precursors and torch gases as well as the oil bath temperature may be controlled (the consequences of which are discussed in the following section). The wafers are situated on a rotating table which is heated to 180 °C in an extracted chamber (see figure 3.3 (A) & (B)) while the torch moves from the edge to the centre and back, known as a "pass" (see fig. 3.3 (C)).

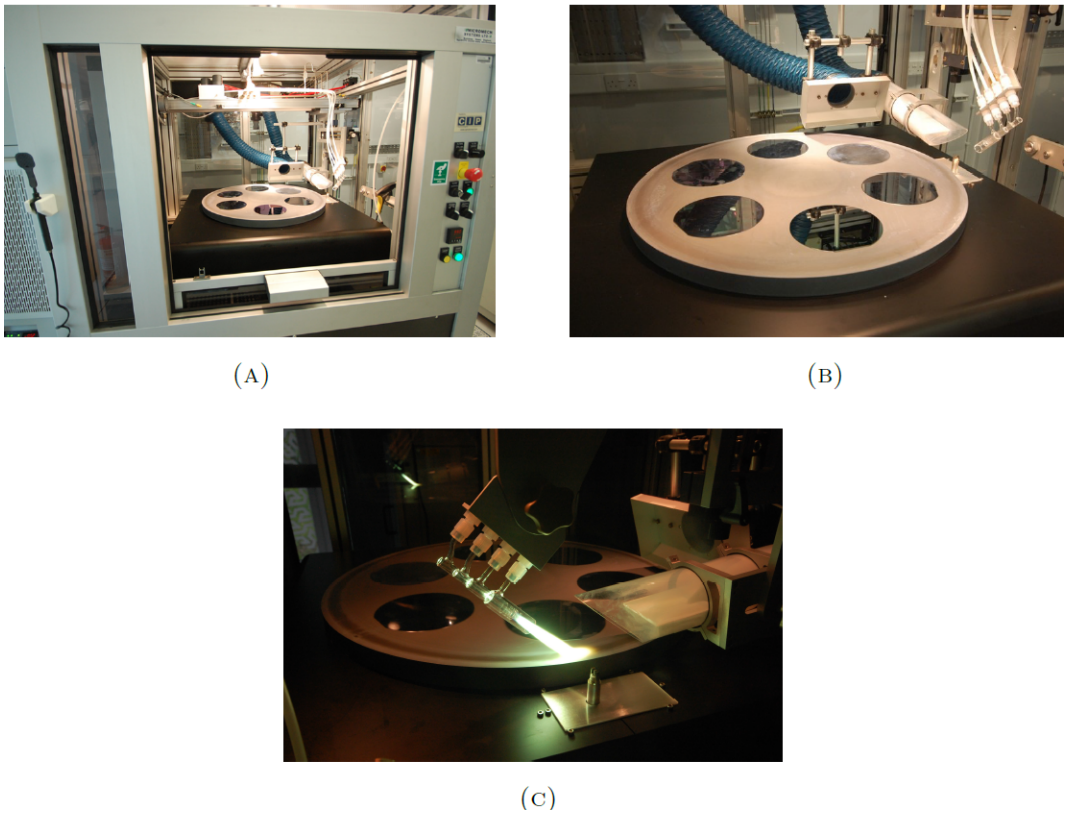

(A) (B)

(C)

FIGURE 3.3: (A) FHD deposition chamber and (B) deposition table with wafers prepared for deposition (C) Flame Hydrolysis Deposition onto silica wafers. The green tint to the flame indicates the presence of Boron. (picture credit: J. Gates).

The soot-deposited wafers are then consolidated at up to 1360 °C in the furnace (see Fig. 3.4 (A) & (B)), this maximum temperature being used for silicate rather than germanate glasses. The ramp rate of the furnace temperature may be controlled and the dwell time at maximum temperature set as well as the ramp down (i.e. cooling) rate although the latter is limited by the lack of an active cooling system. The soot is heated above its melting point and then cooled, undergoing the glass transition at temperature, T_g, wherein it abruptly increases its viscosity while retaining its disordered structure and will remain amorphous provided that the cooling rate is not small enough to cause crystallization. Figure 3.5 shows some of the furnace programs used for consolidation of GeO_2-SiO_2 samples. Consolidation is usually in a helium-oxygen atmosphere, although a pure helium purge may be used to increase the number of oxygen vacancies associated with UV photosensitivity and refractive index change as the number of oxygen vacancies produced is inversely proportional to the square root of the oxygen partial pressure [32].

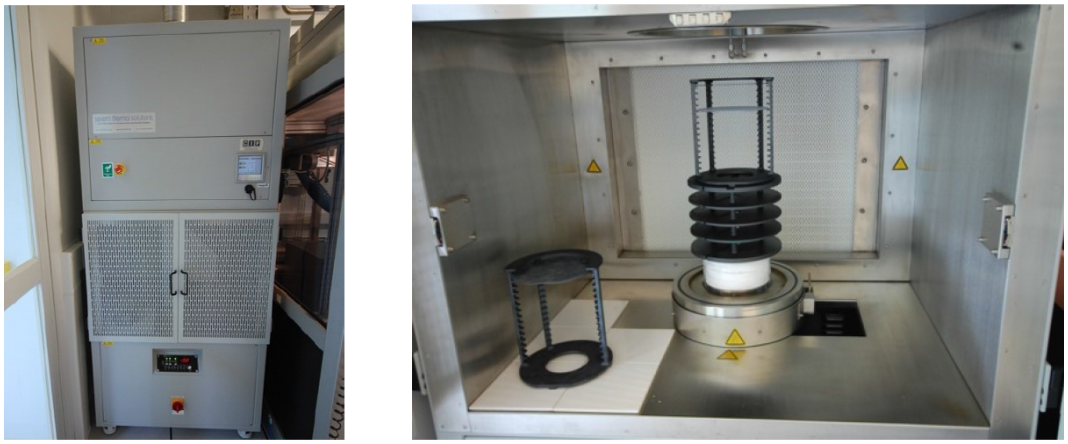

(A) (B)

FIGURE 3.4: Exterior (A) and interior (B) of furnace for the consolidation of FHD wafers. (picture credit: J. Gates).

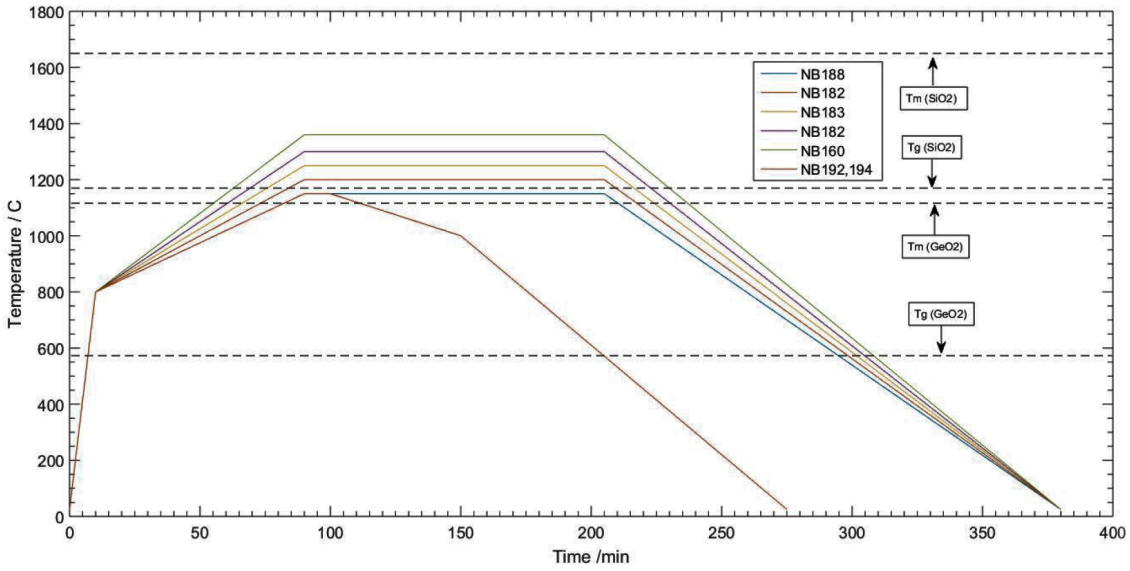

FIGURE 3.5: Consolidation programs for FHD runs NB160-NB194: the melting point and glass transition temperature of germania and silica are given for comparison.

The processes occurring during consolidation of germanate glasses are poorly understood: Some of the GeO_2 layer is lost as it reduces to the more volatile GeO as per equation 3.5 below [36]:

$$GeO_2 \leftrightarrow GeO \uparrow + O_2 \uparrow \tag{3.5}$$

It is well known that water is incorporated into glasses in most fabrication techniques to some degree and this is equally true for FHD: although the furnace atmosphere may be controlled, it is not isolated from the lab and thus will have a similar amount of water vapour. It may also react with water post-deposition:

$$Si - O - Si + H_2O \leftarrow 2SiOH \tag{3.6}$$

The rate of the reaction shown in equation 3.6 is stress-enhanced in silica and this leads to fatigue and deterioration of the glass over time. The same equation is valid for germania [33] and germanate glasses are in fact found to be more prone to reaction with water than silica [19][32]. Water ingression post-consolidation in the lab is also possible, and indeed evidence of both water ingression and reaction with water was seen in high GeO_2 samples, including samples which had been left in wafer boxes over a period of months (see section 3.2.2).

3.1.3 FHD system parameters

The effects of changing various deposition parameters are summarised in table 3.2 below.

TABLE 3.2: Summary of the effects of changing various parameters of the FHD system.

Parameter	Effects
Precursor flow rate	The amount of corresponding oxide soot deposited per pass increases with flow rate.
Bubbler temperature	Increased temperature increases vapour pressure of the halide precursor and thus the volume of soot deposited per pass.
Torch flow rates	Control the temperature and stoichiometry of the flame and thus the GeO_2 content and ODC concentration.
Torch angle	Changes the composition of the deposited soot. Greater angles result in greater GeO_2-content.
Torch position (relative to wafer)	Changes composition of soot and uniformity of consolidated wafer.
Gear ratio	Controls rate of rotation of deposition table and thus translation speed of torch; slow speeds result in more soot deposited per pass.

As mentioned earlier, the precursor and torch flow rates may be adjusted in order to control the composition of the deposited soot. Increasing the GeO_2-content is not solely reliant on increasing the $GeCl_4$ flow rate relative to that of $SiCl_4$: GeO_2 concentration increases with flame temperature up to approximately 800 °C, at which point it begins to decrease [34]. The reduction in either H_2 or O_2 flow rate has the effect of reducing the temperature of the flame [35]. The distance of the substrate from the flame also affects the GeO_2 content due to the temperature profile of the flame: too close and the $GeCl_4$ is neither hydrolysed nor oxidised, too far and the rapid increase in flame temperature causes the GeO_2 formed to be reduced to the more volatile GeO [23]. Similarly, Sakaguchi reports that insufficient temperatures result in hydrolysis dominating, forming hexagonal, i.e. crystalline GeO_2 [19]. While increasing the hydrogen-oxygen ratio increases the number of ODCs formed, which are thought to be directly related to UV photosensitivity, it also decreases the overall GeO_2 content [35]. An increase in the inclination angle of the torch with respect to

the deposition table has also been reported to result in greater GeO_2 concentration and thickness [35]. The bubbler temperature may also be adjusted, and this feature is particularly useful for precursors with comparatively low vapour pressures, e.g. $GeCl_4$ in comparison to $SiCl_4$, as the increase in temperature increases the vapour pressure, increasing the amount of soot deposited per pass even when the maximum flow rate has already been reached; this was utilized in the deposition of GeO_2 on to sapphire wafers (see section 3.2.4) and alumina and sapphire rods (see Chapter 6).

3.1.4 Analysis methods & development of wafers

The following section describes the iterative process of development and analysis of wafer samples. This is summarised in figure 3.6 below.

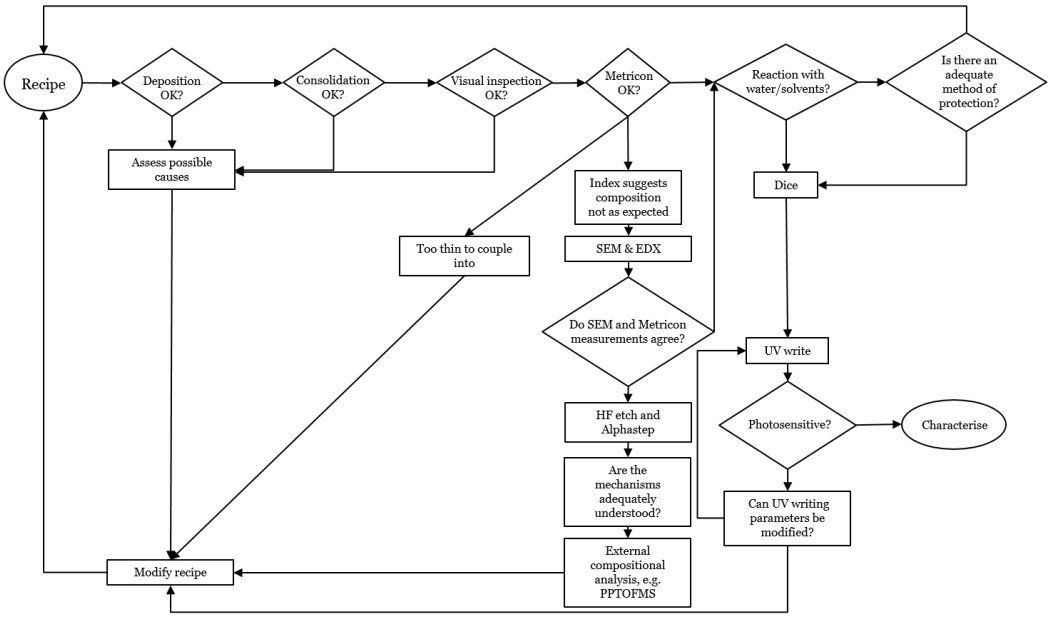

FIGURE 3.6: Flow chart of wafer development.

Samples were initially analysed using the Metricon 2010 prism coupling system to obtain thickness and refractive index measurements, and in some cases propagation loss measurements of the deposited layers. Multiple thickness measurements were used to calculate the percentage thickness variation. In the case of binary SiO_2-GeO_2 glasses, knowledge of the refractive index allows inference of the percentage composition of GeO_2 as there is a linear relationship between percentage GeO_2 content and refractive index [36]. In fact this is an approximation of a more general rule for oxides: the additivity rule. Doweidar provides a clear demonstration of the use of the additivity rule to describe the relationship between boron content in B_2O_3-SiO_2 glasses and GeO_2 content in GeO_2-SiO_2 glasses in [37] as well as the generalised relationships between refractive index, molar fraction, density and thermal expansion coefficient given below:

$$\mu = \Sigma n_u f_u = [j f_{u_1} + m f_{u_2}] N_A \tag{3.7}$$

$$\alpha = \Sigma n_u \alpha_u = [j \alpha_{u_1} + m \alpha_{u_2}] N_A \tag{3.8}$$

Equations 3.7 and 3.8 are the additivity rules for refractive index and thermal expansion coefficient respectively, where μ, n_u, f_u, α_u and N_A are the refractive index, number of moles of the glass, differential refraction of the structural unit u (individual units making up the glass network, e.g. GeO_4, BO_3), differential expansion of the structural unit and the Avogadro constant respectively, where j and m are molar fractions for structural units u_1 and u_2 where $j + m = 1$.

Where there was some doubt or inconsistency in thickness measurements, samples were etched using hydrofluoric acid (HF) and the Alphastep stylus profiler was used to measure the depth of the etched area relative to the surface to obtain a thickness measurement of the deposited layer. In the case of diffused GeO_2-SiO_2 samples, this technique uncovered some interesting and unexpected results in terms of the etch rates (see section 3.3.2) and gave some insight into the structure of these layers. Where composition data and/or accurate thickness measurements of the layers was required, the scanning electron microscope (SEM; Zeiss EVO LS25) and energy-dispersive x-ray spectrometry (EDX; INCA system) analysis were used. The bitmap element maps produced by the EDX were used to graph the count of number of atoms of each element by depth by summing the number of pixels per line, focussing on an end facet rather than the surface of the chip, in order to produce the count with respect to the depth of layers. The additivity rule was then used to check that the calculated percentage GeO_2 and SiO_2 contents were consistent with the measured refractive indices. The EDX has limitations: It has a resolution of a few microns and the amount of noise is demonstrated by the fact that an undeposited thin thermal oxide wafer, imaged for comparison with germanate samples, shows a small but significant signal for germanium, despite its absence. Some of the samples contained boron, which is near the limit of detection by EDX analysis due to its small mass and hence low photon energy, which on many systems will coincide with the noise peak [38] and indeed, boron was not detected in high boron-content samples by the system used in this work. The understanding of the composition of these samples was aided by the use of alternative methods of compositional analysis in addition to those immediately available. Various samples were analysed using ToFSIMS at Imperial College London, Glow-Discharge Mass Spectrometry (GDMS) at Ecole Polytechnique Federale de Lausanne (EPFL) and Plasma Profiling Time-of-Flight Mass Spectrometry (PPTOFMS) at Horiba in Paris (see following sections).

3.1.5 Glow discharge mass spectrometry (GDMS)

GDMS consists of a chamber in which a low-pressure gas, often Argon, has a potential difference of 500-1500V passed through it, causing ionization [39]. The sample to be analysed is used as the cathode and positive ions are accelerated towards it, causing secondary electron emission and dislodging atoms of the sample. The electrons then collide and excite (and subsequently decay to lower levels, releasing their energy as the “glow"), or ionize gas particles, sustaining the collision process. The plasma is analysed using a mass spectrometer to produce composition with respect to depth [39]. Identification of a matrix element, e.g. Si for silicate samples, is essential for the use of this technique.

3.1.6 Time-of-flight secondary ion mass spectrometry (ToFSIMS)

Time-of-flight secondary ion mass spectrometry (ToFSIMS) was carried out at the Royal School of Mines at Imperial College London. The system consists of a caesium ion beam used to cause desorption of the surface ions and electrons. The ions are then accelerated and the time-of-flight of the ions is calculated and their charge-to-mass ratio used to identify them. ToFSIMS is usually used as a surface analysis technique. The three chosen samples, NB188, NB183-2 and NB160-2, were angle polished at 5° to the upper surface (see fig. 3.7 (L)). Rastering the beam across an area of 250x250 μm, centred on the interface between surface and angle polished area allowed analysis with respect to depth of the entire core layer rather than only the top few nm (see fig. 3.7 (R)). As with most mass spectrometry, there is the possibility of interference causing mis-identification of ions, e.g. P^- ions may be incorrectly identified as SiH_3^- ions and vice versa; GeH^- can be mis-identified as As^-. These results were challenging to interpret due to the sheer number of ionic species detected.

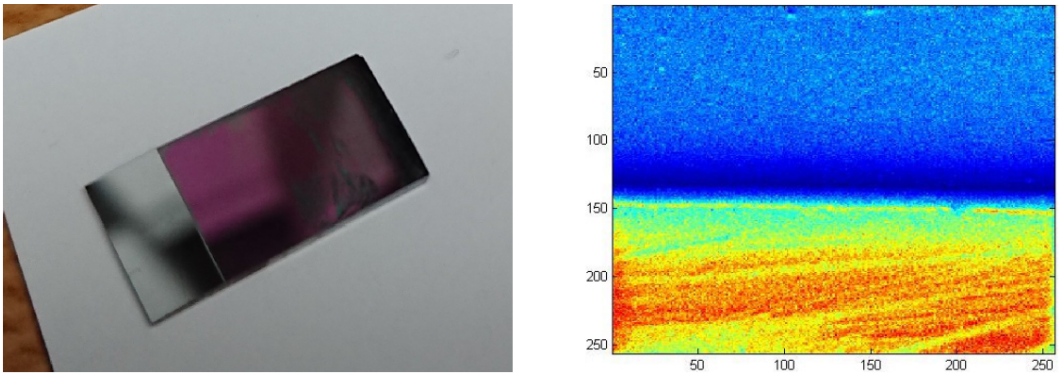

FIGURE 3.7: (L) Angle polished 10×20 mm chip from sample NB160-2 (R) Distribution of OH- ions over an area of 250×250 μm on similarly polished sample NB160-2

3.1.7 Plasma profiling time-of flight mass spectrometry (PPTOFMS)

PPTOFMS analysis is a novel technique designed for use on microelectronic materials, wherein a pulsed radio-frequency signal is applied to the back of the sample, while argon plasma is directed at its surface resulting in fast erosion of the layers [40] (see fig. 3.8). The resulting ions are accelerated and extracted by sampler, which is connected to a time-of-flight mass spectrometer, yielding composition data with respect to time [41]. This technique allows detection of lighter elements such as hydrogen and boron [42] with nanometre resolution, and does not require a matrix as GDMS normally would [41]. Temporal information may be converted to depth information via the use of standards. Thus the use of this technique has not yet been validated for oxide samples, as a suitable sample with an accurately known dopant level would be required[2], so this technique can give only an indication of the composition with respect to depth, however, the semi-quantitative and qualitative data it provides, combined with more established techniques makes it a valuable technique. Three GeO_2-SiO_2 samples were analysed: NB160-2, NB183-2 and NB258-1, along with a P_2O_5- GeO_2-SiO_2 sample, NB89, a B_2O_3-P_2O_5-GeO_2-SiO_2 clad sample, NB254-1 and un-clad B_2O_3-P_2O_5-GeO_2-SiO_2 sample, NB261-1.

[2]Such a sample was sought, but sufficiently accurate data on dopant levels was difficult to obtain

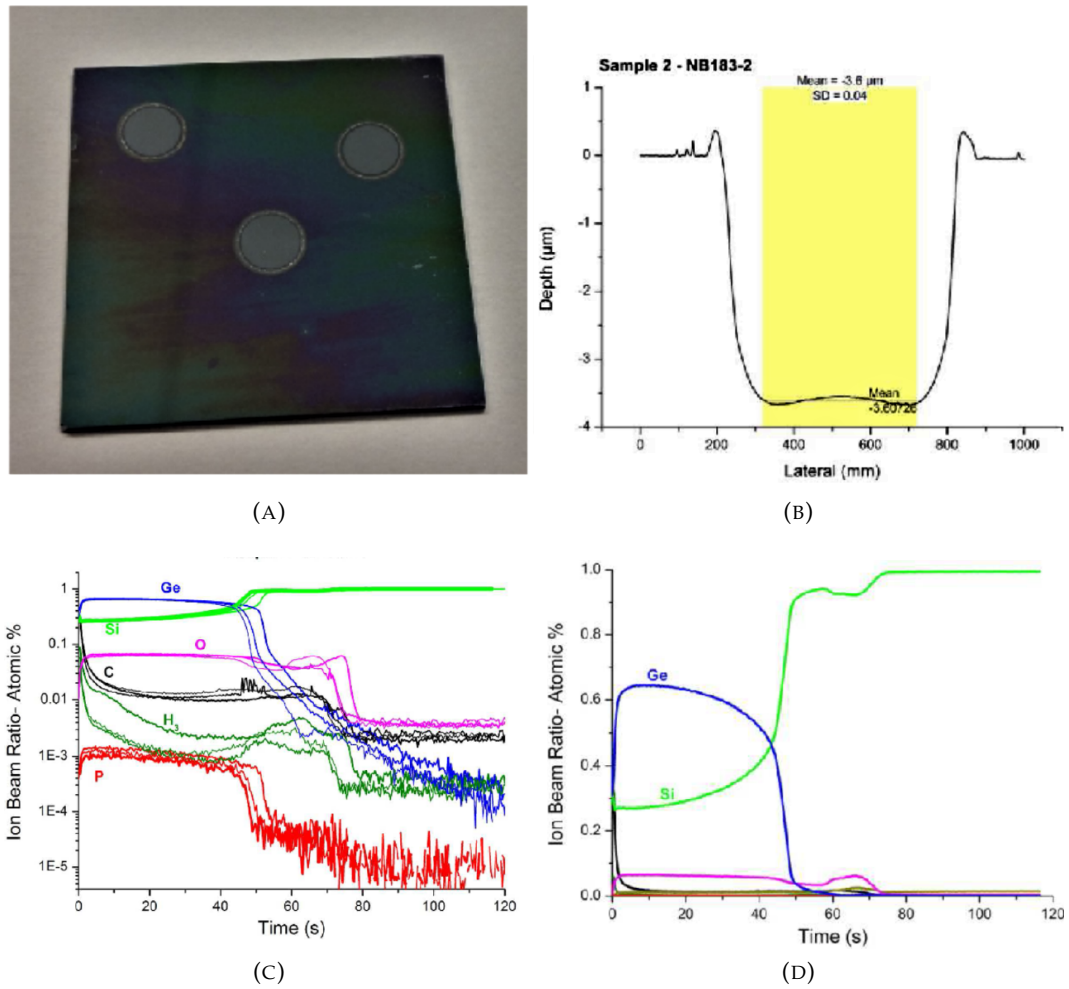

(A) (B)

(C) (D)

FIGURE 3.8: (A) 3.6 μm craters formed via the PPTOFMS technique in 2 minutes; Three craters have been etched to demonstrate repeatability of measurements. (B) Plot of the corresponding etch depth of a crater with respect to time. (C) Composition by time for a germanate sample analysed using PPTOFMS, with three sets of results from the same sample in order to demonstrate repeatability (D) Percentage composition by time for a germanate sample analysed using PPTOFMS

TABLE 3.3: Summary of the analysis techniques used in this work and their limitations.

Technique	**Uses**	**Limitations**
Prism Coupling	Refractive index, thickness	Cannot detect very thin layers (nm).
Propagation loss (via prism coupling)	Loss	Software requires user to select parts of graph to be included in analysis; potential for inconsistency.
SEM	Layer thickness, topography	Cannot provide composition data.
EDX	Composition	Cannot detect lighter elements, e.g. boron. No compound identication.
Element Mapping (EDX)	Composition with respect to depth	Cannot detect lighter elements, e.g. boron. No compound identification.
HF etch + Stylus profiling	Thickness	Inaccurate if layers are diffused
Zescope	Surface roughness, topography	Not ideal for curved surfaces, e.g. rods fabricated in chapter 6.
PPTOFMS	Composition with respect to depth	Method not yet validated for oxides.
ToFSIMS	Composition with respect to depth	Interpretation of results can be complex and time-consuming due to sheer volume of data.
GDMS	Composition	Requires matrix element to be identified. Depth profiling only to a few nm. Low lateral resolution.

3.2 Flame hydrolysis deposited germania layers

Germania soot was deposited on to bare silicon wafers, thin thermal oxide wafers, thick thermal oxide wafers and sapphire windows using the FHD method and consolidated in an oxygen-helium atmosphere at various temperatures between 1360 °C and 1150 °C. Tables 3.3-3.7 provide characterization data for all samples. These are split by substrate type. Thick thermal oxide wafers consist of a silicon wafer with 15 μm of silica, thin thermal oxide consists of a silicon wafer with 1.3-1.4 μm of silica grown over a period of 24 hours in the FHD furnace. The objective was to produce a low-loss, high quality (smooth; uniform; flat), chemically stable, high molar percentage or pure GeO_2 layer of a few microns, suitable for direct UV writing and/or milling to produce a Damascene ring resonator.

3.2.1 Initial investigations

Due to the lack of literature regarding flame hydrolysis deposition of pure germania, as an initial investigation, a silicon wafer and a thin thermal oxide (of approximately 1.3 μm) SiO_2 wafer were deposited with GeO_2 over 14 runs and consolidated at 1360 °C in an oxygen-helium atmosphere (see table 3.4).

TABLE 3.4: Initial FHD run results.
*- calculated from index; †- read from element mapping data;
§- read from PPTOFMS data; ‡- calculated using EDX molar percentage data and the additivity rule.

Wafer code	**NB160-1**	**NB160-2**
Substrate	Oxidised Si	Si
Percentage GeO_2*	36	39
Percentage GeO_2†	36	39
Percentage GeO_2§	-	39
n at 633nm (calc'd)‡	1.5104	1.5151
n at 633nm(Metricon)	1.5104	1.5151
n at 1550nm(Metricon)	1.4983	1.5007
Thickness (Metricon)	2.16	2.47
Thickness (SEM)	2.02	2.52
% thickness variation	9.83	5.41

This resulted in transparent layers, albeit with some apparently crystalline defects in the case of the silicon wafer (see fig. 3.9). The refractive index of both samples was found to be lower than that of pure germania (1.6054 at 633 nm [43]), the silicon (NB160-2) and SiO_2 (NB160-1) wafers having an index and thickness of 1.52 and 2.4 μm and 1.51 and 2.0 μm respectively when measured using the prism coupling technique using the Metricon-2010 prism coupler. The low refractive indices and smaller difference in thickness between the two substrates than might be expected suggest a significant amount of diffusion of germania into the SiO_2 layer in the case of the thin thermal oxide sample, and of both oxidation of the silicon and diffusion of the germania layer in the case of the silicon sample. The greater thickness and index in silicon samples may be attributed to the thinner SiO_2 layer formed via oxidation in comparison to an already present 1.3 μm SiO_2 layer, giving a shallower layer for the germania to diffuse into in sample NB160-2.

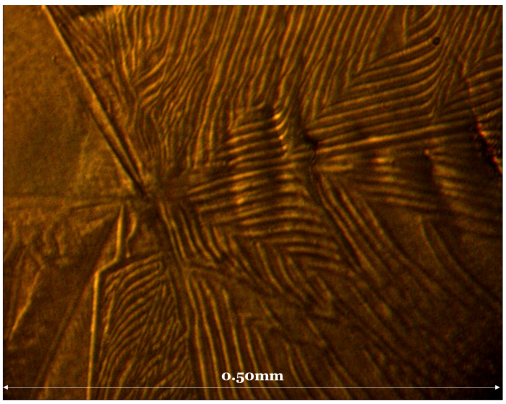

FIGURE 3.9: An apparently crystalline defect on wafer NB160-2.

In order to confirm the presence and extent of diffusion in these samples, they were imaged using the SEM and elemental analysis was performed using EDX spectrometry. Measurements of the layer depth using the SEM images are consistent with the thicknesses calculated by the Metricon. The samples were found to be almost indistinguishable from each other in appearance, despite the difference in substrate. A thin thermal oxide sample from the same FHD run as that used for the thin thermal oxide substrate, with known thickness and composition was also imaged in order to verify the results (see table 3.4). Calculation using the additivity rule for refractive indices gives a layer of about 39% and 36% germania for the silicon and thin thermal oxide wafers respectively. This result is consistent with the normalised germania and silica content in figures 3.11 and 3.13, which were produced from element mapping (see figs. 3.10 & 3.12) combined with SEM images. Note that the lack of clearly defined boundaries in figs. 3.10 - 3.13 are due to the beam being only partially directed onto the sample as it scans across its edge.

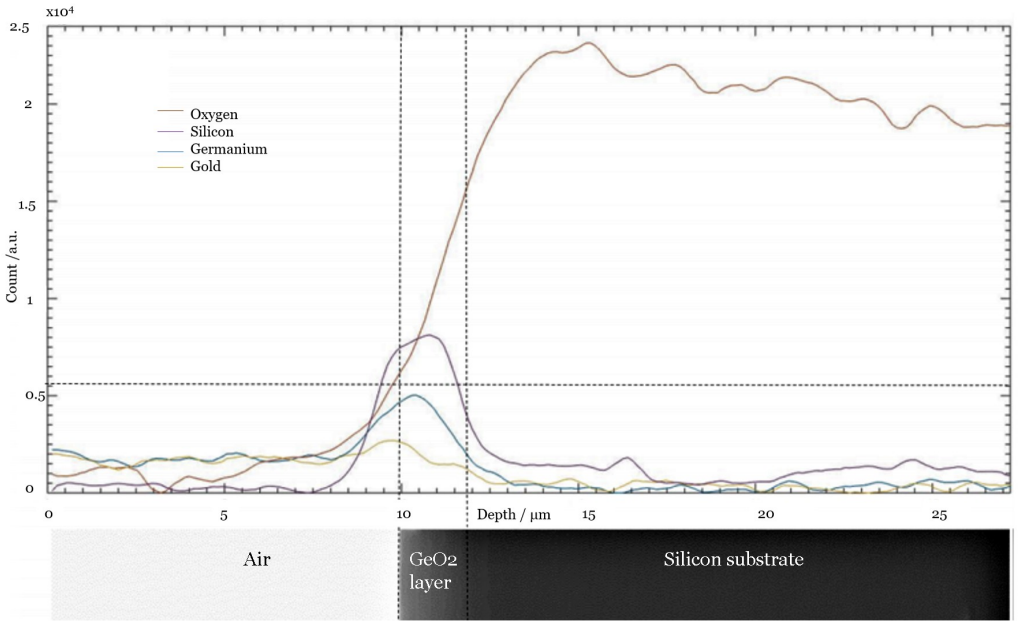

FIGURE 3.10: (A) Composition by depth from EDX element mapping for unclad GeO_2 on oxidised silicon wafer NB160-1 with SEM image. Dashed lines indicate the boundaries of the core layer.

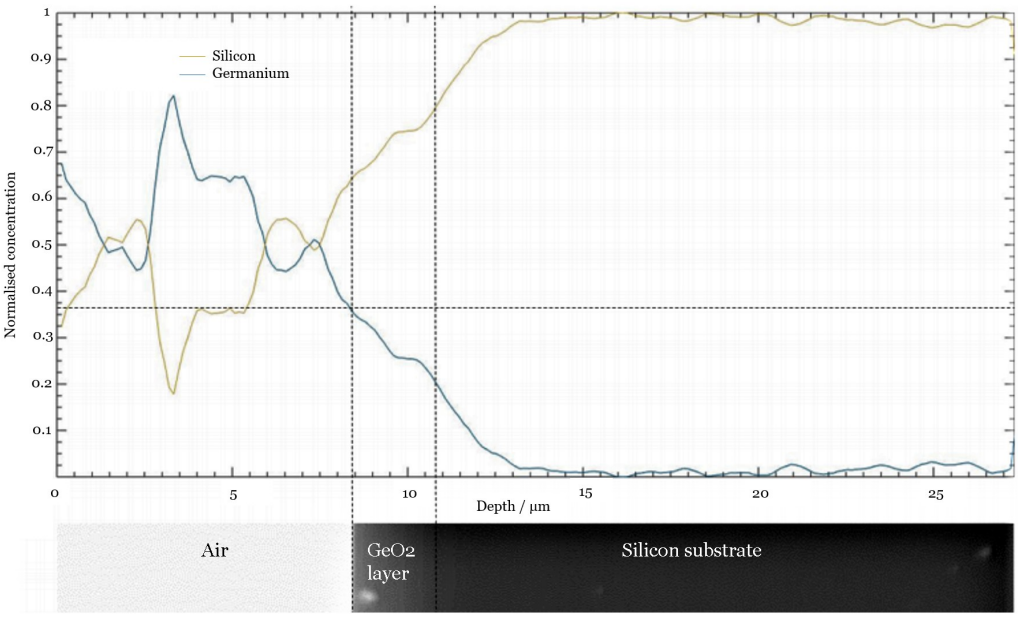

FIGURE 3.11: Normalised composition by depth from EDX element mapping of NB160-1 with SEM image, showing a 36% GeO_2 content. Dashed lines indicate the boundaries of the core layer.

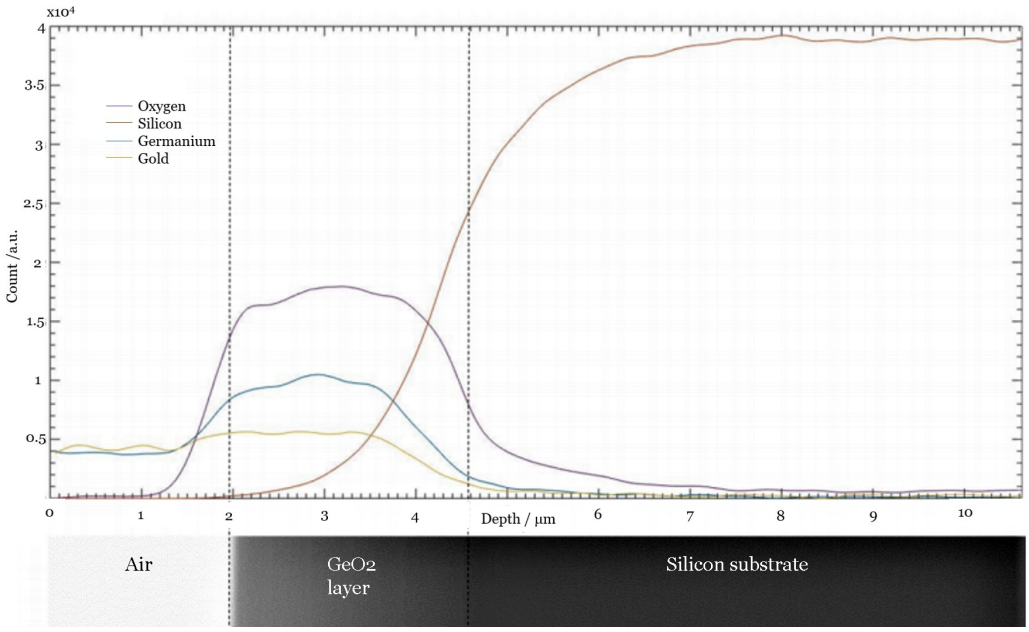

FIGURE 3.12: (A) Composition by depth from EDX element mapping on GeO_2 on silicon wafer NB160-2 with SEM image. Dashed lines indicate the boundaries of the core layer.

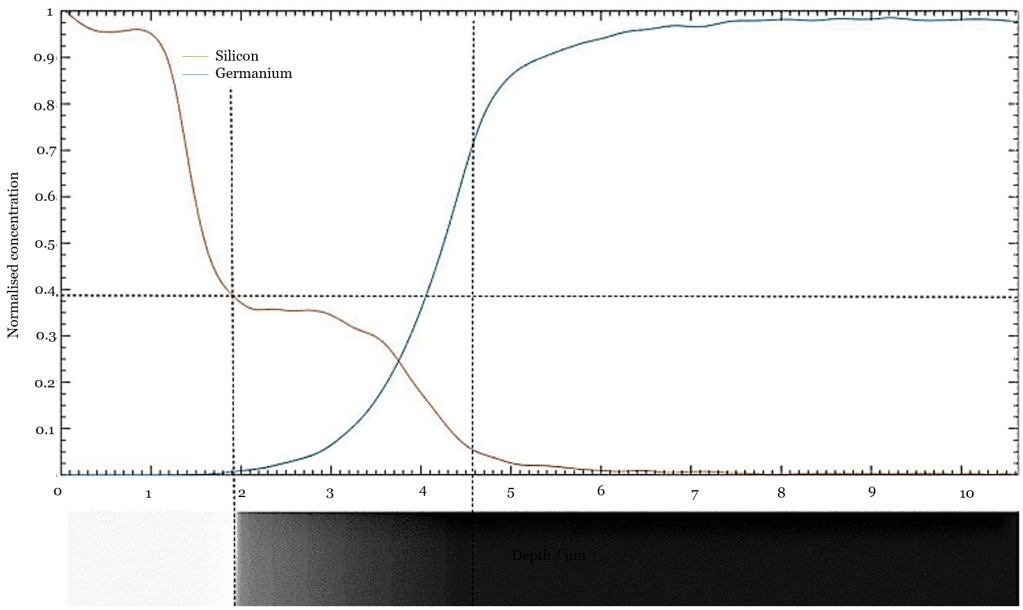

FIGURE 3.13: Normalised composition by depth from EDX element mapping of NB160-2 with SEM image, showing a 39% GeO_2 content. Dashed lines indicate the boundaries of the core layer.

PPTOFMS was later used to investigate the composition of sample NB160-2 (GeO_2 on Si) and this data further confirmed the percentage composition calculated by additivity and element mapping (see fig. 3.14). The consistency between element mapping, additivity rule and measured refractive indices confirmed that calculation of GeO_2 content on the basis of refractive index was a valid and efficient method when only percentage composition of binary GeO_2-SiO_2 samples was required. Due to the unexpected composition data, these samples were etched using hydrofluoric acid (HF), further detailed in section 3.2.3.

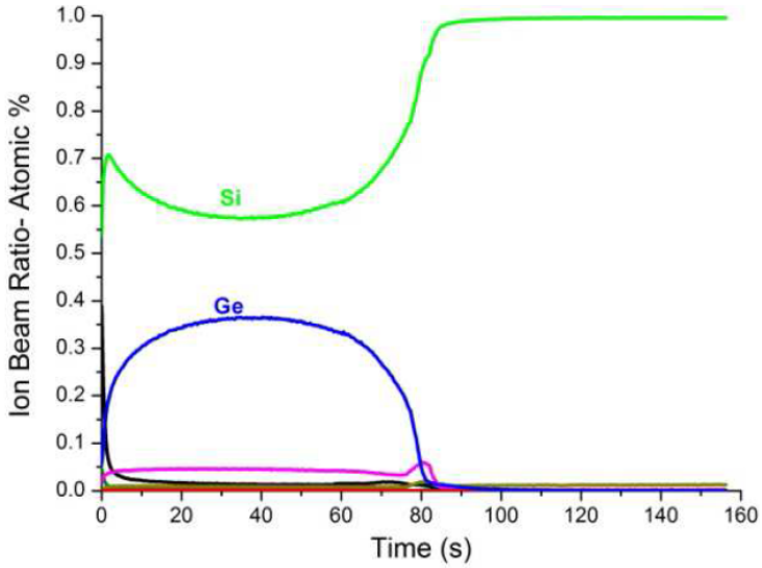

FIGURE 3.14: Composition by depth using PPTOFMS on GeO_2 on oxidised silica sample NB160-1, showing a percentage composition of approximately 36% Ge. The pink line shown represents oxygen and is qualitative only.

Etching these layers was extremely slow in comparison to the known etch rate of silica and the etch rate seen in higher GeO_2 content samples. This is consistent with the idea of diffusion of the deposited layer into the interstices of the SiO_2 layer, regardless of whether the layer was already present or formed via oxidation in the furnace. These results suggest that GeO_2 gets into the SiO_2 interstices, preventing etching and water ingression, consistent with modelling of the structure of high GeO_2-content GeO_2- SiO_2 glasses as spherical particles of one glass immersed in the other by Baral et al, giving a fairly homogenous glass at the concentrations found here [42].

ToFSIMS data was difficult to interpret, due to the number of ionic species identified (see fig. 3.15 (A)).

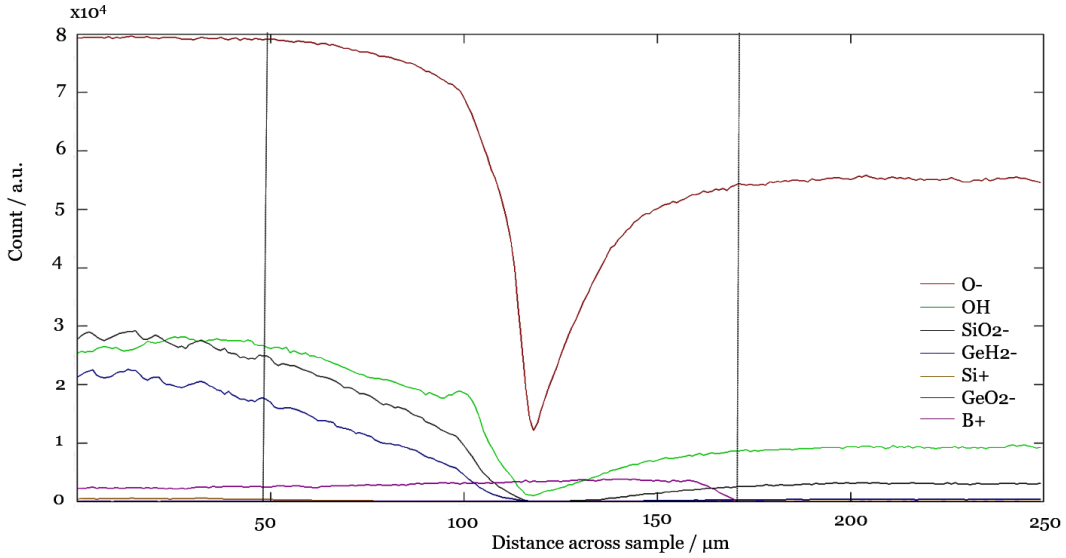

(A)

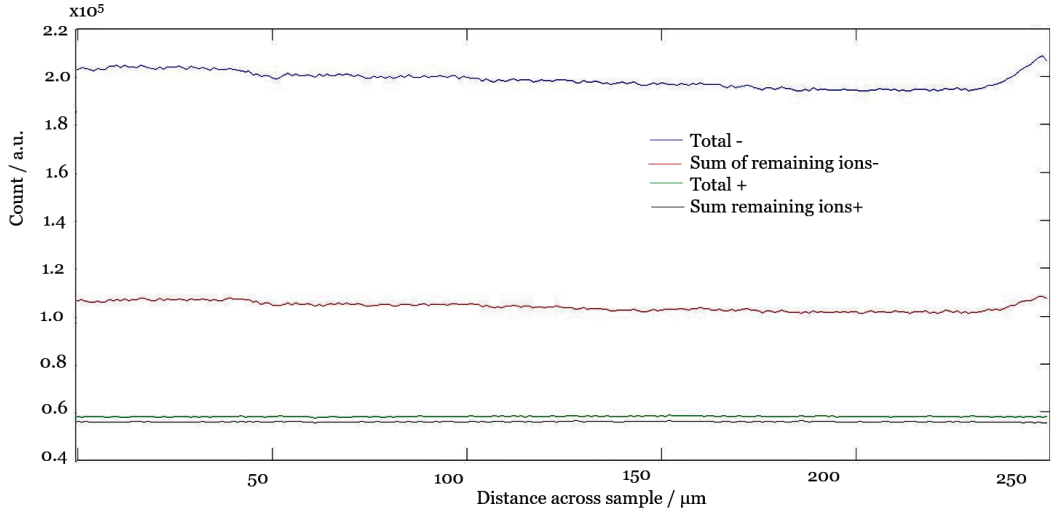

(B)

FIGURE 3.15: (A) Composition by distance across angle polished GeO_2 on silica sample NB160-2 uisng ToFSIMS. The left hand dotted line indicates the start of the angle-polished region; the right hand line the beginning of the substrate layer. (B) Sum of remaining ions unidentified.

There were also a number of ions detected but their distributions not imaged, since this would require identification of all possible ions before analysis, e.g. to detect GeO_2^-, the system must be told to detect it, which requires the user to at least suspect its presence and input it to the software. The unidentified ions are given by the sum of the rest data in fig. 3.15 (B). While the concentration of SiO_2^- and GeH_2^- appear to follow each other, and are approximately in proportion to the concentrations of SiO_2 and GeO_2 seen in the element mapping and PPTOFMS data (assuming the GeH_2^- is a result of water ingression), incomplete data means further analysis is impossible.

3.2.2 Germania on silicon and oxidised silicon substrates

Wafers were prepared and deposited with the same recipe as for NB160 but with lower consolidation temperatures of 1300 °C to 1150 °C with the dwell time at maximum temperature reduced to 10min on later runs in order to further reduce diffusion (see tables 3.5 & 3.6).

TABLE 3.5: Thin thermal oxide wafer FHD results.
*- calculated from index; ‡ - calculated using EDX molar percentage data and the additivity rule.

Wafer code	**NB160-1**	**NB198-5**	**NB183-2**	**NB182-1**	**NB192-1**
Consolidation temp. /°C	1360	1300	1250	1200	1150
% GeO_2*	36	63	74	86	93
n calc'd ‡	1.5104	1.5514	1.5668	1.5841	1.5958
n at 633nm	1.5104	1.5511	1.5667	1.5840	1.5957
n at 1550nm	1.4983	-	1.5489	1.5639	1.5800
Thickness /μm	2.09	4.73	2.79	3.01	3.42
% thickness variation	9.83	10.56	5.54	4.50	8.32

TABLE 3.6: Silicon wafer FHD results.
*- calculated from index; †- read from element mapping data; §- read from PPTOFMS data; ‡- calculated using EDX molar percentage data and the additivity rule.

Wafer code	**NB160-2**	**NB198-1**	**NB183-1**	**NB182-2**	**NB192-2**
Consolidation temp. /°C	1360	1300	1250	1200	1150
% GeO_2*	39	79	74	92	96
% GeO_2§	39	-	71	-	-
n calc'd‡	1.5151	1.5744	1.5689	1.5937	1.5990
n at 633nm	1.5151	1.5744	1.5688	1.5936	1.5990
n at 1550nm	1.5007	-	1.5503	1.5692	1.5815
Thickness /μm	2.55	2.31	3.26	3.33	3.16
% thickness variation	5.41	8.62	10.91	2.74	4.19

This resulted in increasing layer thickness with decreasing temperature (see fig. 3.16). Refractive indices approached that of pure germania (1.6054 at 633 nm [43]) as the temperature was reduced, and thus the germania content inferred from the

additivity rule was found to increase with reduced temperatures (see fig. 3.17). It is presumed these effects are due to reduced diffusion.

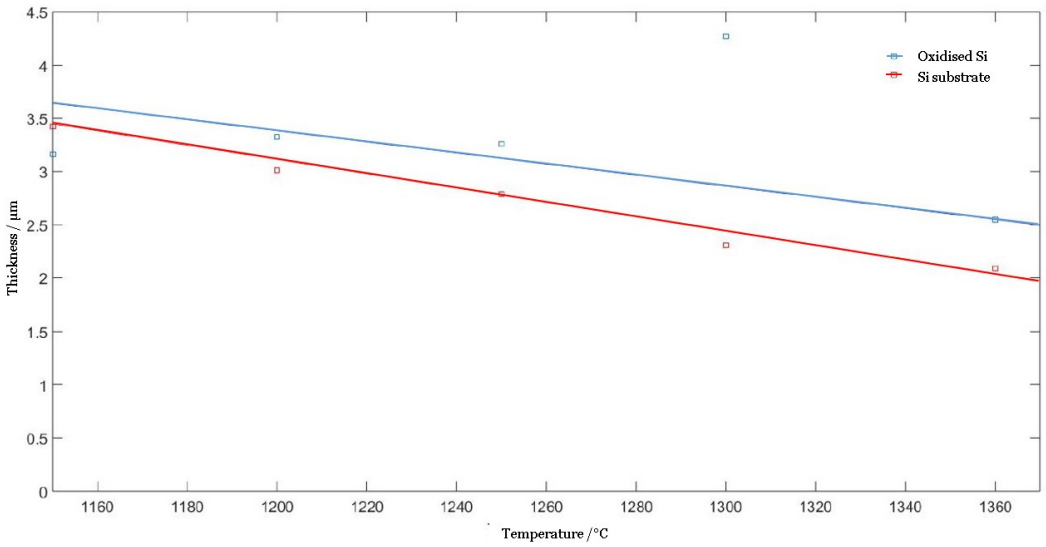

FIGURE 3.16: Temperature versus thickness of GeO_2-SiO_2 layer.

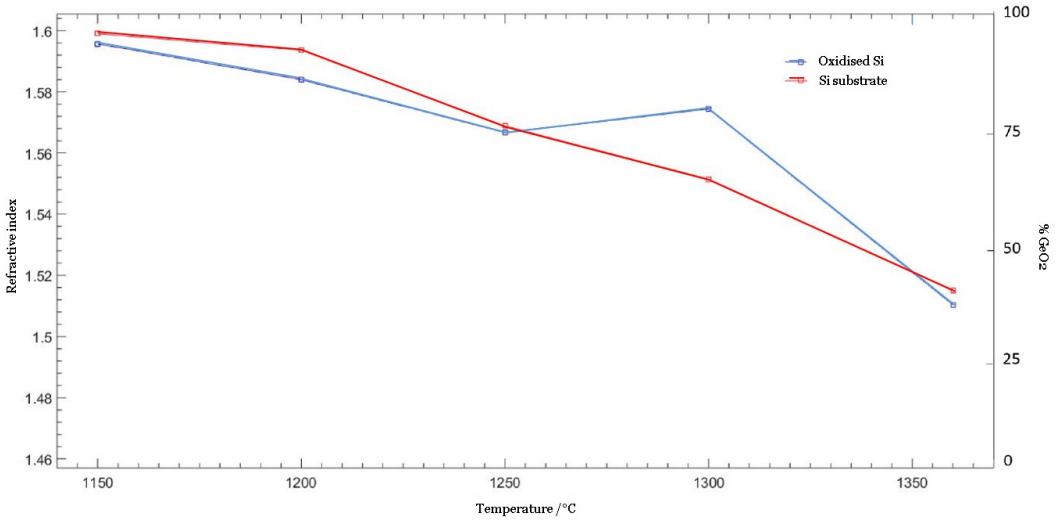

FIGURE 3.17: Temperature versus index and percentage GeO_2-content.

However, samples consolidated at 1250 °C and below showed high sensitivity to water, IPA and acetone, with which the deposited layer could be rubbed off with little effort. If not abraded, the surface nevertheless deteriorated immediately on exposure to water, showing a pearlescent appearance (see fig. 3.18 (A)) and granular appearance under a microscope (see fig. 3.16 (B)), which is associated with phase-separation [34], and prism coupling following exposure to water or solvents was impossible. As an extreme example, a wafer consolidated at 1150 °C, NB194-2, deteriorated to the point that it was completely pearlescent in a matter of months kept in an unopened wafer box in a lab. The pearlescence was noticeably particularly bad around the edges of wafers, although not at the extreme edges (see fig. 3.18 (C)), suggesting that this phenomenon is stress-related that there is a radial difference in

temperature and pressure during consolidation, which causes edge effects, the composition being significantly different from the rest of the layer, perhaps with lower GeO_2 content and thus less stress due to CTE mismatch. The stress in the layer is also known to increase with distance from the interface [16]. The required stress for crystallinity is thus perhaps less than for aiding reaction with water.

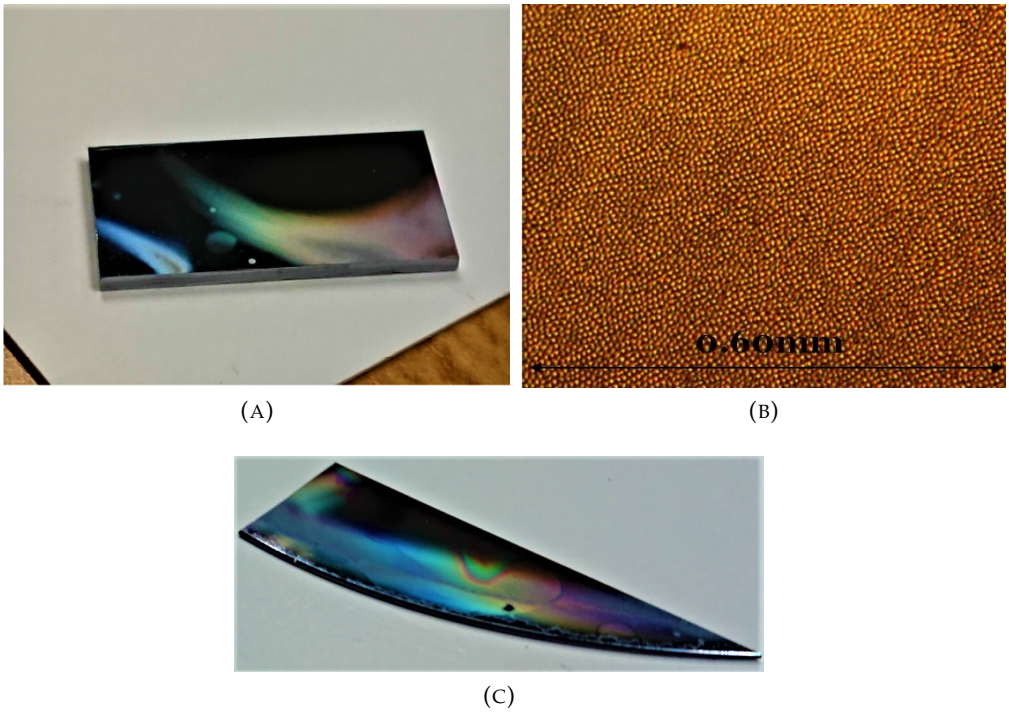

(A) (B)

(C)

FIGURE 3.18: (A) Pearlescence on wafer NB183-2 post dicing. (B) Microscope image of a pearlescent area on sample 183-2 due to water contact. (C) An area of pearlescence on sample NB183-2 at 5x magnification. Note the apparently crystalline defect near the curved edge.

3.2.3 HF Etching

Etching these samples using HF showed slow etching for the high temperature consolidated layers with greatest diffusion and fastest for low-temperature consolidated samples which have been determined via their refractive index and EDX analysis to have larger germania concentration. Silica samples with no germania deposition were found to have etch rates somewhere between that of germania and that of mixed layers (see fig. 3.19). Sample NB183-2 was analysed using PPTOFMS (see fig. 3.18) . As with the PPTOFMS and ToFSIMS results for NB160-1, the PPTOFMS results for NB183-2 (see fig. 3.19) are in-keeping with the refractive index data and inferred GeO_2 content, but the ToFSIMS data is incomplete. As such, the SiO_2^- and GeH_2^- concentrations are seen to be approximately consistent with the rest of the data but without identification of the "missing" ions, little more can be concluded.

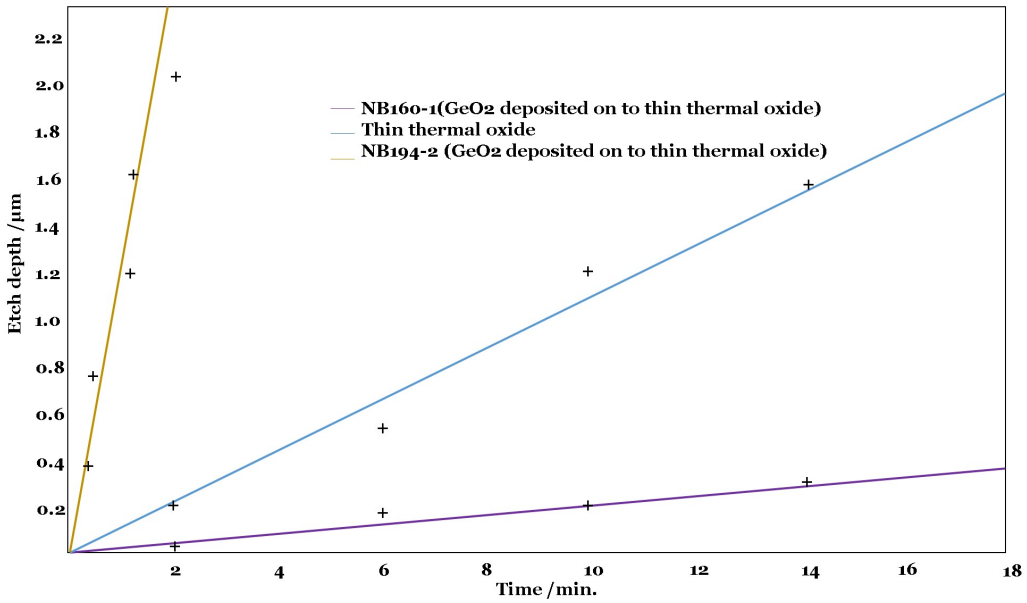

FIGURE 3.19: HF etch rates for three samples; NB160-1, NB194 (a copy of oxidised silicon wafer NB192-1, consolidated at 1150 °C) and thin thermal oxide. NB160-1 has an etch rate of approximately 0.02μm/min., the thin thermal oxide sample approximately 0.1μm/min. and NB194-2 approximately 1μm/min.

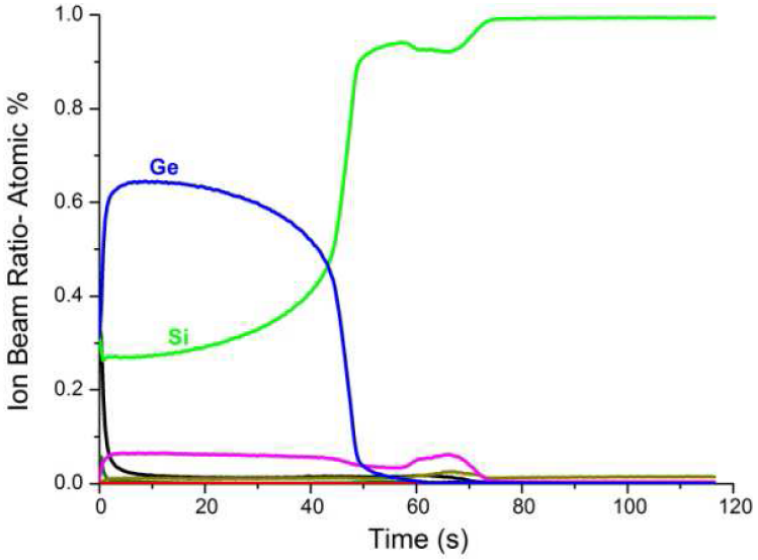

FIGURE 3.20: Composition by depth using PPTOFMS on GeO_2 on silica sample NB183-2. The pink line shown represents oxygen and is qualitative only. Exclusion of all but Ge and Si gives a GeO_2 content of around 71%.

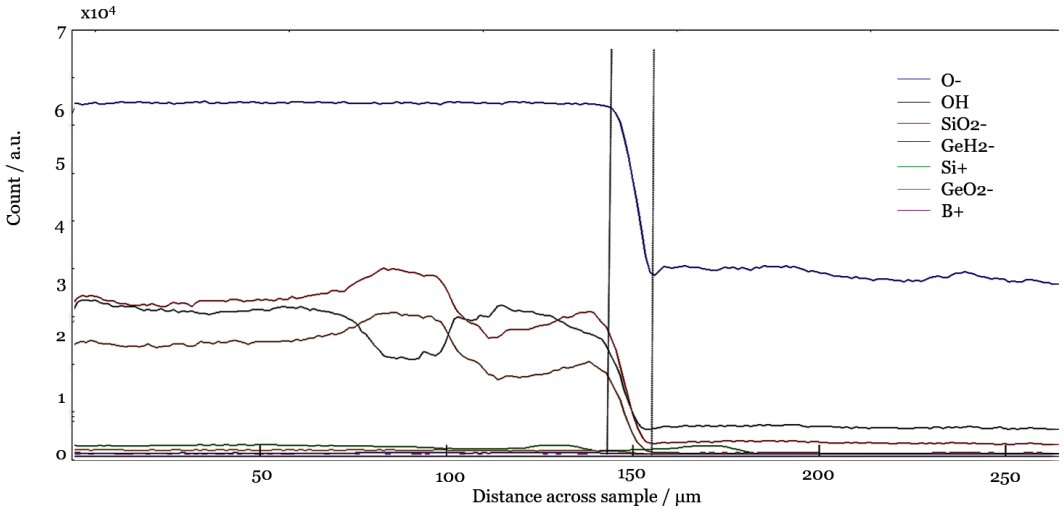

FIGURE 3.21: Composition by distance across angle polished GeO_2 on silica sample NB183-2 uisng ToFSIMS. The left hand dotted line indicates the start of the angle-polished region; the right hand line the beginning of the substrate layer.

In summary, high temperatures cause diffusion of the germania into the silica layer, which results in mixed GeO_2-SiO_2 layers which resemble a heavily germania-doped silica layer. In the case of the silicon wafer, diffusion of germania occurs in addition to oxidation the substrate. Lower temperatures (1250 °C and below) result in less diffusion and thus separate layers with a large CTE difference between them. GeO_2 is known to be more sensitive to water in comparison to silica [19][32]. Stress appears to aid water ingression and the reaction which destroys GeO_2 [33]. Therefore the purer the germanate layer, the more susceptible it is to water ingression and degradation when consolidated on silica wafers, due to the mismatch of CTE rather than germania content per se.

3.2.4 Low-on-high temperature consolidated germania layers

In order to reduce sensitivity to water by reducing the thermal expansion mismatch, a germania layer was deposited on to a 15 μm thermal oxide wafer, consolidated at high temperature, and a second layer deposited and consolidated at lower temperature (see table 3.7).

TABLE 3.7: Low-on-high temperature consolidated GeO_2 results. *- calculated from index; §- read from PPTOFMS data.

Wafer code	**NB258-1**	**NB223-1**	**NB203-1**
% GeO_2 in upper layer*	94	100	91
% GeO_2 in upper layer§	97	-	-
n at 633nm	1.5959	1.6054	1.5920
Thickness /μm	1.57	3.49	1.19
Loss at 1550nm (dB/cm)	3.44	-	6.01

This sample (NB258-1) showed much reduced sensitivity to water and solvents, and could be carefully cleaned without damage. Dicing, however still damaged the germania layer (see fig. 3.20), and resulted in the pearlescent appearance seen in previous water-damaged samples (see fig. 3.16).

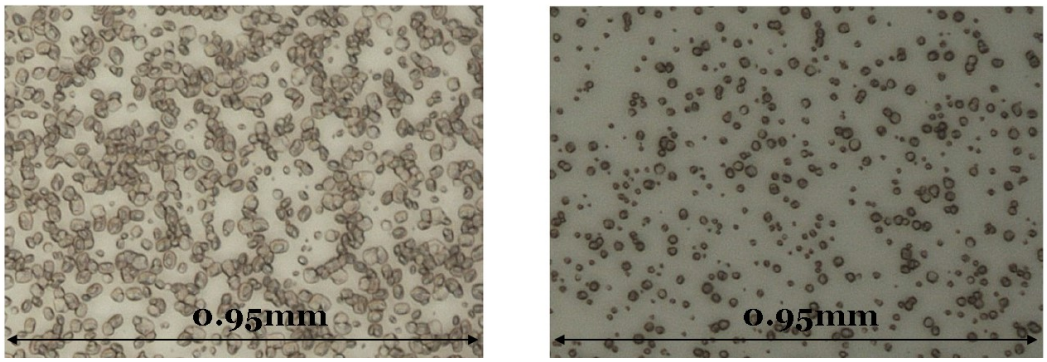

FIGURE 3.22: Microscope images of NB203-1: (L) pearlescent area due to water contact (R) An area of semi-pearlescence.

GDMS was used on sample NB258-1 for compositional analysis. However, germanium could not be found as a matrix element and it is suspected that the cleaning process used in preparation for analysis removed most of the GeO_2 layer, leaving only the low GeO_2 content part which varied in composition from 30-3% with increasing depth. A cleaved sample showed some UV photosensitivity (see chapter 4) and further samples were fabricated with the same recipe in order to investigate this. Both the Metricon and PPTOFMS (see fig. 3.21) confirm the existence of distinct layers of different GeO_2 contents.

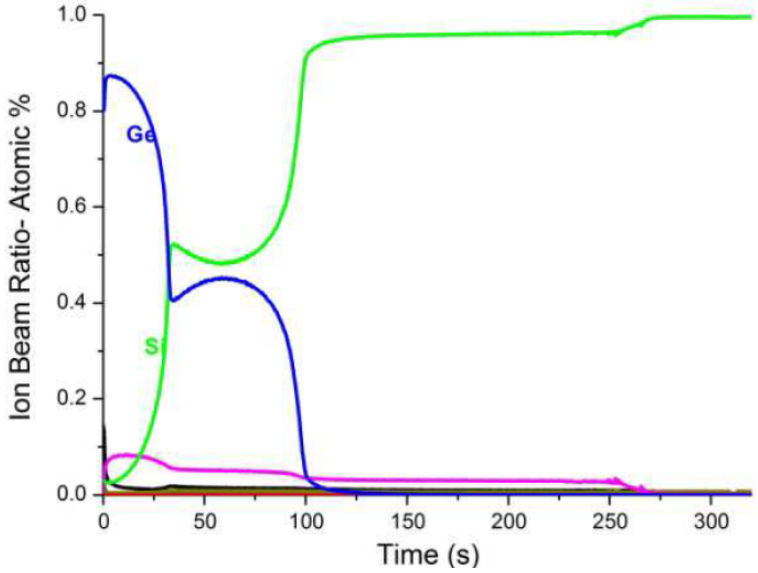

FIGURE 3.23: Composition by depth using PPTFOMS on GeO_2 on silica sample NB258-1. The pink line shown represents oxygen and is qualitative only. Exclusion of all but Ge and Si gives a GeO_2 content of around 94%.

As mentioned earlier, CTE may also be calculated via a similar additivity rule as for index and GeO_2 content (see equation 3.6, section 3.2). Using this rule, the CTE of the upper layer is estimated to be around 7.08×10^{-6} K^{-1} and that of the lower

layer around 3.79x10^{-6} K^{-1}. The significant difference in thermal expansion between these two layers supports the idea that the reaction with water is not down to high germania content, but the CTE difference between it and the lower layer. If a further “buffer" layer was consolidated at an intermediate temperature, and thus an intermediate GeO_2-content and CTE, it may be possible to produce stable, near pure germania layers.

3.2.5 Pure germania on sapphire substrates

Deposition onto a sapphire window was investigated for comparison with the work of Sakaguchi, and consolidation was attempted at 950 °C and 1150 °C. Sample NB238-1, consolidated at 950 °C had a visibly poor quality layer (See fig. 3.22 (A)), and microscope images appeared to show possible crystallinity, cracking (despite a closer CTE to germania in comparison to silica substrates), and striations of the surface (see fig. 3.23 (A) - (C)). However, germania layers were successfully consolidated onto sapphire windows at 1150 °C, resulting in transparent glass layers (see fig. 3.22 (B) & (C) and fig. 3.23 (D)).

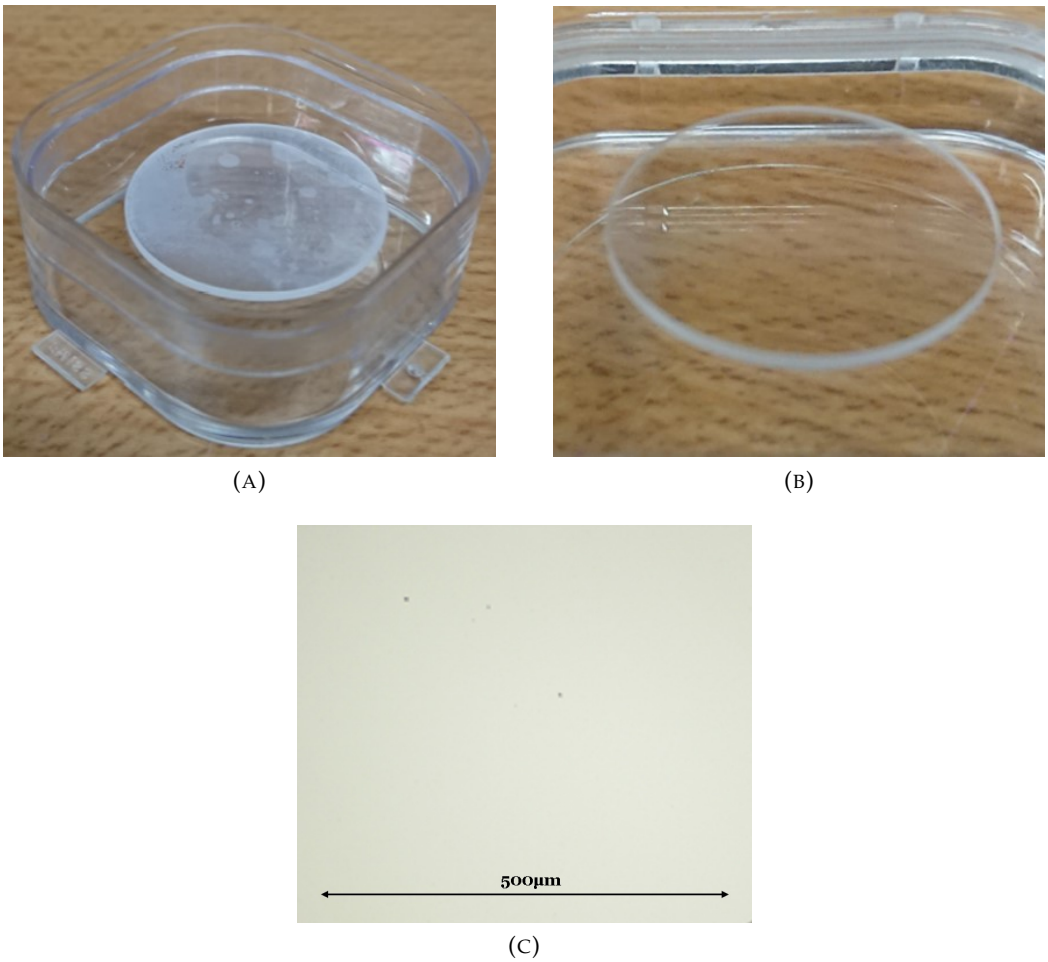

(A) (B)

(C)

FIGURE 3.24: (A) Poor quality layer on 25mm diameter sapphire window NB238, consolidated at 950 °C. (B) Transparent germania layer on 25 mm diameter sapphire window NB203, consolidated at 1150 °C (C) Microscope image of the transparent layer deposited on to sapphire window NB203.

These layers were impossible to measure using the prism coupling technique, and it was considered if, due to insufficient depth and in addition, the high refractive index sapphire substrate of 1.74 at 633 nm [43] meant that any modes seen would be wide and indistinct rather than sharp. Underclad layers were fabricated with several different flow rates (see table 3.8), with the aim of determining an appropriate flow rate to give an approximately 0.8% refractive index contrast as in Sakaguchi's work and allow prism coupling.

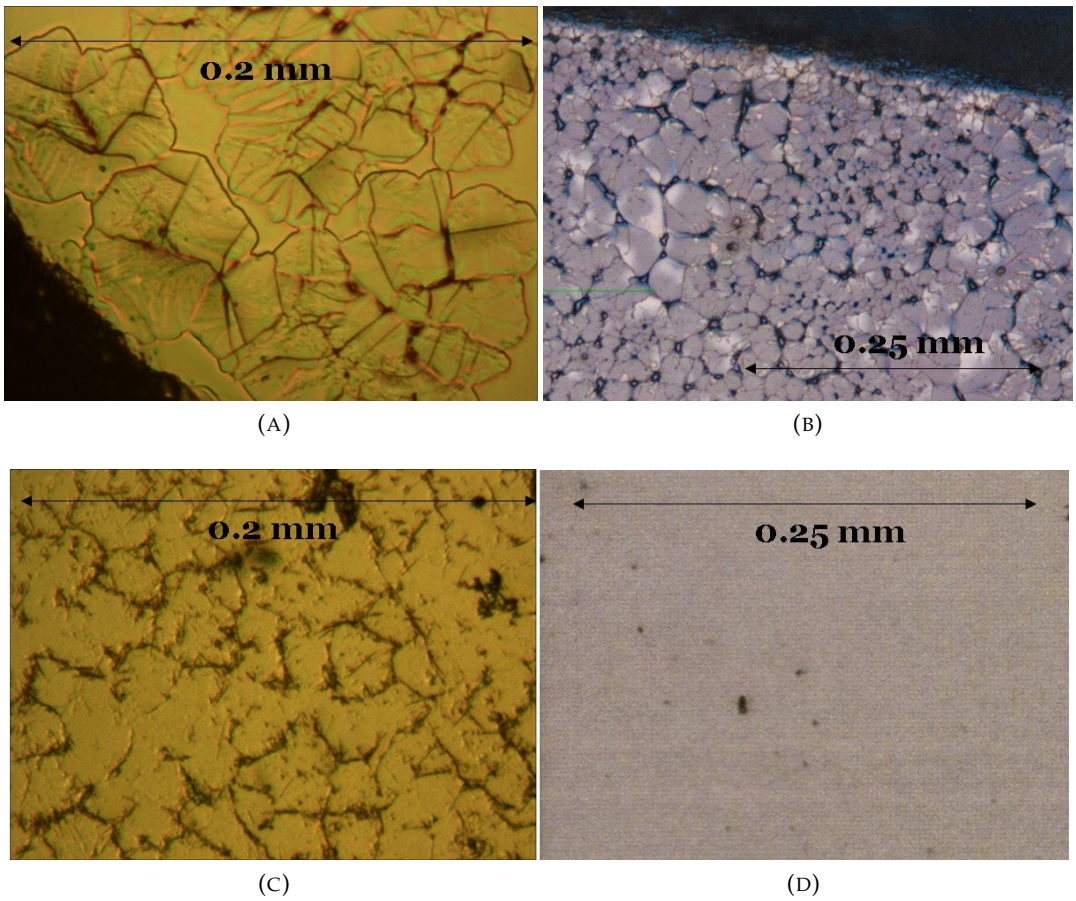

(A) (B)

(C) (D)

FIGURE 3.25: (A) Defects on sapphire window NB238-1 which appear semi-crystalline. (B) White area on NB238-1. (C) Striations on NB238-1. (D) Good quality surface on NB203.

The first wafer fabricated, NB314, although of apparently good quality, was impossible to couple into using prism coupling, so no refractive index data could be obtained. Again, it was suspected that the layer was too thin to couple into. An area of one wafer of the following run, NB322, had its soot removed pre-consolidation in order to measure its approximate depth using the Alphastep and this was found to be 2.0 μm (HF etching, as would be done with a silicon wafer would be a poor choice here as, while HF will not etch sapphire, it will damage the surface [44]). This depth should have allowed prism coupling, even on a high index substrate, and the seeming impossibility of prism coupling was surprising. The depth of the layer was confirmed by SEM images and the composition of the silica-germania layer was determined using EDX spectrometry, meaning that the approximate refractive index could be inferred as the relationship between index and germania content of binary silica-germania glasses is additive [36]. Germania content was found to be around

89%, corresponding to a refractive index of around 1.59. A pure germania layer was subsequently successfully deposited onto the silica-germania layer (NB330), its depth measured using the Alphastep and found to be approximately 2.5 μm.

TABLE 3.8: Sapphire Wafer FHD Results. †- calculated from EDX data; ‡- calculated fromindex; §- measured by alphastep.

Wafer code	**NB203**	**NB238-1**	**NB314**	**NB322**	**NB330**	**PX100**
$SiCl_4$:$GeCl_4$ flow rate /sccm	0:190	0:190	38:190	38:190	0:190	3:190
Passes	14	14	10	14	25	25
Consol. Temp./°C	1150	950	1150	1150	1150	
% GeO_2†	-	-	89	90	90	
%GeO_2‡	-	-	-	-	-	82
n at 633nm	-	-	-	-	-	1.5946
Thickness /μm			2.0§	2.5§		

NB314 and NB322 were fabricated using the same recipe, with the only difference being the number of passes (10 and 14 respectively). Notably, the EDX detected 1.7% Al_2O_3 in NB314, which suggested some diffusion of silica-germania into the sapphire layer at a consolidation temperature of 1250 °C, the diffusion of Al_2O_3 being noted as a problem by Ballato et al. [22]. The high index substrate appeared to have diffused into the core layer, such that no distinct layers were present. This led to consideration of the possibility that the increasing index with depth resulted in the mode being "trapped" in the layer. Thicker layers were deposited in order to avoid the diffusion of sapphire extending fully into the core. This was achieved by raising the bubbler temperature by 5 °C to 28 °C, and this was further by aided by adjusting the gear ratio and rotation speed of the deposition table in order to slow the translation speed of the torch. Despite the poor quality of the resulting layers prism coupling was possible. Samples NB314, NB322, NB330 and PX100 were of sufficient quality for UV writing at 244nm and 213nm (See Chapter 5).

3.2.6 Cladding of high germania content wafers

Cladding has a significant influence on birefringence [45], and is thus worthy of investigation as UV written and Damascene ring resonators will inevitably be more susceptible to birefringence-based effects in comparison to straight waveguides. With this in mind, fabrication of a clad sample was attempted, for comparison when UV writing, with the intention of optimising the FHD parameters at a later point when a suitable core layer had been produced. A thick thermal oxide wafer, deposited with germania and consolidated at 1150 °C without oxygen was clad at 1200 °C with 9 μm of B- and P-doped silica. An area with white dots could be seen with the naked eye, which, it became apparent were bubble-like defects when observed under a microscope (see fig. 3.26 (A) & (B)).

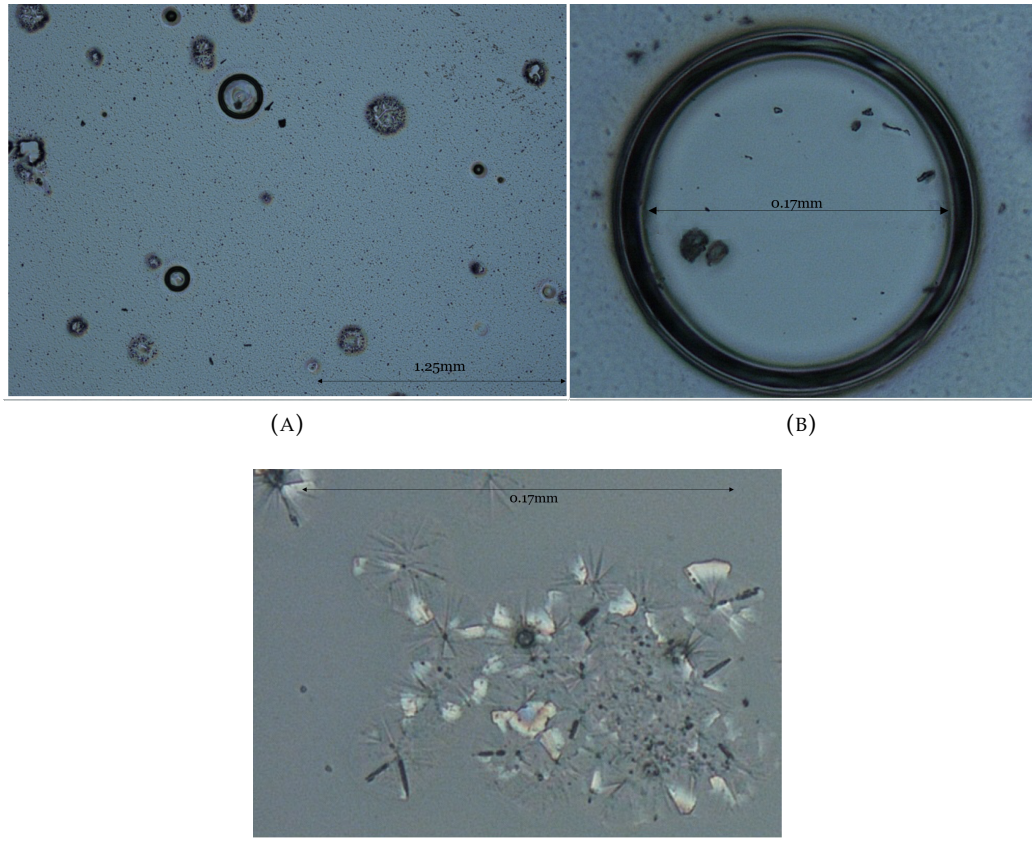

(A) (B)

(C)

FIGURE 3.26: (A) Microscope image of clad sample NB203-1, showing a number of defects. (B) Close-up image of a bubble similar to those seen in (A). (C) Close-up image of rosette cracking seen in (A).

In addition areas of possible crystallinity or “rosette" cracking (see fig. 3.26 (C)) as seen in Watts’ work when the consolidation time is excessive were observed [46]. Further diffusion of germania is likely, as well as loss of germania due to its reduction to GeO and diffusion of the gas through the upper layer. A lower temperature clad is necessary in order to prevent this. The addition of dopants such as Boron may help to lower the melting point of the silica clad and allow cladding at lower temperatures, thus avoiding this. Intriguingly, the structure of bubbles, with their uniform rings could be another method of fabricating ring resonators, were it not for the lack of control of the size of the bubbles. The use of dopants may be worth consideration in order to facilitate low temperature consolidation of the clad layer.

3.3 Conclusions

The useful properties of germania such as its potential for outstripping silica losses as wavelengths increase have been outlined. Literature related to germanate glass deposition, in particular FHD, has been reviewed and the scarcity of research concerning of high germania-content glass deposition noted. The working of the FHD system has been described, including the likely effects of adjusting various parameters. The principles behind the flame hydrolysis deposition, such as the relevant equations are outlined. The methods of compositional analysis used have been reported, and the concepts behind any non-standard techniques or those carried out by third parties described. Compositional analysis such as EDX and element mapping have been used and their consistency with Metricon measurements of refractive index and the additivity rule have been considered. PPTOFMS analysis carried out in Horiba, Paris was found to be particularly helpful in verifying that interpretation of EDX, SEM and Metricon data was correct. ToFSIMS was found to be difficult to interpret, and in retrospect perhaps not the best choice of compositional analysis due to its usual use for surface analysis. GDMS confirmed characterisation data for silicate glasses, but due to the robust cleaning method, much of the germania layer of NB258-1 was removed and as a result a matrix element could not be found.

3.3.1 High temperature consolidated germania layers

Germania has been successfully deposited onto silica wafers at temperatures of 1300-1360 °C. These samples show extensive diffusion of germania into the silica layer in the case of silica-on silicon substrate, and oxidation of the silicon layer and diffusion into this layer in the case of the silicon wafer, resulting in little difference in layer depth between the two. The layer is between 35-40% germania, and is suspected to consist of germania glass immersed in an SiO_2 glass, as described by Baral et al [42], and this is supported by the slow HF etch rates seen in these samples, which are slower than the etch rate of either SiO_2 or the very high germania content GeO_2 glasses consolidated at lower temperatures. These samples were of adequate quality for UV writing. The processes occurring during consolidation are summarised in figure 3.27.

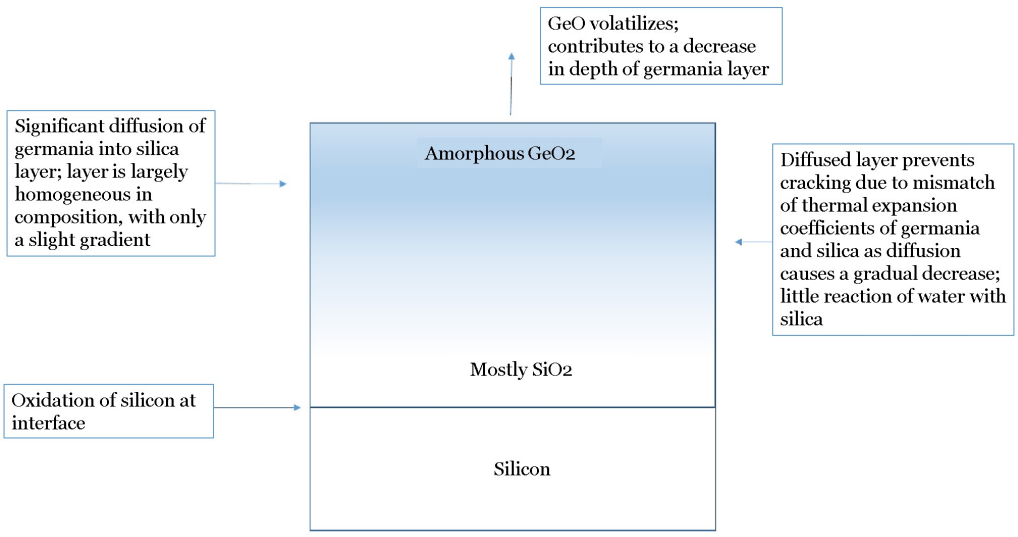

FIGURE 3.27: Model of diffusion in high temperature consolidated GeO_2-on-silica

3.3.2 Low temperature consolidated germania layers

High germania-content samples have been fabricated on silicon and silica substrates at temperatures of 1250 °C and below. However, these samples showed high sensitivity to water and solvents. It is suspected that this is due to the much reduced amount of diffusion, forming a separate germania layer on top of the silica or silicon substrate with a large difference in CTE between the layers, resulting in high internal stresses. The reaction of germania and silica with water is aided by stress, and it is suspected that it is this, rather than the high germania content which makes the layer chemically unstable. The difference in appearance of water damaged samples is interesting, as is the crystalline appearance of samples where the germania layer has delaminated. The granular appearance seen is often associated with phase separation and crystallinity [34]. However, further analysis, e.g. differential thermal analysis (DTA), is required in order to establish this. The processes occurring during consolidation and after are summarised in figure 3.28.

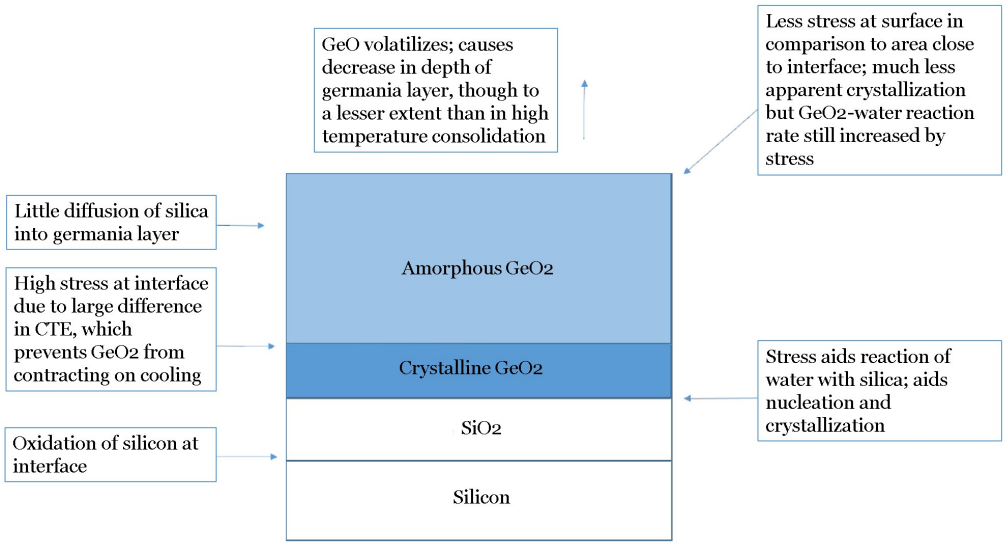

FIGURE 3.28: Model of diffusion in low temperature consolidated GeO_2-on-silica

3.3.3 Low-on-high temperature consolidated germania layers

Fabrication of high germania content wafers with improved stability was possible when a "buffer" layer of germania was deposited onto a silica wafer consolidated at 1360 °C to form a germania-silica layer and used as a substrate, followed by another layer, deposited under the same conditions but consolidated at 1150 °C. However, these samples still showed damage when diced, and methods of protecting them when dicing in preparation for UV writing were trialled (see section 5.4.1). An intermediate layer, consolidated at for example 1250 °C may provide a smaller difference in CTE, further improving the stability of these samples. The reduced sensitivity to water and solvents while retaining high germania content is consistent with the abrupt change in composition and hence CTE making the wafers unstable rather than the high germania content. The reduced sensitivity to moisture made UV writing of the samples possible (see section 5.4), although this relied on cleaving of the sample rather than dicing.

3.3.4 Germania on sapphire

Fabrication of germania glass on sapphire was achieved at a consolidation temperature of 1150 °C, albeit with substantial diffusion, which it is suspected may have hindered prism coupling due to the high confinement of the mode and lack of an interface required for TIR. Consequently 25 passes were required and the $GeCl_4$ had to be increased to 28 °C from a usual temperature of 23°C in order to raise the vapour pressure and deposit more soot per pass. Surprisingly, consolidation at 950 °C was unsuccessful, considering that Sakaguchi's work reported the fabrication of germania layers on sapphire at 850 °C. These samples showed good stability to water and solvents. The mixed SiO_2-GeO_2 layers intended as underclad layers were in fact of better quality than pure germania layers. Pure germania layers showed areas of defects and areas suitable for UV writing had to be chosen carefully. These samples were UV written at both 244 nm and 213 nm (see section 5.4).

3.3.5 Cladding of germania layers

Cladding of germanate wafers using a standard silica clad was attempted but resulted in bubbles forming during consolidation, resulting in poor quality of the clad. A clad which it is possible to consolidate at lower temperature, while retaining the lower refractive index of silica in comparison to germania is required. This is likely to involve the use of dopants such as boron in order to lower the glass transition temperature. The use of dopants is described in the next chapter, in the context of core layers rather than clad layers, although the work is clearly highly relevant to developing a suitable clad layer for germanate glasses.

3.4 Bibliography

[1] L. M. Dennis & A. W. Laubengayer, "Fused Germanium Dioxide and Some Germanium Glasses", *J. Phys. Chem.*, 30: 1510-1526, 1926.

[2] K. A. Krakau, "Effects of Adding Germanium Dioxide on the Optical Properties of Glass", *Opticomechanical Industry USSR*, 15-17, 1939.

[3] X. Jiang, J. Lousteau, W. Richards & A. Jha, "Investigation on germanium oxide-based glasses for infrared optical fibre development", *Opt. Mat.*, 31: 1701-1706, 2009.

[4] E. M. Dianov & V. M. Mashinsky, "Germania-Based Core Optical Fibers", *J. Lightwave Tech.*, 23 (11): 3500-3508, November 2005.

[5] A. Margaryan, & W. Liu, "Prospects of using germanium dioxide-based glasses for optics", *Opt. Eng.*, 32(8): 1995-1996, August 1993.

[6] J. P. Bange, L. S. Patil, & D. K. Gautam, "Growth and Characterization of SiO_2 Films Deposited by Flame Hydrolysis Deposition System For Photonic Device Application", *Progress In Electromagnetics Research M*, 3: 165-175, 2008.

[7] M. Takahashi, A. Sakoh, Y. Tokuda, T. Yoko, J. Nishii, H. Nishiyama & I. Miyamoto, "Photochemical process of divalent germanium responsible for photorefractive index change in GeO_2-SiO_2 glasses", *J. Non-Crys. Solids*, 99 (11): 3677-3684.

[8] M. J. Holmes, D. L. Williams & R. J. Manning, "Highly Nonlinear Optical Fiber for All-Optical Processing Applications", *IEEE Photonics Tech. Lett.*, 7 (345): 1045-1047, September 1995.

[9] A. Schliesser, N. Picque & T.W. Hansch, "Mid-IR Frequency Combs", *Nature Photonics*, 6 (6): 440-449, July 2012.

[10] J. W. Fleming, "Dispersion in GeO_2:SiO_2 Glasses", *Appl. Opt.*, 23 (24): 4486-4493, December 1984.

[11] S. Sakaguchi & S. Todoroki, "Optical Properties of GeO_2 Glass and Optical Fibres", *Appl. Opt.*, 36 (27): 6809-6814, September 1997.

[12] G. C. Righini & A. Chiappini, "Glass optical waveguides: a review of fabrication techniques", *Opt. Eng.*, 53 (7): 07819-1-017819-14, July 2014.

[13] J. M. Ruano, V. Benoit, J. S. Aitchison & J. M. Cooper, "Flame Hydrolysis Deposition of Glass on Silicon for the Integration of Optical and Microfluidic Devices", *Anal. Chem.*, 72 (5): 1093-1097, March 2000.

[14] S. Garcia-Blanco, A. Glidle, J. M. Cooper, R. M. De La Rue & J. S. Aitchison, "Characterization of Germanium-Doped Silica Layers Deposited by Flame-Hydrolysis", *Optical Materials*, 27: 365-371, 2004.

[15] T. Kominato Y. Ohmori H. Okazaki & M. Yasu, "Very Low-Loss GeO Doped Silica Waveguides Fabricated by Flame Hydrolysis Deposition Method", *Electronics*

Lett., 26 (5): 327-328, March 1990.

[16] P. Tandon & H. Boek, "Experimental and Theoretical Studies of Flame Hydrolysis Deposition Process for Making Glasses for Optical Planar Devices", *J. Non-Crys. Solids*, (317): 275-289, March 2002.

[17] M. Jamal Deen & P. K. Basu, "Silicon Photonics: Fundamentals and Devices", *Wiley Series in Materials for Electronic & Optoelectronic Applications*, ISBN: 978-1-119-94090-6, March 2012.

[18] C. Li, R. Boudreau, & T. Bowen, "Study of MPACVD Processing Technologies for Planar Integrated Optics", *SPIE Conference on Optoelectronic Materials and Devices*, 3419: 85-92, 1998.

[19] S. Sakaguchi, "Consolidation of GeO_2 Soot Body Prepared by Flame Hydrolysis Reaction", *J. Non-Crys. Solids*, 171, 1994.

[20] R. D. Maurer & P. C. Schultz, "Germania containing optical waveguide," U.S. Patent 3 884 550, May 1975.

[21] K. Richardson, D. Krol & K. Hirao, "Glasses for Photonic Applications", *Int. J. of Appl. Glass Sci.*, 1 (1): 74-86, 2010.

[22] J. Ballato & P. Dragic, "Rethinking Optical Fiber: New Demands, Old Glasses", *J. Am. Ceram. Soc.*, 96 (9): 2675-2692, 2013.

[23] P. Tandon & M. Murtagh, "Particle-vapor interaction in deposition systems: influence on deposit morphology", *Chem. Eng. Sci.*, 60: 1685-1699, 2005

[24] T. Kominato, Y. Ohmori, H. Okazaki & M. Yasu, "Very Low Loss GeO_2-doped Silica Waveguides Fabricated by Flame Hydrolysis Deposition Method", *Elec. Lett.*, 26 (5): 327-329, March 1990.

[25] K. Sanada, T. Moriyama & K. Inada, "Chlorination and vaporization of GeO_2 component in SiO_2:GeO_2 porous preform in dehydration process by VAD method and spontaneous formation of SiO_2 cladding layer during the dehydration by selective vaporization of GeO_2", *J. Non-Crys. Solids*, 194: 163-172, 1996.

[26] V. M. Mashinsky, V. B. Netstruev, V. V. Dvoyrin, S. A. Vasiliev, O. I. Medvedkov, I. A. Bufetov, A. V. Shubin, E. M. Dianov, A. N. Guryanov, V. F. Khopin & M. Y. Salgansky, "Germania Glass Core Silica Glass Cladding Modified Chemical Vapour Deposition and Optical Fibers: Optical Losses, Photorefractivity and Raman Amplification", *Opt. Lett.*, 29 (22): 2596-2598, November 2004.

[27] R. Sidharthan, S. Yoo, D. Ho, L. Zhang, W. Qi, M. Yue, L. Zhu, X. Dong & S. Tjin, "Stress-Loss Correlation and Dispersion Control in Highly GeO_2-Doped Fibers", *IEEE Photonics Tech. Lett.*, 28 (14): 1521-1524, July 2016.

[28] R. A. Bellman, G. Bourdon, G. Alibert, A. Beguin, E. Guiot, L. B. Simpson, P. Lehuede, L. Guiziou & E. LeGuen, "Ultralow Loss High Delta Silica Germania Planar Waveguides", *J. Electrochem. Soc.*, 151 (8): 541-547, 2004.

[29] S. Valligatla, A. Chiasera, N. Bazzanella, L. Lunelli, A. Miotello, M. Mazzola, D. Narayana Rao & M. Ferrari, "CO_2 Laser irradiation of GeO_2 planar waveguide fabricated by rf-sputtering", *IOP Conf. Series: Mat. Sci. & Eng.*, 73 (012006): 1-6, 2015.

[30] P. V. S. Marques, J. R. Bonar, A. M. P. Leite & J. S. Aitchison, "Simultaneous UV Direct Writing of Channel Waveguides and Bragg Gratings in Germanium-Doped Planar Silica", *IEEE J. Selected Topics in Quantum Elec.*, 8 (6): 1316-1322, 2002.

[31] K. B. McAfee Jr., R. A. Laudise & R. S. Hozack, "Equilibria Concentrations in the Oxidation of $SiCl_4$ and $GeCl_4$ for Optical Fibers", *J. Lightwave Tech.*, LT-1 (4): 555-561, December 1983.

[32] M. K. Schurman & M. Tomozawa, "Equilibrium Oxygen Vacancy Concentrations and Oxidant Diffusion in Germania, Silica and Germania-Silica Glasses", *J. Non-Crys. Solids*, 202: 93-106, April 1996.

[33] J. E. Shelby, "Introduction To Glass Science and Technology" (2nd Edition), *Royal Society of Chemistry* ISBN 0-85404-639-9, 2005.

[34] R.F. Cuevas, E.H. Sekiya, A. Garcia-Quiroz, E.C. Da Silva & C.K. Suzuki, "Effect of processing parameters on control of defect centers associated with second-order harmonic generation and photosensitivity in SiO_2:GeO_2 glass preforms", *Nucl. Instr. and Meth. in Phys. Res. B*, 247: 285-289, 2006.

[35] Y. Seo, S. Shin, O. Kwon, B. Lee, Y. Kim, D. Yoon, H. Yoon & Y. Min, "Influence on the film properties of torch inclination angle in FHD process", *Opt. Fiber & Planar Waveguide Tech. II*, 4904: 359-362, 2002.

[36] A. Margaryan & M. A. Pilliavin, "Germanate Glasses: Structure, Spectroscopy and Properties", *Artech House* ISBN 0-89006-506-3, 1993.

[37] H. Doweidar, "Considerations on the structure and physical properties of B_2O_3-SiO_2 and GeO_2-SiO_2 glasses", *J. Non-Crys Sol.*, 357: 1665-1670, February 2011.

[38] J. Berlin, "Analysis of Boron with Energy Dispersive X-ray Spectrometry", *Imaging & Microscopy*, 13: 19-21, May 2011.

[39] A. Bogaerts & R. Gijbels, "New developments and applications in GDMS", *Fresenius J. Anal. Chem.*, 364: 367-375, 1999.

[40] A. Tempez, S. Legendre & P. Chapon, "Depth profile analysis by plasma profiling time of flight mass spectrometry", *Nucl. Instr. and Meth. in Phys. Res. B* , 332: 351-354, 2014.

[41] A. Tempez, S. Legendre, J. Barnes & E. Nolot, "Combining plasma profiling TOFMS with TOF-SIMS depth profiling for microelectronic applications", *J. Vac. Sci. Tech. B*, 34 (3): 03H120-1-03H120-6, May/June 2016.

[42] K. Baral, P. Adhikari, W. Ching, & S. Sinnott, "Ab initio Modeling of the Electronic Structures and Physical Properties of a-Si1-xGexO2 Glass (x=0 to 1)", *J.American*

Ceramic Soc., 345 & 346: 323-327, 2016.

[43] RefractiveIndex.INFO Refractive Index Database. URL http://www.refractiveindex.info. (Accessed 2019-04-03).

[44] K. Kirby, K. Shanmugasundaram, V. Bojan & J. Ruzyllo, "Interactions of Sapphire Surfaces with Standard Cleaning Solutions", *ECS Transactions*, 11 (2): 343-349, 2007.

[45] A. Kilian, J. Kirchhof, B. Kuhlow, G. Przyrembel & W. Wischmann, "Birefringence Free Planar Optical Waveguide Made by Flame Hydrolysis Deposition (FHD) Through Tailoring of the Overcladding", *J. Lightwave Tech.*, 18 (2): 193-198, 2000.

[46] S. P. Watts, "Flame Hydrolysis Deposition of Photosensitive Silicate Layers Suitable for the Definition of Waveguiding Structures Through Direct Ultraviolet Writing", (Thesis), University of Southampton, September 2002.

Chapter 4

Flame hydrolysis deposition of doped germanate glasses

4.1 Introduction

Germania has long been used as a dopant itself in planar layers and fibres, however doping of germanate glasses has remained far less common [1]. However, the effects of the addition of some dopants to germania is known (see table 4.1), and helped guide the choice of dopants in this work. Alleviation of some of the problems associated with germania and germania-silica on silica described in the previous chapter, such as stress-aided reaction with water due to thermal expansion mismatch was a primary motivation for exploring the use of dopants. Additionally, doping presented the possibility of enhancing already-present properties such as nonlinearity and photosensitivity. This chapter reports the development and characterisation of doped FHD germania glass layers with a view to their use as photosensitive core layers or as core layers in damascene resonators. Phosphorus-and boron-doping were achieved via the FHD system, while bismuth-doping was achieved via the solution-doping method. Later work involved the fabrication of germanate glass on rods and tubes in silica, and the composition and optical data presented here also proved useful in developing these samples.

4.1.1 Bismuth-doped germanate glasses

Bismuth germanate, often referred to as BGO, shows promise as a dopant as while its thermal expansion coefficient is similar to germania [2], its addition lowers the melting point and glass transition temperature. This aids re-flow at usual consolidation temperatures, potentially improving loss and uniformity, and potentially allows consolidation at much lower temperatures, perhaps alleviating some of the stresses seen in GeO_2-SiO_2 glasses. The chemical stability of bismuth germanate is good, especially over long periods of time [3], it is non-hygroscopic [4], has a high refractive index [2] and nonlinearity [5], which increase proportionally with volume fraction [6], and has shown photoluminescence in the UV region [7].

Solution doping has been chosen as the method. This technique has also previously been used in the fabrication of rare earth-doped fibres [8] and later further developed for planar substrates for laser sources [9]. Most significantly, successful fabrication of aluminium, erbium and neodymium-doped silica wafers via FHD and solution doping has been demonstrated before within the group [10]. The technique relies upon diffusion of the dopant through the glass matrix, or integrated via ionic bonds, usually with sintering to semi-consolidate the layer and aid porosity [10]. The

majority of the solvent evaporates in the extracted chamber and any still remaining evaporates during consolidation.

4.1.2 Phosphorus-doped germanate glasses

Doping germanate glass with P_2O_5 has merit when fabricating a glass suitable for fabrication of a ring resonator, since its thermo-optic coefficient is negative [11], thus augmenting GeO_2's high thermo-optic coefficient, a property which will inevitably become detrimental to the working of a ring resonator gyroscope (see section 2.4.6 and 2.4.7.) without either temperature controls or athermal fabrication techniques. Additionally, UV photosensitivity resulting in positive refractive index change has been reported in P_2O_5-doped germania [12] and silica [13] as well as Ge-doped phosphate glass [14].

However, the effect on thermal and optical properties of germanate glasses of doping with P_2O_5 is complex and highly affected by the change in coordination number of germania from 4 to 6, which is itself affected by the molar percentage of P_2O_5 [15]. Refractive index increases with P_2O_5-content, as GeO_2 coordination number increases, but after approximately 20% P_2O_5-content, it starts to decline. Similarly, the glass transition temperature, T_g, was found to increase in the range 5-20% P_2O_5-content whereupon it declined again [16], while Shibata et al. found the minimum T_g to be at a molar percentage of 90% GeO_2 [17].

4.1.3 Boron-doped germanate glasses

The FHD system allows deposition of B_2O_3 soot. As a dopant, boron has some useful properties as well as some unhelpful ones. B_2O_3 is known to aid photosensitivity in germanate glasses [20], and low GeO_2-B_2O_3 content silicate glasses have previously been successfully used within the group to fabricate layers suitable for DUV of Bragg gratings [19]. B_2O_3-doped germania has a higher CTE than pure germania [17][18], however, its glass transition temperature is substantially lower [20], allowing lower temperature consolidation, improved reflow and thus potential for low loss.

4.1.4 Phosphorus & boron co-doped germanate glasses

Co-doping of FHD germanate glass gives the possibility of combining some of the useful properties of phosphorus and boron- doped glasses described above, e.g. improved reflow [21][22]. The effects of addition of various dopants to germanate glasses are summarised in table 4.1.

TABLE 4.1: Effects of doping using various dopants. While SiO_2 and Al_2O_3 are not being used as dopants here per se, their inclusion is on the basis that there is highly likely to be some transport of their oxides into the core layer, as seen in the previous chapter and thus their effects on important parameters should be considered. * The response to UV in GeO_2-SiO_2 glasses is dependent on factors such as fabrication technique rather than solely on percentage and varies in sign and magnitude. † denotes assumed effect based on the relevant property of the dopant. Percentages indicate the percentage of dopant for which the effect is seen.

Dopant	**Refractive index, n**	**Thermal expansion coefficient, α**	**Glass transition temp., T_g**	**UV-induced refractive index change, Δn**
SiO_2	decreases [21]	decreases [21]	increases [25]	varies*
Bi_2O_3	increases [26]	small decrease†	decreases [27]	increases [18]
B_2O_3	decreases [28]	increases [28]	decreases †	increases
B_2O_3				in SiO_2 [29]
Al_2O_3	increases†	increases†	increases †	not detrimental [17]
P_2O_5	increases	increases	increases	increases
	(<20%)[30]	(5-20%) [16]	gradually [17]	in SiO_2 [12]
P_2O_5	decreases	decreases [16]	small decr.	increases
	(>20%) [30]		(5-10%) [17]	in SiO_2 [12]

4.2 Solution doping using bismuth chloride

There are a variety of techniques for solution doping, e.g. spray pyrolysis, which the technique described here is closely based on. Figure 4.1 shows the extracted chamber used for $BiCl_3$ solution doping of FHD germania wafers. The wafer sits on a platform heated to around 50°C via an electrical heater and monitored by a thermocouple attached through the holes at the front of the chamber. A hand pump connected to a reservoir of 2ml capacity, the tube of which may be fed through the holes at the front of the chamber, sits on rails in order to adjust its position relative to the wafer and is filled with a solution of $BiCl_3$. An extract is connected to the top of the chamber (not visible in fig. 4.1) in order to extract fumes from the solvent.

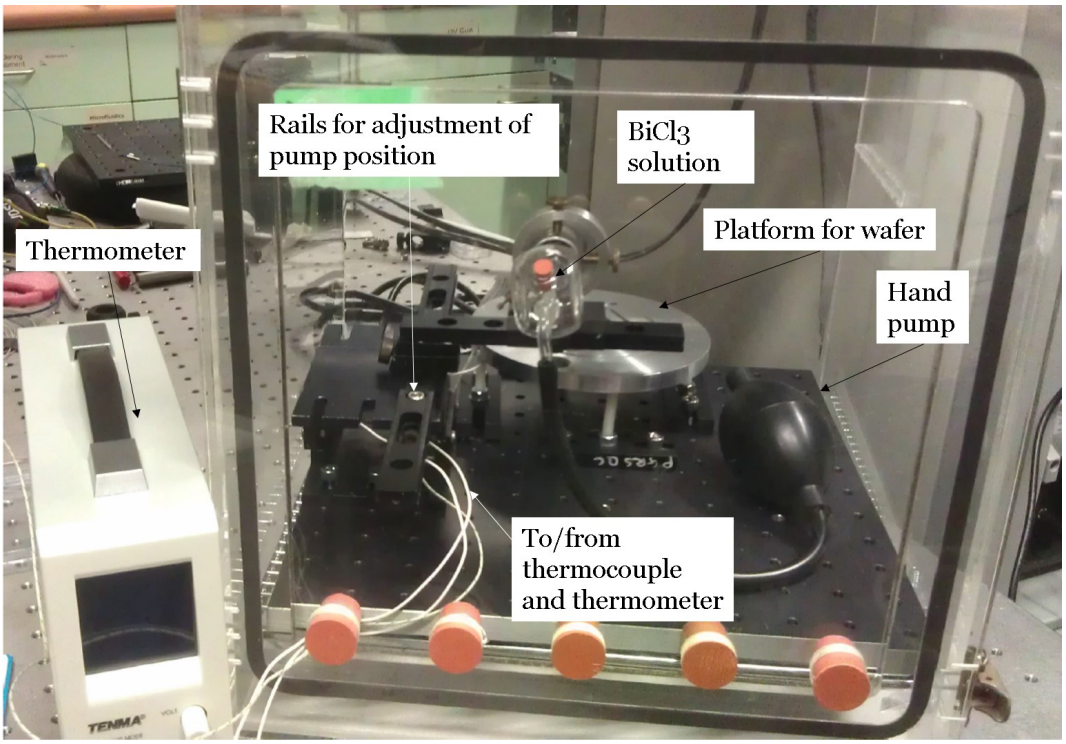

FIGURE 4.1: Solution doping set-up for $BiCl_3$.

Solvents used were methanol, as previously used by Guilhot in rare earth solution doping of silica wafers [10], and later acetone and isopropyl alcohol (IPA). Concentrations varied, the maximum used being approximately 2ml 0.02M $BiCl_3$ solution in order to obtain a germania layer doped with around a few percent bismuth. An optional sintering step, which consisted of placing the wafers in the furnace at 500°C for 45 mins directly after deposition was later added in order to increase porosity of the layers before solution doping and improve the incorporation of $BiCl_3$ into the layer and improve quality. After solution doping, the wafers were consolidated, evaporating any remaining solvent, in the furnace at 1150°C as usual in a helium atmosphere in order to aid formation of ODCs. The results of these depositions, onto silicon, thick thermal oxide and thin thermal oxide wafers, are shown in tables 4.2-4.5. The first attempt at solution doping via this method, initially without a sintering step (NB243), resulted in a very uneven distribution of bismuth due to the tendency of the pump to drip (see fig. 4.2). It was suspected that the amount of bismuth used was excessive and that this resulted in a layer of crystalline bismuth covering the core.

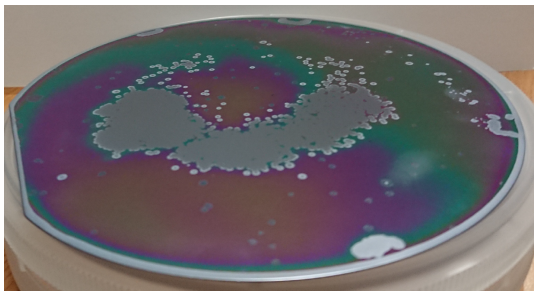

FIGURE 4.2: Bismuth doped germanate wafer with visible defects where the pump dripped.

There were however small areas where the layer of bismuth had cracked, making the layer below accessible to the Metricon prism coupler, and the refractive index was found to be approximately 1.63, above the refractive index of germania, suggesting that a layer of doped germania was present beneath the layer of bismuth.

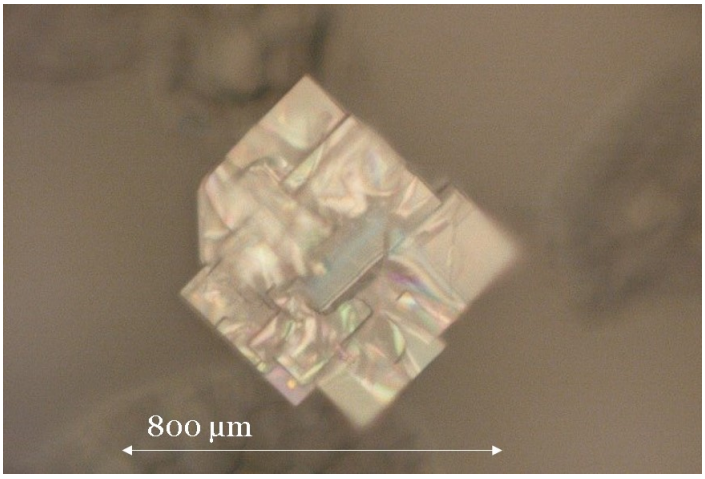

(A)

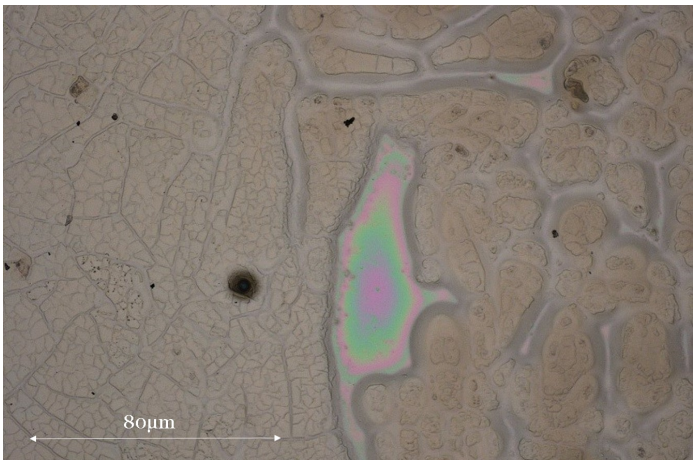

(B)

FIGURE 4.3: Microscope image of bismuth-doped germania sample NB246 showing areas of possible crystallinity.

These layers delaminated on contact with water. Thickness measurements using the Metricon were around 5 μm, compared with around 2.5-3 μm for a pure germania wafer consolidated under the same conditions. This suggests that the presence of

bismuth prevents loss of germania via reduction to germanium monoxide, either by providing a physical barrier or by its interaction with the germania layer. A second attempt with a weaker solution of 0.01M $BiCl_3$ (NB246) yielded a layer of doped germania with areas of possibly crystalline bismuth (see fig. 4.3). Again, prism coupling was extremely difficult and only rough measurements of refractive index of approximately 2.2 were possible. These, however were consistent with the known range of refractive index values for bismuth germanate [2][31].

TABLE 4.2: Doped Germania FHD Results (methanol, consolidated at a temperature of 1150°C).

Wafer	Substrate	Solution	n	Thickness	Reaction with water
NB243-2	15μm SiO_2	0.02M	-	-	delaminated
NB243-3	Si	0.02M	-	-	delaminated
NB243-4	1.4μm SiO_2	0.02M	1.6324	5.1	N
NB246-1	Si	0.01M	-	-	delaminated
NB246-2	15μm SiO_2	0.01M	2.2	-	N
NB246-3	1.4μm SiO_2	0.01M	-	-	delaminated

Acetone and IPA were trialled as solvents (NB251) to see if there was any difference in layer quality, with the added benefit that both are non-toxic. None of these samples delaminated, nor appeared to react with water, and there was a visible improvement to the quality of the layer. However the layers were not measurable by prism coupling and a layer of bismuth could be seen on the surface (see fig. 4.4), which delaminated on contact with water. The following run (NB257) using the weaker (0.01M) solution was consolidated at 1300°C to see if the higher temperature resulted in any improvement in quality of the layer by increasing diffusion of $BiCl_3$, with no noticeable improvement.

TABLE 4.3: Doped Germania FHD Results (IPA and Acetone); no Metricon data was possible.

Wafer	Temp	Substrate	Solution	Solvent
NB251-1	1150	15μm SiO_2	0.01M	Acetone
NB251-2	1150	6μm SiO_2	0.01M	IPA
NB251-3	1150	Si	0.01M	IPA
NB251-4	1150	Si	0.02M	Acetone
NB257-2	1300	6μm SiO_2	0.01M	Acetone
NB257-3	1300	Si	0.01M	Acetone
NB257-5	1300	Si	0.01M	IPA

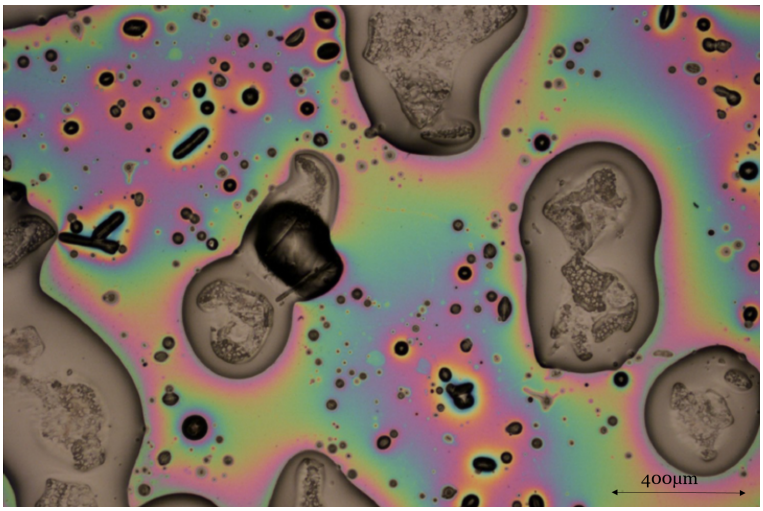

FIGURE 4.4: Microscope image of an area of Bismuth on germanate wafer NB251-5.

In response to previous results, the concentration of $BiCl_3$ was further reduced to 0.005M. Prior work showed that sintering stabilised the solution doping process [10], thus sintering was attempted in order to produce a partially consolidated porous layer into which bismuth may diffuse.

TABLE 4.4: Sintered Bismuth doping; no Metricon data was possible.

Wafer	Temp	Substrate	Solvent	Sinter
257-6	1300	Si	Acetone	45min at 500°C
258-2	1150	6μm SiO_2	Acetone	45min at 500°C
258-3	1150	6μm SiO_2	Acetone	-
258-4	1150	Si	IPA	45min at 500°C
258-5	1150	Si	Acetone	45min at 500°C
258-6	1150	Si	Acetone	-

A sintering step consisting of a 45 min dwell at 500°C appeared to give some improvement in the quality of layer, however diffusion was still not sufficient to give a doped layer and the bismuth still appeared to be sitting on top of the germania layer after consolidation. Smoother layers were obtained, which did not react or delaminate on contact with water but were still not measurable using prism coupling. Boron was added in order to reduce the glass transition and melting point, with the aim of improving incorporation of the dopant. This was found to aid quality of the layer and allowed consolidation at 650°C. Sintering combined with the addition of boron was found to improve the quality of layers considerably: NB266 and NB268, doped using 0.005M solution of $BiCl_3$ in IPA and acetone were consolidated at 800°C and 650°C respectively and cooled in air. The use of IPA as a solvent resulted in visually better quality layers with fewer visible defects or un-diffused areas of bismuth in comparison to acetone and allowed prism coupling. In the case of sample NB266-2, a loss measurement was possible via prism coupling, giving the relatively low loss of 0.58dB/cm at 1550nm. However, sample NB268-1 was not stable over time, presumably due to the mismatch in CTE being exacerbated by the addition of boron, resulting in stress-aided reaction with moisture.

TABLE 4.5: Sintered bismuth & boron co-doping. BCl_3 flow rate was 30 sccm for all runs; $BiCl_3$ solution was 0.005M for all samples.

Wafer code	**Temp /°C**	**Solvent**	**Refractive index, n**	**Thickness /μm**	**Uniformity (%)**	**Loss /dBcm^{-1}**
NB266-2	800	IPA	1.4590	3.10	2.81	0.58
NB266-3	800	Acetone	-	-	-	-
NB268-1	650	IPA	1.5345	4.90	3.97	-
NB268-2	650	Acetone	-	-	-	-

Further investigation of the use of sintering to determine optimum temperature and dwell time, optimal flow rate of BCl_3, combined may improve this, although concentrations must also be investigated to ensure uniform doping as this was a concern in previous work on solution doping [10]. Ultimately this approach to doping of germanate layers would have required much further work in order to optimise sintering and consolidation parameters, find ideal compositions for UV writing, aid stability over time, and it was judged that exploring the use of other dopants was more pragmatic such as phosphorus and boron due to the ease and repeatability of doping using the FHD system along with their potential for UV sensitivity. The technique nevertheless shows some promise, and to the best of the author's knowledge, is the first successful attempt at solution doping of germania glass with $BiCl_3$, resulting in a relatively low loss layer, far outstripping Sakaguchi's reported 6dB/cm obtained for pure FHD-fabricated germania [31].

4.3 Phosphorus doping

Stable, high-quality phosphorus doped glass layers have previously been fabricated within the group and direct UV written to produce low loss waveguides and Bragg gratings. However, little analysis has been done to understand the origins of the photosensitivity or structure and composition of these samples. Phosphorus percentages were thought to be around 20% in these previously fabricated samples, regardless of the flow rate of PCl_3 used, consistent with claims by Margaryan & Pilliavin [25]. Three samples with different PCl_3 flow rates of 150sccm, 100sccm and 50sccm (with a $GeCl_4$ flow rate of 150sccm) were prepared on thick (15μm) thermal oxide wafers using FHD (see table 4.6).

TABLE 4.6: Phosphorus-doped germania FHD Results.* indicates calculation via EDX; † indicates calculation via element mapping; ‡ indicates calculation via PPTOFMS results; § indicates calculation by additivity rule using EDX data.

Wafer code	**NB298-1**	**NB299-1**	**NB300-1**	**NB89**
PCl_3:$GeCl_4$ flow rate /sccm	150:150	100:150	50:150	192:192
Deposition passes	5	5	5	7
Percentage P*	10.6	6.2	3.7	7.6
Percentage Ge*	16.6	17.9	17.7	16.9
Percentage P†	26	15	21	11
Percentage Ge†	27	27	21	20
Percentage P‡	-	-	-	6.5
Percentage Ge‡	-	-	-	18.5
Calculated index§	1.4826	1.4884	1.4840	1.4883
n at 633nm	1.4987	1.5020	1.4987	1.4952
Thickness(μm)	5.25	3.55	2.26	9.81
% thickness variation	2.93	3.77	15.2	8.7
Loss at 1550nm (dB/cm)	0.08	1.56	4.00	-

EDX analysis indicates that the core layer in these and previous samples fabricated by others in the group, is predominantly silica, with 16-18% germania and varying percentages of phosphorus according to flow rate, indicating substantial diffusion of the deposited layers into the thick thermal oxide below. Refractive index data is consistent with this conclusion, as is the PPTOFMS analysis of NB89 (see fig. 4.5), a sample fabricated before this work began. The higher refractive indices of these samples in comparison to those calculated using additivity is consistent with this idea, as the addition of germania and phosphorus would be expected to raise the refractive index at these percentage compositions due to the change in coordination number of Ge from 4 to 6 [17]. EDX of the core layers of the three samples and the earlier sample NB89, allowed calculation of composition and element maps of the layers were used to calculate composition with respect to depth (see figs. 4.6, 4.7, 4.8 & 4.9). The additivity rule for oxides gives calculated refractive index values close to those found via prism coupling (within 1%) and the discrepancy may be explained by the fact that the addition of P_2O_5 up to around 20% is known to change GeO_2 coordination number from 4 to 6, resulting in a slight increase in T_g and refractive index [30].

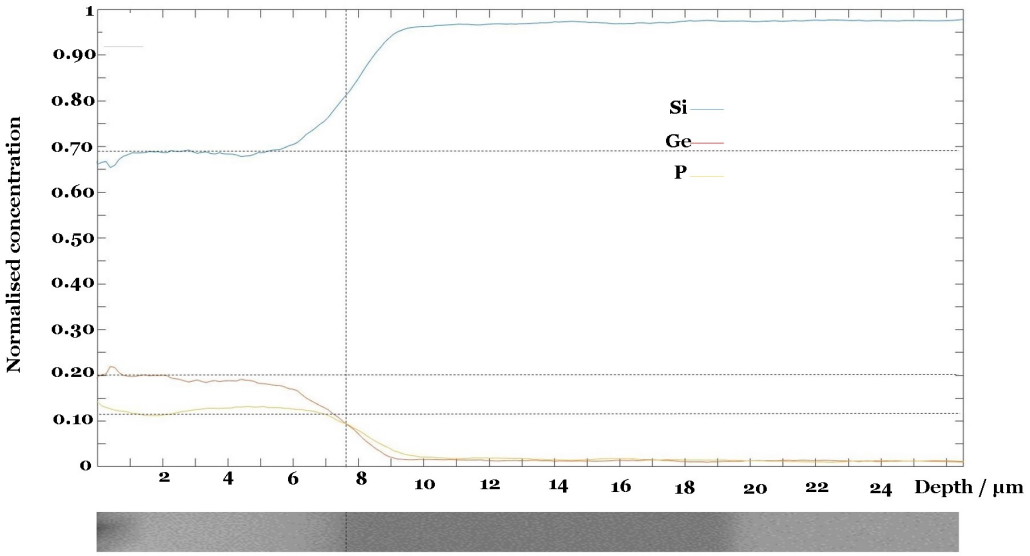

FIGURE 4.5: Element mapping of sample NB89: Composition at the centre of the layer is 69% silicon, 20% germanium (possibly with some proportion being six-coordinated), and 11% phosphorus.

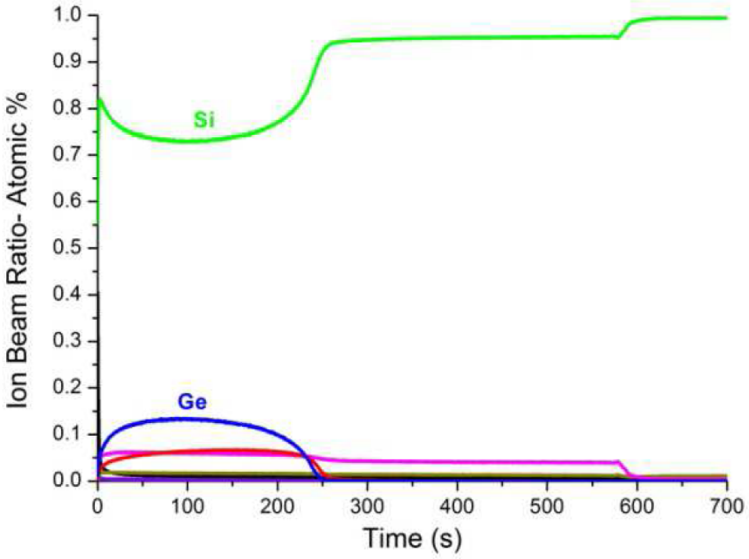

FIGURE 4.6: PPTOFMS analysis of sample NB89: Composition is calculated to be 75.0% silicon, 18.5% germanium (possibly with some proportion being six-coordinated), and 6.5% phosphorus.

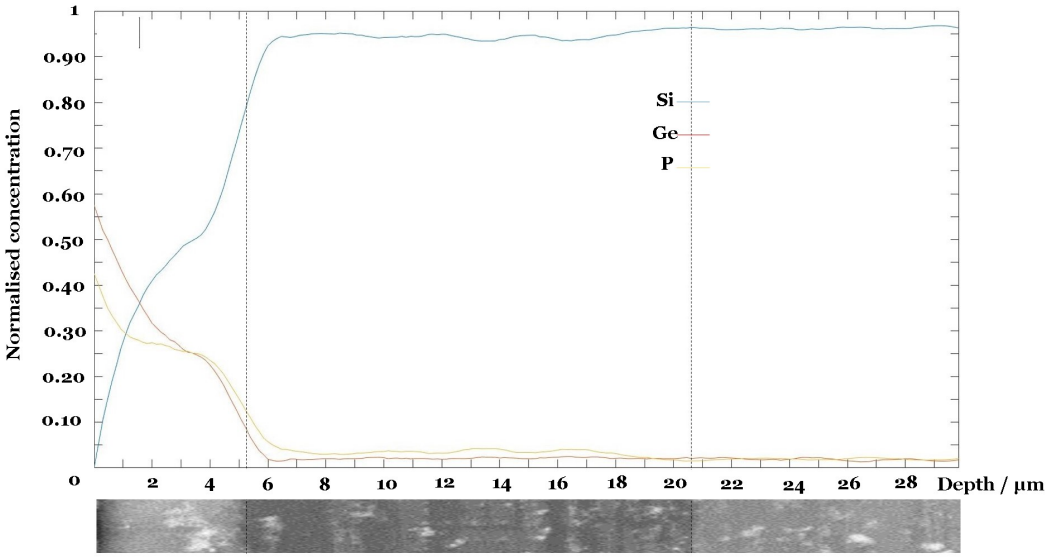

FIGURE 4.7: Element mapping of sample NB298: Composition at the centre of the layer is 47% silicon, 27% germanium (possibly with some proportion being six-coordinated), and 26% phosphorus.

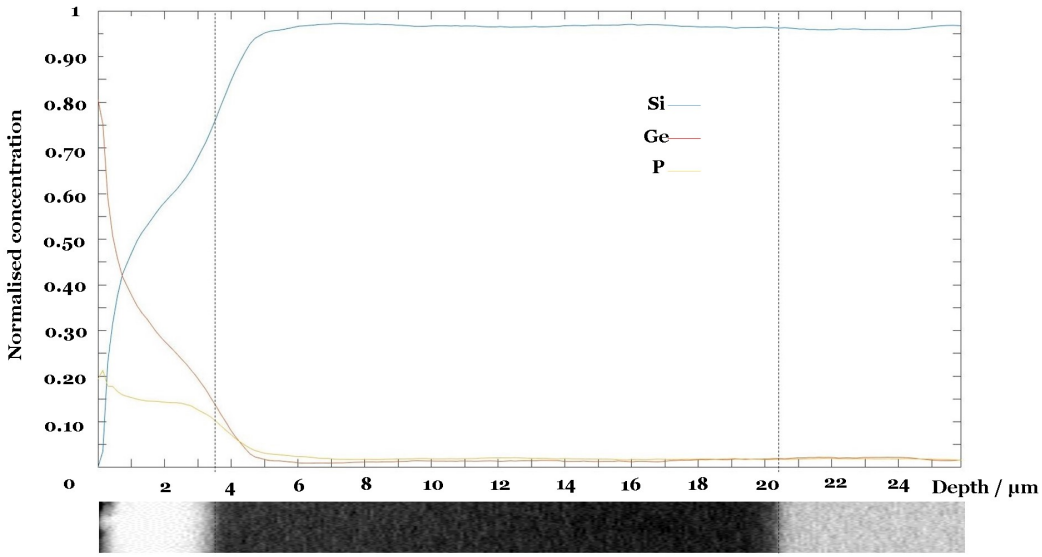

FIGURE 4.8: Element mapping of sample NB299: Composition at the centre of the layer is 58% silicon, 27% germanium (possibly with some proportion being six-coordinated), and 15% phosphorus.

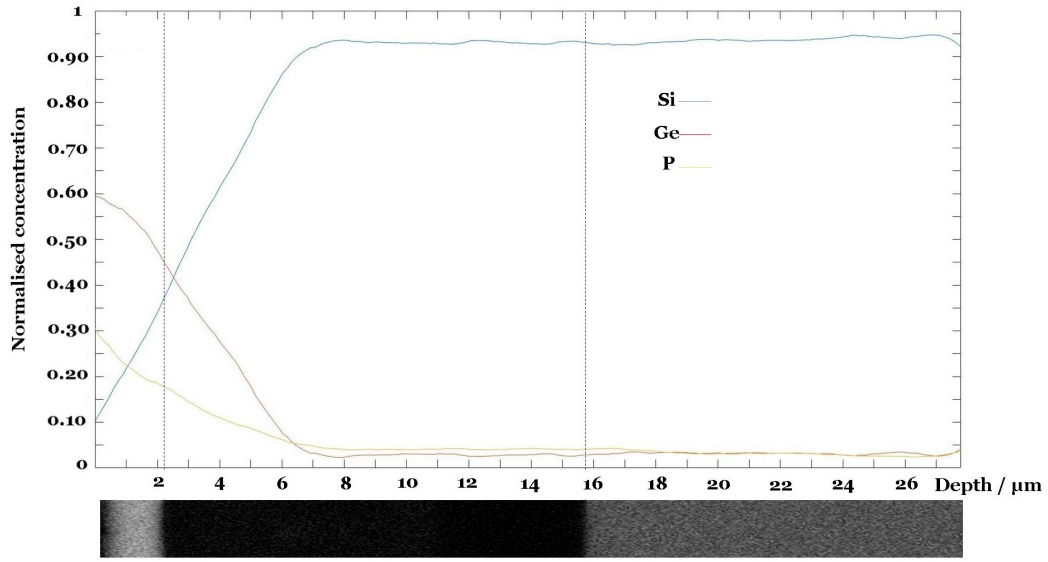

FIGURE 4.9: Element mapping of sample NB300: Composition is 26% silica, 53% germania (with some proportion being six-coordinated), and 21% phosphorus.

There may also be some inhomogeneity in the layer, resulting in slight compositional differences which may also explain the small discrepancies in calculated refractive index. Flow rates of 190:190 still did not reach the 20% limit claimed by Margaryan and Pilliavin [25], although they do not report any diffusion, which in this work has reduced the percentage P_2O_5 considerably. NB298, with a P_2O_5 percentage of around 11% (see fig. 4.7), was found to be stable over time in that there was no visible deterioration in the layer over two years. Both NB299 and NB300 did degrade over time, forming grey, opaque layers which could not be prism coupled. NB298 was also found to be the most uniform and to have the lowest loss measured using prism coupling. Samples of NB298 were diced and UV written (See Chapter 5).

4.4 Borogermanate on silica & sapphire substrates

Germania layers doped with boron were deposited on to thick thermal oxide wafers. The loss of these layers was measured to be 0.5dB/cm: low in comparison to the 6dB/cm Sakaguchi recorded in planar germania on sapphire [31]. However, the addition of boron raises the CTE [20]. These samples were seen to degrade over a matter of weeks even when kept in an unopened wafer box. Similarly, layers deposited onto sapphire wafers deteriorated over a period of months in an unopened wafer box, which is presumed to be due to CTE mismatch and resulting stress-aided reaction with moisture.

TABLE 4.7: Deposition of B_2O_3-GeO_2 on silica wafers. * Calc'd using additivity.

Wafer code	**NB266-1**	**PX60**	**PX72**	**PX73**	**PX74**	**PX100**
$GeCl_4$:$SiCl_4$:BCl_3						
flow rate /sccm	190:30:0	190:3:8	190:3:8	190:3:8	190:3:3	190:3:3
Deposition passes	14	25	25	25	25	13
Consol. Temp. /°C	800	1250	1150	1150	950	950
Oil bath temp. /°C	23	23	23	23	23	28
Calculated index*	1.4826	1.4884	1.4840	1.4883		
n at 633nm	1.5519	1.54	1.6567	-	-	1.571
Thickness /μm	4.1	3.5	5.9	3.2	3.2	4.3

Wafers were prepared with various BCl_3 flow rates on silica and sapphire. Silica samples showed high quality layers of refractive index around 1.55, with low loss, but these deteriorated quickly on exposure to water and samples kept in wafer boxes reacted with moisture, destroying the core (see fig. 4.10 (A)).

(A) (B)

FIGURE 4.10: (A) Deterioration of a boron-doped germania layer on a thick thermal oxide wafer. (B) Deterioration of a boron-doped germania layer on a sapphire wafer.

As a result, sapphire wafers were used due to their much higher thermal expansion coefficient of 7.5x10^{-6}. Nevertheless, early samples with flow rates of 8 sccm, in

comparison to $GeCl_4$ flow rates of 190 sccm, deteriorated in appearance (see fig. 4.10 (B)) over a period of six months and were no longer able to be measured via prism coupling. Further reduction in BCl_3 flow rate to 3 sccm, and later 1 sccm improved this to the point that these samples did not appear to deteriorate over a year, and indeed no appreciable deteriorate appears to have occurred to date. Prism coupling of these samples, although possible, proved difficult. It was assumed that this was due to lack of depth of the layer, and further layers were deposited and consolidated, with an increased oil bath temperature in order to increase $GeCl_4$ vapour pressure. These subsequent layers showed defects in places, resembling bubbles. It was later found that, as with pure GeO_2 on sapphire, a thickness of 2-2.5 μm was measured by an area where the soot had been removed pre-consolidation and stylus profiled in order to measure depth. SEM imaging, EDX and a line scan (see fig. 4.11) of sample PX100 confirmed diffusion into the sapphire layer.

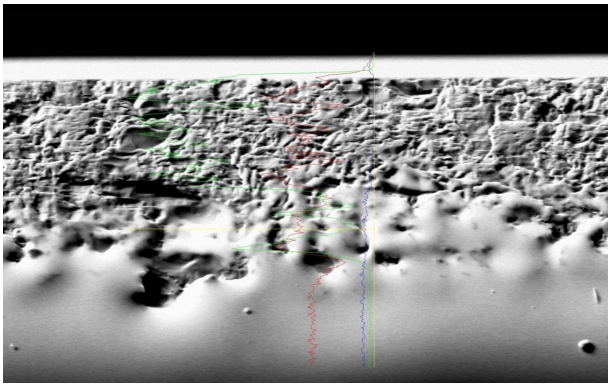

FIGURE 4.11: Line scan showing distribution of Ge, O and Al in the core and substrate layers of sample PX100

Interestingly, the diffusion appears to have resulted in some of the germania remaining on the top and some diffusing/sinking towards the bottom of the substrate, with proportionally less in the upper substrate.

4.5 Phosphorus & boron co-doping

A previously successful recipe including both B and P was used, and different P flow rates used to see what flow rate resulted in just reaching the 20% limit (see table 4.8) and also to provide alternative samples for UV writing of rings and comparison with other samples in terms of photosensitivity, loss, as both theses dopants are known to aid these.

TABLE 4.8: Phosphorus & boron co-doped germania FHD results. * indicates calculation via EDX; † indicates calculation via PPTOFMS results; § indicates calculation by PPTOFMS data and addtivity rule.

Wafer code	**NB261-1**	**NB261-2**	**NB261-3**
BCl_3:$GeCl_4$:BCl_3 flow rate /sccm	87:100:100	87:100:50	87:100:25
Percentage Ge/P*	5.5/11	9.5/7.3	10.4/6.1
Percentage Ge/P (excluding B) †	4.4/9.5	-	-
Percentage B/Ge/P†	20/3.5/7.5	-	-
Calculated index§	1.4670	-	-
n at 633nm	1.4774	1.4731	1.4710
Thickness	10.47	9.60	8.80
Uniformity	5.25	5.26	3.27
Loss at 1550nm	0.58	-	-

NB261-1 was analysed using PPTOFMS (see fig. 4.12) as well as prism coupling and SEM/EDX, allowing measurement of the boron concentration which would otherwise be impossible. PPTOFMS of NB261-1 was approximately consistent with EDX data.

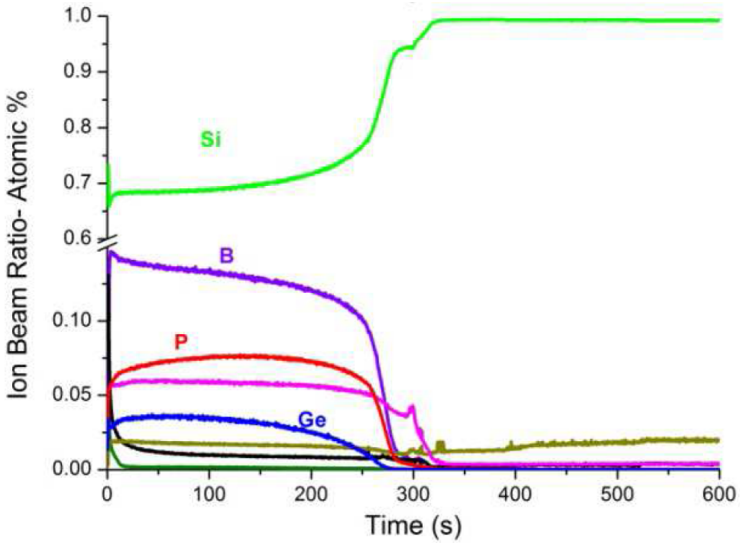

FIGURE 4.12: PPTOFMS analysis of sample NB261-1: Composition is calculated to be 69.0% silicon, 20.0% boron, 3.5% germanium (with some proportion possibly being six-coordinated), and 7.5% phosphorus. The light green, black, pink and dark green lines represent qualitative concentrations of N, C, O and H_3 respectively.

NB261-1, with the highest phosphorus concentration, showed relatively low loss, presumably due to good reflow (reliable loss measurements were not possible on NB261-2 & NB261-3, due to a large variation in loss and thus little repeatability), highest index, despite the lower germania content, presumably due to the change in coordination number of Ge from 4 to 6, and the highest thickness, due to having the greatest over-all dopant concentration (B and P combined), since both dopants have been shown to hinder either volatilization of GeO or its formation. The lowest phosphorus concentration, seen in NB261-3, has resulted in the best uniformity, perhaps due to improved reflow.

4.6 Conclusions

4.6.1 Solution doping using $BiCl_3$

Bismuth-doped germanate glass layers were fabricated for the first time using FHD and solution doping. They were measured to have a refractive index of around 2.2 but as the samples had large areas of Bismuth on the top layer, rather than incorporated into the glass, these were unsuitable for UV writing or damascene ring fabrication and coupling. Ultimately, though promising, this approach had to abandoned due to the amount of work required to optimise solution, doping conditions, mechanics, consolidation temperature, but is nevertheless one worthy of further investigation, especially due to bismuth-doped germania's desirable properties of being non-hygroscopic.

4.6.2 Phosphorus doping

Stable GeO_2-P_2O_5-SiO_2 layers were fabricated. These layers showed good uniformity and chemical stability and were thus suitable for direct UV writing. Lowest loss and uniformity was seen in sample NB298, with approximately 12% P_2O_5 and 19% GeO_2, perhaps due to a decrease in glass transition temperature and therefore improved reflow. Results bring into question at what percentage the refractive index starts to decline with addition of P_2O_5%. Higher P_2O_5-content samples resulted in greater thickness, suggesting that the addition of P_2O_5 inhibits either the volatilization of GeO or the reduction of GeO_2 to GeO. The considerable discrepancy in percentage composition of these samples between EDX and element mapping may be due to the change in coordination number, which as it may change with composition it seems likely that it will also change with depth. It is also notable that the discrepancy reduces with P_2O_5 content. EDX was done on the surface of these unclad samples. Element mapping was centred on the core layer. These samples of adequate quality to be UV written.

4.6.3 Boron doping

Borogermanate on sapphire was also unstable, although it showed low loss. Boron-Bi-doped germania does show very good loss results in comparison to pure germania so some boron content may be desirable as long as the CTE is appropriately matched. These samples were UV written (see section).

4.6.4 Phosphorus & boron co-doping

Low loss layers were seen in NB261-1, doped with approximately 3.5% germanium, 20% boron and 7.5% phosphorus content according to PPTOFMS results. Uniformity was better in lower P_2O_5-content samples. Disparity between the calculated index and that found by prism coupling indicates that either there has been a change in the coordination number of some or all of the germanium from 4 to 6, with a corresponding increase in index, or that the PPTOFMS results are inaccurate.

4.7 Bibliography

[1] T. Storgaard-Larsen, C. V. Poulsen & O. Leistiko, "Nitrogen Doped Germania Glasses with Enhanced Optical and Mechanical Properties", *J. Electrochem Soc.*, 144 (6): 2137-2142, June 1997.

[2] P. A. Williams, A. H. Rose, K. S. Lee, D. C. Conrad, G. W. Day & P. D. Hale, "Optical, Thermo-Optic, Electro-Optic and Photoelastic Properties of Bismuth Germanate ($Bi_3Ge_4O_{12}$) ", *Applied Optics*, 35 (19): 3562-3569, July 1996.

[3] J. Qiu, M. Peng, J. Ren, X. Meng, X.Jiang & C. Zhu, "Novel Bi-doped glasses for broadband optical amplification", *J. Non-Crys. Solids*, 354: 1235-1239, 2008.

[4] T. G. Xi, Y. Fei, W. P. Leung & C.L. Choy, "Thermal properties of bismuth germanate $Bi_4Ge_3O_{12}$", *J. Mat. Sci. Lett.*, 8: 1317-1319, 1989.

[5] W. Fan, B. H. Kim, L. Htien & W. T. Han, "Linear and nonlinear optical properties of Bi-doped germano-silicate optical fiber", *J. Optics*, 14 (012006): 125201, 2012.
[6] G. Lin, D. Tan, F. Luo, D. Chen, Q. Zhao & J. Qiu, "Linear and nonlinear optical properties of glasses doped with Bi nanoparticles", *J. Non-Crys. Sol.*, 357: 2312-2315, 2011.

[7] A. A. Veber, O. V. Usovich, L. A. Trusov, P. E. Kavin & V. B. Tsvetkov, "Luminescence Centers in Sillicate and Germanate Glasses Activated by Bismuth", *Bulletin of the Lebedev Physics Institute*, 39 (11): 305-310, November 2012.

[8] J.E. Townsend, S.B. Poole & D.N. Payne, "Solution-doping technique for fabrication of rare-earth doped optical fibres", *Opt. Lett.*, 23 (7): 329-331, 1987.

[9] J.R. Bonar, J.A. Bebbington, J.S. Aitchinson, G.D. Maxwell & B.J.Ainslie, "Low threshold Nd-doped silica planar waveguide laser", *Electr. Lett.*, 30 (3): 229-230, 1994.

[10] D. A. Guilhot, "UV-Written Devices in Rare-Earth Doped Silica-on-Silicon Grown by FHD", (Thesis, University of Southampton), December 2004.

[11] P. D. Dragic, M. Cavillon, & J. Ballato, "On the thermo-optic coefficient of P_2O_5 in SiO_2", *Opt. Mat. Exp.*, 7 (10): 3654-3661, October 2017.

[12] P. J. Lemaire, A. M. Vengsarkar, W. A. Reed & D. J. DiGiovanni, "Thermally enhanced ultraviolet photosensitivity in GeO_2 and P_2O_5 doped optical fibers", *Appl. Phys. Lett.*, 66: 2034-2036, 1995. URL doi:10.1063/1.113683.

[13] B. Malo, J. Albert, F. Bilodeau, T. Kitagawa, D. C. Johnson, K. O. Hill, K. Hattori, Y. Hibino & S. Gujrathi, "Photosensitivity in phosphorus-doped silica glass and optical waveguides", *Appl. Phys. Lett.*, 65 (4): 394-396, July 1994. URL doi:10.1063/1.112312.

[14] S. Suzuki, A. Schulzgen, S. Sabet, J. V. Moloney & N. Peyghambarian, "Photosensitivity of Ge-doped phosphate glass to 244nm irradiation", *Appl. Phys. Lett.*, 89:171913-1-171913-3, 2006. URL doi:10.1063/1.2370411.

[15] K. Sugiyama, Y. Waseda & M. Ashizuka, "Environmental Structure Around Germanium Atoms in GeO_2-P_2O_5 Glasses by the Anomalous X-ray Scattering Method", *Materials Transactions*, 32 (11): 1030-1033, 1991.

[16] J. W. Zwanziger, J. L. Shaw, U. Werner-Zwanziger & B. G. Aitken, "A Neutron Scattering and Nuclear Magnetic Resonance Study of the Structure of GeO_2-P_2O_5 Glasses ", *J. Phys. Chem. B*, 110 (41): 20123-20128, 2006.

[17] S. Shibata, U Y. Fukui, T. Oonishi, T. Yano, M. Yamane & S. Sakaguchi, "Intrinsic Optical Losses of GeO_2-P_2O_5-Al_2O_3 Glasses for Optical Fibers", Opt. Fiber Tech., (3): 90-95, 1997.

[18] H. Doweidar, "Considerations on the structure and physical properties of B_2O_3-SiO_2 and GeO_2-SiO_2 glasses", *J. Non-Crys Sol.*, 357: 1665-1670, February 2011.

[19] H. L. Rogers, S. Ambran, C. Homes, P. G. R. Smith & J. Gates, "*In situ* loss measurement of direct UV-written waveguides using integrated Bragg gratings", *Opt. Lett.*, 35 (17): 2849-2851, September 2010.

[20] J. E. Shelby, "Properties and structure of B_2O_3-GeO_2 glasses", *J. Appl. Phys.*, 45 (12):5272-5277, December 1974.

[21] Rajni & K Pita, "Photosensitivity of solgel derived inorganic xB_2O_3:$20GeO_2$: (80-x) SiO_2 system with various boron", *J. Phys. D: Appl. Phys.*, 39: 3235-3239, 2006.

[22] G. Baret, R. Madar & C. Bernard, "Silica-Based Oxide Systems I. Experimental and Calculated Phase Equilibria in Silicon, Boron, Phosphorus, Germanium, and Arsenic Oxide Mixtures", *J. Electrochem. Soc.*, 138 (9): 2830-2835, September 1991.

[23] D. L. Simpson, R. T. Croswell, A. Reisman, D. Temple & C. K. Williams, "Planarization Processes and Applications II. B_2O_3/P_2O_5 Doped GeO_2-SiO_2 Glasses", *J. Electrochem. Soc.*, 146 (10): 3872-3885, 1999.

[24] R. T. Croswell, A. Reisman, D. L. Simpson, D. Temple & C. K. Williams, "Differential Thermal Analysis of Glass Mixtures Containing SiO_2, GeO_2, B_2O_3, and P_2O_5", *J. Electrochem. Soc.*, 146 (12): 4569-4579, 1999.

[25] A. Margaryan & M. A. Pilliavin, "Germanate Glasses: Structure, Spectroscopy and Properties", *Artech House* ISBN 0-89006-506-3, 1993.

[26] M. E. Voronchikhina, N. G. Gorashchenko, V. B. Tsvetkov & Zh. S. Kuchuk, "Bi_2O_3-GeO_2 Glass and Transparent Glass Ceramic Based on it", *Glass and Ceramics*, 68 (1-2): 47-51, May 2011.

[27] S. P. Singh & B. Karmakar, "Ch. 9: Bismuth Oxide and Bismuth Oxide Doped Glasses for Optical and Photonic Applications", *Mat. Sci. & Tech. (Nova)*, 2012.

[28] J. Ballato & P. Dragic, "Rethinking Optical Fiber: New Demands, Old Glasses", *J. Am. Ceram. Soc.*, 96 (9): 2675-2692, 2013.

[29] D. Shin, "Effect of boron concentration on the UV photosensitivity of silica glass

film for planar lightwave circuit", *Appl. Surf. Sci.*, 253: 8003-8007, 2007.

[30] N. Terakado & K. Tanaka, "Photo-induced Phenomena in GeO_2 Glass", *J. Non-Crys. Sol.*, 352: 3815-3822, August 2006.

[31] S. Sakaguchi, "Consolidation of GeO_2 Soot Body Prepared by Flame Hydrolysis Reaction", *J. Non-Crys. Solids*, 171, 1994.

Chapter 5

Direct UV writing of planar germanate glasses

5.1 Introduction

Photosensitivity in germanate glasses was first observed by Hill et al. in 1978, using germania doped silica fibres [1]. Germania has been regularly used in photosensitive glass since the nineties, notably in Maxwell's 1995 paper, which reported the first UV-written directional coupler and the highest refractive index change seen in any photosensitive glass at the time [2]. Since then, Germania has frequently been used in both fibres and planar samples to enhance UV photosensitivity, and with far higher refractive index changes [3], but rarely in its pure form, nor widely at high GeO_2 contents. In spite of its well-documented photosensitivity, the mechanisms causing refractive index change on exposure to UV light remain poorly understood, rarely is this phenomenon as simple a case as increasing GeO_2 content to increase photosensitivity. Unsurprisingly, UV photosensitivity is highly dependent on fabrication technique and a wide variation in response in the deep UV is seen between various fabrication types and GeO_2-contents, including both extent of refractive index change and sign, with negative refractive index change often seen in thin films and positive change more frequently seen in micron-scale thicknesses and bulk glasses [4]. This chapter will summarise the main photosensitivity models: the colour centre, compaction-densification and stress-relaxation models, methods of sensitization. It then briefly reviews the literature regarding UV writing and photosensitive response in germanate glasses, before presenting the results of UV writing of the planar samples whose fabrication has been described in chapters 3 and 4.

5.1.1 Photosensitivity models

The compaction-densification model

This model ascribes the positive refractive index change in response to UV exposure to compaction of the glass matrix and corresponding increase in density [5][6]. This effect has been seen in non-H_2-loaded GeO_2-SiO_2 glasses, and is perhaps allied to the stress-relief model, described in the following section, as associated decreases in density are often linked to stress-release in the core [3][7]. Refractive index changes ascribed to this model are found to be thermally reversible, resembling type I Bragg gratings [3]. This model is found to be especially accurate for quantifying 213 nm photosensitivity in GeO_2-SiO_2 glasses [8].

The stress-relief model

Though more usually applied to fibre photosensitivity [9], the role of stress in photosensitive planar glass is presently not well understood although there is no reason why the model should not hold some validity for planar glasses. During fabrication and cooling, the CTE between core and clad results in tensile stresses in the core, which are relaxed on exposure to UV radiation. The stress-optic effect causes this to result in a change in refractive index [9].

The colour centre model

First proposed by Hand & Russell [10], this model relies on the fact that germania oxygen-deficient centres exist in germanate glasses. These oxygen-deficient centres are precursors to further defects, which may absorb at different energies in the UV region [11] (summarised in table 5.1).

TABLE 5.1: Germanium Oxygen-Deficient Centres. • denotes a "dangling bond" or free electron; ○ denotes a hole or missing electron; - represents an oxygen bond.

Defect	**Structure**	**Absorption peak (eV)**	**Notes**
NOMV	≡ Ge-Ge≡	5.06	Precursor defect.
GeE′	≡Ge•	6.3	Product of NOMV single photon reaction. reaction under UV
GeO_3^+	≡Ge○	-	Product of NOMV single photon reaction; optically inactive.
NODV	=Ge:	5.16	Precursor defect.
(alternative structure)	≡Ge-Ge-Ge≡		Suggested by Janer et al. [11]
GEC (1)	≡Ge• -O-Ge	4.7	Product of NODV two photon reaction.
GEC (2)	≡Ge• -O-Si	5.7	Product of NODV two photon reaction.
GLPC	-Ge○-	5.5	Product of NODV two photon reaction.

The main two precursor vacancies which the colour centre model ascribes refractive index change to are Neutral oxygen Mono-Vacancies (NOMVs; two four-coordinated

Ge atoms with a "wrong bond", i.e. missing a bridging oxygen) and Neutral Oxygen Di-Vacancies (NODVs; see table 5.1 for possible structures). NOMVs absorb at 5.06 eV, resulting in the formation of GeE′ centre (a four coordinated Ge atom with a dangling bond), a free electron and the optically inactive ion GeO_3^+:

$$\equiv Ge - Ge \equiv \xrightarrow{h\nu} \equiv GeE' + GeO_3^+ + e^- \qquad \text{(NOMV one-photon reaction)} \tag{5.1}$$

NODVs absorb at 5.16 eV, producing a germanium GEC (a germanium atom with a non-bonding electron pair attached via an oxygen atom to either a germanium or silicon atom), a germanium lone pair centre (GLPC; a germanium joined to two oxygens and missing two electrons) and a free electron [11].

$$\equiv Ge : \xrightarrow{2h\nu} GEC + GLPC \qquad \text{(NODV two-photon reaction)} \tag{5.2}$$

Under pulsed radiation, NOMVs may undergo the following reaction:

$$\equiv Ge - Ge \equiv \xrightarrow{2h\nu} GeE' + GeE' \qquad \text{(NOMV two-photon reaction)} \tag{5.3}$$

The products of the reactions of NOMVs and NODVs are usually detected via electron paramagnetic resonance (EPR) due to the presence of unpaired electrons and their concentrations may be used to infer concentrations of the original precursor defects [12].

5.1.2 Sensitization, annealing and hydrogen-loading

Strongly associated with the colour centre model is the use of hydrogen as a sensitizing agent [9] as first demonstrated by Lemaire et al. [13]. There are two main sensitization techniques; hydrogen loading, wherein the sample is placed in a high pressure, low-temperature H_2 atmosphere for a period of days to weeks; or annealing in a H_2-N_2 atmosphere, often at around 500°C. The effect of both is to maximise the concentration of ODCs, aiding UV-induced refractive index change. The placing of samples in a high pressure H_2 atmosphere for days/weeks at low temperature is believed to aid photosensitivity via formation of hydroxyls in the following reaction [7][9]:

$$\equiv Ge - O - Ge \equiv + H_2 \rightarrow \equiv Ge - Ge \equiv + Ge - OH \tag{5.4}$$

The NOMV formed then reacts under UV exposure via the reaction in equation 5.1 or 5.2. It is notable that of the literature concerning hydrogen loading, the majority uses low germania content glass. The small amount of literature which concerns pure or high germania content uses annealing in an H_2-N_2 atmosphere rather than hydrogen loading if any form of sensitization is used[1]. Under high temperature H_2-N_2 annealing, reduction of Ge-O-Ge to Ge-Ge occurs, as per the equation below [9]:

$$\equiv Ge - O - Ge \equiv + H_2 \rightarrow \equiv Ge - Ge \equiv + H_2O \tag{5.5}$$

Liu et al. amongst others acknowledge that the three models described are not mutually exclusive [3][8] [14]. Whether any of these reactions are in fact stress-enhanced (or indeed hindered) is unknown.

[1] Most of the literature is unclear on why, although the high sensitivity of GeO_2 to the damp conditions in hydrogen loading make this technique less than ideal.

5.2 Photosensitvity in germanate glasses

Literature regarding direct UV writing of flame hydrolysis deposited germanate glasses is scarce, and of this, none concerns pure germania to the best of the author's knowledge, and few demonstrate UV writing of high GeO_2-content samples. Table 5.2 summarises the literature on direct UV writing of FHD germanate glass.

TABLE 5.2: Photosensitvity in non-FHD GeO_2-SiO_2 Glasses. * denotes percentage GeO_2 calc'd from index contrast; §denotes where absorption at around 5 eV was measured rather than index change; †denotes CW radiation.

Fabrication Technique	**% GeO_2**	**Sensitization Method**	λ **/nm**	**Max. Δn (1550nm)**	**Ref.**
LPD	pure	H_2:N_2 anneal	broadband	575-17cm^{-1}§	[19]
mCVD*	97	-	244	-1.5x10^{-3}	[20]
mCVD*	75	-	244	-1.5x10^{-3}	[20]
mCVD*	75	H_2-loaded	244†	-2.6x10^{-3}	[21]
mCVD*	75	-	244†	4x10^{-4}	[21]
sol-gel	45	H_2-N_2 anneal	242	-3.1x10^{-5}	[22]
peCVD	43	-	248	2.0x10^{-3}	[14]
peCVD	43	ambient anneal	248	1.5x10^{-3}	[14]
Sputtering	<30	-	244	1%	[24]
Sputtering	$\geq$30	-	244	-3%	[24]
FHD	$\geq$25	H-loaded	248	-4-8%	[24]
FHD	<25	H-loaded	248	0.4%	[24]
mCVD*	24.5	-	244	3x10^{-4}	[20]
peCVD	13	D_2-loaded	244†	7x10^{-3}	[23]
FHD	12	H-loaded	248	0.33%	[25]
peCVD	11	ambient anneal	244†	2.5x10^{-3}	[26]
FHD	10	H-loaded	248	0.341%	[5]
peCVD	7	H_2 anneal	248	5000cm^{-1}§	[27]
FHD	5* Δn	H-loaded	248	6x10^{-3}	[28]
peCVD	15 (8% B_2O_3)	-	248	2.4x10^{-3}	[14]
melt quenching	20 (24% B_2O_3 +P_2O_5)	ambient anneal	248	1x10^{-3}	[15]

In reviewing the literature, it is notable that the relationship between GeO_2 content, change in refractive index and method of sensitization is complex and somewhat counter-intuitive - with apparently similar fabrication techniques, post-fabrication processing and GeO_2 contents yielding vastly different results, even in terms of the sign of the refractive index change. In high GeO_2 content samples Δn often changes sign from positive to negative with increasing fluence, as seen in type II gratings [7] or shows a strong decrease in response to UV exposure. The addition of boron may be used to aid positive index change [14][15]. Expansion is also mentioned frequently in relation to UV exposed layers of high germania content: Nishii reported an 18% volume increase with 3% index decrease in $\geq$30% GeO_2 sputtered films [16]. The opposite is reported by Marques et al. in an FHD GeO_2-SiO_2 of low GeO_2 content. There is also a correlation between refractive index change and the thickness of the layer: Thin films tend to show negative index changes and bulk glasses positive

ones [17]. Finally, it is noted in much of the literature that the three photosensitivity models are not mutually exclusive [3][7][18].

5.2.1 The direct UV writing system

The direct UV writing system consists of a translation stage on which a vacuum chuck is mounted in order to hold a (usually 10×20 mm) chip. A frequency-doubled Ar-ion laser produces a 244 nm beam which is split via a beam splitter into two beams which are cross-focussed down to an approximately 5 μm writing spot (although a single beam could be used to write a waveguide). Waveguides are written via translation of the sample under the writing spot, slower speeds resulting in greater energy exposed to the sample and thus results in higher fluences. Modulation of the beam via an electro-optic modulator results in variation in the intensity of the light, resulting in variations of the refractive index, and thus the formation of Bragg gratings (see fig. 5.1) [29].

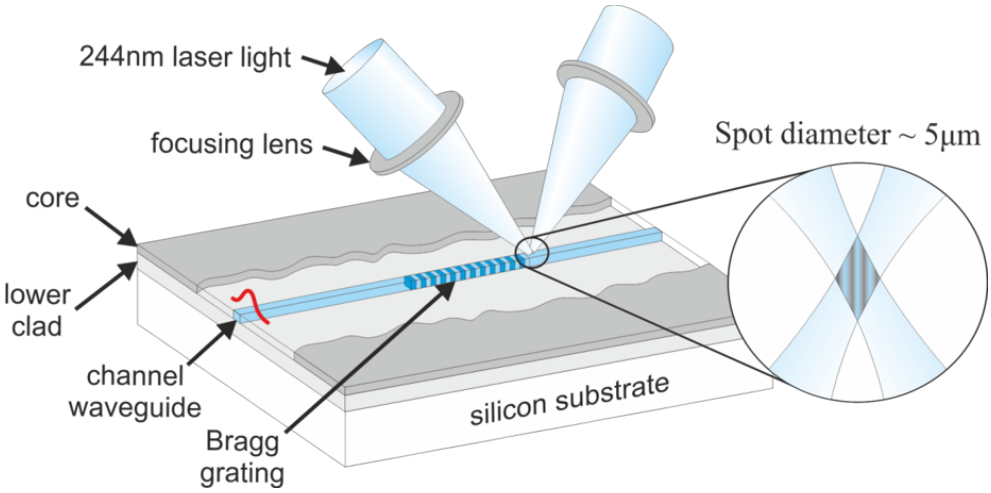

FIGURE 5.1: UV writing of a planar sample, from Lepert et al. [30].

Samples are usually hydrogen loaded for around a week in order to increase photosensitivity sufficiently that waveguides and Bragg gratings may be produced. The 213 nm is a similar system, albeit with a single beam. The radiation in this case is pulsed and the fluence as well as power may be adjusted. Analysis of the strength of Bragg gratings and refractive index change is generally quantified by launching 1550 nm light first into one end and then the other, giving a loss measurement for each Bragg grating. This can be used to quantify the refractive index change and loss via Gaussian fitting of reflectance versus fluence and measurement of the reflectance in both directions as described in [31].

5.3 Direct UV writing of planar germanate glasses

As described in chapters 3 and 4, a range of germanate samples on various substrates suitable for UV writing was fabricated. These were UV written at a range of fluences, both with and without hydrogen loading. Where samples had previously shown sensitivity to water or fast deterioration of the layer quality, methods of protecting wafers were investigated, including the use of photoresist, use of UV tape used in dicing, and of cleaving rather than dicing to avoid exposure to water. Later samples, e.g. germania-on-sapphire, were UV written at 213 nm, the new 213 nm direct UV writing system having been under construction during this work.

5.3.1 GeO_2-SiO_2

Samples NB160-NB194 were UV written at 244 nm, both with and without hydrogen-loading (see table 5.3). Hydrogen-loaded samples remained in the hydrogen cell for a minimum of three days. Fluences ranged from 3 kJcm^{-2} to 48 kJcm^{-2}.

TABLE 5.3: Results of UV writing at 244 nm for GeO_2-SiO_2 wafers.

Wafer	**Temp, atmos.**	**protection**	**H_2**	**Fluence /kJcm^{-2}**	**Response**
NB160-1	1360, He-O_2	-	N	3-48	None.
NB160-1	1360, He-O_2	-	Y	3-48	None.
NB160-2	1360, He-O_2	-	N	3-48	None.
NB160-2	1360, He-O_2	-	Y	3-48	None.
NB183-1	1250, He-O_2	Tape	N	3-48	None.
NB183-1	1250, He-O_2	Tape	Y	3-48	None.
NB183-2	1250, He-O_2	Tape	N	3-48	None.
NB183-2	1250, He-O_2	Tape	Y	3-48	None.
NB182-1	1200, He-O_2	Tape	N	3-48	None.
NB182-1	1200, He-O_2	Tape	Y	3-48	None.
NB182-2	1200, He-O_2	Tape	N	3-48	None.
NB182-2	1200, He-O_2	Tape	Y	3-48	None.
NB188-1	1150, He	Tape	N	3-48	None.
NB188-1	1150, He	Tape	Y	3-48	None.
NB188-2	1150, He	Tape	N	3-48	None.
NB188-2	1150, He	Tape	Y	3-48	None.
NB192-1	1150, He	S1813	N	3-48	None.
NB192-1	1150, He	S1813	Y	3-48	None.
NB192-2	1150, He	S1813	N	3-48	None.
NB192-2	1150, He	S1813	Y	3-48	None.
NB194-1	1150, He	SU-8	N	3-48	None.
NB194-1	1150, He	SU-8	Y	3-48	None.
NB194-2	1150, He	SU-8	N	3-48	None.
NB194-2	1150, He	SU-8	Y	3-48	None.

No refractive index change or change in appearance under a microscope was seen, nor was any fluorescence, often associated with refractive index change [32] seen. A flip-out mirror was used to bypass the board, beams splitters and EOM and expose a large area of each sample (approx. 2.5 mm), without translation of the stage, resulting in an approximate fluence of 360 $kJcm^{-2}$ when exposed for 10 minutes, with a sacrificial chip on top of the sample in order to provide a straight, clear boundary between exposed and unexposed areas on one side, but no response was seen.

It was concluded that either these samples are not photosensitive or such a high fluence is required that it is unrealistic to expect DUV to be practical. The possible reasons for this vary according to temperature (1300°C and above; 1250°C and below) due to the stability of the layer, but can be summarised as below:

- ODCs are not formed in significant numbers during deposition and/or consolidation.
- H_2-loading is unsuccessful due to composition (crystalline phase, existence of some alternative form of germania, Ge_xO_y), or number of oxygen vacancies produced is lower than required for refractive index change.
- ODCs are formed but are annihilated by moisture in the air/reaction with water/in damp conditions of the H_2 cell.
- ODCs are formed but the lack of stress resulting from diffusion in high temperature consolidated samples means that the required reactions do not take place, either in sensitization or in response to UV.
- ODCs are formed but the reduction in stress in low temperature consolidated samples when the layer reacts with moisture means that the required reactions do not take place, either in sensitization or in response to UV.
- The layer is extremely homogenous, which hinders photosensitivity and this is not reducible by H_2-loading [33].

Hydrogen-loading would be expected to aid photosensitivity if the latter is caused by an insufficient number of ODCs, assuming the sample consists of mainly amorphous GeO_2, which could conceivably not be the case. While the H_2 loading periods are short, these are unclad samples, so the diffusion of H_2 should be efficient. Diffused high temperature consolidated samples could conceivably hinder diffusion of H_2, but the lack of response of the low temperature consolidated samples, even when protected indicates that this cannot be the sole factor. Longer loading times of a few weeks still resulted in no response, suggesting that this is unlikely to be the cause. Some low temperature samples appeared slightly pearlescent after hydrogen, indicating a reaction with water in the damp environment, annihilating ODCs. However, the stability of the high temperature samples suggests that they should not be unduly affected by this, but nevertheless show no apparent photosensitivity. Homogeneity of GeO_2 layers has been cited as a reason for lack of photosensitivity, but high GeO_2-content and pure samples have been successfully written, using similar techniques with presumably similar levels of purity and homogeneity. Diffused samples would perhaps be expected to be at least slightly photosensitive in the absence of any other factors. A likely possible cause is the lack of stress in diffused layers, and reaction with water in low temperature layers causing relaxation. Low temperature layers which were protected showed no response to UV exposure, so

either protection is inadequate or reaction with water/resulting lack of stress is not the cause.

In the hope of reducing sensitivity to water due to stress, and consequent relaxation of it, it was decided that high temperature diffused layers were to be used as substrates for low temperature layers, reducing the CTE mismatch between layers, reducing stress to avoid reaction with moisture but retaining some in case of any causal relationship with UV photosensitivity. The possibility that composition may prevent photosensitivity, either due to existing in its crystalline phase or the presence of some alternative form of germania [4], Ge_xO_y, cannot be discounted.

5.3.2 Low-on-high temperature GeO_2-SiO_2

NB258 (low-temperature consolidated germania on top of high temperature consolidated germania on silica) showed visible lines on UV exposure with fluences of 8, 10, 12, 14, 16, 18 & 20 $kJcm^{-2}$, both with and without hydrogen-loading (see table 5.4 for results for this and other samples). However the apparent waveguides were not visible under the microscope. The appearance is likely due to exposed areas becoming hygroscopic, but without any accompanying change in refractive index.

The slight photosensitive response seen in these samples supports the idea of balancing tensile stress and sensitivity to water, meaning high temperature samples with a large amount of diffusion lack the requisite stress, and low temperature samples suffer from water ingression and reaction, annihilating vacancies. These samples may have enough stress in the layers to allow the reactions to happen resulting in hygroscopy, but a limited (though nevertheless fairly high) sensitivity to water in comparison to low temperature consolidated samples. Either the stresses are not enough to result in refractive index change, or there is some additional reason for the lack of photosensitivity.

5.3.3 Protection of wafers

Wafers NB258-1, 183-3, 203-1 and 223-1 were protected from moisture using various methods, as shown in table 5.4. Dicing in order to produce smooth edges resulted in reaction and the pearlescent appearance seen in previous samples on exposure to water. Samples were cleaved instead, however the difficulty in cleaving accurately made coupling impossible. Protection using thin layers of S1813 photoresist resulted in delamination of the germania layer with the photoresist layer when diced or cleaned (the S1813 becoming soluble in acetone where exposed). Plasma ashing may perhaps be used in future to remove the photoresist without damage to the germanate layer.

Initially, protecting wafers using negative photoresist SU-8 appeared to work well, as the wafers did not react to water while dicing and the SU-8 was removable with acetone. However, samples protected in this way and hydrogen loaded showed cracking, possibly due to the damp environment. While the surface of the chips were protected, the sides were not, allowing diffusion of and reaction with water. It was noticed that samples diced and hydrogen loaded at a later date, though from the same wafer showed more severe cracking.

TABLE 5.4: UV writing results for Low-on-high temperature consolidated wafers.

Wafer	protection	H_2	Response
NB258-1	-	N	No response; Water damage from dicing
	-	Y	No response; Water damage from dicing
	cleaved	N	Apparent waveguides but not visible under microscope.
	cleaved	Y	As above.
	tape	N	As above.
	tape	Y	As above.
	S1813	N	Impossible to remove photoresist without destruction of core.
	S1813	Y	As above.
NB183-3	tape	N	No response.
	tape	Y	Apparent waveguides but not visible under microscope.
NB203-1	tape	N	Apparent waveguides but not visible under microscope. Red-purple fluorescence.
	tape	Y	Apparent waveguides but not visible under microscope.
NB223-1	tape	N	Apparent waveguides but not visible under microscope.
	SU-8	Y	Weak waveguides; extensive cracking.

Sample NB183-3 (consolidated at 1250°C on thick thermal oxide in a He-O_2 atmosphere) was consolidated several months before being UV written, so the possibility of degradation of the sample over time exists, and some water damage at the edges of the chip could be seen as a result of dicing, despite the use of protective tape. The lack of UV photosensitivity is likely due to reaction with water, resulting in annihilation of oxygen vacancies.

NB203-3 (consolidated at 1150 °C on thick thermal oxide in He) Wafer NB203-1 was hydrogen loaded and UV written at fluences of 3-12 kJcm^{-2}. Its lack of photosensitivity is likely due to previous reaction with water, aided by existence (and subsequent annihilation) of oxygen vacancies formed in oxygen-free consolidation. NB223-1 (consolidated at 1150 °C without oxygen in He) was UV written both with and without hydrogen loading. In the hydrogen loaded sample, red-purple fluorescence was seen to build up over a period of a few seconds while exposed to UV radiation. Waveguides could be seen under a microscope and were visible when coupling into the chip at 633 nm (see fig. 5.2 (A)), although were difficult to detect at 780 nm, possibly due to the background noise obscuring the small back reflections from the weakly guiding waveguides. A second sample from wafer NB223-1 was written at various fluences: 3, 10, 8, 10, 12, 14 kJcm^{-2}. Fluorescence was again seen on exposure to UV light. Ablations could be seen where the sample was aligned, (effectively writing at low fluence).

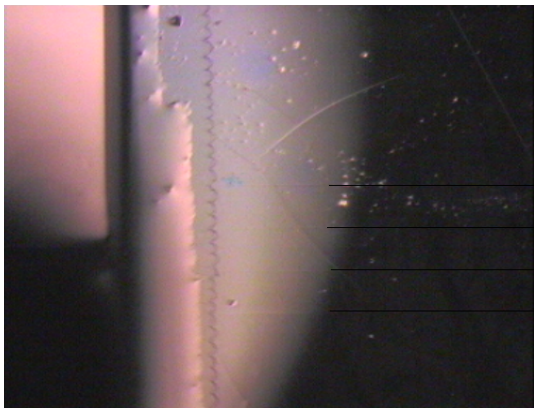

(A)

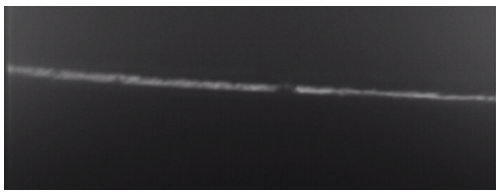

(B)

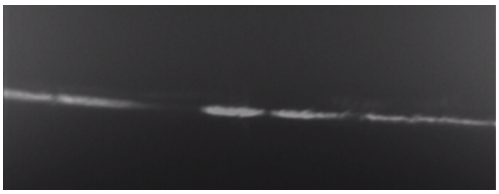

(C)

FIGURE 5.2: UV written waveguides on NB223-1: (A) Top view of NB223-1 while coupled to 633nm (B) End view of chip NB223-1away from UV-written waveguides and (C) centred on UV-written waveguides, with indications of interference fringes.

Ablations which intersected a crack appeared to disappear either side of the crack. During characterisation interference fringes could be seen via camera (see fig. 5.2 (B) & (C)), suggesting that the light directly from the source and that reflected by the waveguide is interfering.

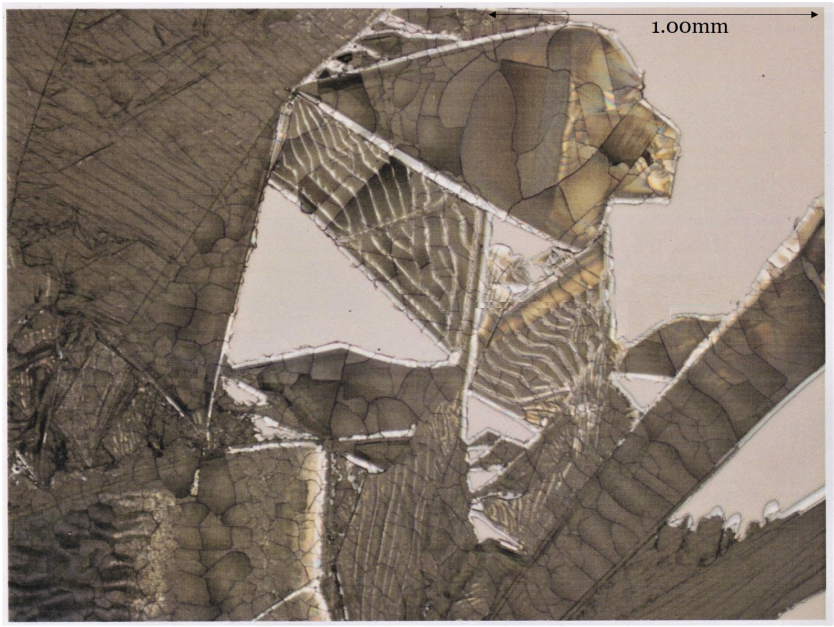

FIGURE 5.3: Cracking of the surface layer of sample NB223-1, protected using SU-8 negative photoresist and hydrogen-loaded before being UV written.

Severe cracking of the germania layer could be seen clearly, possibly due to hydrogen loading and/or the damp conditions involved in hydrogen loading combined with the non-porous layer of SU-8 deposited (the microscope image in fig. 5.3 shows the extent of cracking). The sample showed more cracking than the previous one from the same wafer, and it seems clear that the use of SU-8 offers limited protection, since the only difference between the two samples was that the second was diced hydrogen loaded a week later than the first. The combination of weak guiding and severe cracking of the sample made characterisation of these samples impossible. It should be noted that the outgassing time for both NB223-1 chips was relatively long due to issues with alignment of the chip and G-code controlling the UV writing system. The fact that weak guiding was only seen when protected and hydrogen-loaded suggests that adequate tensile stress, use of hydrogen-loading (due to insufficient numbers of ODCs) and protection from moisture (to avoid annihilation of ODCs or destruction of the core) are essential for photosensitivity in these samples. Suitable clad layers may reduce outgassing but require slightly longer periods of hydrogen-loading.

5.4 Phosphorus- & boron- doped glasses

Phosphorus-doped samples were written at 244 nm at fluences between 12-48 kJcm^{-2} (see table 5.5). No response was seen in either NB298 or NB299 (NB300 had degraded such that it was of insufficient quality to UV write). Previous compositional analysis suggested the presence of some unknown proportion of germania existing as GeO_6, as supported by the literature, and occasionally proposed to exist in small rings [4]. The lack of four-coordinated germania would prevent both the NOMV one-photon reaction and reaction 5.4 from occurring with hydrogen-loading.

TABLE 5.5: Results of UV writing at 244 nm for phosphorus doped wafers.

Wafer	**H_2**	**Fluence(s) /kJcm^{-2}**	**Response**
NB298	N	12, 15, 18, 24, 48	None.
NB298	Y	12, 15, 18, 24, 48	None.
NB299	N	12, 15, 18, 24, 48	None.
NB299	Y	12, 15, 18, 24, 48	None.

Phosphorus and boron co-doped samples were written at 244 nm at fluences between 12-48 kJcm^{-2} (see table 5.6). No response was seen in NB261-2 (NB261-3 had degraded such that it was of insufficient quality to UV write). NB261-1, with the highest phosphorus content showed hydrophobicity when hydrogen loaded but no other UV response. The method of exposing a large area of a sample to UV light at high fluence using the flip-out mirror, as described in section 5.3.1 was again tried, with no obvious UV-induced response.

TABLE 5.6: Results of UV writing at 244 nm for phosphorus and boron co-doped wafers.

Wafer	**H_2**	**Fluence(s) /kJcm^{-2}**	**Response**
NB261-1	N	12, 15, 18, 24, 48	None.
NB261-1	Y	12, 15, 18, 24, 48	Apparent waveguides at all fluences but not visible under a microscope.
NB261-2	N	12, 15, 18, 24, 48	None.
NB261-2	Y	12, 15, 18, 24, 48	None.

5.5 Germania on sapphire

Sapphire samples were written at 244 nm (see table 5.7) and 213 nm (see table 5.8) . The samples deposited at high deposition rates, with the oil bath temperature raised to 28°C, PX99 and PX100, had a large number of defects.

TABLE 5.7: Results of UV writing at 244 nm for GeO_2 on sapphire wafers.

Wafer	**Temp, type**	**H_2**	**Fluence(s) /kJcm^{-2}**	**Response**
NB314	1360, GeO_2-SiO_2	N	12, 15, 18, 24, 48	None.
NB314	1360, GeO_2-SiO_2	Y	12, 15, 18, 24, 48	None.
NB322	1360, GeO_2-SiO_2	N	12, 15, 18, 24, 48	None.
NB322	1360, GeO_2-SiO_2	Y	12, 15, 18, 24, 48	None.
NB330	1250, GeO_2	N	12, 15, 18, 24, 48	None.
NB330	1250, GeO_2	Y	20	Apparent waveguides visible under a microscope.
NB330	1250, GeO_2	Y	30	Apparent waveguides visible under a microscope.
PX100	1250, GeO_2-B_2O_3	N	12, 15, 18, 24, 48	None.
PX100	1250, GeO_2-B_2O_3	Y	12, 15, 18, 24, 48	None.

While little response was seen in these samples at 244 nm, at 213 nm these areas ablated at as low a fluence as 1 kJcm^{-2} and 0.3 mW. Squares of 5mm were written via rastering the laser, at 1 mW and 0.5 mW at fluences of 0.5, 0.2 and 0.1 kJcm^{-2} on sample PX100 (see fig. 5.4).

TABLE 5.8: Results of UV writing at 213 nm for GeO_2 and B_2O_3-GeO_2 on sapphire wafers.

Wafer	**H_2**	**Fluence(s) /kJcm^{-2}**	**Power /mW**	**Response**
PX99-1	N	1, 0.5, 0.1	1	Ablated.
PX99-1	N	0.05, 0.01	1	None.
PX99-1	N	1, 0.5	0.5	Ablated.
PX99-1	N	0.1, 0.05, 0.01	0.5	None.
PX99-1	N	2, 1.5, 1	0.3	Ablated.
PX99-1	N	0.5	0.3	None.
NB322	N	1, 5, 10, 20, 40	2.5	None.
NB322	Y	0.1, 0.5, 1.0, 5.0, 10	2.5	None.
NB322	Y	5, 10, 15, 20, 25, 30	2.5	Apparent waveguides but impossible to couple into.

Ablations were more prominent where the sample already had visible defects, increasing with power and fluence. Although at some powers and fluences there was no response, no ablation threshold could be found. Samples fabricated using standard deposition rates and oil bath temperature showed slight photosensitivity, but the (presumably) small index change made coupling impossible. The rate of deposition inevitably affects the composition of the deposited soot, thus compositional data would be helpful in understanding the reasons for the difference in photosensitive response in order to maximise it. The method of exposing a large area of a sample to UV light at high fluence using the flip-out mirror, as described in section 5.3.1 was again tried, with no obvious UV-induced response.

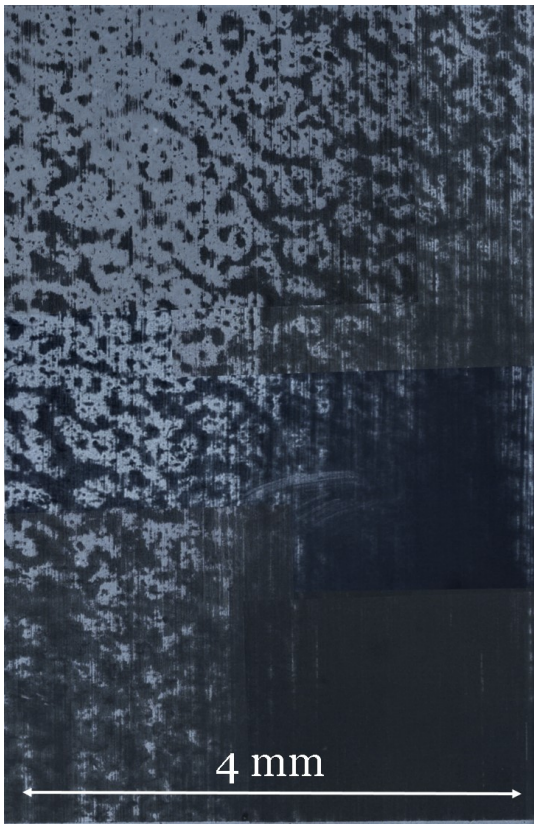

(A)

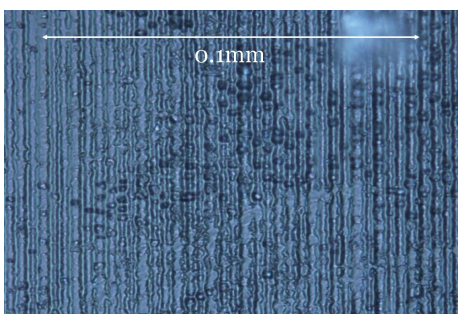

(B)

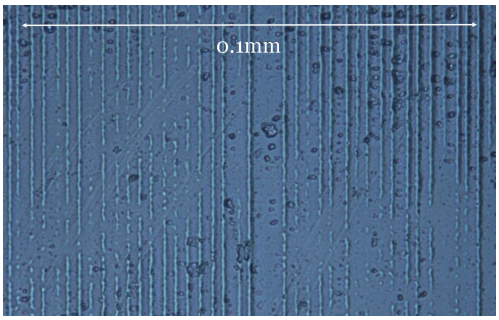

(C)

FIGURE 5.4: (A) Composite microscope image of sample PX100 after writing at 213 nm at 1 mW, showing variation in UV response according to surface quality. (B) & (C) Microscope images of two different areas of sample PX100 after writing at 213 nm at 1 mW. The vertical lines are where the sample has been UV-exposed.

5.6 Conclusions

Various samples have been written at both 213 nm and 244 nm, with and without hydrogen loading. Various methods of protecting the high GeO_2-content layers on silica samples from water ingression have been investigated. Due to the lack of availability of the 213 nm UV writing system, phosphorus and boron doped germania layers were only UV written at 244 nm.

5.6.1 Germania on silica and silicon substrates

It is suspected that high temperature samples lack the oxygen vacancies as their formation decreases with temperature. The diffused layers result in lack of tensile stress and consequently the reactions thought to occur during hydrogen loading are unable to happen. Low temperature samples react easily with water and solvents, destroying oxygen vacancies, relaxing stresses and destroying the glass layer itself. NB258-1 was UV written but could not be diced or cleaved accurately, so optical coupling was not possible. (A diced sample showed weak gratings due to degradation due to water during dicing process.) Protecting with S1813 resulted in removal of the layer with the photoresist. It is suspected that the small amount of photosensitivity seen is due to a) ODCs forming due to lower temperature b) internal stresses due to the CTE mismatch between high temperature diffused layer and low temperature core layer, which do not relax due to the lower sensitivity to water.

5.6.2 Germania on sapphire

Sapphire has shown some promise at both 244 nm and 213 nm, however results are inconsistent, with ablation being especially severe at high fluence and high power but no obvious effects at lower power and fluence. Areas of wafers which were fabricated using high deposition rates and a higher oil bath temperature resulted in a high number of defects. However, the samples appear to show a greater photosensitive response at 213 nm. Presumably there is some combination of power and fluence which results in index change rather than ablation, however this threshold was not found. Samples fabricated at standard deposition rates showed little photosensitive response at 213nm. Response at 244nm is unclear: most tests resulted in no response, other than one hydrogen-loaded sample written at 20 and 30 $kJcm^{-2}$, but this was not reproducible.

5.6.3 Phosphorus & boron-doped germania on silica

The samples NB298 and NB299 showed hydrophobicity post UV writing, rather than photosensitive refractive index change. NB261-1 also showed hydrophobicity after being hydrogen-loaded and UV written at 244nm The lack of photosensitivity is perhaps due to change in coordination number of germania (if indeed this is occurring) from 4 to 6, with P_2O_5 forming PO_4 groups. This would result in a lack of Ge-Ge oxygen deficient centres, resulting in no response to UV light.

5.7 Bibliography

[1] K. O. Hill, Y. Fujii, D. C. Johnson & B. S. Kawasaki, "Photosensitivity in optical fiber waveguides: Application to reflection filter fabrication", *Appl. Phys. Lett.*, 32: 647-649, 1978.

[2] G. D. Maxwell & B. J. Ainslie, "Demonstration of a directly written directional coupler using UV-induced photosensitivity in a planar silica waveguide", *Electronics Lett.*, 31 (2): 95-96, Jan.1995.

[3] M. Douay, W. X. Xie, T. Taunay, P. Bernage, P. Niay, P. Cordier, B. Poumellec, L. Dong, J. F. Bayon, H. Poignant & E. Delevaque, "Densification Involved in the UV-Based Photosensitivity of Silica Glasses and Optical Fibers", *J. Lightwave Tech.*, 15 (8): 1329-1342, Aug.1997.

[4] N. Terakado & K. Tanaka, "Photo-induced Phenomena in GeO_2 Glass", *J. Non-Crys. Solids*, 352: 3815-3822, Aug. 2006.

[5] L. Zhang, H. Zhang, J. Wang, J. Zheng, W. Zheng & Y. Zhang, "Photosensitivity in GeO_2-SiO_2 glasses and optical waveguides", *Mat. Lett.*, 60: 3610-3613, April 2006.

[6] F. X. Liu, J. Y. Qian, X. L. Wang, L. Liu & H. Ming, "UV irradiation-induced defect study of GeO_2-SiO_2 glasses by Raman spectroscopy", *Phys. Rev. B*, 56 (6): 3066-3071, August 1997.

[7] E. Salik, D. S. Starodubov & J. Feinberg, "Increase of photosensitivity in Ge-doped fibers under strain", *Opt. Lett.*, 25 (16): 1147-1149, Aug. 2000.

[8] S. Pissadakis & M. Konstantaki, "Photosensitivity of germanosilicate fibers using 213nm, picosecond Nd:YAG radiation", *Optics Express*, 13 (7): 2605-2610, Apr. 2005.

[9] M. Fokine, "Photosensitivity, chemical composition gratings, and optical fiber based components", (Thesis), Royal Institute of Technology, Stockholm, 2002.

[10] P. Hand & St. J. Russell, "Photoinduced refractive-index changes in germanosilicate fibers", *Opt. Lett.*, 15: 102-104, 1990.

[11] C. Janer, A. Carballar, L. Navarro, J. L. Gao & R. M. Rubio,"Photosensitivity Color-Center Model for Ge-Doped Silica Preforms", *IEEE Photonics Journal.* 5 (4): 6100511-1-6, 2013.

[12] T. E. Tsai, D. L. Griscom & E. J. Friebele, "Radiation induced defect centers in high-purity GeO_2 glass", *J. Appl. Phys.* 62 (6): 2264-2268, Sept. 1987.

[13] P. J. Lemaire, R. M. Atkins, V. Mizrahi & A. W. A. Reed, "High pressure H_2 loading as a technique for achieving ultrahigh UV photosensitivity and thermal sensitivity in GeO_2 doped optical fibres", *Elec. Lett.*, 29: 1191-1193, 1993.

[14] M. Takahashi, A. Sakoh, Y. Tokuda, T. Yoko, J. Nishii, H. Nishiyama & I. Miyamoto,

"Photochemical process of divalent germanium responsible for photorefractive index change in GeO_2-SiO_2 glasses", *J. Non-Crys. Solids*, 345 & 346: 323-327, 2004.

[15] D. Shin, "Effect of boron concentration on the UV photosensitivity of silica glass film for planar lightwave circuit", *Appl. Surf. Sci.*, 253: 8003-8007, 2007.

[16] J. Nishii, "Permanent index changes in Ge-SiO_2 glasse by excimer radiation", *Mat. Sci & Eng. B*, 54: 1-10, 1998.

[17] N. Terakado & K. Tanaka, "Photo-induced Phenomena in Sputtered GeO_2 Films", *J. Non-Crys. Solids*, 351: 54-60, July 2004.

[18] F. X. Liu, J. Y. Qian, X. L. Wang, L. Liu & H. Ming, "UV irradiation-induced defect study of GeO_2-SiO_2 glasses by Raman spectroscopy", *Phys. Rev. B*, 56 (6): 3066-3071, August 1997.

[19] C. Jing, H. Shan, C. Zhang & J. Chu. Preparation of thick GeO_2 glass film with high UV photosensitivity. J. Non-Crys. Solids, 356: 2884-2888, 2010.

[20] V. M. Mashinsky, V. B. Netstruev, V. V. Dvoyrin, S. A. Vasiliev, O. I. Medvedkov, I. A. Bufetov, A. V. Shubin, E. M. Dianov, A. N. Guryanov, V. F. Khopin & M. Y. Salgansky, "Germania Glass Core Silica Glass Cladding Modified Chemical Vapour Deposition and Optical Fibers: Optical Losses, Photorefractivity and Raman Amplification", *Opt. Lett.*, 29 (22): 2596-2598, November 2004.

[21] O. I. Medvedkov, S. A. Vasiliev, P. I. Gnusin & E. M. Dianov, "Photosensitivity of optical fibers with extremely high germanium concentration", *Opt. Mat. Express*, 2 (11): 1478-1489, November 2012.

[22] K. Simmons-Potter & J. Simmons, "Band bleaching and growth dynamics in 45% GeO_2 55% SiO_2 films", *Appl. Phys. Lett.*, 66: 2104-2106, 1995.

[23] M. Svalgaard & M. Kristensen, "Direct UV written silica-on-silicon planar waveguides with low loss", *Electronics Lett.*, 33 (10): 861-863, May 1997.

[25] Y. Wu , H. Xing, L. Zhang, A. Li, Y. Yu & Y. Zhang, "Preparation of a Waveguide Array in Flame Hydrolysis Deposited GeO_2-SiO_2 Glasses by Excimer Laser Irradiation", *Chin. Phys. Lett.*, 19 (12): 1877-1880, 2002.

[26] M. Svalgaard, C. V. Poulsen & O. Poulsen, "Direct UV writing of buried single-mode channel waveguides in Ge-doped silica films", *Electronics Lett.*, 30 (17): 1401-1403, Aug. 1994.

[27] T. Hattori, E. Irisawa & H. Nishikawa"Effects of thermal anneal on the UV photosensitivity for writing of Bragg gratings on Ge-doped silica thin films by a plasma CVD method", *Proc. of 2005 Symp. on Elec. Insulating Mat.*, 2 (27): 636-639, 2005.

[28] P. V. S. Marques, J. R. Bonar, A. M. P. Leite & J. S. Aitchison, "Simultaneous UV Direct Writing of Channel Waveguides and Bragg Gratings in Germanium-Doped Planar Silica", *IEEE J. Selected Topics in Quantum Elec.*, 8 (6): 1316-1322, 2002.

[29] C. Holmes, C. Sima, P. Mennea, L. Carpenter, J. C. Gates & P. G. R. Smith, "Fabricating Fiber Bragg gratings using phase modulated direct UV writing", *Proceedings of SPIE - The International Society for Optical Engineering*, 2014.

[30] G. Lepert, M. Trupke, E. Hinds, H. L. Rogers, J. C. Gates & P. G. R. Smith, "Demonstration of UV-written waveguides, Bragg gratings & cavities at 780nm & an original experimental measurement of group delay", *Opt. Express*, 19: 24933-24943, 2011.

[31] H. L. Rogers, S. Ambran, C. Holmes, P. G. R. Smith & J. C. Gates, "*In situ* loss measurement of direct UV-written waveguides using integrated Bragg gratings", *Opt. Lett.*, 35 (17): 2849-2851, 2010.

[32] K. D. Simmons, B. G. Potter, Jr. & G. I. Stegeman, "Red photoluminescence and optical absorption in hydrogen-treated GeO_2-SiO_2 sol-gel-derived planar waveguides", *Appl. Phys. Lett.*, 64 (19): 2537-2539, May 1994.

[33] H. Hosono, K. Kamamura, H. Kawazoe & J. Nishii, "Nanometre scale heterogeneity in GeO_2-SiO_2 preforms prepared by the vapour phase axial deposition method', *J. Appl. Phys.*, 80: 3115-3117, May 1996.

Chapter 6

FHD & direct UV writing of germanate rods & tubes

6.1 Introduction

The rod resonator provides an alternative geometry to planar ring resonators, while relying on the same principles and underpinning mathematics. The use of these structures to produce resonators, and further, frequency combs, has previously been investigated by other groups, notably those of Vahala and Del'Haye on CO_2 laser-machined rods at NIST in the US and NPL in London respectively [1]. However, to the best of the author's knowledge none has yet exploited the phenomenon of UV photosensitivity in order to fabricate such a device, nor attempted fabrication of such a device in any of the novel glass compositions detailed in this work.

The machined rods fabricated at NPL are thus far being coupled into via tapered fibres, which lacks versatility and robustness. Direct UV written rod resonators offer an advantage over tapered fibre-coupled resonators in that coupling may be achieved via the end of the rod, spiralling down to the ring. Multiple rings with varying refractive indices and widths may be easily written, in order to have control over the mode volume, Q and other properties of each ring.

In this work the core layer is produced by depositing a layer of germanate glass onto a silica, alumina or sapphire rod via flame hydrolysis deposition (FHD) and consolidating simultaneously using the FHD torch. This technique made the stability of the samples to water less critical, as the rods were suitable for dicing using a bone saw, avoiding exposure to water, the effects of which having been described in previous chapters.

This chapter details the adaptations to the FHD and UV writing systems in order to deposit germanate glass layers suitable for direct UV writing or CO_2 laser machining, the latter being a collaboration with Pascal Del'Haye's group at NPL. Material characterisation was via SEM and EDX, as before, since prism coupling was impossible due to the geometry of the sample, although, surprisingly, optical profiling was found to be possible (see section 6.4.3). Note that rods for UV writing and machining were developed in parallel with planar samples.

6.2 Adaptations to the FHD and DUV systems

6.2.1 Adaptations to the flame hydrolysis deposition system

In order to deposit FHD glasses onto rods, an additional system was needed. A frame was designed to sit just above the deposition table, in order to accommodate an air-bearing spindle on which the substrate rods were mounted in order to producing a glass layer of uniform thickness (see fig. 6.1 (A)).

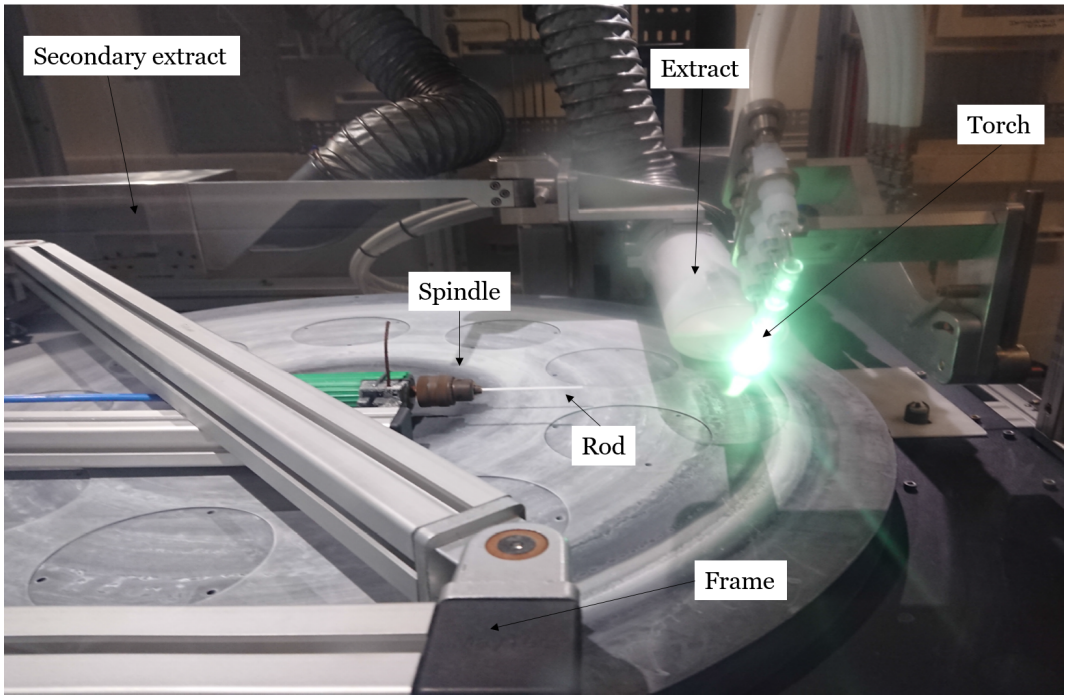

(A)

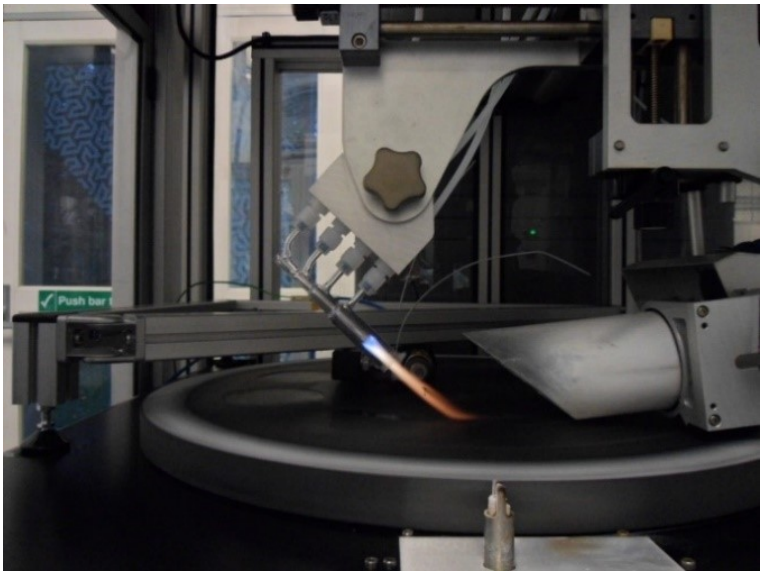

(B)

FIGURE 6.1: (A) The flame hydrolysis system as adapted for rod depostion. (B) Side-view showing the position of the rod within the flame.

The layer was deposited and immediately consolidated due to its position within the H_2-O_2 flame (see fig. 6.1 (B)). Changing the flow rates of the torch gases allowed rough control of the temperature of the flame and hence the consolidation temperature, albeit without any method of measurement. However, some approximate idea of the temperature could be gained from noting if the rods melted or began to soften sufficiently to result in bending or slumping of the rod. A number of trial runs were carried out in order to determine appropriate torch flow rates.

In order to ensure even deposition, the control software for the FHD system increases the table rotation speed as the distance of the torch from the centre of the table decreases (otherwise the constant speed of torch translation would result in greater volume of soot being deposited at smaller distances from the centre of the table). The software does not allow decoupling of the torch translation speed and table rotation, meaning that limiting the rate of rotation of the deposition table also reduces the speed of translation of the torch accordingly. Although this increases deposition times, it also results in and thicker layers being deposited, the latter being an advantage in this case, due to the small volume of soot deposited on the rod per pass. Thus the secondary extract was not put across in order to reduce turbulence and the speed of rotation of the deposition table was limited in order to reduce air flow around the rod.

The air bearing spindle was tested to determine the minimum rotation speed without stalling, which was found to be approximately 150 rpm. The position of the feet of the frame in relation to the deposition table were marked in the chamber to ensure consistency of position of the rods relative to the flame. The optimum position of the torch on the new system was noted[1]. While the preceding work on planar samples was useful, the compositions of the rods and planar samples fabricated under the same flow rates could not be assumed to be similar, due to the position of the rod within the flame. The higher temperature affects both the substrate temperature and the reactions taking place within the flame [2], producing different soot compositions, phases [3] and consolidation conditions.

6.2.2 Adaptations to the UV writing system

The UV writing system was adapted to allow writing of the rod by using a mirror inclined at 45° to direct the beam horizontally onto the rod and code written to rotate the rod during writing and alignment (see fig. 6.2). The rod holder uses precision ER collets of 1 mm, 2 mm and 3 mm in order to ensure verticality of the rod (see fig. 6.3). Alignment of the rod with the centre of rotation was essential and this was carried out by inserting a cannula with a fibre in it into the collet and rotating the holder under a microscope with a camera attached. Precession of the light from the fibre indicated that the holder was not central and the X-Y controls were adjusted to minimise precession at increasing magnification from $\times 5$ to $\times 40$.

[1] This was not possible to adjust on the older FHD system.

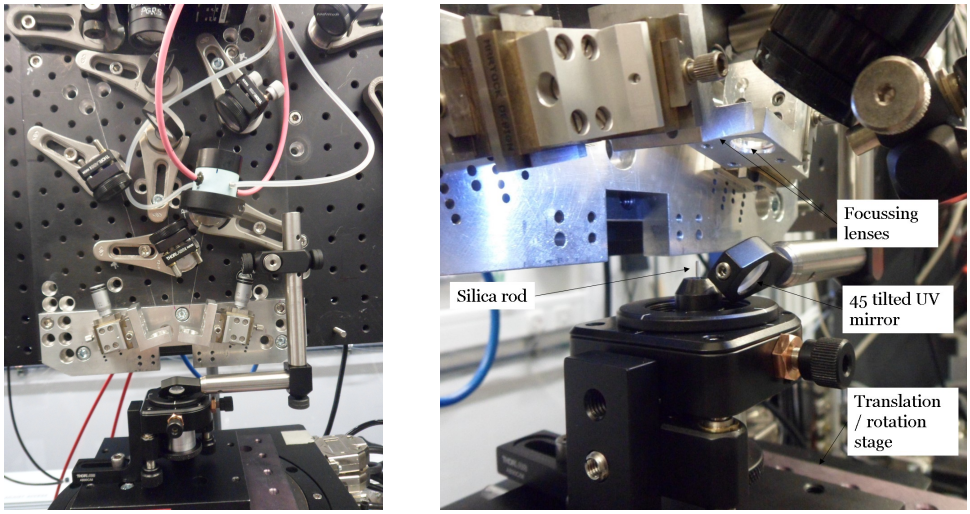

(A) (B)

FIGURE 6.2: (A) & (B): UV writing system with board for UV writing of 1550 nm Bragg gratings adapted for UV writing of rods.

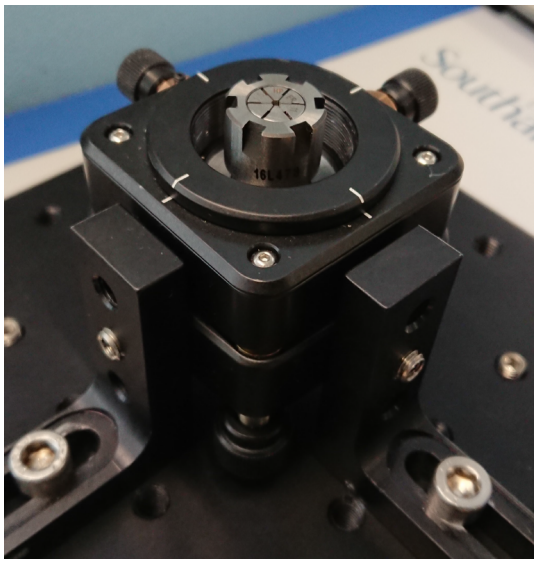

FIGURE 6.3: Rod holder for UV writing of rods and tubes, allowing 4-axis control of tip, tilt and (x,y) position.

Having checked alignment of the beam, it was then directed onto the rod and the rod rotated in order to check verticality (indicated by constant size and position of the writing spot over a full rotation) and the tip and tilt controls adjusted if the rod was not vertical. Then the x,y position was adjusted to ensure the system was central. After the rod was aligned relative to the stage system, it was then aligned to the focus of the UV beam.

6.3 FHD & direct UV writing of germanate glass on silica rods

6.3.1 FHD of P_2O_5-GeO_2 on silica rods

A number of trial runs were carried out in order to make minor adjustments to the alignment of the frame relative to the torch to ensure that the rod and the torch traverse were parallel and to find optimal torch flow rates and numbers of passes. Four initial runs were completed (see table 6.1) and cross sections of each of the deposited rods at various positions from the end of the rod were imaged using an SEM to assess concentricity of the deposition with respect to the centre of the rod, and the quality and uniformity of the layer.

TABLE 6.1: P_2O_5-GeO_2 on 1.3 mm diameter silica rods. $GeCl_4$ and PCl_3 flow rates were both 75 sccm. Bracketed numbers indicate warm-up passes.

Dep. no.	**H_2/O_2/Ar flow /l/min**	**Passes**	**Notes**
R1	5.4/2.7/8.0	1	Flame too hot; rod bent; torch flows progressively lowered for subsequent runs.
R2	2.4/1.0/6.0	(1) 1	800 nm-1.5 μm layer; O_2 flow rate further lowered as rod still glowed faintly.
R3	2.4/0.8/6.0	(1) 1	350-700 nm layer.
R4	2.0/0.8/5.0	4	Cracks propagated over time; 6-11 μm layer.

The surfaces of the consolidated rods were imaged using a microscope and compared on the day of deposition, four days post-deposition and a week post-deposition. For R1, the torch flow rates used were the same as those for deposition of planar germania. The rod slumped due to overheating so the flow rates were reduced significantly for subsequent runs. For R2 cracking of the surface was observed, increasing over a period of several weeks. A slight glow was observed during deposition, so the O_2 flow rate was reduced slightly in order to reduce the temperature. SEM images indicated layers of 800 nm-1.5 μm and 350-700 nm for R2 and R3 respectively. The large variation in depth of deposited layer in R2 was attributed to the spindle stopping rotation towards the end of the deposition. A single area of cracking was seen on rod R3 which did not show any deterioration over time, so it is suspected that a defect existed in the silica rod before deposition.

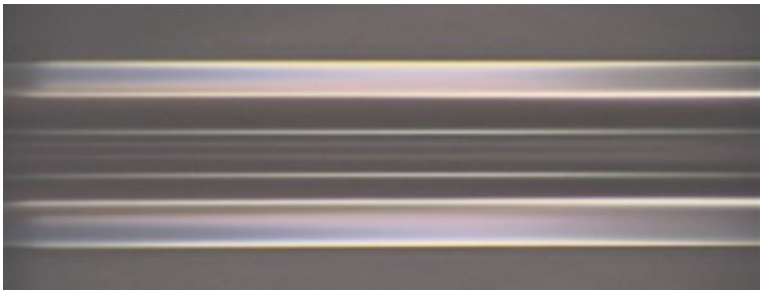

FIGURE 6.4: High quality glass layer deposited on to silica rod R3.

Sample R3 was otherwise of good quality (see fig. 6.4 and 6.5 (A)). The number of passes was thus increased for R4 in order to increase the depth of the deposited layer. Rod R4 showed severe cracking (see fig. 6.5 (B) & (C) and fig. 6.6), despite the lower flow rates of the torch gases, and hence a lower deposition and consolidation temperature.

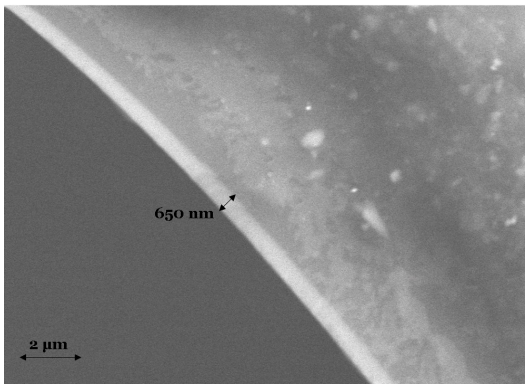

(A)

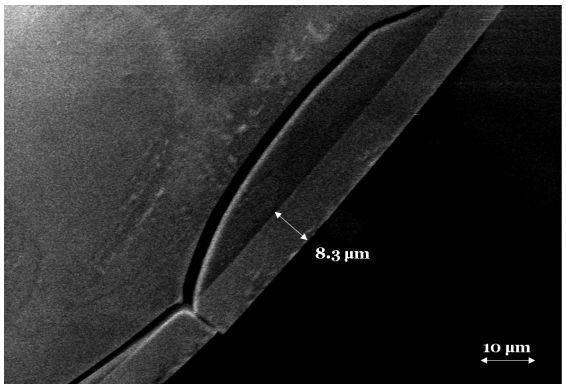

(B)

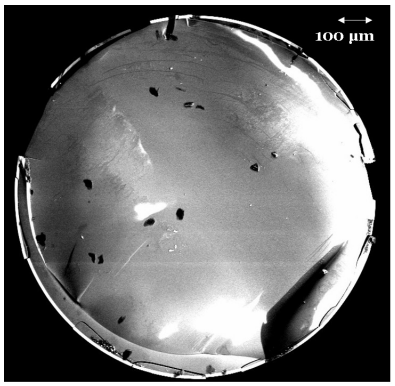

(C)

FIGURE 6.5: SEM images of (A) Rod R3, showing a layer of approximately 650 nm; (B) Cracking beneath the approximately 8.3 μm depth core layer of rod R4 & (C) The end view of rod R4.

In this case, cracking was noted to deteriorate further over time. The latter is likely to be due to thermal expansion coefficient mismatch ($0.55\times10^{-6}K^{-1}$ for silica compared with $6.25\times10^{-6}K^{-1}$ for phosphogermanate glass of 45.8% P_2O_5 and $7.25\times10^{-6}K^{-1}$ for pure germania [4]), exacerbated by the thicker phosphogermanate layer due to the larger number of passes. The variation in thickness of the layers caused by lack of concentricity was assumed to be due to poor positioning of the rod relative to the axis of rotation of the spindle. In the absence of any immediate solution to this problem, extra care was taken when preparing for subsequent deposition runs to check for any precession of the rod before deposition.

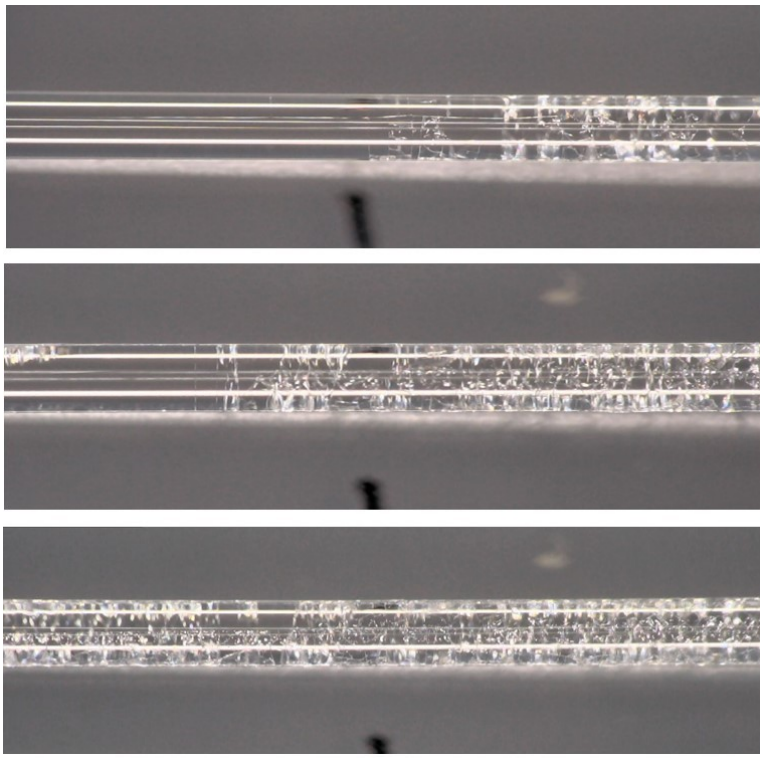

FIGURE 6.6: (Top) Rod deposition R4 on day of deposition, (middle) two days later and (bottom) a week later. The black mark indicates the same position along the rod for comparison.

Due to the thickness of the layer on rod R4, the number of passes was reduced from 4 to a maximum of 2 for subsequent runs (see table 6.2).

TABLE 6.2: P_2O_5-GeO_2 on 1.3 mm diameter silica rods. $GeCl_4$ and PCl_3 flow rates were both 75 sccm

Dep. no.	**H_2/O_2/Ar flow /l/min**	**Passes**	**Notes**
R5	2.0/0.8/5.0	1	Opaque in middle; aborted at 1 pass due to poor positioning of rod.
R6	2.0/0.8/5.0	2	Slightly glassy; 500-700 nm layer.
R7	2.0/0.8/5.0	2	Glassy; rod showed some vertical movement; 2.3 μm layer.
R8	2.6/0.9/6.6	1	Glassy; 1.7 μm layer; Slight cracks appeared after approx. 1 day.
R9	2.9/1.0/7.2	1	Rod cloudy from first half pass, indicating non-consolidation.
R10	3.1/1.1/7.8	1	Glassy.
R11	2.9/1.0/7.2	1	Glassy.
R12	3.1/1.1/7.8	1	Glassy; 1.1-1.4 μm layer.

R5 was aborted at one pass as it was not consolidating in the flame due to its poor positioning. R6 did consolidate, and showed a layer of 500-700 nm, although this

run was also aborted at 1 pass as the rod was clearly precessing around the centre of rotation and had to be re-placed on the spindle. R7 was successfully consolidated, producing a transparent glass layer of 2.3 μm of suitable quality for UV writing. R8 was deposited using increased flow rates but a single pass to compare quality and stability over time with R7. A clear layer of 2.3 μm of sufficient quality for UV writing was produced, although this was found to crack over a period of months. Torch flow rates were increased for each deposition from R9 - R12, in order to investigate the effect of high torch flow rates with a single pass, which appeared to give better quality rods, but cracks appeared in these samples over a matter of a week. R7 and R8 showed significantly less cracking than other samples, having been consolidated using moderate flow rates and thus temperature. While clear layers were obtained at greater H_2-O_2 flow rates (R9-R12), these samples showed more severe cracking after a period of a few weeks, presumably due to increased stresses on cooling. Lower flow rates (R5 & R6) resulted in incomplete consolidation, with soot able to be rubbed off the rods. Annealing in order to reduce stresses in these rods was considered but ultimately deemed unnecessary for rods such as R7 and R8, which appeared stable over time and unhelpful for samples such as R4, as cracking was seen to propagate along the rod on cooling from deposition.

6.3.2 Direct UV writing of P_2O_5-GeO_2 on silica rods at 244 nm

Samples R7 and R8 were the only samples with sufficiently little cracking that they were suitable for UV writing. However, no response to 244nm light was seen in either of these samples with or without hydrogen loading at fluences of 30, 60, 120, 240 & 480 kJcm^{-2} (see table 6.3). The slight yellow fluorescence seen in non-H_2-loaded samples is unexpected and has no obvious explanation. No fluorescence was seen in P_2O_5-GeO_2 planar samples under UV exposure at 244 nm, however this would have been difficult to see due to the silicon substrate.

TABLE 6.3: UV writing of FHD rods at 244 nm results. Laser power 62 mW; 1.44 mm radius.

Dep. no.	**Sensitization method**	**Outgassing time /min**	**Fluence /kJcm^{-2}**	**Notes**
R7	-	-	30-480	Slight yellow fluorescence.
R7	H_2 loaded	6	30-480	No response.
R8	-	-	30-480	Slight yellow fluorescence.
R8	H_2-loaded	3	30-480	No response.

In summary, deposition of stable P_2O_5-GeO_2 layers of approximately 2μm was found to be possible provided torch flow rates were sufficiently low to avoid slumping during deposition or later cracking due to thermal expansion coefficient mismatch. Yellow fluorescence was seen in these samples on exposure to 244 nm UV light in non-hydrogen-loaded samples, but no refractive index change was seen with or without hydrogen-loading.

6.4 FHD & direct UV writing of germanate glasses on alumina rods & tubes

Fabrication of rod samples was carried out in parallel with fabrication of planar samples. At this point, it had been established that the thermal expansion coefficient mismatch between SiO_2 and GeO_2 was the likely cause of the deterioration and sensitivity to water. Deposition of GeO_2-SiO_2 on to a silica rod resulted in cracks propagating along the rod under a minute after deposition, confirming that similar problems were likely with germanate on silica rods, and thus an alternative to silica was sought. As germania had been successfully consolidated onto planar sapphire, alumina and sapphire rods and tubes of 1-3 mm were used. Again, numerous trial runs were carried out in order to establish suitable torch flow rates. The range of flow rates was much wider than for P_2O_5-GeO_2 on silica rods, and higher H_2 and O_2 flow rates could be used due to the high melting point of alumina.

6.4.1 FHD of SiO_2-GeO_2 layers on alumina

GeO_2-SiO_2 layers were deposited onto alumina rods in order to provide an underclad layer of lower index than that of GeO_2 to prevent the mode sitting in the high-index alumina substrate. The adaptations to the FHD system successfully tested previously were used with a range of deposition and consolidation conditions, summarised in table 6.4.

TABLE 6.4: GeO_2-SiO_2 on 1.5 mm diameter alumina rods. * Re-consolidation of rod R16. †denotes a 2 mm diameter alumina rod.

Dep. no.	H_2/O_2/Ar flow /l/min	$GeCl_4$/ $SiCl_4$ flow /sccm	Passes (consol.)	H_2/O_2/Ar flow /l/min (consol.)	Notes
R13	2.0/0.8/5.0	125/25	1	-	V. little soot deposited; Surface rough.
R14	2.0/0.8/5.0	190/38	1	-	Rough.
R15	2.0/0.8/5.0	190/38	5	-	Not consol'd.
R16	2.0/0.8/5.0	190/38	10	-	Not consol'd.
R17	2.4/1.2/6.0	190/38	5	-	Glowed orange.
R18	2.6/1.3/6.0	190/38	5 (2)	3.6/1.8/7.0	Glassy.
R19*	-	N/A	0 (1)	3.6/1.8/7.0	Uneven; stable
R20	3.6/1.8/7.0	190/38	10	-	Rough.
R21	2.0/0.8/5.0	190/38	10 (1)	3.6/1.8/7.0	Rough.
R22	2.0/0.8/5.0	190/38	5 (1)	4.0/2.0/7.0	Glows; glass visible; rough
R23†	2.0/0.8/5.0	190/38	6 (1)	4.0/2.0/7.0	Poor alignment in flame.
R24†	2.0/0.8/5.0	190/38	5 (1)	4.0/2.0/7.0	Glassy.

Due to the novelty of the technique, it was impossible to predict the number of passes required to result in a layer of germania of a few microns, so to ensure a thick enough layer for UV writing, a large number of passes in comparison to previous experiments using P_2O_5-GeO_2 glass were used. Adjustment of the flame temperature via adjustment of torch flow rates was essential to ensure that it was high enough

to consolidate but low enough to avoid melting or softening of the rod. Little soot was deposited on the first few runs and precursor flow rates were subsequently increased, followed by an increase in the number of passes. Samples were found to not be consolidating, leaving the soot easily removable by touch, so torch flow rates were gradually increased over several samples. A separate, single consolidation pass at higher flow rates than the deposition passes was trialled after R19, and deposition $H_2/O_2/Ar$ flow rates were reduced back to 2.0/0.8/5.0 sccm. This allowed maximisation of the layer thickness. The glass layer deposited onto the rods appeared opaque apart from the ends where the torch moves more slowly, allowing reflow of the glass layer, so reduction of the translation speed of the torch was necessary in order to ensure a sufficiently smooth surface all the way along the rod. It was noted that at torch flow rates above the minimum required for consolidation, the alumina rods showed areas of brown discoloration, and the surface showed ridges of glass rather than a smooth layer. The higher temperatures associated with greater H_2/O_2 flow rates is likely to result in increased reflow, exacerbating the effects of any horizontal or vertical motion or precession of the rod during deposition, causing ridges. The brown discoloration could be due to overheating of the spindle, causing iron oxide deposition, consistent with the lack of discoloration at the torch end of the rod. Care was taken to avoid excessive H_2/O_2 flow rates and thus temperatures after these observations.

6.4.2 FHD of pure germania layers on to pre-deposited SiO_2-GeO_2 on alumina rods

Previously deposited SiO_2-GeO_2 on alumina rods R22 and R24 (see table 6.4) were found to be of sufficient thickness and smoothness to be used as substrates for deposition of a "core" layer of pure GeO_2 for direct UV writing (see table 6.5). The quality of the surface and composition of the layers was analysed using SEM and EDX analysis respectively. A combined (i.e. both GeO_2 and SiO_2-GeO_2 layers) depth of approximately 40 μm was obtained using 5 passes for the SiO_2-GeO_2 layer, followed by 10 passes for the germania layer (R24 (underclad) & R25 (core)).

TABLE 6.5: GeO_2 on SiO_2-GeO_2 underclad on alumina FHD Results. $GeCl_4$ flow rate was 190 sccm for all samples.

Dep. no. (substrate)	$H_2/O_2/Ar$ flow /l/min	Passes (consol.)	Consol. flow /l/min	Notes
R25 (R24)	2.0/1.8/5.0	10 (1)	3.4/1.8/7.0	Not fully consolidated.
R25	-	(1)	4.0/2.0/7.0	Consol. pass for R25; rough.
R26 (R22)	2.0/0.8/5.0	8 (1)	3.4/1.8/7.0	Uneven deposition.

Samples R22 and R24 were chosen for deposition of GeO_2 as they were of good quality and reasonable thickness. However, after deposition, these samples (GeO_2 on SiO_2-GeO_2) showed rough and uneven layers as seen in fig. 6.7 (A) . Separate SiO_2-GeO_2 and GeO_2 layers were difficult to discern on most SEM images . Figure 6.7 (B) shows one of the few images where separate layers could be discerned, showing a 28 μm germania layer and 14 μm SiO_2-GeO_2 layer on R25. Composition of the SiO_2-GeO_2 layer was found to be around 89% germania and 0.5% Al_2O_3 (with the remainder being SiO_2) by EDX analysis, consistent with the composition of SiO_2-GeO_2 layers deposited onto sapphire wafers in chapter 3.

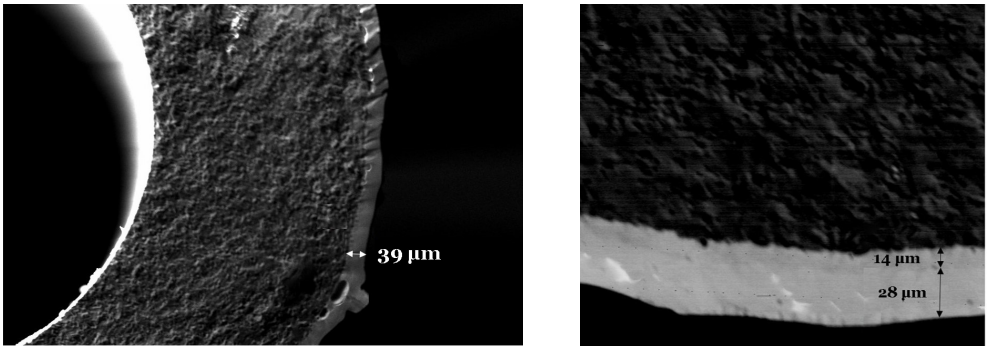

(A) (B)

FIGURE 6.7: SEM images of rod R25 showing (A) the extent of the non-uniformity and poor quality of the deposited layer; (B) underclad and core layers of approximately 14 μm and 28μm respectively.

The germania layer was found to be around 92% germania by EDX analysis, with the remaining 8% being SiO_2, corresponding to a refractive index of around 1.59.

6.4.3 FHD of B_2O_3-GeO_2 layers on alumina rods

In order to improve the smoothness and uniformity of the deposited layer, and potentially lower the consolidation temperature, the addition of boron was investigated (see table 6.6).

TABLE 6.6: FHD B_2O_2-GeO_2 on 1.5 mm diameter alumina rods at high BCl_3 flow rates. Deposition flow rates of $H_2/O_2/Ar$ were 2.0/1.8/5.0 throughout. $GeCl_4/BCl_3$ flow rates were 190 & 30 sccm respectively. †denotes a 2 mm diameter alumina rod. Stability was assessed by visual deterioration after a period of six months.

Dep. no.	Passes (consol.)	Consol. flow /l/min	Notes
R31	1	-	Glassy; stable.
R32	1	-	Depth varied from 50 - 65 μm due to poor rod positioning.
R33	5	-	Rpt. of R32 with improved positioning.
R34	10	-	Glassy; appears to be of high quality; stable.
R35	5	-	Rpt. of R34.
R36	5 (2)	-	Rpt. of R34.
R37	5 (1)	3.6/1.8/7.0	Uneven deposition; unstable.
R38	10	-	Glassy but very uneven.
R39	10 (1)	3.6/1.8/7.0	Very uneven deposition.
R40	5 (1)	4.0/2.0/7.0	Glassy.
R41†	6 (1)	4.0/2.0/7.0	Glassy but uneven; poor alignment.
R42†	5 (1)	4.0/2.0/7.0	Slightly uneven.
R43	5 (2)	-	Smooth; unstable.

These layers were visibly smoother in comparison to either GeO_2 or SiO_2-GeO_2, especially at the end, where the torch engulfs the end of the rods as the temperature is

higher and thus the reflow is greater. The depth of the layers was seen to improve (see fig. 6.8 (A)) compared to pure GeO_2-deposited samples (see fig. 6.7 for comparison), and SEM images show a much more even deposition and concentric rod, but some roughness and variation in the thickness of the layer due to poor rod positioning in the spindle is still present. The evenness of the deposition and concentricity was found to be heavily reliant on precise alignment of the rod to the horizontal, and depths of layers varied substantially around the rod (see fig. 6.8 (B)), even when great care was taken to ensure this.

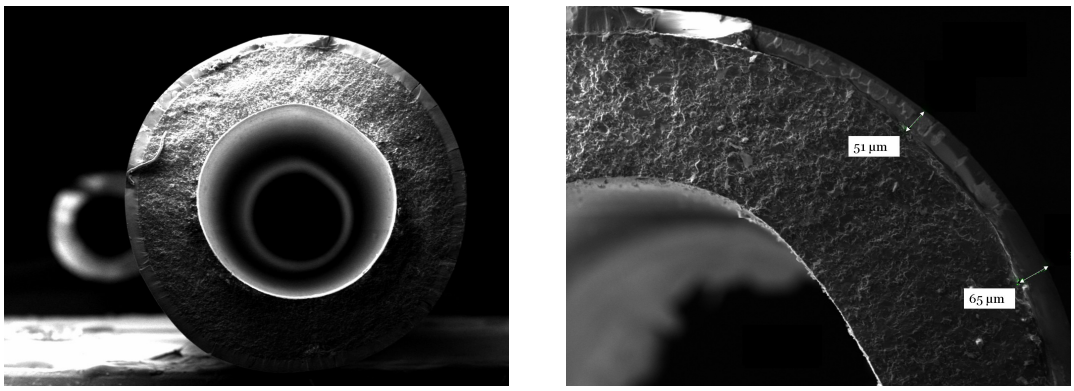

(A) (B)

FIGURE 6.8: SEM images of rod R32 showing (A) the improvement in the quality of the layer in comparison to R25; (B) Variations in depth of the deposited layer.

Rod R34, with its greater number of passes in comparison to R32, was imaged using the ZeScope optical profiler and found to have a surface roughness of approximately 0.5 nm (see fig. 6.9) compared to 30 nm at about 3 cm from end of rod, indicating that high quality layers may nevertheless be fabricated using this technique.

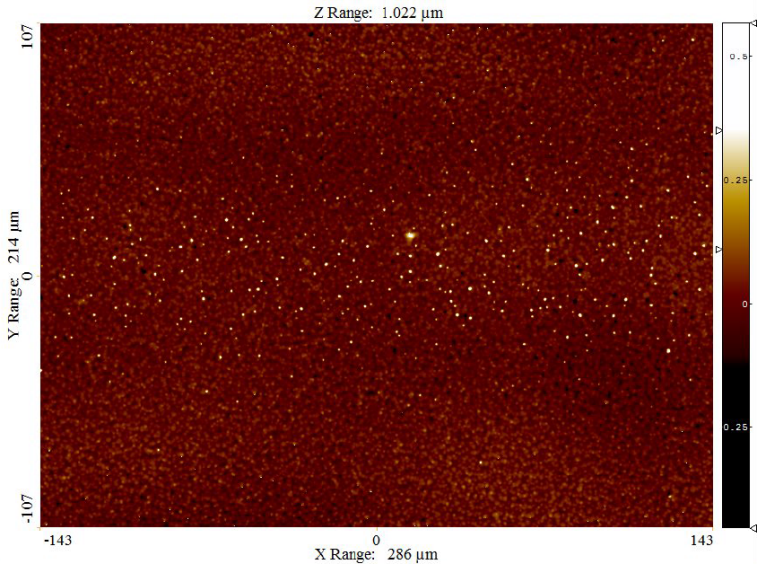

FIGURE 6.9: Zescope image of the surface of rod R34, showing an Sa surface roughness of 0.5 nm.

Some of the boron-doped GeO_2-on-alumina layers were found to be unstable over a period of six months, so further samples were fabricated (see table 6.7), with a reduction in the BCl_3 flow rate, in the hope of avoiding reactions with moisture exacerbated by internal stresses. These new samples showed no obvious change in appearance over a period of several months, and samples R86, R87 and R93 were of sufficient quality for UV writing.

TABLE 6.7: FHD B_2O_2-GeO_2 on 1.5 mm diameter alumina rods at lower BCl_3 flow rates. $GeCl_4/BCl_3$ flow rates were 190 & 15 sccm respectively. †denotes a 2 mm diameter alumina rod; ‡ denotes a 1.35 mm diameter alumina rod.

Dep. no.	**H_2/O_2/Ar flow /l/min**	**Passes (consol.)**	**Consol. flow /l/min**	**Notes**
R44	2.0/1.8/5.0	5	-	Consol. pass unnecessary; smooth.
R45	2.0/1.8/5.0	10	-	Smooth.
R46	2.0/1.8/5.0	10 (1)	3.6/1.8/7.0	Smooth.
R47	2.0/1.8/5.0	5 (1)	4.0/2.0/7.0	Better aligned; smooth.
R48†	2.0/1.8/5.0	6 (1)	4.0/2.0/7.0	Slow rotation; brown discoloration; smooth.
R51‡	2.0/1.8/5.0	5 (1)	4.0/2.0/7.0	Uneven.
R55	2.0/0.8/5.0	8	-	Smooth
R70†	2.0/1.8/5.0	5 (1)	4.0/2.0/7.0	Slow rot; v. uneven; bubbling visible post-deposition.
R72	2.0/1.8/5.0	1	-	Slow rotation; alignment poor; Glassy; cracked on cleaning with acetone/IPA.
R86	2.0/1.8/5.0	10 (1)	3.6/1.8/7.0	Glassy.
R87	2.0/1.8/5.0	5 (1)	4.0/2.0/7.0	Glassy.
R93	2.0/1.8/5.0	5 (2)	-	Glassy.

6.4.4 Direct UV writing of pure GeO_2, SiO_2-GeO_2 & B_2O_3-GeO_2 on alumina layers at 244 nm

Successfully fabricated samples were UV written at 244 nm (see table 6.8) and 213 nm (see table 6.9). A yellow discoloration of the substrate rods where they had been exposed to UV at 244 nm was observed, but no photosensitive refractive index change was seen in any of the germanate on alumina rod samples. The yellowing of the rods may be due to TiO_2 or Fe_2O_3, both of which are often found as impurities in alumina [6]. Photoluminescence was seen in samples R86 and R87 (see fig. 6.10 & 6.11). The photoluminescence was notably absent in hydrogen-loaded samples. Photoluminescence has previously been reported in alumina samples, but has no link to refractive index change [7]. An OVD-fabricated pure GeO_2 rod was provided by another group and UV written for comparison, but with no noticeable response. Different coloured photoluminescence was seen in rod R87 according to the position along the rod from which the sample was taken (see fig. 6.10). Samples taken from the end closest to the spindle showed blue photoluminescence, while those at the opposite end showed purple and red photoluminescence. This implies a change in composition according to distance from the spindle. The extreme end, furthest from

the spindle will certainly be consolidated at higher temperatures due to the flame engulfing the end of the rod.

TABLE 6.8: UV writing of alumina rods at 244 nm results. The GeO_2 rod used was an OVD-fabricated pure GeO_2 rod provided by another group.

Dep. no.	**Sensitization method**	**Outgassing time /min**	**Fluence /kJcm^{-2}**	**Notes**
R22	-	-	8-128	Yellow discoloration.
R24	-	-	8-128	Yellow discoloration.
R25	-	-	15-240	Yellow discoloration.
R26	-	-	15-240	Yellow discoloration.
R34	-	-	8-128	Yellow discoloration.
R79	-	-	8-128	No response.
R86	-	-	12-192	Purple fluorescence; colour varied with distance along rod.
R86	H_2-loaded	6 min.	12-192	No response.
R86	-	-	12-192	White fluorescence.
R87	-	-	8-128	Red-orange fluorescence; colour varied with distance along rod.
R87	H_2-loaded	5 min.	8-128	Dry ice used to reduce rate of outgassing.
R87	-	-	8-128	White fluorescence.
R93	-	-	8-128	No response.
GeO_2	-	-	30-480	No response
GeO_2	H_2-loaded	2 min.	30-480	No response

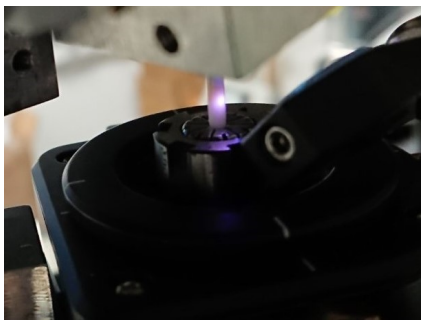

(A)

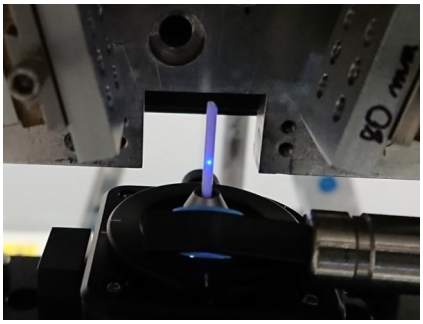

(B)

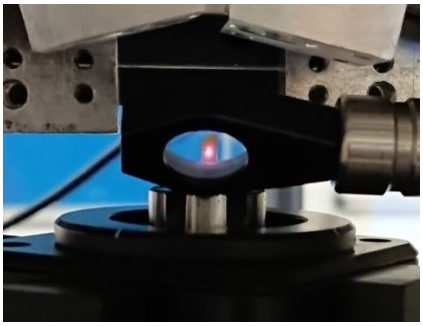

(C)

FIGURE 6.10: Luminescence seen in (A) R86; (B) & (C) R87 during UV writing at 244 nm.

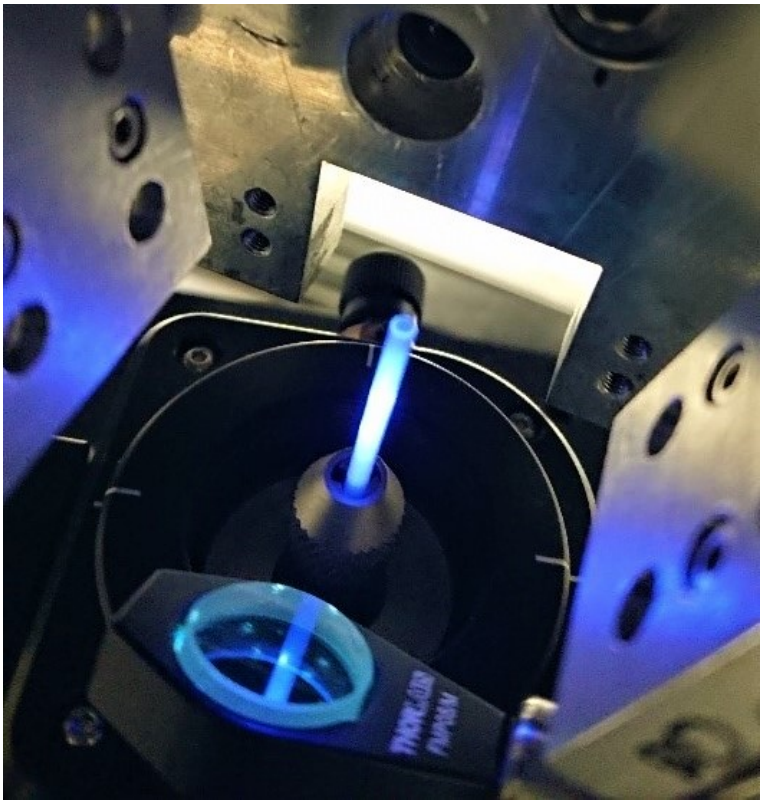

FIGURE 6.11: UV writing of rod R87.

However, the relatively high thermal conductivity (approx. 20 $Wm^{-1}K^{-1}$) of alumina means that the entire rod is kept well above room temperature regardless of the position of the torch on the rod. In short, the different colours observed under UV exposure are likely to be related to temperature differences along the rod resulting in differing thermal history: The red, blue and purple fluorescence indicates at least two different colour centres, one which produces blue fluorescence and one which produces red, with the proportion of each varying with thermal history. The GeE' centre is known to produce faint red fluorescence under 244 nm light. For a full understanding of the mechanisms producing the fluorescence, temperature analysis during deposition, compositional analysis via, for example EPR in order to identify colour centres, and measurement of the wavelength of the emitted fluorescence would be required.

6.4.5 Direct UV writing of pure GeO_2 & B_2O_3-GeO_2 on alumina layers at 213 nm

UV writing of B_2O_3-GeO_2-on-alumina rods R79, R86, R87 and R93 and a pure GeO_2 rod fabricated by another group by OVD, was attempted at 213 nm at fluences of 0.05, 0.1, 0.5, 1 and 5 $kJcm^{-2}$ (see table 6.9) but samples showed ablation even at the lowest fluences. White fluorescence was also observed in R86 and R87, although this was less intense than the coloured fluorescence seen in the same samples at 244 nm. A bare silica rod was also UV written at 213 nm for comparison and no photosensitivity or ablation was seen.

TABLE 6.9: UV writing of FHD rods at 213 nm results. The GeO_2 rod used was an OVD-fabricated pure GeO_2 sample provided by another group. Power was 1 mW for all samples.

Dep. no.	Sensitization method	Outgassing time /min	Fluence /$kJcm^{-2}$	Notes
R79	-	-	0.05-5	Ablation.
R86	-	-	0.05-5	White fluorescence; ablation.
R87	-	-	0.05-5	White fluorescence; ablation.
R93	-	-	0.05-5	Ablation.
GeO_2	-	-	0.05-5	Ablation.
GeO_2	H_2-loaded	5 min.	0.05-5	No response.
SiO_2	-	-	0.05-5	No response.
SiO_2	H_2-loaded	5 min.	0.05-5	No response.

6.4.6 Annealing of germanate glass on alumina rod samples

UV writing at a range of fluences from 4-128 $kJcm^{-2}$ at 244 nm and 0.5-5 $kJcm^{-2}$ at 1 mW at 213 nm showed no waveguides in the samples fabricated thus far. Literature suggests that annealing in a 20:1 N_2:H_2 atmosphere dramatically improves photosensitivity in high germania content/pure germania samples [6]. GeO_2-B_2O_3 deposited rods were fabricated under the conditions in table 6.10. Rod R79 was placed in a tube furnace with 20:1 ratio of N_2:H_2 and annealed for 2 hours at 500 °C. However, there was no response under 244 nm UV exposure, and it was suspected that the presence of boron in the sample may have reduced the photosensitivity by

annealing out oxygen deficient centres [8] and the H_2 content was too low to have an appreciable effect on photosensitivity.

TABLE 6.10: B_2O_3-SiO_2-GeO_2 on 1.5 mm alumina rods for subsequent annealing. †denotes a 2 mm rod.

Dep. no.	**H_2/O_2/Ar flow /l/min**	**$GeCl_4$/ BCl_3 flow /sccm**	**Passes (consol.)**	**Consol. flow /l/min**	**Notes**
R79	1.6/0.8/5.0	190/4	10 (1)	3.6/1.8/7.0	Warm-up pass improved smoothness.
R80†	1.6/0.8/5.0	190/30	5 (1)	4.0/2.0/7.0	OK.
R81†	2.0/1.8/5.0	190/30	6 (1)	4.0/2.0/7.0	OK.

A second, similar sample from rod R79 was annealed in a hydrogen only atmosphere and UV written. EDX analysis showed that the surface was almost exclusively germanium with very small amounts (a few percent) of oxygen. This is evident in fig. 6.12, where the left hand side, which has been deposited, shows a metallic appearance.

FIGURE 6.12: Rod R79 after annealing at 500 °C in a hydrogen-only atmosphere.

UV writing of R79, annealed in 100% H_2, showed clear areas of ablation at a range of fluences from 4, 8, 16, 32, 64 & 128 kJcm^{-2} (see table 6.11), albeit with less ablation at lower fluences (see fig. 6.13).

TABLE 6.11: UV writing of annealed rods at 244 nm results.

Dep. no.	**% H_2**	**Fluence /kJcm^{-2}**	**Notes**
R79	100	12-192	Ablation.
R86	20	12-192	No response.
R87	10	8-128	No response.

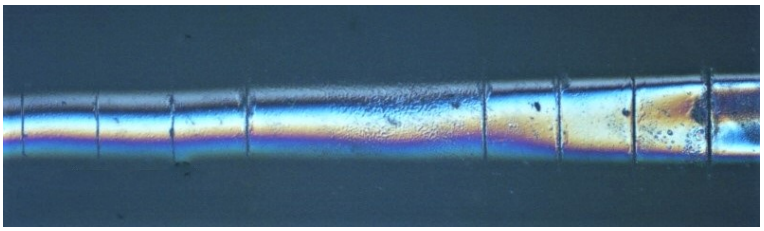

FIGURE 6.13: Ablation on annealed rod R79 as a result of UV writing at 244 nm. Ablated waveguides are spaced 0.25 mm apart.

This suggests that there is photosensitivity (though not necessarily refractive index change, and what defects, if any exist, cannot be inferred) but that the pure hydrogen atmosphere primarily has the effect of reducing the germania to germanium rather than forming oxygen vacancies in significant numbers. The sample was imaged using the SEM and the ablations were confirmed to be trenches rather than simply changes in appearance in response to UV exposure (see fig. 6.14).
An intermediate H_2 content of 20% was used on another sample, R86, which resulted in reduction once again. The H_2 percentage was further lowered to 10%, and sample R87, fabricated under similar conditions to R79 and R86 was annealed. This sample showed little change in appearance after annealing but no apparent improvement in photosensitive response. The same three samples were tested at 213 nm, with no response (see table 6.12).

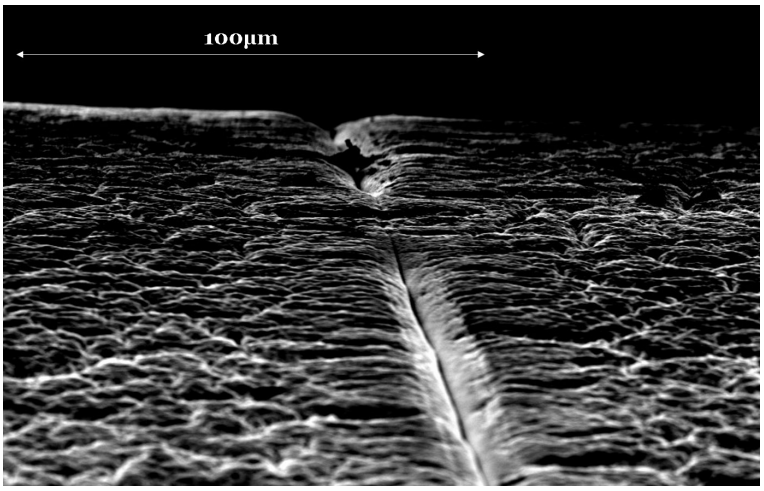

FIGURE 6.14: SEM image of one of the areas of ablation shown in fig. 6.13 indicating removal or compaction of material where exposed.

TABLE 6.12: UV writing of annealed rods at 213 nm results.

Dep. no.	**% H_2**	**Power** mW	**Fluence /kJcm^{-2}**	**Notes**
R79	100	0.3	0.05-5	Ablated “waveguides”.
R87	10	0.3	0.05-5	No response.
R86	20	1	0.05-5	No response.

In summary, stable SiO_2-GeO_2 and pure GeO_2 layers were successfully deposited onto alumina rods and tubes, although the concentricity and quality of the surface

was relatively poor. This was improved by the addition of B_2O_3. No refractive index change was seen in these layers at 244 nm or 213 nm. Discoloration of the samples where UV-exposed was noted and likely to be attributable to impurities such as oxides of Ti and Fe. Photoluminescence of various colours was seen in several of the alumina rods at 244 nm, the colour being dependent on which part of the rod the sample was taken from, i.e. its proximity to the spindle during deposition and consolidation, indicating a longitudinal difference in composition due to differing thermal history during deposition. Annealing of samples in an H_2-N_2 atmosphere resulted in reduction of GeO_2 to Ge at 20% and above and ablation under 244 nm UV exposure. No refractive index change was seen at 10% on UV exposure.

6.5 FHD and direct UV writing of germanate on sapphire rods

6.5.1 FHD of B_2O_3-GeO_2 on sapphire rods

Sapphire rods were deposited with B_2O_3-GeO_2 at low torch flow rates in comparison to alumina rods previously deposited and consolidated at higher flow rates as per the previously fabricated alumina rods. However, the surface of these samples was rough as the rods were provided ground rather than polished (see fig. 6.15).

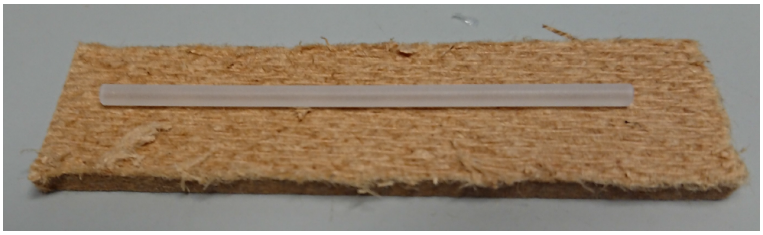

FIGURE 6.15: A bare sapphire rod.

Deposition did not result in transparent layers, resulting in a ridged appearance if temperatures were high (e.g. such that the rod glowed during deposition) and incomplete consolidation if too low. Intermediate flow rates which resulted in even consolidated layers could not be found. A pass at $H_2/O_2/Ar$ flow rates of 5.0/5.0/8.0 sccm was used to soften and reflow the surface of a sapphire rod such that it became smooth and transparent. A layer was subsequently deposited on to R50 and consolidated (see table 6.13), and appeared to be of good quality (see fig. 6.16) and no deterioration was seen over a period of a year. This method was used for all subsequent sapphire samples.

TABLE 6.13: Deposition of B_2O_3-GeO_2 on 2mm diameter sapphire rods.

Dep. no.	**$H_2/O_2/Ar$ flow rate /l/min**	**$GeCl_4/BCl_3$ flow /sccm**	**Passes (consol.)**	**Consol. flow /l/min**	**Notes**
R50	2.0/1.8/5.0	190/15	5 (1)	4.0/2.0/7.0	Consol. pass improved poor surface quality.
R89†	2.0/1.8/5.0	190/15	5 (1)	4.0/2.0/7.0	OK.
R90†	2.0/1.8/5.0	190/15	5 (1)	4.0/2.0/7.0	OK.
R91†	2.0/1.8/5.0	190/30	6 (1)	4.0/2.0/7.0	OK.
R92†	2.0/1.8/5.0	190/30	5 (1)	4.0/2.0/7.0	V. good quality.
R94	2.0/1.8/5.0	190/15	5 (1)	3.6/1.8/7.0	V. good quality.

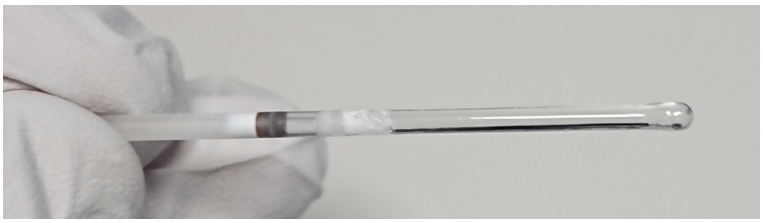

FIGURE 6.16: Sapphire rod R92 after deposition. The white band is unconsolidated soot, the brown band is likely to be iron from the spindle. Note the rounding of the end, which is likely to be due to the raised temperature as the end is engulfed by the torch.

6.5.2 Direct UV writing of B_2O_3-GeO_2 on sapphire rods at 244 nm & 213 nm

UV writing was attempted on the samples described in the previous section at both 244 nm (see table 6.14) and 213 nm (see table 6.15).

TABLE 6.14: UV writing of sapphire rods at 244 nm results.

Dep. no.	**Sensitization method**	**Outgas. time /min**	**Fluence /kJcm^{-2}**	**Notes**
R50	-	-	8-128	No response.
R50	H_2	2 min.	8-128	No response.
R89	-	-	8-128	No response.
R92	-	-	8-128	UV beam coupled into rod.
R94	-	-	8-500	UV beam coupled into rod.
R94	H_2	7 min.	8-500	Dry ice used to reduce rate of outgassing; no response.

At 244 nm the UV beam was seen to couple into the rod (see fig. 6.17). Samples were also UV written at 213 nm at 0.5 mW at fluences of 0.1, 0.5, 1 and 5 kJcm^{-2} and a similar effect was seen. However, no UV-induced refractive index change was seen at any of the fluences attempted. An attempt to couple 633 nm light in to the rod using a tapered fibre was unsuccessful, which is likely to be due to the large difference in refractive index between the rod and the taper preventing all but higher order modes from coupling. However, the clear ability to couple in seen during UV writing, indicative of a high quality deposited layer, made it an ideal sample to try CO_2 laser machining (see chapter 7).

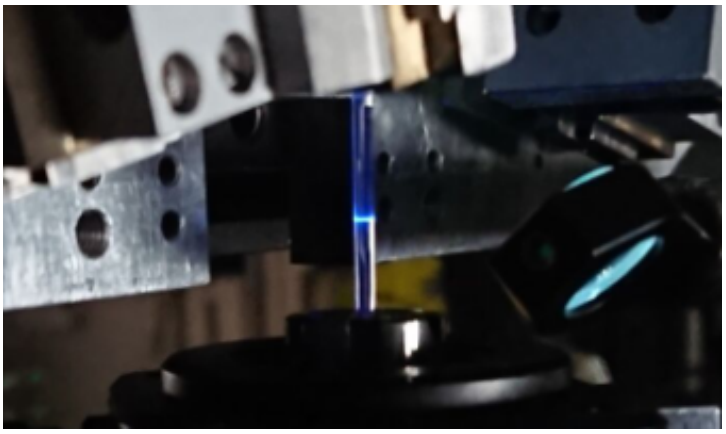

FIGURE 6.17: Sapphire rod R92 undergoing UV writing at 244 nm, with apparent coupling of the beam into the core layer.

TABLE 6.15: UV writing of sapphire rods at 213 nm results.

Dep. no.	**Sensitization method**	**Outgas. time /min**	**Power mW**	**Fluence /kJcm^{-2}**	**Notes**
R89	-	-	0.5	0.1-5	No response.
R92	-	-	0.5	0.1-5	UV beam coupled into rod.
R94	-	-	0.5	0.1-5	UV beam coupled into rod.

To summarise, stable GeO_2 layers were deposited on to sapphire rods. Reflow of the sapphire rods using a high temperature pass before deposition was necessary in order to produce a smooth surface. No UV-induced index change or fluorescence was seen in these samples. The UV beam was seen to couple into the rod, showing promise of producing ring resonators using these samples, one of which was subsequently CO_2 laser machined at NPL.

6.6 Fabrication & direct UV writing of diffused GeO_2-SiO_2 rods

Due to the deterioration of some B_2O_3-GeO_2 on alumina rods, it was decided that a diffused rod GeO_2-SiO_2 might be a better choice due to the stability seen in diffused planar samples NB160-1 & NB160-2. GeO_2 soot was deposited at relatively low flow rates and placed in the holder shown in fig. 6.18 for furnace consolidation.

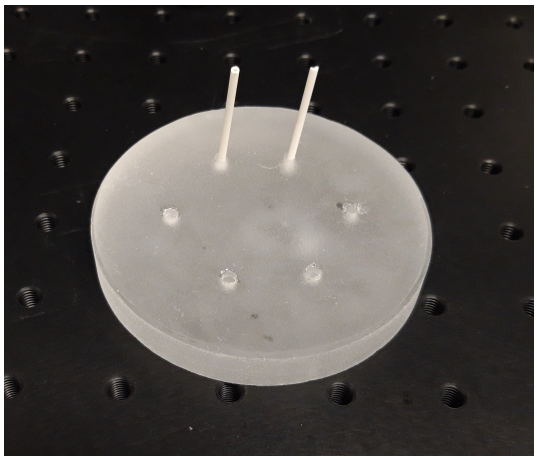

FIGURE 6.18: Fused silica rod holder for furnace consolidation.

Consolidation appeared successful, but no UV-induced refractive index change or fluorescence was seen at 244 nm at fluences of 12, 24, 48, 96 and 192 $kJcm^{-2}$ or 213 nm at 1mW and fluences of 0.1, 0.5, 1 and 5 $kJcm^{-2}$. This sample was subsequently chosen for CO_2 laser machining at NPL, as described in chapter 7.

6.7 Conclusions

Novel FHD-based fabrication of rod samples has been described, along with the adaptation of the FHD system required to achieve this. A number of different combinations have been deposited on to silica, alumina and sapphire rods, with sufficient quality for UV writing or CO_2 laser-machining. Adaptation of the UV writing system in order to accommodate rods has been described. The effect of annealing has been briefly, if not exhaustively investigated.

Phosphorus-doped glass was successfully deposited on to silica rods, but cracking was seen in many of the samples, attributed to the CTE mismatch. An increase in torch flow rates and hence temperature resulted in apparently stable samples of around 2 μm. These samples were not found to undergo refractive index change under UV exposure at 244 nm, although a yellow glow, perhaps attributable to impurities was seen. Hydrogen loaded samples showed no photoluminescence or refractive index change.

SiO_2-GeO_2 samples were successfully deposited on to alumina rods and tubes. Initially, deposited layers were uneven, and lacked concentricity. The addition of boron to samples aided the quality of the deposition, making samples more even and with good surface roughness and allowed cooler torch temperatures. Both SiO_2-GeO_2 and B_2O_3-SiO_2-GeO_2 samples showed yellow to brown discoloration, depending on the fluence of the UV exposure. Non-hydrogen loaded samples showed fluorescence of various colours, dependent upon the position along the rod the sample was taken from, with red fluorescence seen in those furthest from the spindle during deposition. The origin of red photoluminescence is often attributed to the GeE' defect, a product of the NOMV one photon reaction, but no obvious explanation for other colours can be gleaned from the literature to the best of the author's knowledge. These samples were of sufficient quality for CO_2 laser-machining.

B_2O_3-SiO_2-GeO_2 samples were annealed in a H_2:N_2 atmosphere with the intention of increasing UV-induced refractive index change. High H_2 percentages (100% to 20%) resulted in reduction of germania to germanium. 10% hydrogen resulted in a lack of both refractive index change and luminescence.

The use of sapphire rods instead of alumina produced smooth samples provided the rod was first heated by the FHD torch at high temperature without deposition in order to reflow the outside of the rod. These rods could then be deposited using the same recipes as for alumina rods. These rods were found to guide UV light when the beam was directed on to them in order to UV write, but were not found to be photosensitive. They were, however, of sufficient quality for CO_2 laser-machining.

Diffused GeO_2-SiO_2 rods were produced by depositing soot on to a silica rod and consolidating in the furnace. This produced a rod which although not photosensitive, was of sufficient quality for CO_2 laser-machining.

The fabrication of UV photosensitive planar sapphire (described in the previous chapter) at both 213 nm and 244 nm, combined with photoluminescence in alumina rod samples under UV exposure gives hope of producing photosensitive rods for UV writing. This work provides a starting point for further development of the novel deposition and direct UV writing technique. CO_2 laser-machining of the high

quality rods produced here is described in the following chapter.

6.8 Bibliography

[1] P. Del'Haye, T. Herr, E. Gavartin, M. L. Gorodetsky, R. Holzwarth & T. J. Kippenberg, "Octave Spanning Tunable Frequency Comb from a Microresonator", *Phys. Rev. Lett.*, (107): 063901, 2011.

[2] R. F. Cuevas, E. Gusken, E.H. Sekiya, D. Y. Ogata, D. Torikai, C. K. Suzuki,"Effect of H_2/O_2 ratio on the GeO_2 concentration profile in SiO_2:GeO_2 glass preforms prepared by vapor-phase axial deposition", *J. Non-Crys. Solids* 273: 252-256, 2000.

[3] M. Kawachi, S. Sudo, N. Shibata & T. Edahiro, "Deposition Properies of GeO_2-SiO_2 in the Flame Hydrolysis Reaction for Optical Fiber Fabrication", *Japanese J. Appl. Phys.*, 19 (2): L69-L71, 1980.

[4] https://global.kyocera.com/prdct/fc/list/tokusei/bouchou/index.html (Accessed 25.05.2020)

[5] V. Mazurin, M. V. Streltsina & T. P. Shvaiko-Shvaikovskaya, "Handbook of Glass Data Part B: Single Component & Binary Non-silicate Oxide Glasses", Elsevier ISBN 0-444-42484-9

[6] C. Jing, J. Hou, Y. Zhang & X. Xu, "UV-light induced luminescence processes in Al_2O_3 bulk and nanosize powders", *J. Non-Crys. Solids* 353: 4128–4136, 2007.

[7] L. Trinkler, B. Berzina, D. Jakimovica, J. Grabis, I. Steins, "Preparation of thick, crack-free germanosilicate glass films by polyvinylpyrrolidone and study of the UV-bleachable absorption band", *Optical Materials* 32: 789–7957, 2010.

[8] A. Margaryan & M. Piliavin, "Germanate Glasses", Artech House, 1993.

Chapter 7

Optical characterisation of germanate rod & ring resonators

7.1 Introduction

Tapered fibre coupling has long been used for coupling of WGM resonators, and perfected by the Vahala group at Caltech amongst others [1]. Work by Del'Haye's group at NPL has resulted in some of the highest Q factors reported [2]. Resonators have been machined using a CO_2 laser on a variety of diameters of high-purity silica rods (see fig. 7.1).

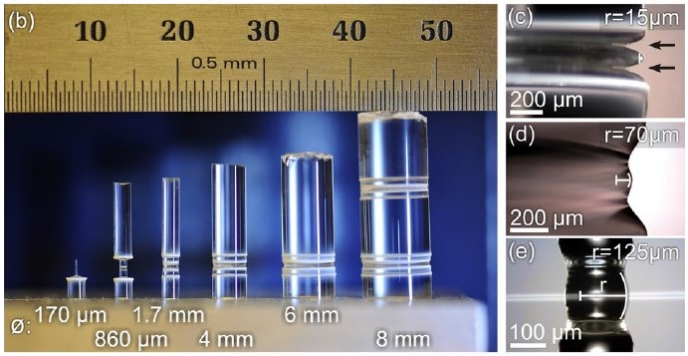

FIGURE 7.1: Laser machined rods fabricated at NPL, from Del'Haye et al. [2].

Nonlinear processes such as Raman scattering, Brioullin scattering and four-wave mixing leading to frequency comb spectra have been demonstrated using these devices [2]. As an alternative to UV written rods, the possibility of using the same techniques on germanate glass rods was explored. Having successfully deposited FHD germanate glass onto silica and sapphire rods and in the hope of successful UV writing of rod samples, a characterisation set-up was required. Prior to fabrication, in order to better understand coupling, tapered fibres were coupled to silica spheres. This provided a useful set-up for characterisation of planar milled ring resonators. A ring resonator chip fabricated using LPCVD and RIE by Ma's group at Zheijiang University was characterised, providing a useful characterisation set-up.

Finally, having established that photosensitivity of rods was proving difficult, an alternative approach, in collaboration with Pascal Del'Haye's group at NPL, was found. FHD fabricated rods were machined using a CO_2 laser and characterised at both NPL and Southampton. The work in this section was carried out at the end of my PhD and was a way of exploring other methods of fabrication of resonator structures in the light of difficulties caused by the material.

7.2 Characterisation of glass spheres and planar resonators

7.2.1 Modes in a glass sphere and tapered fibre

In order to produce a characterisation set-up for planar ring resonators, a set-up was first constructed for glass spheres for later adaptation. Light from a broadband source was coupled into a 3 mm diameter glass sphere via a 20 μm diameter tapered fibre fabricated using the Fujikura LZM-100 CO_2 laser splicer on SMF28[1]. This was bent into a "U" shape in order to aid evanescent coupling and mounted on a translation stage in order to vary the coupling distance. Adjustment of the coupling position was aided by the use of a microscope and 633 nm diode laser in order to maximise the depth of the resonances, before connection to a broadband source (Agilent 81950A). An optical spectrum analyser (OSA; Yokogawa AQ6370D-12) was used to measure the spectral response in the range 1549-1551 nm (see fig. 7.2 (A)). The Fourier transform results, shown in fig. 7.2 (B), were windowed using a Hamming function.

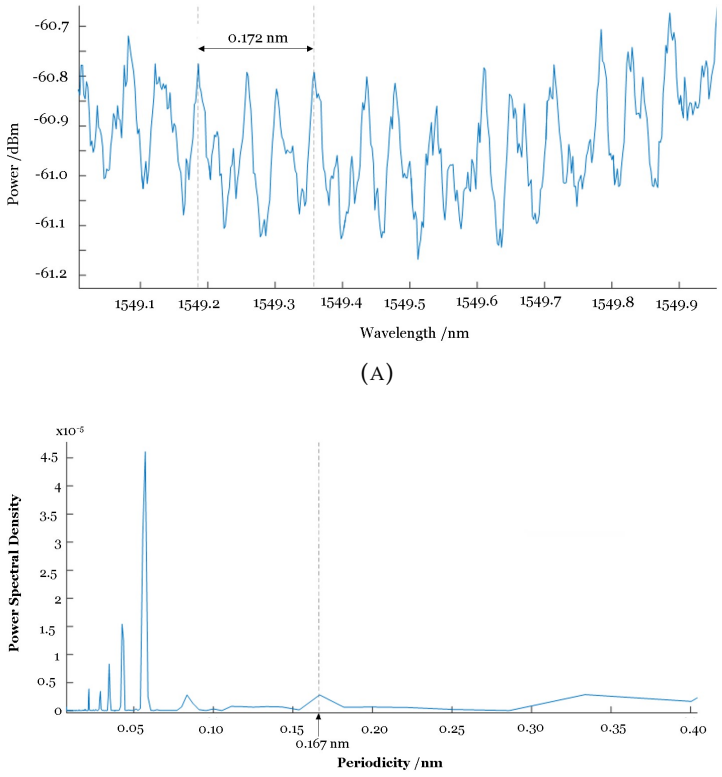

FIGURE 7.2: Glass sphere spectra (A) and Fourier transform (B) 20 μm taper.

The results were compared to a previous experiment using a similar set up with a 6 μm tapered fibre fabricated by another group in the ORC, coupled into the same glass sphere and the spectral response recorded over the range 1551-1554 nm (see fig. 7.3). For the larger taper, λ=1549.5 nm, sphere radius, r=1.5 mm, effective refractive index, n_{eff}=1.444, the FSR was calculated to be 0.176 nm. For the smaller taper,

[1]Tapers of 8-10 μm were later fabricated in this work using this system, although they often required multiple unsuccessful attempts, and their lack of consistent quality precluded their use in these experiments.

λ=1552.5 nm, i.e. taking into account chromatic dispersion, the FSR was calculated to be 0.177 nm. FSR was found to be 0.167 nm using the Fourier transform for the larger taper and 0.188 nm for the smaller taper.

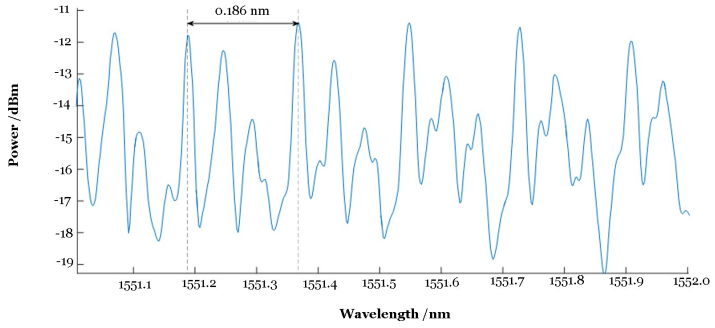

(A)

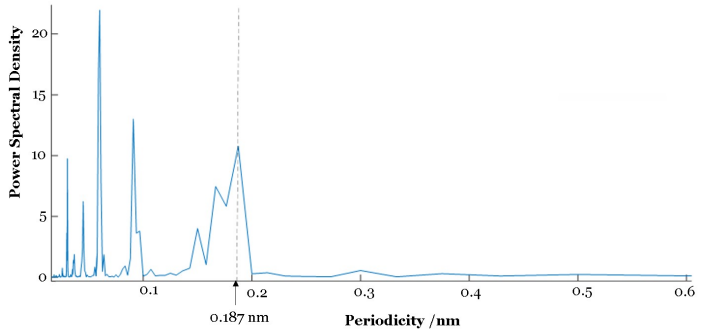

(B)

FIGURE 7.3: Glass sphere spectra (A) and Fourier transform (B) 6 μm taper.

The latter showed more efficient coupling. The poor radial confinement (in comparison to planar ring resonators) of the relatively large spheres resulted in multi-mode resonances. In summary, a useful set-up for characterisation of ring resonators was produced, and the use of tapered fibres using the laser splicer deemed successful, despite the present inability of the system to produce small tapers of 2 μm and below as are usually used in experiment of this type. It is noted that the maximum observable Q is limited by the OSA's resolution, which in this case was 2 pm, giving a maximum observable Q of 7.75×10^4. It is therefore possible that high Q modes are being missed due to insufficient resolution.

7.2.2 Milled and Damascene ring structures

Milling a ring into a silica substrate and filling it with GeO_2 to produce a Damascene ring resonator has the advantage in comparison to etching that sharp changes in index are avoided due to diffusion during consolidation in the furnace. This results in less scattering due to the gradual change in refractive index and the lack of a distinct sidewall. An early attempt to fabricate a damascene ring resonator structure similar to the one described [5] consisted of using an ultra-precision milling machine with the tool shown in fig. 7.4 to produce a Damascene ring.

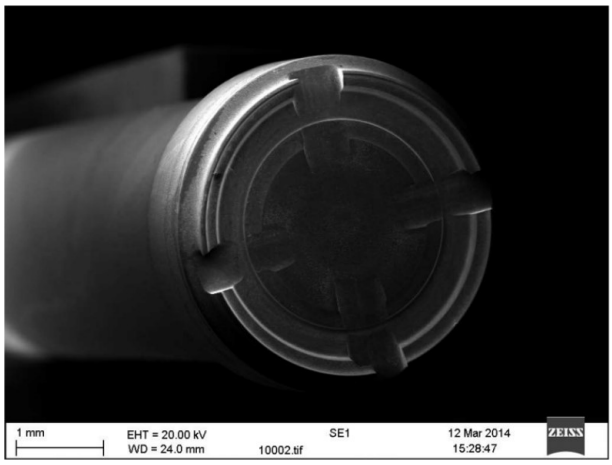

FIGURE 7.4: SEM image of diamond tool used to mill 3 mm diameter ring resonator structures. (picture credit: P. A. Cooper).

Rings of 2.5 mm diameter and 50 μm width were milled into 10×20 mm silica-on-silicon chips. These were then deposited onto with germania soot and consolidated as per the fabrication of planar wafers described in earlier chapters. Levelling of the platform on which the rings were milled such that it was perpendicular to the spindle was insufficiently accurate, resulting in rings positioned at a slight angle to the surface with varying depth around their circumference. At the extreme, the rings were incomplete circles, and the non-uniformity was visible with the naked eye (see fig. 7.5).

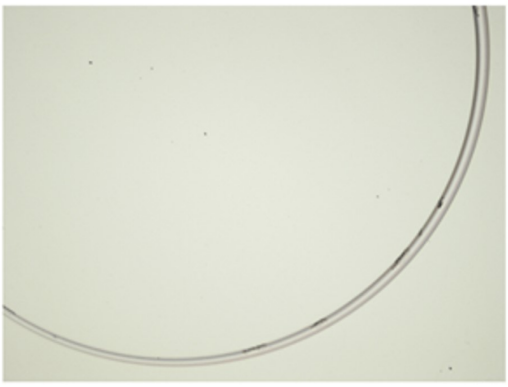

FIGURE 7.5: Microscope image of milled resonator on silica substrate fabricated using the tool pictured in fig. 7.4 demonstrating the uneven width of milled rings due to inadequate levelling of the milling platform.

The surface of the ring resonator structure was investigated using a ZeScope optical profiler. These data showed that the depth of the germania layer in the ring was found to vary with position around the ring by as much as 6 μm, in even the most uniform. Deposition of soot and reflow was problematic as soot was preferentially deposited on the outer side of the trench (see fig. 7.6) and reflow was minimal.

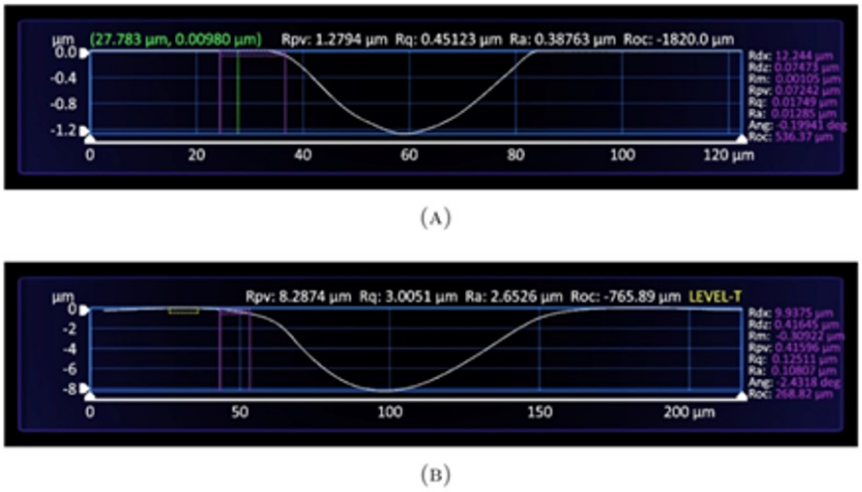

FIGURE 7.6: Zescope measurements of a ring (A) Before deposition and (B) After deposition of GeO_2 and consolidation. The asymmetry in (B) demonstrates the uneven deposition of the soot, and therefore glass post-consolidation.

The uneven deposition of soot was exacerbated by the non-uniform ring depth. Adaptations to the milling system were not practical within the time limits of this work, and levelling the milling platform using shims under the corners did not adequately solve this problem and lacked repeatability. The most uniform ring was selected for GeO_2 deposition and characterisation in order to determine the effect of its non-concentricity on its spectrum. The ring was deposited with germania and consolidated at 1200 °C (pictured in fig. 7.7).

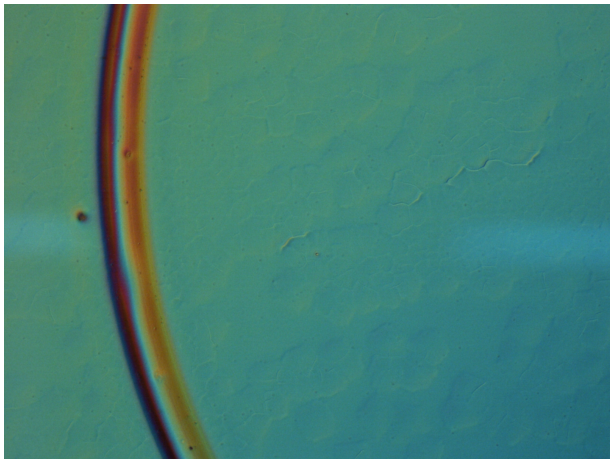

FIGURE 7.7: Microscope image of milled resonator fabricated using the tool pictured in fig. 7.4 and deposited with a layer of GeO_2.

Using a similar set up to that used for investigating coupling into the glass sphere, light from a broadband source was coupled into the damascene ring resonator structure using a 20 μm tapered fibre. The ring resonator chip was mounted on an angled translation stage for easy coupling and the spectral response measured using an OSA. Multiple measurements were taken with the taper in the same position, in order to ascertain whether the resonance dips coincided (see figs. 7.8 and its Fourier transform in fig. 7.9). Measurements were also taken with the taper uncoupled to

the ring and with the taper placed at the centre of the ring for comparison (for which a Fourier transform can be seen in fig. 7.10 and 7.11 respectively) and at multiple different resolutions, in order to determine if features seen on the spectra were in fact part of the spectrum or noise-related. Once again, it is noted that high Q modes could be missed due to insufficient resolution of the OSA.

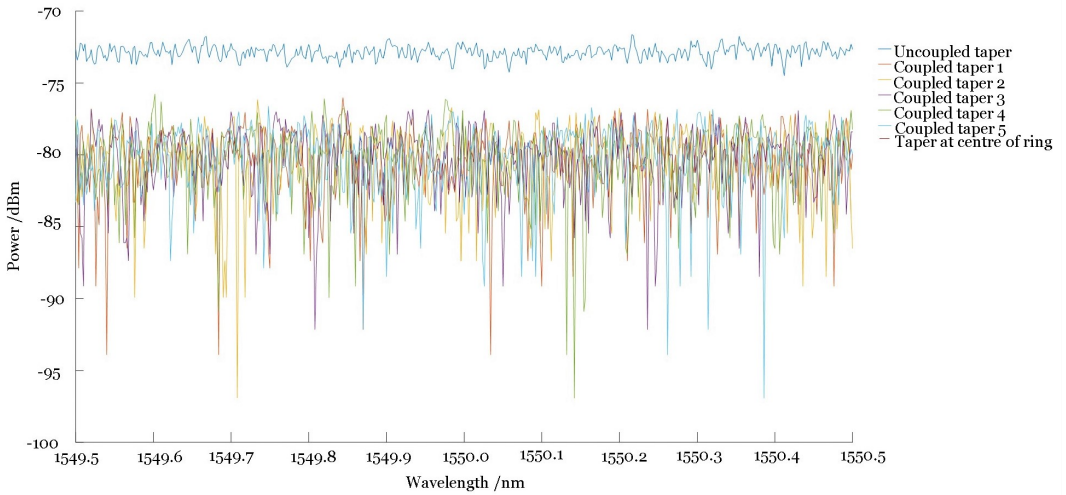

FIGURE 7.8: Damascene ring spectra for the ring pictured in fig. 7.7.

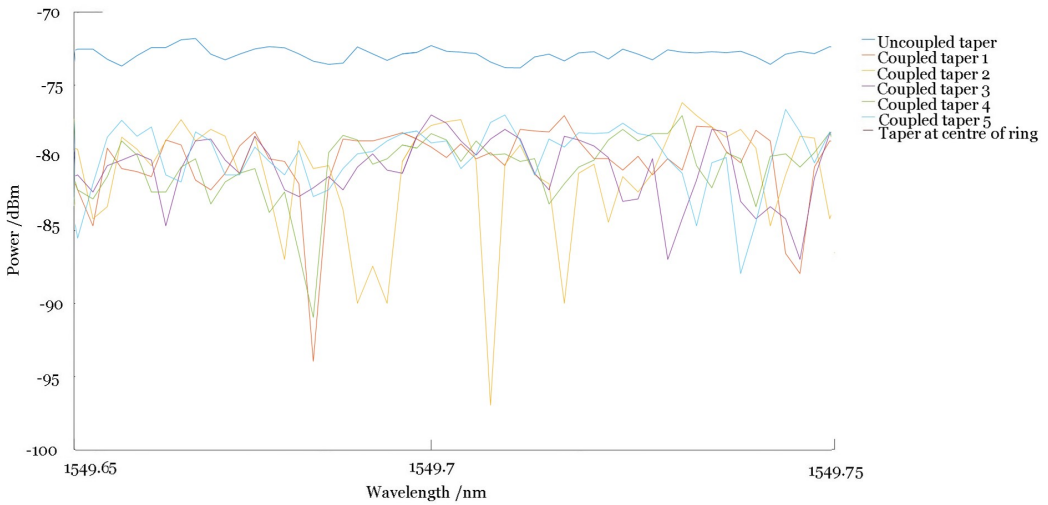

FIGURE 7.9: Close-up of Damascene ring spectra for the ring pictured in fig. 7.7, showing a lack of coincidence of resonances.

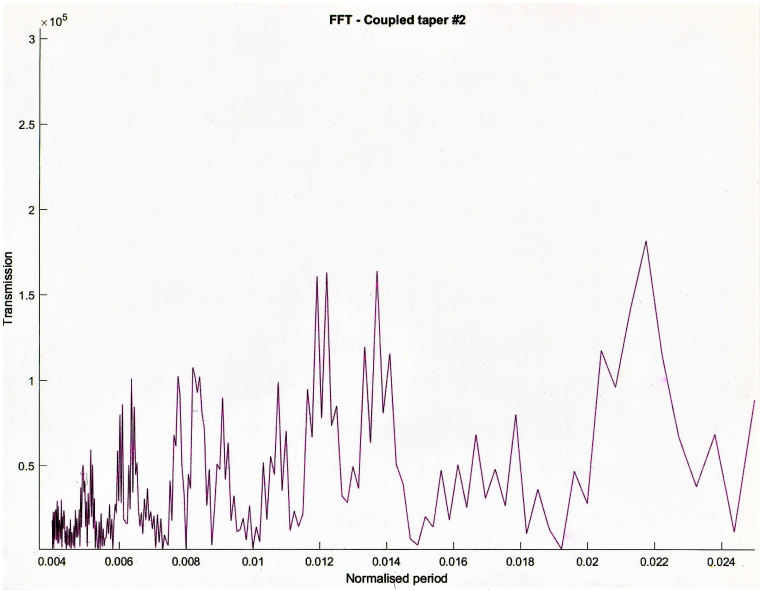

FIGURE 7.10: Damascene ring Fourier transform for the ring pictured in fig. 7.7.

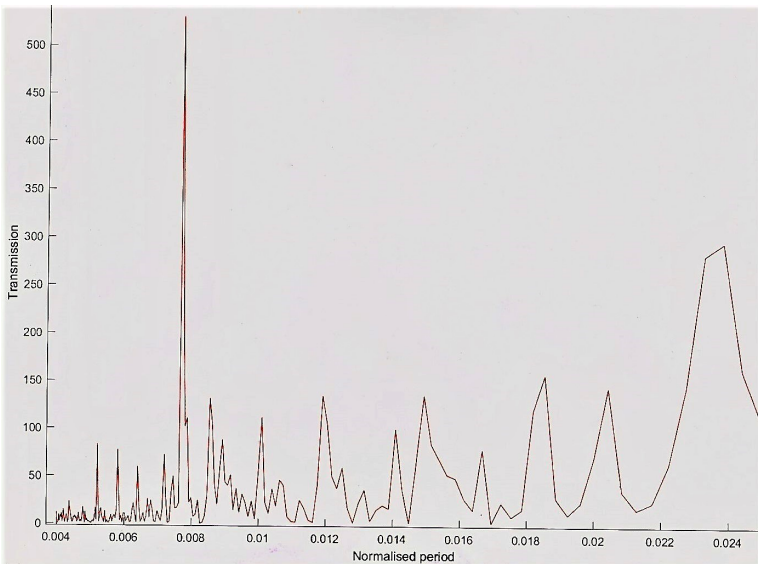

FIGURE 7.11: Fourier transform for an uncoupled tapered fibre.

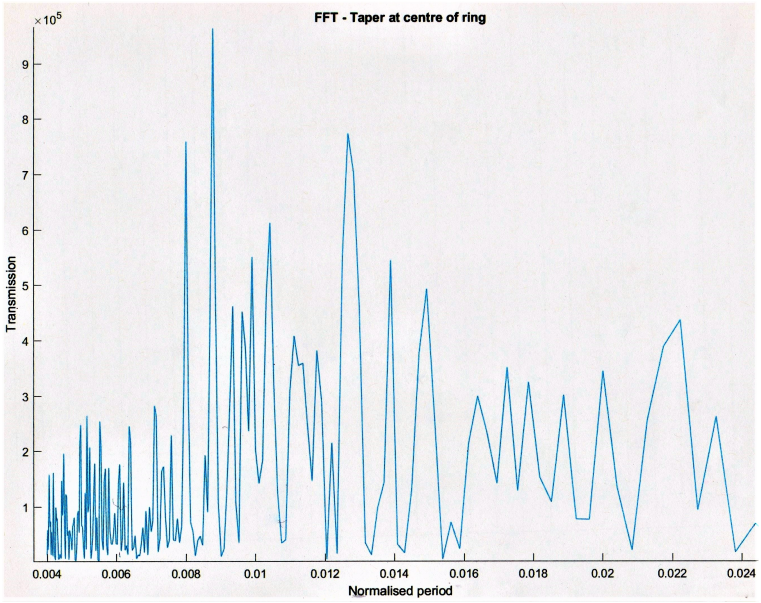

FIGURE 7.12: Damascene ring Fourier transform for the ring pictured in fig. 7.7, with the tapered fibre placed at the centre of the ring.

It can be seen from the spectrum in fig. 7.8 that apparent resonances of repeat measurements do not coincide, suggesting that these are not resonances. However, the stark difference in spectral response when the taper was not in proximity to the ring resonator structure compared with when "coupled" suggests that there is some interaction of the light with the material (reflection, absorption due to defects), if not the ring itself. A Fourier transform was used to compare the FSR of data sets (see fig. 7.9). When the taper was placed at the centre of the ring, response seen was similar to when coupled, but "resonances" seen on the spectrum did not appear to align with any previous data sets. For λ=1550 nm, r=1.25 mm, n_{eff}=1.605, FSR was calculated to be 0.191 nm, but the Fourier transform does not appear to show any such periodicity. It is noted that while attempts were made to avoid movement of the taper using a plastic cover to shield it from air currents, some movement of was inevitable and the unevenness of the ring further exacerbated the difficulties of consistent coupling conditions. It cannot therefore not be ruled out that the structure is acting as a ring resonator, and further investigation at higher resolutions and with better minimisation of air currents, e.g. boxing equipment in, would be helpful in drawing conclusions in this regard.

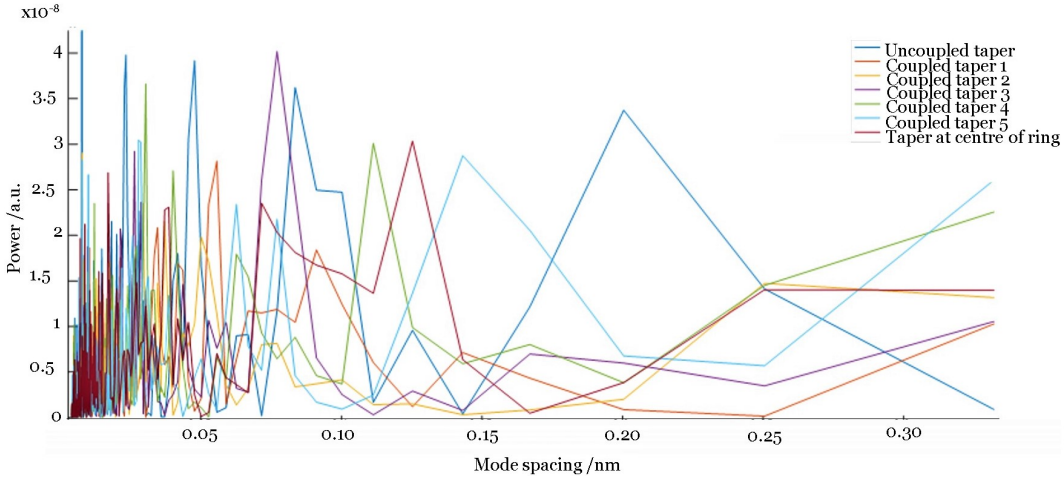

FIGURE 7.13: Damascene ring Fourier transforms for the ring pictured in fig. 7.7.

Ultimately this approach was considered to be extremely challenging and time-consuming with the present milling machine due to the inability to level the platform in order for the ring to have uniform depth. Uniform deposition was also extremely difficult, due to the method of deposition and uneven geometry of the milled ring. Coupling into the device fabricated via a tapered fibre was difficult and the spectra produced appeared pseudo-periodic, as confirmed by Fourier transforms which show components at irregularly spaced intervals, in contrast to silica spheres characterised earlier. For this reason it was decided that direct UV writing was more likely to result in successful fabrication and characterisation of a ring resonator (Fabrication of Damascene resonator structures were investigated at the beginning of this work, at which point the difficulties of fabricating a photosensitive layer could not be foreseen), the development of a suitable material for which having been described in chapters 5 and 6.

7.2.3 Characterisation of a racetrack resonator gyroscope chip

As part of a collaboration with Prof. Huilian Ma's group at Zheijiang University, a ring resonator gyroscope chip was received for an investigation into its suitability for UV writing. The silica waveguide racetrack resonator chip was fabricated on a silicon substrate using LPCVD and RIE at Zheijiang University as described in [6] was sent to the group in order to verify their FSR and finesse measurements and allow real-time monitoring of UV writing of tilted Bragg gratings. This gave an opportunity to produce a useful set up for future characterisation of planar ring resonator chips (see fig. 7.13).

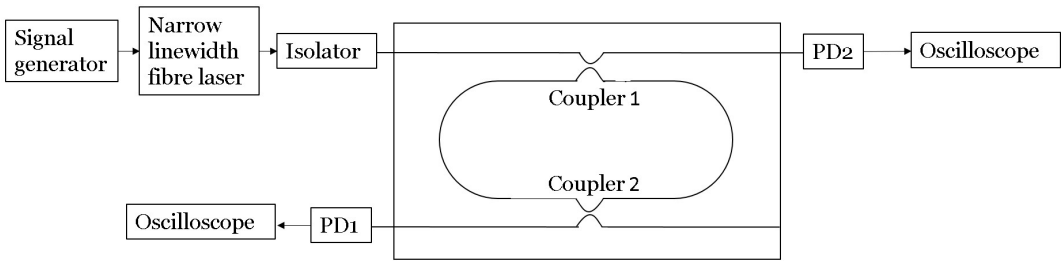

FIGURE 7.14: Temporal finesse characterisation set-up for racetrack ring resonator, based on the one described in [2].

A 30 kHz linewidth fibre laser source with a central wavelength of 1546.92 nm (The Rock RFLM-25-3-1546.92-0-005) was thermally tuned over a bandwidth of around 150 MHz and ramped approximately linearly through the range over a period of 100 s by changing temp by around 5 °C[2]. The FSR and FWHM were then measured temporally (see fig. 7.14) using an oscilloscope, in contrast to the previously described method using an OSA in order to calculate the finesse and Q for both transmission and reflection spectra in the frequency domain [3]. The length of the racetrack was 17.7 cm, with a diameter of 5.63 cm.

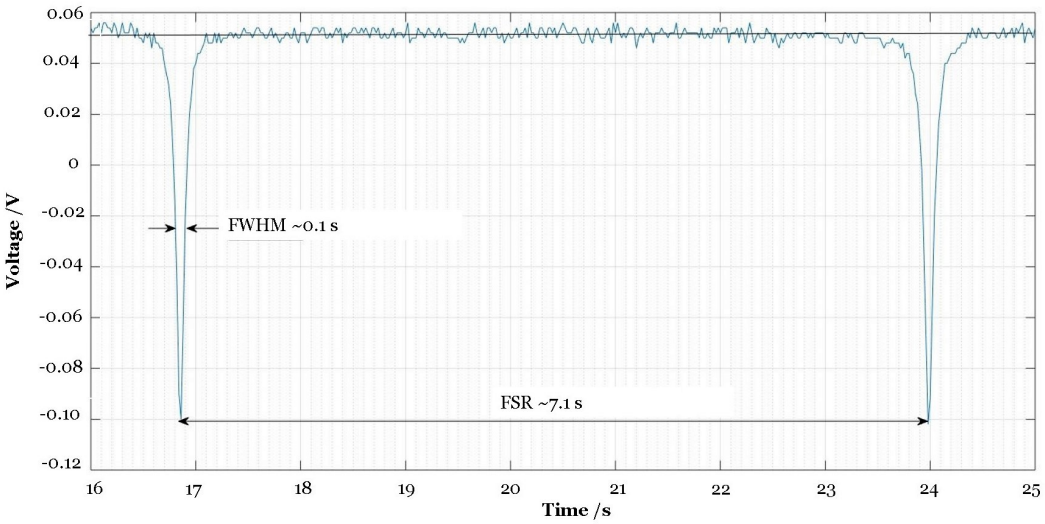

FIGURE 7.15: Temporal finesse characterisation of racetrack resonator from Ma's group, consistent with the finesse determined in their paper.

Ma et al. determined the finesse to be 78.8 for reflection and 80 for transmission, and these figures were found to be broadly consistent with the finesse of 72 found in this work (see fig. 7.11). While the set-up was found to be adequate for determination of the FSR, the modes at the beginning and end of the ramp are seen to be further/closer together due to the somewhat nonlinear response of the thermal tuning. The use of thermal tuning also required slow tuning in order to maximise linearity. A better method of ramping through the wavelengths is needed to ensure linearity, perhaps via modulation of the laser's fast piezo drive. However, this experiment provided a useful characterization set-up and demonstrated the use of the method used by Ma et al. to determine FSR and Q for future experiments.

[2]The laser source lacked a fast piezo drive which would normally be used for tuning

[3]The calculations for Q and finesse remain the same when being calculated in the time domain

7.3 Fabrication & characterisation of CO_2 laser-machined rods at NPL

7.3.1 Germanate glass on sapphire and alumina rods

Laser machined rods at NPL in collaboration with NIST have been successfully fabricated and shown to have ultra-high Qs [2]. These have been used to produce frequency comb sources [3]. The system at NPL consists of a CO_2 laser directed at a motorized spindle for mounting of rods (see fig. 7.15).

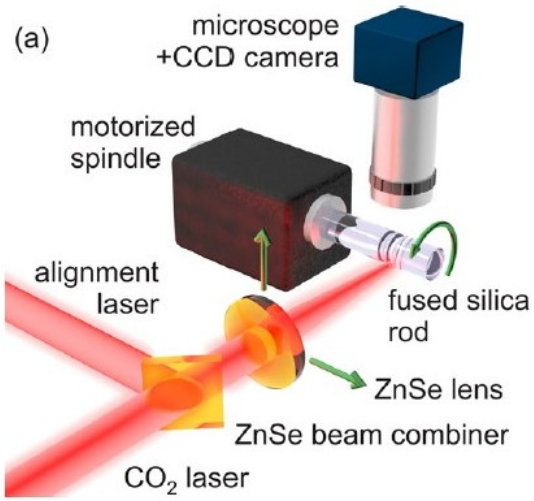

FIGURE 7.16: CO_2 laser machining of silica rods, from Del'Haye et al. [2].

A green laser is used for horizontal alignment of the rods. Rotation speed of the spindle, distance d between the machined "valley" areas and laser power may be adjusted to produce the profile shown in fig. 7.16 by removal of material. Samples used are normally high-purity silica rods.

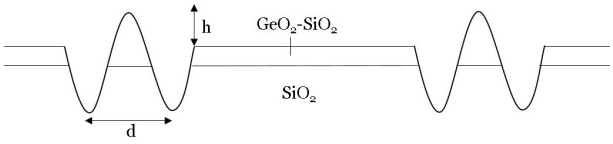

FIGURE 7.17: "Two-point" CO_2 laser-machined rod resonator.

Numerous samples were prepared and taken to NPL for machining. Laser machining of layers on the sapphire rods resulted in discoloration of the machined areas (see fig. 7.17) due to absorption of the laser radiation by the sapphire substrate and localised heating of the machined areas, resulting in reflow of the core layer.

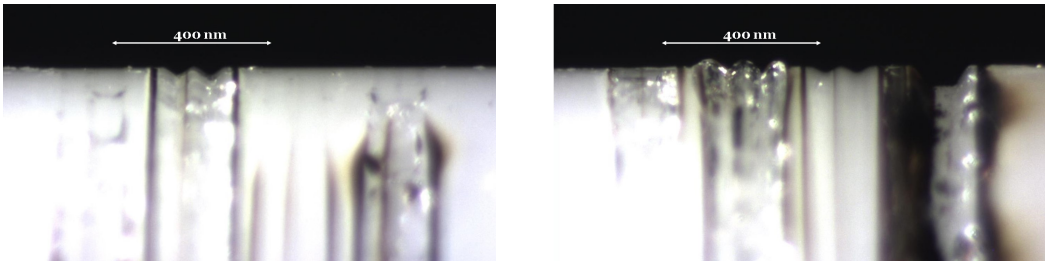

(A) (B)

FIGURE 7.18: "Two-point" CO_2 laser-machined sapphire rod resonators on sample R92. Laser damage can be clearly seen on the machined areas.

A similar experiment was performed on an alumina rod with a thicker germanate layer, R93. A variety of devices were fabricated and are shown in table 7.1 and fig. 7.18. Much less discoloration was seen in comparison to the sapphire rod sample.

TABLE 7.1: Laser machining parameters for sample R93.

Resonator	**Power (W)**	**Pulses (no. × period)**	**RPM**	**Valley spacing, d /μm**	**Height, h /μm**
Res 1	5	11×0.1s	4000	187.5	13
Res 2	5	3×0.1s	2500	250	11
Res 3	5	3×0.1s	2500	250	19
Res 4	5	8×0.1s	4000	250	11
Res 5	5	11×0.1s	4000	218.75	13

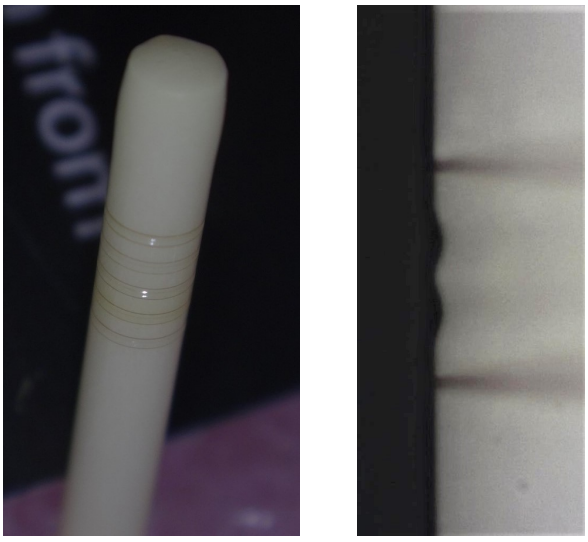

(A) (B)

FIGURE 7.19: CO_2 laser-machined rod R93. (A) Resonators are numbered 1-5 from the top; (B) Machined resonator 5 on rod R93.

Coupling in to these resonators was not possible using silica fibres. While it is not impossible that these structures may function as resonators, a suitably high-index fibre would be required, due to the high index of the rod. Future work to continue this project could perhaps include fabrication of a suitable fibre [4] or alternative means of coupling for high index rods.

7.3.2 Diffused GeO_2-SiO_2 on silica rods

The diffused GeO_2-SiO_2 on silica rod described in section 6.6 was also machined at NPL, with the hopes of its silica-based composition making it more likely to work, being similar to the silica rods machined in the Del'Haye group previously. Parameters for machining are given in table 7.2.

TABLE 7.2: Laser machining parameters for sample R75. Single pulses of 0.1 s were used.

Resonator	**Power (W)**	**RPM (no. × period)**	**Valley spacing, d /μm**	**Height, h /μm**	
Res 1A	8	4000	187.5	-	
Res 1B	7	2000	-	18	Re-machining of resonator 1 in order to better match fig. 7.16
Res 2	5	4000	125	18	
Res 3	6	4000	125	8.5	
Res 4	7	4000	125	15	Pulses visible, implying power too high.
Res 5	7	2500	125	20	
Res 6	7	1000	-	8.5	Much shallower.
Res 7	6	2000	-	32	

FIGURE 7.20: CO_2 laser-machined resonators on sample R75. Resonators are numbered 1-5 from the top.

[4] Having sought one unsuccessfully.

No discoloration was seen as a result of machining this sample, and it remained a high quality appearance post-machining (see fig. 7.19). A variety of different resonator profiles, some of which may be seen in fig. 7.20 were machined into this rod.

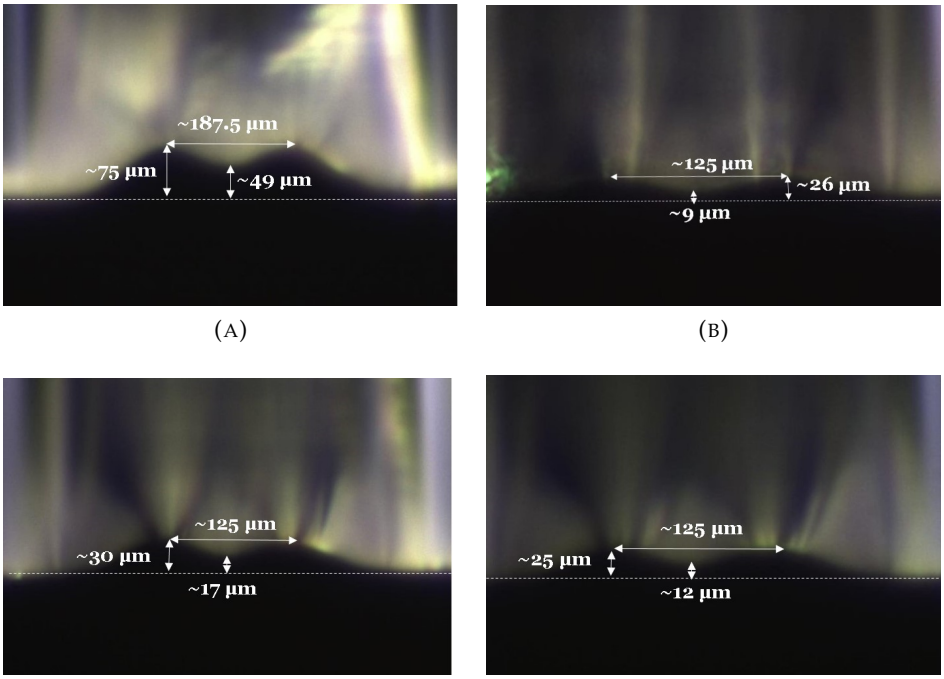

(A) (B)

(C) (D)

FIGURE 7.21: Machined resonators (A) 1 (B) 2 (C) 6 & (D) 7 on rod R75, showing variation in the depth of machined "valleys".

Rod R75 was coupled into a broadband source and its spectrum over the interval 1540-1560 nm recorded. Four of the resonators were coupled into, Res.1, 2, 6 and 7. The experiment was repeated at Southampton (see fig. 7.22) with the same results (see table 7.3 and figs. 7.23 - 7.27) .

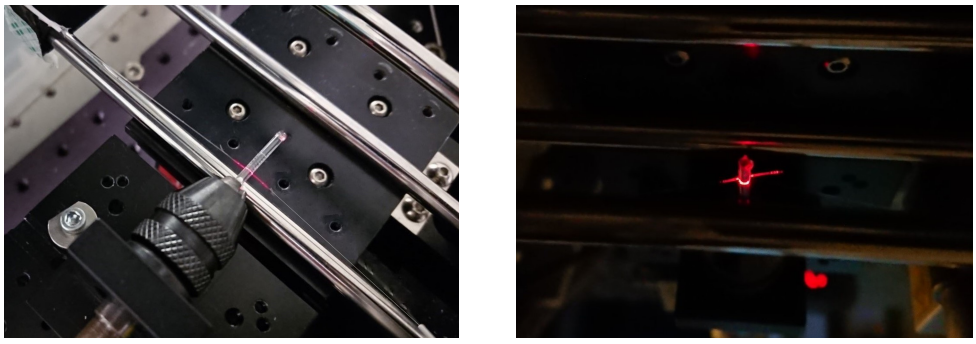

(A) (B)

FIGURE 7.22: (A) & (B): Coupling into resonator 1 of CO_2 laser-machined rod R75, showing significant scattering around the fibre taper and rod.

TABLE 7.3: Laser-machined resonator coupling results. λ=1550 nm; set of modes (1) and (2) are the right-most peak and the peak adjacent to it from the Fourier transforms shown in figs. 7.20-7.24

Resonator	**FSR /nm (1)**	**FSR /nm (2)**	**FWHM (1)**	**Q (1)**	**Finesse (1)**
Res 1	0.2857	0.2000	0.0100	$1.6x10^5$	29
Res 2	0.2778	0.2020	0.0063	$2.5x10^5$	45
Res 6	0.2778	0.2000	0.0075	$2.1x10^5$	37
Res 7	0.2740	0.2000	0.0063	$2.5x10^5$	44
Between res 1 & 2	0.2857	0.2000	0.0055	$2.8x10^5$	52

The presence of two sets of modes, one with m=1 having an FSR of 0.28 nm and another with an FSR of 0.20 nm is intriguing. Calculation of the FSR for r=1.0045 mm, λ=1550 nm, n_{eff}=1.444 gives 0.2636 nm. Calculation of the FSR for r=1.0045 mm, λ=1550 nm, n_{eff}=1.59 gives an FSR of 0.2394 nm. The larger FSR indicates that the mode is perhaps sitting closer to the centre of the rod rather than in the GeO_2-SiO_2 layer. The smaller FSR indicates that the mode is sitting closer to the surface of the rod, and that there is either a slightly greater radius due to the machining process, or a slightly higher refractive index, due to inhomogeneous composition, or possibly both. In any case, there appears to be two unrelated sets of modes, with different FSRs and refractive indices. In all but resonator 1, the set of modes with FSR=0.2857 is the more intense.

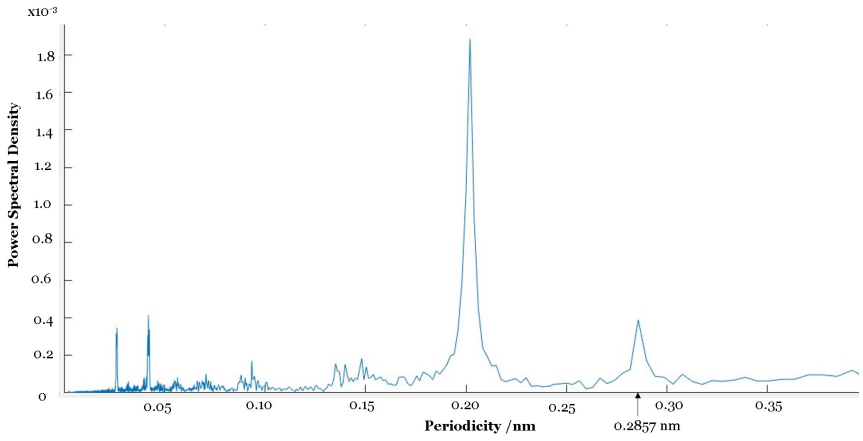

FIGURE 7.23: Fourier transform indicating the FSR for machined resonator 1 on rod R75.

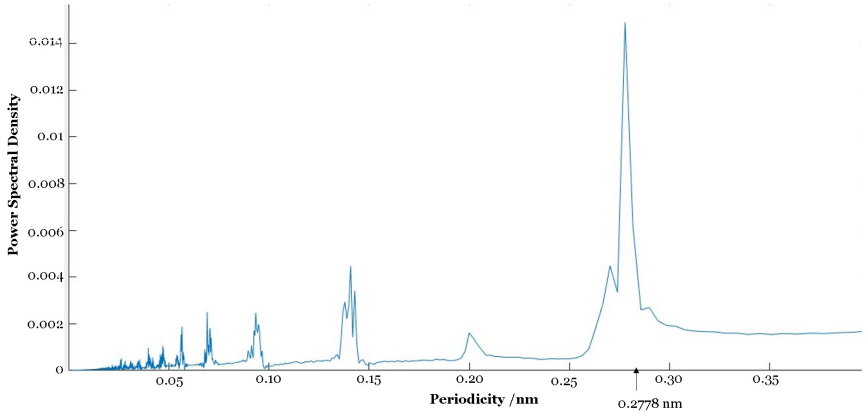

FIGURE 7.24: Fourier transform indicating the FSR for machined resonator 2 on rod R75.

Surprisingly, it was possible to couple into the area between resonators 1 and 2 and resonances could be seen, with a Q of approximately 2.8×10^5.It is possible that light is reflecting off the sloped sides of the areas between machined resonators and a those which fit in an integer number of times are interfering constructively, i.e. multi-mode interference is occurring. However, confirmation of this would rely on a more accurate FSR measurement at higher resolution to avoid missing high Q modes.

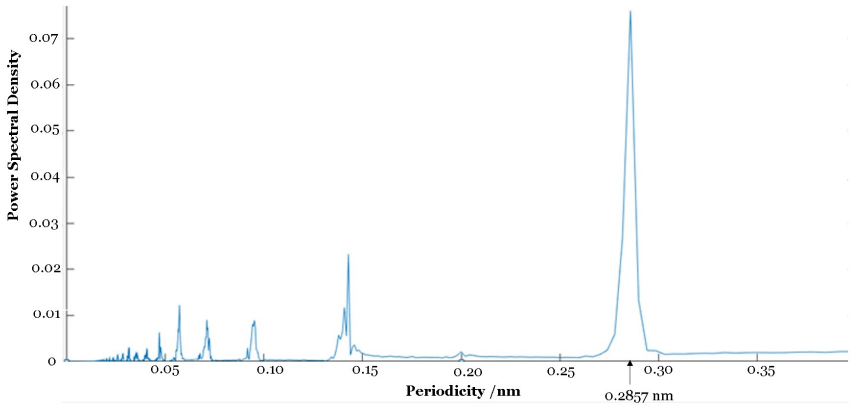

FIGURE 7.25: Fourier transform indicating the FSR for the area between machined resonators 1& 2 on rod R75.

7.3.3 Flame hydrolysis deposition of pre-machined rods

A selection of various rods were machined at NPL for subsequent deposition at Southampton, in order to produce silica rods with a diffused GeO_2-SiO_2 layer. These were characterised at NPL, but only resonator 1 was possible to couple into. The remaining resonators were cleaned in case of having accumulated dust or other particulates during transit, with no improvement, and it was assumed that these were of too poor quality to couple into. The reason for this was unclear, considering all were fabricated under the same conditions.

TABLE 7.4: Laser machining parameters for sample R98.

Resonator	**Power (W)**	**Pulses**	**RPM**	**d /μm**	**h /μm**	**Notes**
Res 1	5	11×0.1s	4000	187.5	13	Q=10^6
Res 2	5	3×0.1s	2500	250	11	
Res 3	5	3×0.1s	2500	250	19	
Res 4	5	8×0.1s	4000	250	11	
Res 5	5	11×0.1s	4000	250	13	

Resonator 1 nevertheless showed a Q of 10^6. This is likely to be due to the deposition post-machining, leading to a higher refractive index area at the apex of each machined ridge, which in the sample (deposited then machined) could easily have been machined away. The Q seen in this sample is the highest seen in this work, showing promise for fabrication of high Q rods suitable for use in rotation sensing or frequency comb sources, and any continuation of this work should certainly include further investigation of pre-machined rods, ideally with characterisation both before and after deposition.

7.4 Conclusions

7.4.1 Characterisation of glass spheres and planar resonators

This chapter has provided details on the characterisation of ring resonators. Glass spheres were characterised. 6 μm tapers and above were found to be adequate for coupling in but multi-mode due to poor radial confinement, as would be expected in a glass sphere, in contrast to a ring resonator. Fimmwave modelling suggested that a 2 μm taper would be single-mode and this is backed up by literature. However, the laser splicer could not reliably fabricate tapers at this diameter. Damascene ring resonators were coupled via 6 μm tapered fibres using the same experimental set-up, but the spectra proved to be pseudo-periodic on examination of their Fourier transforms, with no coincidence of modes when coupled multiple successive times via the same fibre. This does not necessarily preclude these structures acting as resonators: The structures' geometry is uneven due to issues levelling the milling platform and while every effort was made to avoid air currents moving the taper, this could not be eliminated. Combined with the limitations in the maximum observable Q, few conclusions can be drawn here, although high Q is unlikely to due to the unevenness of the ring. Finally, useful characterisation set-ups were also produced for a racetrack resonator chip in preparation for characterisation of planar UV-written waveguides.

7.4.2 CO_2 laser-machined alumina and sapphire rods

B_2O_3-GeO_2 glasses deposited on to alumina and sapphire rods were CO_2 laser-machined at NPL. Darker lines around the deepest machined areas could be seen, perhaps due to easy removal of the core layer and subsequent reduction of Al_2O_3. The laser power had to be reduced in order to avoid this. A thicker germanate layer will be required in order to more easily machine these samples in future. Resonator structures were nevertheless produced, but characterisation was not possible with standard SMF-28 tapered fibres, which is likely to be due to the large difference in refractive index between the taper and the rod.

7.4.3 CO_2 laser-machined diffused silica rods

Silica rods consolidated in the furnace at high temperature in order to produce GeO_2-SiO_2 as described in the previous chapter. These samples were CO_2 laser-machined and briefly characterised at NPL. Q of around 10^5 was seen for the ring resonators, all of which were found to be multi-mode. It was found that by placing the taper between resonators it was possible to couple into the rod and that the spectra seen were similar to those coupled into machined resonators. These results were confirmed by further characterisation at Southampton. It is suspected that the light coupling in may be reflected off the sides of the machined areas, with modes which fit into the circumference interfering constructively to produce multi-mode interference.

7.4.4 Pre-machined diffused silica rods

Various rod structures were machined into un-deposited silica rods at NPL, and subsequently deposited with GeO_2 and consolidated in the furnace at 1360 °C to produce diffused GeO_2 rods. Only one resonator structure on one of the rod samples could be coupled into. However, this resonator was found to have a Q of approximately 10^6. The pre-machining of the rods means that the mode resides in the

GeO_2-rich area of the resonator structure. In the samples deposited and then machined this area would be largely removed, so the pre-machined sample is likely to have better confinement and thus a higher Q, and may be superior to deposition and subsequent machining. The high Q seen here shows that this method has promise for development of CO_2 laser machined flame hydrolysis deposited rod resonator structures for use in gyroscopes or frequency comb sources.

7.5 Bibliography

[1] M. Cai, O. Painter, and K. J. Vahala,“, Observation of Critical Coupling in a Fiber Taper to a Silica Microsphere Whispering-Gallery Mode System”, *Phys. Rev. Lett.* 85: (74) 2000.

[2] P. Del'Haye, S. A. Diddams & S. B. Papp, “Laser-machined ultra-high-Q microrod resonators for nonlinear optics”, *Appl. Phys. Lett.* 102: 221119, 2013.

[3] S. B. Papp, P. Del'Haye & S. A. Diddams, “Mechanical Control of a Microrod-Resonator Optical Frequency Comb”, *Phys. Rev. X,* 3: 031003, 2013.

[4] T. J. A. Kippenberg, “Nonlinear Optics Ultra-high-Q Whispering Gallery Optical Microcavities”, (Thesis), California Institute of Technology, 2004.

[5] R. Sun, J. Cheng, J. Michel & L. Kimerling,“Transparent amorphous silicon channel waveguides and high-Q resonators using a damascene process”, *Opt. Lett.* 34 (15): 2378-2380, August 2009.

[6] H. Ma, S. Wang & Z. Jin, “'Measurements of the excess loss of the crossed waveguide using optical waveguide ring resonators”, *Optics Comms.* 281: 6016-6018, 2008.

Chapter 8

Towards ring resonator-based inertial sensing

8.1 Summary of work completed

Flame hydrolysis deposition of planar germanate glasses has been investigated. This included development of recipes for deposition of silica-germania, pure germania on to thermal oxide, silicon and oxidised silicon wafers and sapphire wafers. Doping of germanate glasses with phosphorus and boron, facilitated by the FHD system and bismuth using solution doping on silica, silicon and sapphire wafers was also investigated. The composition, optical properties and response to UV writing of these samples was studied.

Pure and high germania-content glasses are found to be unstable when deposited onto silica and silicon wafers, and this is attributed to the large difference in thermal expansion coefficient causing internal stresses which aid reaction with water and solvents. An improvement in stability of germania on silica layers by high temperature consolidation followed by low temperature consolidation shows promise in terms of developing stable pure germania-on silica layers, due to the gradual change in CTE. The deposition of stable germanate layers on to sapphire, with its similar CTE to germania has been described. Little photosensitivity is seen in these glasses. A small, but not quantifiable response is seen in hydrogen-loaded low-on-high temperature wafers, but coupling is impossible due to deterioration of the sample due to the damp hydrogen-loading environment. Further stress reduction may make UV writing of these samples possible. Photosensitivity has been seen in a germania on sapphire sample at 244nm and ablation has been seen at 213 nm, giving hope that further work may improve these responses.

The deposition of FHD germanate glass on to rods and tubes as an alternative geometry to the planar ring resonator and development of this process and successful recipes has been described. Adaptation and development of the FHD and UV writing processes in order to accommodate the rods has been described. Photoluminescence of various colours has been seen in B_2O_3-GeO_2 on alumina rods under UV excitation. This phenomenon has not been mentioned in the relevant literature to the best of the author's knowledge.

CO_2 laser-machining of germanate glass on alumina, sapphire and diffused GeO_2-SiO_2 on silica rods to form resonator structures at NPL has been described. Diffused GeO_2-SiO_2 on silica rods show promise as high Q resonators, with a Q of 10^6 recorded in a pre-machined sample deposited with GeO_2 and consolidated at high temperature in order to produce a diffused layer. The phenomenon of spectra being

produced when coupled via a fibre placed between resonators is both unexpected and intriguing and requires further investigation to confirm the presence or otherwise of multi-mode interference. A suitable fibre is needed to attempt coupling into germanate on sapphire and alumina in order to determine whether these structures may be usable as resonators. In summary, the following have been achieved:

- Fabrication of stable GeO_2-SiO_2 layers by consolidating at high temperatures of 1300 °C and above, due to the diffusion of silica into the germania layer, reducing stresses.
- High germania content glasses can be made more stable by depositing onto a high temperature layer
- The first known fabrication of Bismuth-doped germania using FHD and solution doping has been achieved.
- Stable pure and high germania content glasses have been consolidated onto sapphire wafers, attributed to the similar CTE.
- Stable germanate glass layers have been deposited onto alumina rods.
- Stable diffused GeO_2-SiO_2 layers have been consolidated on silica rods
- Characterisation set-ups for glass spheres, planar ring and rod resonators and ring resonator chips have been realised
- A stable, diffused FHD GeO_2-SiO_2 layer on silica rod has been CO_2 laser machined to produce resonators with Qs on the order of 10^5.
- Possible multi-mode interference has been seen in the above resonator.
- Stable diffused GeO_2-SiO_2 layers on pre-machined rods have been used to produce resonators with Q factors on the order of 10^6.

8.2 Work required to complete or further the project

The sensitivity to water and solvents has been a considerable and recurrent problem in the development of germanate glasses described in this work. Further stress reduction may improve the stability of planar germania and doped germanate glasses and make UV writing of GeO_2 on silica samples possible. The technique of depositing a high temperature consolidated layer on top of one of lower temperature was seen to reduce sensitivity to water and solvents and this method could potentially be further developed to incorporate multiple layers.

There are suggestions of photosensitivity in germania on sapphire layers at 244 nm, and further fabrication, characterisation and UV fluence testing would be useful to maximise any photosensitive refractive index change. At 213 nm, germania on sapphire ablated but at lower power and fluence no response was seen. There is presumably some point where refractive index change is seen without ablation, even if only a narrow range of powers and fluences are acceptable, and this warrants further experimentation. Photoluminescence in germanate glasses is often attributed to colour centres such as the GeE′ centre, and it would be useful to gain a deeper understanding of the composition of these samples, presence of colour centres and reactions which produce them. In terms of developing a planar ring resonator, UV writing of a ring resonator in low germania content glass, already established as photosensitive, would be helpful and allow investigation into the use of Bragg gratings.

The development of rod samples shows much promise in terms of both UV writing and CO_2 laser-machining. Further compositional analysis of germanate on alumina rods is required in order to understand the origin of photoluminescence of varying colours under UV exposure at 244 nm, and to aid in finding methods of increasing any UV-induced refractive index change. Coupling in of UV light in to a germanate-on-sapphire rod during UV writing indicates a high quality surface. If suitable parameters for CO_2 laser machining could be made possible, high Q could be possible in these samples. The apparent multimode interference seen when coupling between laser-machined resonators needs further investigation in order to determine if this phenomenon is in fact occurring.

Machined rods may be further developed: FHD recipes for pre-machined rods may be improved, and the machining parameters, e.g. valley spacing and depth, may be optimised in order to provide maximum Q. This may also aid confinement as well as the small mode volume required for nonlinear processes to occur, opening up the possibility of using the rods to produce frequency comb spectra. Thus the following are needed in order to further the project:

- UV writing of low-germania content glass ring resonator and characterisation.
- Further material analysis, e.g. stress testing, EPR for identification of colour centres in photoluminescent rod samples.
- Further UV writing at various fluences and subsequent characterisation of waveguides and Bragg gratings in germania-on-sapphire planar samples.
- Further fabrication and characterisation of diffused rod samples in order to establish presence of multi-mode interference.

- Suitable tapered fibre or other method of coupling into alumina and sapphire rod resonators.
- Development of FHD recipes and machining parameters (e.g. control of valley depth via laser power, distance between valleys) in order to maximise Q in FHD rod resonators.
- A method of producing high resolution spectra for coupled rods in order to allow determination of high and potentially ultra-high Q and allow investigation of whether the apparent multi-mode interference seen in rod R75 is indeed occurring.

8.3 Outlook

The original aim of this work was to provide proof of concept of a ring-resonator-based rotation sensor as a step towards development of a compact, portable inertial sensing system and additionally investigate its potential for use as a frequency comb source.

While material and fabrication difficulties initially proved a barrier to swift progress (in particular the sensitivity of germania to moisture and solvents, exacerbated by stresses caused by CTE mismatch), this lead to the exploration of an alternative geometry in rod resonators. The eventual development of stable planar germania on sapphire samples detailed here, and in particular the indications of UV photosensitivity give hope of UV writing a ring resonator and coupling waveguides and Bragg gratings.

FHD-germanate glass deposited CO_2 laser-machined rod resonators show much promise and novelty in fulfilling the original aim, showing high Q, and potential for higher Q due to the upper limit on determination of Q due to the resolution of the system used. More accurate determination of Q may indeed demonstrate higher Qs and resonators machined into Germania-on-alumina and sapphire may yet show high Q. The possible MMI seen in one sample is certainly intriguing and worthy of further investigation.

A robust method of coupling is required for rod resonators, and development for use as a rotation sensor will require careful consideration of athermal techniques and suitable materials in order to minimise thermo-optic coefficient and thermal expansion coefficients, the former being a significant source of error. The nonlinearity of these samples is unknown, and unwanted nonlinear effects such as the Kerr effect may further hinder rotation sensing. Conversely, a highly nonlinear material would be ideal for production of a frequency comb source.

In summary, accurate determination of Q, nonlinearity, will allow a better assessment of the use of these devices as rotation sensors or frequency comb sources. The high Q seen gives promise that, with refinements to fabrication and composition of deposited glass layers, combined with appropriate signal processing and development of a robust coupling technique, rod resonators could be developed for use in an inertial sensing system in the future.

Appendix A

Publications

M. T. Turvey, P. L. Mennea, C. Holmes, P. G. R. Smith, & J. C. Gates, "Direct UV Written Waveguides in Phosphogermanate Planar Glass Layers Fabricated via Flame Hydrolysis Deposition," in Advanced Photonics 2016 (IPR, NOMA, Sensors, Networks, SPPCom, SOF), OSA technical Digest (online) (Optical Society of America, 2016), paper ITu3A.3.

C. Gawith, J. C. Gates, P. L. Mennea, L. G. Carpenter, S. A. Berry, C. Holmes, S. Lynch, M. Posner, R. Bannerman, M. T. Turvey, P. A. Cooper & P. G. R. Smith,"Fabrication of integrated optical waveguides for use in new quantum technologies", International Conference on Photonics 2016, Sarawak, Malaysia. 14 - 16 Mar 2016.

P. G. R. Smith, J. C. Gates, C. Gawith, C. Holmes, Carpenter, L. G. Carpenter, S. A. Berry, T. I. Ferreiro, P. L. Mennea, M. Posner, P. A. Cooper, S. Lynch, R. Bannerman, M. T. Turvey & A. Jantzen, "Planar integrated optics for quantum technologies", Progress in Electromagnetic Research Symposium, Shanghai, China. 08 - 11 Aug 2016.